Broadband excitation of fuel cells for online condition monitoring using different switch-mode DC-DC mode topologies

Prepared by:

SURPRISE MAHLANGU

Department of Electrical Engineering
University of Cape Town

December 2022

Submitted to the Department of Electrical Engineering at the University of Cape Town in fulfilment of the academic requirements for a Master of Science degree in **ELECTRICAL ENGINEERING**

Declaration

1. I know that plagiarism is wrong. Plagiarism is to use another's work and pretend that it is one's own.
2. I have used the IEEE convention for citation and referencing. Each contribution to, and quotation in, this final year project report from the work(s) of other people, has been attributed and has been cited and referenced.
3. This final year project report is my own work.
4. I have not allowed, and will not allow, anyone to copy my work to pass it off as their work or part thereof

Name: **SURPRISE MAHLANGU**

Signature: Signed by candidate **Date:** 02 June 2023

Acknowledgements

A great number of people were involved, in supporting me and assisting me through the postgraduate journey in one way or another, for those not mentioned, please know that I express my gratitude.

Firstly, I would like to thank my supervisor for the research opportunity I was afforded, for taking me as his student and supervising me. I appreciate the support he has provided throughout the research journey, constructive criticism and assistance, more especially during the COVID-19 period. Thanks! Prof. Paul Barendse.

I express my gratitude to the AMES group and staff, special thanks to Mr Maysam Soltanian, Riyaad Jacobs and Hoosain Salie for your assistance in the Power Engineering Lab. Thanks to Linda and John for the guidance through the research journey, and thanks to the following people, Kwabena Koraheng ,Nosi Kwini, Musa Thokwe, Simamnkele Dingiswayo, Themba Makamu, Ronaldo Ndlovu, Oyetunji O Iyanuoluwa and Kukhokukhle Tsengwa , for the companionship.

Thanks to Nkateko Tergo Ngobeni and Mzamo Mncibi for assisting with the proof-reading of the final draft, with special thanks to Kwabena Koraheng, for the proof-reading and suggestions with the final draft.

And last but not least, I express my gratitude to NRF and UCT PFGO, and my family for supporting me through the research journey. Lastly, I would like to thank myself for keeping it all together-*Rick and Morty*~S2E7.

I would like to thank God who has given me the strength, knowledge and perseverance to complete the project.

Abstract

There is a great demand for renewable energy sources, and these include solar and wind energy sources. However, a renewable energy source with a continuous energy supply is desired, but energy sources from wind and solar energy sources are intermittent, i.e., solar energy is only available during the day, and wind energy's availability is dependent on the season of the year and climate in the area. This, in essence, makes fuel cell systems desirable as a renewable energy source and storage in the form of green gases obtained from electrolysis or other processes using these intermittent green energy sources.

Online condition monitoring of fuel cell systems without the need for additional hardware is desired in both stationery and transportation applications. Recent work has explored the use of online impedance spectroscopy for batteries using multi-sine signals through a single dc-dc converter. However, for fuel cells, the non-linearity of both the converter and the fuel cell poses a challenge to the online monitoring process. There is also a need for faster diagnostics due to the internal operating conditions of the fuel cell needing immediate control and regulation. This study demonstrates the use of the pseudo-random binary sequence (PRBS) to perform impedance spectroscopy in comparison to a single sinusoid injection. This is done to show the comparison between the two signals and to show the decrease in impedance estimation time brought about by PRBS in comparison to multi-sine signals. PRBS is a faster and easier technique to implement compared to the single-sine signals used in the condition monitoring of batteries. The tolerance of error brought by the implementation of impedance spectroscopy through PRBS and single-sine signals through a dc-dc converter is compared to the benchmarked theoretical results. This is demonstrated in simulation and experimentally. Results obtained from the Frequency Response Analyzer (FRA) are compared to the results obtained through a dc-dc converter using PRBS and Electrochemical Impedance Spectroscopy (EIS) as testing signals.

Thereafter, this study demonstrates the feasibility and compares the use of the buck-boost and boost converters to perform impedance spectroscopy, and this is done by modelling and designing the converters for a linearized region of operation to accommodate different operating conditions of the fuel cell. This is achieved mainly using the double loop control strategy, which is rarely used in literature yet brings the benefits of controlling the power transfer and IS implementation. A practical buck-boost converter has discontinuous input current, more switching harmonics, and noise compared to the boost converter. As such, the contribution and influence of these factors are explored with regard to impedance estimation. The comparison of tolerance of error brought about by the implementation of impedance spectroscopy through PRBS and multi-sine signals using the boost and buck-boost converters are compared to the benchmarked theoretical results and Frequency Response Analyzer results.

Table of Contents

Table of Figures

List of abbreviations

AC	Alternating Current
ADC	Analogue to Digital Converter
BIS	Broadband Impedance Spectroscopy
DAC	Digital to Analogue Converter
DC	Direct Current
DFT	Discrete Fourier transform
DUT	Device Under Test
EEC	Electrical Equivalent Circuit
EIS	Electrical Impedance Spectroscopy
ESR	Equivalent Series Resistance
FFT	Fast Fourier Transform
FRA	Frequency Response Analyser
GM	Gain Margin
LTI	Linear Time-Invariant
MIMO	Multiple Input Multiple Output
NI	National Instruments
PEM	Proton Exchange Membrane
PM	Phase Margin
PRBS	Pseudorandom Binary Sequence
PWM	Pulse Width Modulation
QFT	Quantitative Feedback Theory
RHP	Right Half Plane
SIMO	Single Input Multiple Output
SMC	Switch-Mode Converter
SNR	Signal to Noise Ratio

Chapter 1

Introduction

1.1 Background to the study

With the challenge of load-shedding in South Africa, and the efforts to reduce global warming caused by the rise in greenhouse gases, there is a need for green energy that reduces carbon footprint. There are several renewable sources, such as wind and solar energy sources, that are geographically dependent; these sources are fluctuating and intermittent. As such, when they produce peak power at times when the load demand is minimal, they need energy storage. The storage of these systems can be stored in high-energy capacitors, lithium-ion or lead batteries, compressed air, pumped hydro, or hydrogen. However, these storage sources have their limitations, with hydrogen having the advantage of being useful when there is a need for a large scale of energy to be stored for short and long periods. Fig. 1.1 shows the typical discharge time and power ratings for different energy sources.

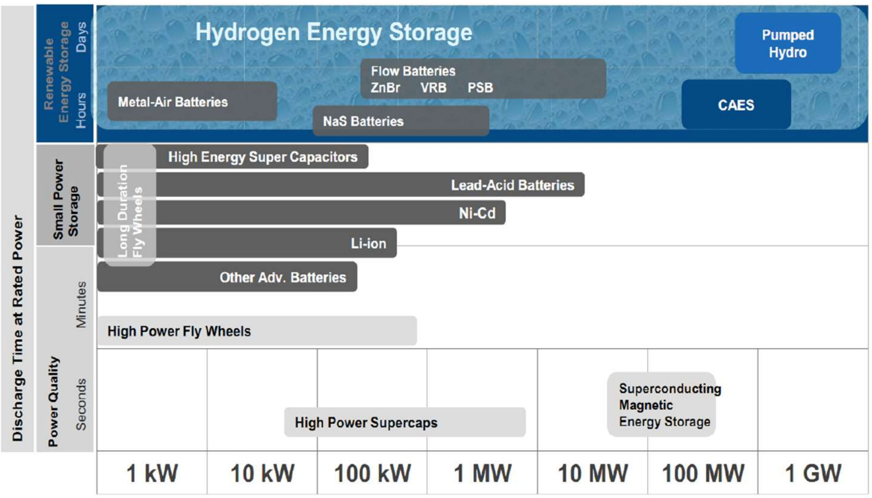

Fig. 1.1: Storage systems [1]

Hydrogen is used in many applications, this includes applications in stationary and mobile applications, and they are also used as backup power in remote areas within the telecommunication industry. There are at least 20 thousand cooled hydrogen generators worldwide, with an estimated value of over USD 0.8 billion [2]. These come as the potential of hydrogen due to its unique characteristics such as an abundance of raw hydrogen in water, water electrolysis has a high hydrogen conversion efficiency and the environmental friendliness when it produces electricity and water as by-products.

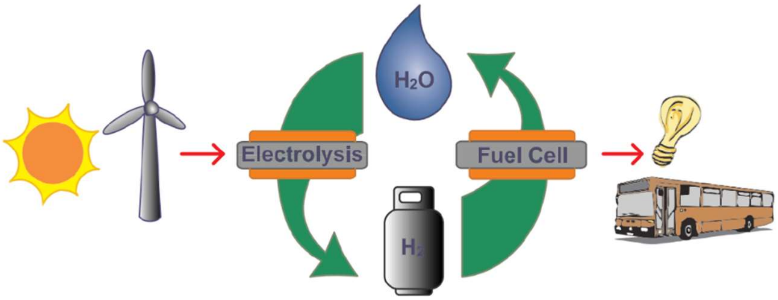

Fig. 1.2: ideal cycle for fuel cell [1]

Given the benefits of fuel cell systems as storage units and the benefits of hydrogen as an energy carrier, there are larger operation and maintenance costs associated with these systems, the cost of maintenance accounting for part of the system's cost. When operating the fuel cell systems, there are faults and degradation of the system performance observed, as such fault detection mechanisms that are affordable and faster are desired to quickly return the system to operation.

Predictive maintenance is more advantageous compared to preventative maintenance [1] [2]. As such, since the Proton Exchange Membrane Fuel Cell (PEMFC) is a multi-physics system, predicting its dynamic response is desirable, and this means the proper management of the system operating conditions such as the water, temperature, and pressure conditions [1]. The complete control and management of these operating conditions result in the optimized performance of the PEMFC. However, some challenges are associated with the condition estimation of the PEMFC system during operation.

1.2 Research questions

Based on the problems identified, the research questions considered are as follows:

i. What are the common faults observed in fuel cell systems, and what current techniques are used to detect these faults?

ii. Given the non-linear nature of converters, how do they impact the inducted signal used for condition monitoring?

iii. What control techniques are best suited for online impedance spectroscopy of fuel cells?

iv. What parameters are obtained for the electrical equivalent circuit of the fuel cell and how do the variations in the parameters affect the overall dynamic system.

1.3 Research Purpose and objectives

The main purpose of this study is to estimate the fuel cell water management in real-time using different dc-dc converters to perform a process called Impedance Spectroscopy (IS). [3] shows the use of a boost converter to perform IS, however this is different from this study by that in this study a different modelling technique of the converter is used, which is average current modelling and [3] does not investigate different operating conditions. The study demonstrates the use of the buck-boost and boost converters to simultaneously facilitate power transfer whilst implementing IS for condition monitoring. The work presented in this study aims to compare the boost converter to the buck-boost converter, to investigate the contribution/influence of the switching current harmonics associated with the converters in online condition monitoring whilst adopting the double loop control strategy [4] to control the fuel cell input current and the dc-dc converter output voltage.

A Pseudo-Random Binary Sequence (PRBS) signal is investigated along with the single sinusoid signal and is compared against the benchmarked Frequency Response Analyzer (FRA) results to ascertain their accuracy, given that they both allow online condition monitoring. The contribution of the work lies in pairing the excitation signals with its preferred dc-dc topology based on its accuracy in determining impedance. In addition, determining the influence of the buck-boost converter switching harmonics and discontinuous input current when performing online condition monitoring.

To address the questions raised in line with the aim of this research study, the following objectives are pursued:

- Explore fuel cell state of health.
- Describe the test rig to emulate different fault scenarios.
- Explore signal synthesis for rapid estimation and implement for the fuel cell. Incorporate the dc-dc converter for online monitoring using impedance extraction.
- Investigation of the buck-boost converter’s discontinuous input current, switching harmonics, and noise in relative to the boost converter. As such, the influence of these factors will be explored through impedance estimation.

- Compare the feasibility of the two converters to perform IS, and the associated error of each converter when doing impedance estimation.

1.4 Scope and limitations

1.4.1 Scope of the study

The focus will be on the characterization and monitoring of the PEMFC. The fuel cell online condition monitoring will be limited to the internal water management of the fuel cell system, and this is the impedance characterization of the normal, flooding and drying operating conditions.

1.4.2 Limitations of the study

The fuel cell systems testing will be conducted in the laboratory; the tests will be performed with the laboratory's available equipment and components. Given the cost limitations, the fuel cell system will be emulated, and the power rating of the emulated fuel cell system will be approximately 100 W, which will be a scaled-down version of a fuel cell system with a power output of $1kW$.

1.5 Plan of development

The organization of this study is detailed below.

1.5.1 Chapter 2

This chapter reviews in detail the chemical properties and electrical processes of fuel cell systems. It dives into the types, thermodynamics, Nernst and Butler-Volmer relationships, power generation and losses associated with the fuel cells. It then explores the fuel cell conditioning and the basic characteristics, fuel cell efficiency and converter applications.

1.5.2 Chapter 3

This chapter reviews impedance spectroscopy as a linear characterization technique. It further develops the understanding of using a single sinusoid signal for injection along with it its respective parameter selection. i.e., the amplitude, phase, and signal frequency. Thereafter, the PRBS signal is described, its characteristics and design optimization for performing online condition monitoring. The impedance spectroscopy consideration follows, then the modelling of fuel cell systems from the application of impedance spectroscopy.

1.5.3 Chapter 4

The operation of a basic buck-boost converter is explored, and thereafter this chapter details the analytical modelling of the buck-boost converter using the Kirchhoff's voltage and current laws. The buck-boost converter's modes of operation are analyzed, and the governing equations are derived. These derived governing equations are used to design the converter system requirements, as these derived equations assist with the components selection, and this is followed by the state-space average modelling, state-space average model linearization and state-space s-domain Laplace transformation.

The transfer functions of the buck-boost converter relating the input current, inductor current and input voltage to the output voltage and current using the duty cycle as the control signal are derived, and the transfer function equation that is used to inject the input current into the converter when the signal is in open-loop is also presented. Along with the double loop control strategy of the converter being presented, in addition to the incremental simulation results of the converter when in open loop and closed loop, where in each configuration, the power transfer and implementation of IS is presented, in addition to the impedance extraction and error analysis.

1.5.4 Chapter 5

Similar to chapter 4, the boost converter's basic operation is explored; this chapter also details the analytical modelling of the boost converter from Kirchhoff's voltage and current laws. The boost converter's modes of operation are analyzed, and the governing equations are derived. These derived governing equations are used to design the converter system requirements, as these derived equations assist with the components selection from chapter 4.

The state-space average modelling, state-space average model linearization and state-space s-domain Laplace transformation are performed. The transfer functions of the boost converter relating the input current, inductor current and input voltage to the output voltage and current using the duty cycle as the control signal are derived. The transfer function equation that is used to inject the ac input current into the converter when the signal is in an open loop is also presented. Lastly, the design of the double loop control strategy of the converter is presented, along with the incremental simulation results of the converter when in open loop and closed loop, where in each configuration, the power transfer and implementation of IS are presented, along with the impedance extraction and error analysis of the boost converter comparing the EIS and PRBS signal.

1.5.5 Chapter 6

This chapter details the practical aspects of the project, and this includes the equipment, components and the circuit used to perform the tests to generate and acquire signals that will then be used for the digital signal processing to achieve online condition monitoring.

The fuel cell emulation procedure is described, along with the parameters associated with the fuel cell with respect to the electrical Randle circuit and the chemical property of the Randle circuit parameters in a fuel cell system. Thereafter, the Frequency Response Analyzer is described, along with the calibration process, the modules it contains, its application limitation when operating in galvanostatic and potentiostatic mode and the process that was followed to obtain the benchmark results. The dc supply equipment used, the components used (MOSFETS and diodes) are presented, as well as the drive circuits. Lastly, the filters used along with the measuring probes and the DAQ are presented.

1.5.6 Chapter 7

The experimental results of the boost converter obtained following the hardware setup described in chapter 6 are presented. These results start with the open-loop results of the boost converter without the fuel cell system integration for power transfer and both power transfer and impedance spectroscopy. Thereafter, it presents the closed-loop experimental results of the boost converter when facilitating power transfer only and when performing both power transfer and impedance spectroscopy at the same time; this is done when the fuel cell is integrated and not integrated into the boost converter. This is to show the analysis of the converter with each step. Lastly, the extracted impedance results are presented along with their associated error from the two signals, the EIS and PRBS.

1.5.7 Chapter 8

Similar to chapter 7, the experimental results of the buck-boost converter obtained following the hardware setup described in chapter 6 are presented. These experimental results presentations start with the open-loop results of the buck-boost converter without the fuel cell system integration for power transfer and both power transfer and impedance spectroscopy. Thereafter, it presents the closed-loop experimental results of the buck-boost converter when facilitating power transfer only and when performing both power transfer and impedance spectroscopy at the same time. This is done when the fuel cell is integrated and not integrated into the buck-boost converter; this is to show the analysis of the converter with each step. Lastly, the extracted impedance results are presented along with their associated error from the two signals, the EIS and PRBS.

1.5.8 Chapter 9

A comparison of the boost converter and buck-boost converter is presented. The chapter firstly presents the simulation comparison of the two converters when performing impedance spectroscopy when using EIS and PRBS separately. The Nyquist impedance results and the error analysis of each signal across the converters. Lastly, it presents the experimental impedance results when performing impedance spectroscopy using each signal (PRBS and EIS) across the two converters before concluding on the error performance of the two converters when using the two distinct signals.

1.5.9 Chapter 10

This chapter presents the conclusions reached and recommendations for possible future work.

1.6 Contributions and research outputs

This research contributes towards impedance spectroscopy using dc-dc power converters for fuel cell applications. This was firstly done by using a double loop control strategy to facilitate power transfer whilst implementing impedance spectroscopy. This was done to improve the accuracy and ease of control whilst enabling faster measurements using the PRBS signal. In application, two converters were designed and built to facilitate these, and to validate their results, whereby it is compared against results from a commercial FRA device (Nova auto lab), to determine whether it has potential real-time state of health determination.

Conference Publications

1. S. Mahlangu and P. Barendse, "Online Condition Monitoring of Fuel Cells (FC) by Implementing Electrical Impedance Spectroscopy using a Switch-Mode DC-DC Converter," in 2021 IEEE Energy Conversion Congress and Exposition (ECCE), Vancouver, 2021.
2. S. Mahlangu and P. Barendse,” Fuel Cell Stack Broadband Excitation for Online Condition Monitoring Using Different Switch-mode DC-DC Topologies”, in 2022 IEEE Energy Conversion Congress and Exposition (ECCE), Detroit, 2022.

Chapter 2

Fuel cell overview

2.1 Introduction

This section will present the fundamental components of a fuel cell, while also describing its electrochemical process. Additionally, the theoretical models derived from the Butler-Volmer equations will be presented to express the relationship between chemical energy and electrical energy. Fuel cells are categorized based on their distinct properties, such as material constituents and operating temperature. Some of these fuel cells are [4], [5]:

- Proton-Exchange Membrane Fuel Cell (PEMFC)
- Phosphoric Acid Fuel Cell (PAFC)
- Alkaline Fuel Cell (AFC)
- Solid-Oxide Fuel Cell (SOFC)
- Molten Carbonate Fuel Cell (MCFC)

From the variety of fuel cells presented, the Proton-Exchange Membrane Fuel Cell is the most commonly used fuel cell because of its viability and simplicity [6]. That is why it has been chosen to be the focus of this research.

2.2 The fuel cell as an electrochemical system

The study of the interrelation between the chemical and electrical (i.e. the movement of electrons and ions) realm is called electrochemistry [5]. Electrochemical principles are used for a range of applications such as electrophoresis, electroplating of metals and electrochemical displays. In these electrochemical systems the production of electrical energy is related to the chemical reaction through the flow of the electrical current, that is electrons [4], [7].

An electrochemical cell is composed of an electrolyte and two electrodes, whereby the electrolyte is used for ionic conduction and the electrodes for electrical conduction [4]. On the location of the electrode where oxidation occurs it is called the anode, and where reduction occurs it is called the cathode [4], [1]. Electrochemical cells which have spontaneous chemical reactions are called galvanic cells, and electrochemical cells where the chemical reactions are non-spontaneous are called electrolytic cells. Galvanic cells are usually used for the generation of electrical energy from chemical compounds that react spontaneously, such as fuel cells and batteries. On the other hand, electrolytic cells are usually used for industrial purposes such as the large-scale production of elements like aluminum, chlorine and the production of hydrogen. Fig. 2.1 illustrates the configuration of a galvanic cell and an electrolytic cell [4].

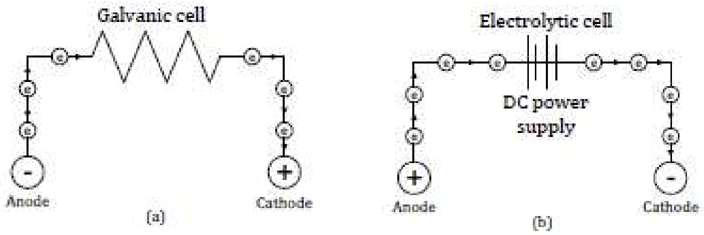

Fig. 2.1: Electrochemical system (a) a Galvanic cell and (b) an Electrolytic cell [4]

Fig. 2.1 is a spontaneous reaction (galvanic cell), whereby the positive electrode is the cathode, and the negative electrode is the anode, which is the opposite in an electrolytic cell. The fuel cell is a galvanic cell, as the chemical reaction is exothermic. As such, the reactions that take place are as follows [1], [4]:

Anode half-reaction (2-1):

$$2H_2 \rightarrow 4H^+ + 4e^- \qquad (2\text{-}1)$$

Cathode half-reaction (2-2):

$$O_2 + 4H^+ + 4e^- \rightarrow 2H_2O \qquad (2\text{-}2)$$

Overall reaction (2-3):

$$2H_2 + O_2 \rightarrow 2H_2O \qquad (2\text{-}3)$$

The illustration of this overall reaction in a PEM fuel cell is shown in Fig. 2.2.

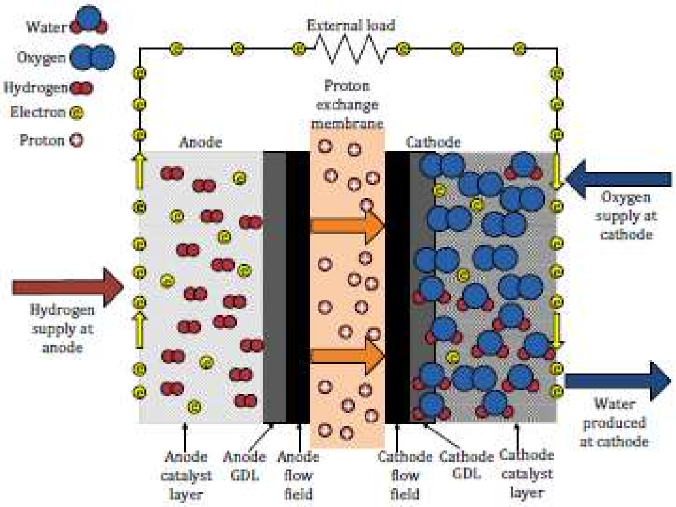

Fig. 2.2: PEM fuel cell [8]

The oxygen is supplied at the cathode, and hydrogen is supplied at the anode. At the anode, the hydrogen splits into electrons and protons, whereby the protons are transported through the electrolyte to the anode side, where they combine with oxygen and electrons to form water. The electrons in the cathode side flow through the external load, which results in electricity [1].

2.3 Electrochemical fundamental principles

The thermodynamics of an electrochemical reaction can be understood using the Nernst equation, and the kinetics (reaction rates) can be understood using the Butler-Volmer equation. The thermodynamic potential of electrochemical cells is described using the overpotential. As such, to give a general overview of the working principles of an electrochemical cell, the interrelation between the overpotential and the current exchange density is further described below [5] [7] [4].

2.3.1 Nernst equation

The Nernst equation is used to describe the thermodynamic reactions of the fuel cell. As a result, the Nernst equation can be used to indicate the Oxidation Reduction Potential (ORP) at Equilibrium.
In an electrochemical cell where the following reactions occur given by (2-4) [7],

$$O + ne^{-} \rightarrow R \tag{2-4}$$

Where O is the reactant and R is the product. The Gibbs free energy is used to describe the process taking place [7].

2.3.2 Gibbs free energy.

The Gibbs free energy was defined in 1873 by Josiah Willard Gibbs [7], as "a quantity that is used to measure the maximum amount of work done in a thermodynamic system when the temperature and pressure are kept constant" [1]. This potential thermodynamic phenomenon is used to determine whether a process will occur spontaneously at a constant temperature and pressure. This is a measure of the energy from a chemical reaction (a thermodynamic system) that can be used to do work. The Gibbs free energy(G) is given by the sum of the systems enthalpy (H) and the product of the temperature(T) in kelvin and the entropy (S) of the system, and this is shown by equation (2-5).

$$G = H - TS \tag{2-5}$$

And the change in the Gibbs free energy (ΔG) is given by the equation (2-6).

$$\Delta G = \Delta H - T\Delta S \tag{2-6}$$

Whereby ΔH is the change in enthalpy, and ΔS is the change in entropy whilst T is the absolute temperature. Enthalpy (H) is the thermodynamic potential of a system that cannot be measured directly. However, the change in enthalpy is more useful as it indicates the change in energy of the system as a reaction takes place [1], [4]. ΔG is zero at equilibrium; positive for non-spontaneous processes(endergonic) and negative for the spontaneous (exergonic) process. The change in Gibbs free energy can also be expressed as (2-7):

$$\Delta G = \Delta G^0 + RT \ln \frac{[R]}{[O]} \tag{2-7}$$

Whereby ΔG^0 is defined as the standard free energy, , T is defined as the absolute temperature whilst R is the universal gas constant. The variable $[R]$ and $[O]$ are defined as the activity of the product and reactant at equilibrium respectively. The Gibbs free energy affect the electrical potential of an electrochemical reaction as it is defined as," a measure of the electrical work done by the electrochemical reaction.", and this can be described by equation (2-8):

$$\Delta G = -nFE \tag{2-8}$$

The right side of the equation (2-8) represents the work done by the reaction, where n is the number of electrons present in the reaction, F the Faraday constant and E is the electrode potential.

From the $\Delta G = -nFE$ and $\Delta G = \Delta G^0 + RT \ln \frac{[R]}{[O]}$. The electrode potential is derived into (2-9) [7]:

$$E = E^0 - \frac{RT}{nF} \ln \frac{[R]}{[O]} \tag{2-9}$$

Where E^0 is the standard thermodynamic potential at $25°C$. The above equation is known as the Nernst equation.

Butler-Volmer equation

The Nernst equation has its shortcomings, and it is unable to indicate the rate at which the electrochemical reaction is occurring. However, it can be utilized to provide knowledge on the reaction direction and the thermodynamics occurring at the electrodes. As such, the Butler-Volmer equation is used to indicate the relationship between the reaction rate and the electrode potential [7].

2.3.3 Butler-Volmer

For the chemical reaction described by $O + ne^- \rightarrow R$, the forward reaction rate expressed as current density is expressed by equation (2-10).

$$i_{frr} = i_o e^{(-\frac{\alpha F n}{RT})} \tag{2-10}$$

Where i_{frr} is the forward reaction current density, i_o is the current exchange density.

$$i_{brr} = i_o e^{(\frac{(1-\alpha) F n}{RT})} \tag{2-11}$$

i_{brr} is the backward reaction rate. When expressed in term terms of current density, it is given by equation (2-11).

$$i = i_{frr} - i_{brr} = i_o \left(e^{\left(\frac{\alpha F n}{RT}\right)} - e^{\left(\frac{(1-\alpha) F n}{RT}\right)} \right) \tag{2-12}$$

The rate of the total reaction is the backward reaction subtracted from the forward reaction given by equation above [9].

2.3.4 Overpotential

Overpotential is the potential above the thermodynamic requisite needed to drive an electrochemical reaction at a specific rate. From $O + ne^- \rightarrow R$ equilibrium is reached when the net rate of the forward and backward reaction is zero. The Nernst potential or the thermodynamic potential is referred to as the potential at equilibrium conditions. The difference between the enforced potential and the Nernst potential is given by equation(2-13).

$$\eta = E - E^0 \tag{2-13}$$

Where η is the overpotential, E the enforced potential and E^0 is the Ernest potential. The overpotential needs to be maintained at the smallest value possible as this ensures efficiency during the operation of an electrochemical cell since the higher the overpotential, the higher the current density will be.

2.4 Fuel cell losses

In practical applications, the output voltage of the fuel cell system is usually lower than the thermodynamically set potential. This is observed even when the fuel cell system is connected to an external load, as the voltage drop is observed to be larger when the external load is sourced by the fuel cell system. The observed voltage drops are associated with various loss mechanisms within the fuel cell system. As such, this section presents some of the key losses within a fuel cell.

2.4.1 Activation losses

Activation loss is experienced when the fuel cell system is connected to an external circuit, electrons that are accumulated on the anode are conducted to the cathode side, whilst the hydrogen ions are transported to the cathode side from the anode through the electrolyte; this means the electrode potential must be reduced, as such the activation loss is the voltage that is needed and used to start the operation of the fuel cell [7]. The open voltage of the fuel cell is given by (2-14).

$$v_o = E - v_{act} \tag{2-14}$$

Whereby v_{act} is described by (2-15).

$$v_{act} = \frac{RT}{\alpha nF} \ln \frac{j + j_i}{j_o} \tag{2-15}$$

When the exchange current density increases it results in reduced activation loss, as such the relationship obtained is utilised to improve the fuel cell's performance. As a result, the thermodynamic deviation of the potential due to the activation voltage is presented by (2-14).

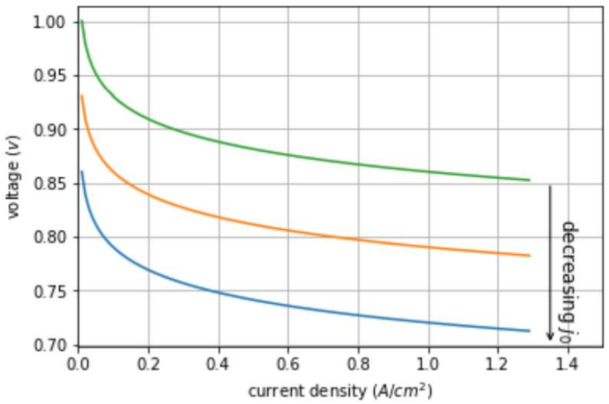

Fig. 2.3: Varying values of j_o depicting the fuel's cell activation potential effect when $\alpha = 5$, $T = 353.15K$, n=2 [6]

Fig. 2.3 depicts the changes observed on the activation potential when different current densities are used.

2.4.2 Internal current losses

When the fuel cell is in normal operating condition, some of the losses arise from leaked currents. Ideally, the fuel cell system is designed and desired to only allow current to flow through the external circuit; however, there is some undesired passage(leakage) of electrons from the anode to the cathode through the electrolyte. The effect of this current is negligible since the leaked current is very small when compared to the current flowing through the external circuit [6].

2.4.3 Ohmic losses

This type of loss, "ohmic polarization", comes from the intrinsic resistance of the flow of ions and electrons of conductive material. The main components that contribute to this electrical resistance are the electrolyte, the catalyst later, bipolar plates, the gas diffusion layer, interface contacts and the terminal connections

One way to reduce this ohmic loss is to make the electrolyte as thin as possible. However, this is done with the trade-off of the electrolyte thickness, which is essential for preventing gas mixing and the mechanical stability of the system. The voltage loss included the electronics and ionic contribution to the fuel cell resistance, and this is expressed by equation (2-16) below.

$$V_{ohmic} = iR_{ohmic} = i(R_{elec} + R_{ionic}) \tag{2-16}$$

R_{ionic} is more dominant in equation (2-16) since the ionic transport offers more resistance than the electronic charge transport. R_{ionic} is the ionic resistance of the electrolyte, whereas and R_{elec} is the electrical resistance of cell interconnects, contacts, bipolar plates, and other cell components in which electrons flow [6].

2.4.4 Mass transport losses/concentration

“The mass transfer losses occur when the rate of mass transport of a species to or from the electrode limits the current productions. It generally occurs at high current densities due to the limited mass transfer of chemical species by diffusion to the electrode” [6] Therefor the lack of sufficient mass transport results in reactant depletion or product accumulation [6].

2.5 Fuel cell conditioning and basic characteristics

2.5.1 Introduction

The performance of the cell (i.e. system specific requirements such as voltage, current and power requirement, amongst others) is affected by the operating condition, such as the operating temperature, pressure, flow rates of reactants and the humidity of reactants (also, these operating conditions depend on the cell and fuel cell stack design). Each operating condition must be set for the good performance of the fuel cell system, and these conditions are set at different stages depending on the configuration of the fuel cell configuration. As a result, any change in these operating conditions can lead to the performance degradation of the fuel cell system. This section presents the key conditions of the fuel cell system.

2.5.2 Temperature conditions

Higher temperature improves the reaction rate of the PEMFC due to the improved mass transfer that is attained at higher temperatures. The optimum PEMFC operation is indicated by the reduction in cell resistance and improved polarization curve, which is facilitated by an improved mass transfer rate. As much as an increase in temperature results in improved performance of the PEMFC, evident by the increase in PEMFC output voltage. Care should be taken when selecting the operating temperature, such that the chosen temperature is within a predetermined designed limit while also considering the system requirements. The typical operating temperature is usually between $70°C - 100°C$. This is due to those temperatures above 100°C resulting in the accumulated water at the cathode evaporating, changing it from liquid to gas phase [5]. In addition, the operation of the PEMFC above the boiling point results in steam which has the capability of reducing the partial pressure of oxygen and resulting in oxygen starvation which contributes to poor performance of the fuel cell.

2.5.3 Pressure conditions

Due to the gaseous state of the fuel supply (oxygen and hydrogen supply), pressure has an important role. The electrochemical rate of reaction of a PEMFC is directly proportional to the partial pressure of the reactant gases, i.e., hydrogen and oxygen. The Nernst equation describes this relationship between pressure and reversible potential. The fuel cell system can be operated at either ambient pressure or higher pressure. When the fuel cell system is operated at a higher pressure, it implies a higher pressurizing force exerted on the reactant gases to get them closer in contact with the electrolyte, resulting in improved performance. However, there is a need to select an optimal pressure of the fuel cell as there are challenges that come with higher pressure compression of the reactants, which is the potential of the gas leakage or rupture of the membrane [10]

2.5.4 Humidity condition

Humidity or relative humidity can be described as the measure of the gas's capability to maintain its water content at a certain pressure and temperature. There is a need for the efficient control and regulation of water contents inside the fuel cell, as this is essential to maximise the operation of the fuel cell system. For instance, a humidified hydrogen gas results in humified hydrogen ion(humified proton) as it passes through the membrane in its ion exchange reaction taking place within the PEMFC. When adequate humidification is not met, it causes mechanical stress to the cell as it forms rifts and holes in the membrane-this in essence, increases the ionic resistance, chemical short-circuiting and formation of hot spots. This results in poor performance of the fuel cell system, and the worst-case scenario is that this can lead to reactants mixing, which can result in a fire outbreak. The hydration should, however, not be too much, as this would inhibit the flux of gaseous reactants, which can also lead to a drop in the cell's performance.

2.6 Fuel cell efficiency

As mentioned, a fuel cell system is an electrochemical system that converts chemical energy obtained from the fuels into electrical energy. As such, its energy efficiency is measured by the ratio of the useful output energy to the entire system's input energy. This is presented by the equation.

$$Effecincy, \eta = \frac{usable\ energy}{total\ available\ energy} \tag{2-17}$$

The total available energy is composed of both electrical and thermal energy, and both are depicted as enthalpy(H). The useful electrical energy is given by the free Gibbs energy(G), and this corresponds to the maximum usable electrical energy that can be obtained when hydrogen combines with oxygen.

There is a maximum theoretical limit for the electrical efficiency that can be produced by a fuel cell system, which is given by the division of the Gibbs free energy to the heat combustion of the fuel.
At room temperature and pressure, the Gibbs free energy and heat combustion values of the fuel cell are -237.17kj/mol and -285.83kj/mol [3], respectively. This gives the thermodynamic efficiency shown below [8].

$$\eta_{thermo} = \frac{\Delta G}{\Delta H} = \frac{-237.17\text{kj/mol}}{-285.83\text{kj/mol}} = 0.83 \tag{2-18}$$

There are other factors that contribute to the drop in efficiency of the fuel cell, and these include the losses due to the voltage losses (these include the kinetic losses) and inefficient fuel conversion losses as a result of typical processes when in operation. Not all of the supplied fuel participates in the main process of producing electrical energy; some of the fuels are leaked while others are involved in side reactions; as such, the overall efficiency of the fuel cell can be easily by the equation (2-19) below.

$$\eta_{overall} = \eta_{thermo} \times \eta_{voltage} \times \eta_{fuel} \tag{2-19}$$

2.7 Converter applications in fuel cell systems

Fuel cell systems are used in a range of applications, and these include the telecommunication, mining industries and transportation.

2.7.1 Transportation

The fuel cells have potential use in the transportation sector due to that they are environmentally friendly, whilst fossil fuels are not yet depleting. The power rating of fuel cells in the transportation sector ranges up to $70\ kW$.

The integration of PEM fuel cell systems in the automobile industry requires an energy management system, hence the need for accurate online condition monitoring. The other concern is the hydrogen economy and the associated technology [11]. A concern in fuel cell vehicles is the potential of a hydrogen explosion, as such direct conversion fuel processors are used (usually used in buses, i.e., converts fuel into hydrogen and then into hydrogen then energy), which minimises the potential of explosions; however, this comes with an added cost and additional maintenance (including a complex feedback control system).

The main concerns for integrating the PEM fuel cell technology into the transportation sector is the long start-up time, relatively low power density which is a challenge for small automobiles, and low operating lifespan [11].

2.7.2 Grid connections and distributed power generation

In distributed power generation, PEMFC has potential as they can range up to $500\ kW$. They have potential since they have a low carbon footprint, a high efficiency, and a modular structure, making them able to expand the electric network at any feasible point of connection. This means that different parts of loads in the grid network can easily be managed by different sources supplied by fuel cells, reducing the demand on the power generation plants. As such, the fuel cell has the potential to be used in these applications [12]:

- The main power source in isolated rural places.
- Supplementary power source to power generation plants.
- The utilisation of hybrid renewable systems, such as wind generating plants and solar plants, can thus provide energy when these intermittent systems are not available to meet the grid demand.
- Use as an emergency backup for the unstable grinds in places like South Africa.

However, the application of these systems also has their own caveats which are a need for lower noise levels if used indoors, and short start-up time for emergency applications. In cases of outdoor applications, there is a need of withstanding extreme ambient conditions and increase of operational time from 40 000 to 80 000 hours, i.e., 5 to 10 years.

2.7.3 Applications for portable power systems

PEMFC applications can be divided into two main types, applications that have a power rating less than $100\ W$, and applications with a power rating of more than $1\ kW$ [11].
However, for such applications, the concerns are the operating hours, size, and weight of the fuel cell system [11].

2.8 Converter control for electrochemical applications

The epitome of online condition monitoring is the ability to perform real-time diagnostics without interrupting system operation or disconnecting the equipment used for diagnostics. This, in essence, allows the ability to control and diagnose your electrochemical system in a remote setting, allowing power management and the ability to predict future failure, assuming that a historical data set is available, which can be used in the condition monitoring and can also be attained using the set configuration [13].

However, in literature, the range of converter applications in fuel cell systems condition monitoring and other electrochemical systems can be categorised into two types. These two categories are differentiated in that the first type uses a converter that is already facilitating power transfer and then use it to inject EIS through the duty cycle. The second type as in [10], uses a linear load [14] to generate EIS signals into the cell.

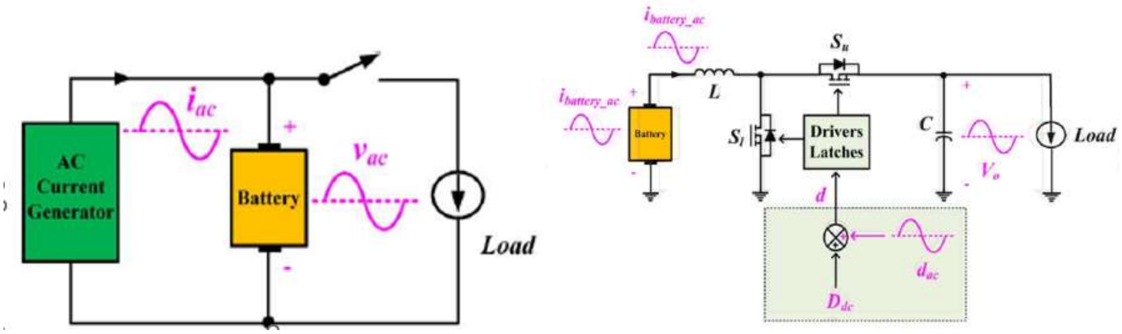

(a) (b)

Fig. 2.4: Different EIS injection circuits (a) load current generator (b) switch-mode converter [14]

Implementation using a switch-mode dc-dc converter is shown in Fig. 2.4(b) [15]. The major advantage of this technique is that it manipulates the duty cycle of the existing converter, facilitating power transfer, whilst performing EIS. The caveat posed by this technique is the noise associated with the modulated signal. Fig. 2.4(a) shows the linear electronic load used to inject the ac sinusoidal signal. The technique requires a separate circuit to facilitate power transfer and a circuit to perform ac sinusoidal injection, however the noise is low. Its disadvantage is that the linear EIS amplifier consumes additional power from the electrochemical system, as shown in [16] [6] [17]. The addition of this circuity contributes to cost and weight which is not desired for mobile applications.

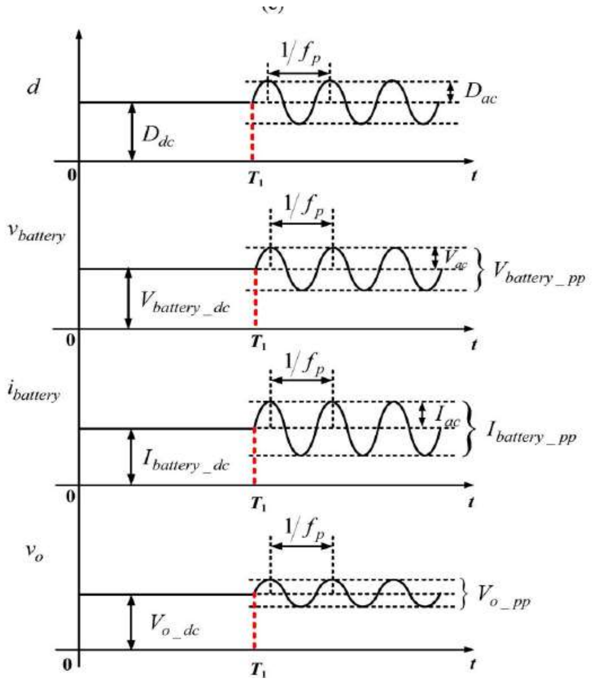

Fig. 2.5: Fundamentals of EIS operation using a switch-mode DC-DC converter [14]

Fig. 2.5 shows a duty-cycle manipulation to perturb the sinusoidal signal into the electrochemical system [14].

2.8.1 Overview of dc-dc converters

Dc-dc converters may be classified into isolated and non-isolated topologies. The non-isolated topologies don't require any output transformer. However, isolated converters are used when there is a need for isolation due to safety reasons or to reduce dependence and loading effects on connected circuits. This research focuses on non-isolated, [15], [18], [19], this is because they are needed to perform online monitoring on the power source, hence the interaction between the power source and dc-dc converter is needed; below are the common dc-dc converters:

- Buck converter
- Boost converter
- Buck-boost converter
- Cuk-converter

The boost and buck converters are the basis of the other converters, i.e., buck-boost and Cuk converter, as these two converters do both functions done by the boost and buck converter. As such, the boost and buck-boost converter will be discussed in detail in the sections to follow. The relation of boosting or bucking is denoted by the duty cycle D of the converter, and the relationship for the most common dc-dc converters are given in table below [18].

Table 2-1: Voltage conversion ratio for each converter topology and voltage

Converter	Conversion ratio	$Vout$
Buck	D	Stepped down
Boost	$\frac{1}{1-D}$	Stepped up
Buck Boost	$-\frac{D}{1-D}$	Inverted stepped up/down
Cuk	$-\frac{D}{1-D}$	Inverted stepped up/down

The conversion ratio relationship of the input voltage and output voltage is only valid when the current through the inductor is always more than zero. That is, the converter operates in the continuous conduction mode (CCM). Some applications use discontinuous conduction mode, however, this project focuses on CCM due to its linearity [15], [18], [19], [20].

2.8.2 Converter control

The control of converters for fuel cell systems is similar to that of other electrochemical systems. As such, this section briefly describes the control strategies commonly used. In most applications, a simple PI, or PID controller is sufficient to control the system. However, other methods that are more sophisticated are used, depending on the application. In this study, the root locus method was used, which is briefly described, and the QFT method, which was considered due to its capability of being able to control plants with different operation points.

i. Root Locus controller design

This is a control technique aiming to stabilise the system by placing the poles optimally on the S-plane. In equation (2-20) is a transfer function of a system with its poles placed at $s = \mp b$ on the real axis of the S-plane, b being a positive number. The placement of a pole in the Open Left Half (OLH) of the real axis, i.e., $s = -b$ gives a stable system,

$$P(s) = \frac{a}{s \pm b} \tag{2-20}$$

Similarly, placing the pole in the Open Right Half of the real axis. i.e., $s = -b$ results in an unstable system. The first priority of the root locus is to make the system stable, thereafter, meet any specifications that are desired for the system. Such specifications can be the overshoot, the bandwidth, and the steady error [21], [22].

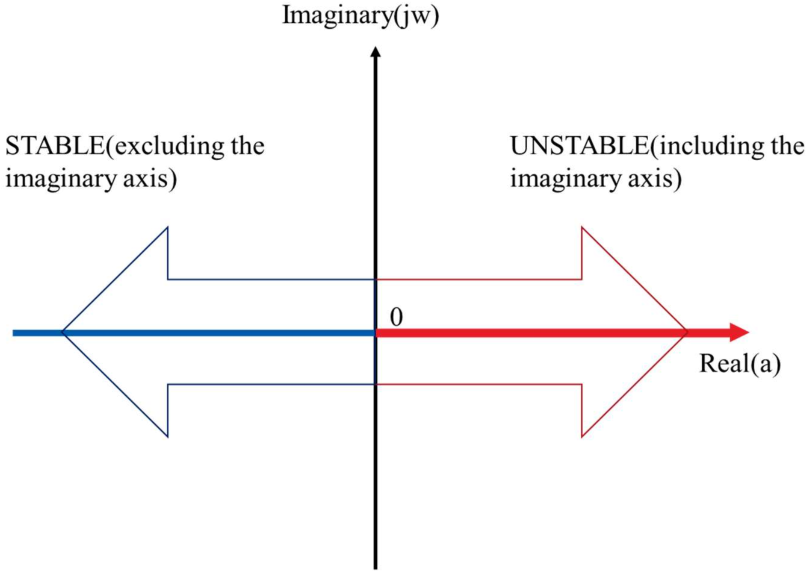

Fig. 2.6: Root Locus S-plane, OLH(STABLE) and ORH(UNSTABLE) pole direction.

ii. QFT Controller Design:

This technique focuses on the frequency characteristics of the system [23]. In [23] it is briefly described as a control technique that allows disturbance rejection, minimising of plant uncertainties whilst maintaining systems stability. This technique it is similar to the root locus by that it also place the poles of the system in the OLH of the plane in for facilitating system stability. Like most control methods, the QFT method utilizes feedback. It takes into account that systems in practical applications have uncertainty and could be subjected to disturbances, and some plants are unstable due to varying conditions over time, hence the use of feedback theory [23], [24], . This technique is different to other techniques due to its quantitative analysis of the frequency domain, whereby most of its analysis is mostly concerned with monitoring the behavior of a system in the frequency domain, such as the monitoring of the phase margin, gain margin and the bandwidth. This is elaborated mathematically by Plant $P(s)$ in Fig. 2.7 with designated Controller $G(s)$. The system is already interpreted in the S-domain after the Laplace transform has been performed.

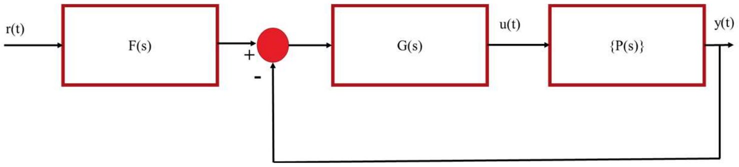

Fig. 2.7: Plant P(s) in a feedback loop with Controller G(s)

It is worth noting that designing the controller $G(s)$ for Plant $P(s)$ in Simulink will give the ideal results. However, in reality, the behavior of the plant over time is dynamic (it changes over time), and the reason for that might be the change in environmental parameters. This can be expressed mathematically by the equation below:

$$P(s) = \left\{ \frac{\prod_i (s + z_i)}{\prod_j (s + p_j)} \ ,\forall z_i \in \left[z_{i,min}, z_{i,max}\right], p_j \in \left[p_{j,min}, p_{j,max}\right] \right\} \tag{2-21}$$

Whereby the numerator are zeros denoted by variable Z, and the denominator are the poles denoted by the variable P. Thus, unlike classical control (PID controllers), the controller which is designed to control the plant for a range of plant variations (variation in poles and zeros); hence making it worthwhile to explore since it allows for the design of robust control. In this technique $L(s) \ = G(s)P(S)H(s)$, whereby $H(s)$ is assumed to be the sensor gain, for Fig. 2.7 $H(s) = 1$.

Thus *L(s)* is mapped and then modified in the Nichols chart ($\frac{L}{1+L}$) and the Inverse Nichols Chart ($\frac{1}{1+L}$) depending on the parameter which is to be optimized.

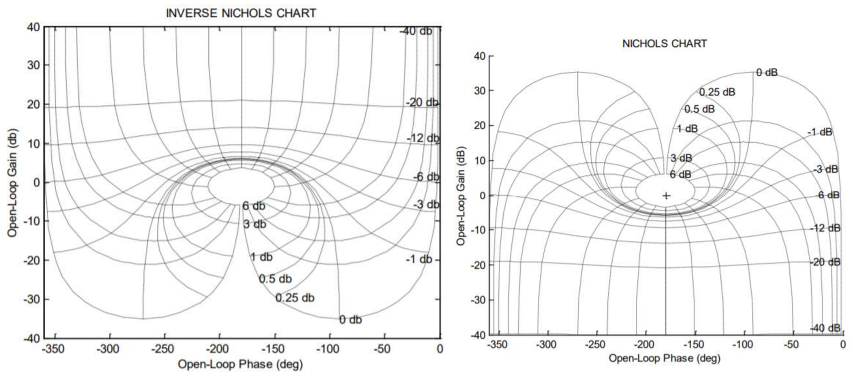

(a) **(b)**

Fig. 2.8: (a) The Inverse Nichols Chart and the (b) Nichols chart [23]

This technique allows for **Loop Shaping** by mapping $L(s)$ into either one of the charts and then modifying $L(s)$ by changing the G(s) so that the specification which one desires to achieve for $L(s)$ is based on the desired performance can be achieved. Fig. 2.9 illustrates how $L(s)$ is mapped into the Inverse Nichols Chart.

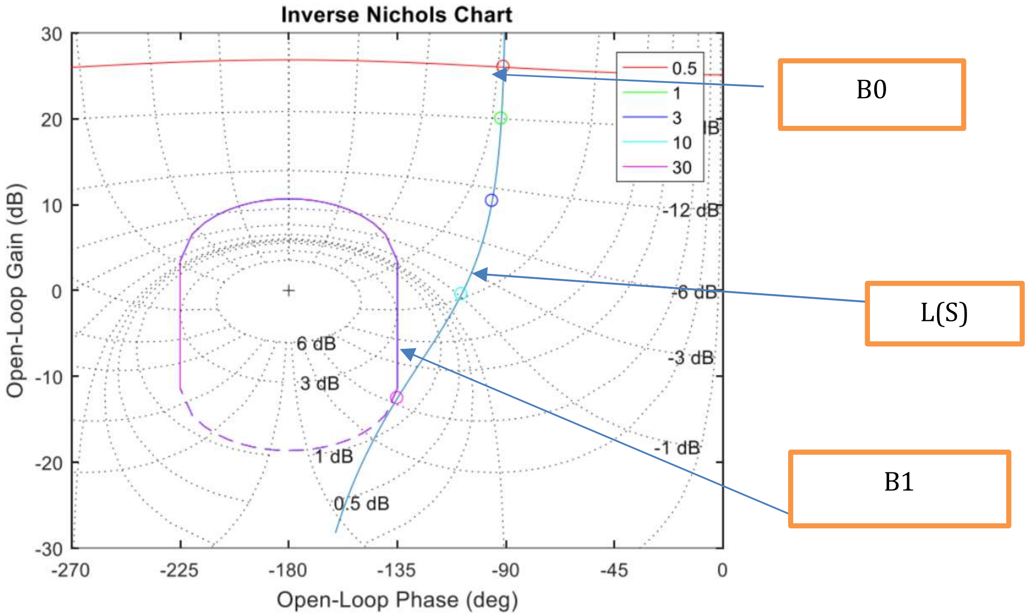

Fig. 2.9: Loop shaping in the Inverse Nichols Chart for non-varying operating conditions (ideal).

In Fig. 2.9, $L(s)$ is mapped into the Inverse Nichols Chart, then $B0$ and $B1$ are the boundaries in the frequency domain that are specified for $L(s)$. $L(s)$ for the lowest frequency 0.5 $rads/s$, it must be above the red line (BO), and for the highest frequency 30 $rads/s$ it must be outside the circle ($B1$) to achieve the specified specifications [22] , [23] . One tries to make the loop far away from the boundary as much as possible whilst making sure that the controller is realistic and cost-effective as much as possible. Thus, the controller is designed by adding a gain to $L(s)$, which will either shift it upwards or downwards depending on the sign of the gain, then the loop is shifted to the left or right by adding zeros or poles to the loop $L(s)$ on a particular frequency to achieve the extra specifications that one might desire in the frequency domain.

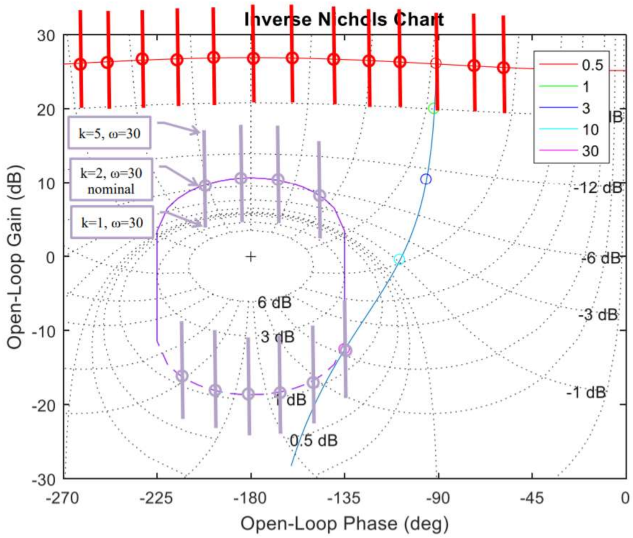

Fig. 2.10: L(s) is mapped in the Inverse Nichols Chart for a plant with varying operating conditions

Thus Fig. 2.10 illustrates the design of a controller for a plant with varying conditions. The controller design is computed in MATLAB using QFT packages (there is some mathematics behind the loop shaping). This technique, however, is suited for Single-Input-Single-Output (SISO) systems. However, it must be noted that there is a relationship between the Inverse Nichols chart and the bode plots. This helps when designing the controller, as it allows for tuning the controller.

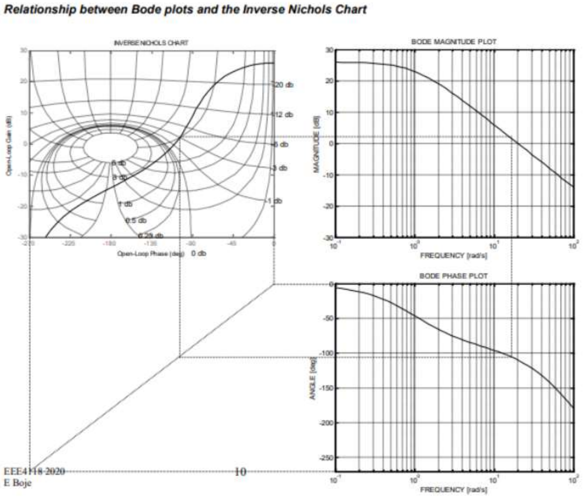

Fig. 2.11: Plot showing the relationship between the Inverse Nichols Chart and the Bode plot

This is a brief overview of the QFT control technique; Fig. 2.11 shows the relation between the Nichols chart and the bode plot in case there is a need to analyse the bode plot for interpretation [25].

2.9 Fuel cell system simulation and emulation

This section details the model that has been used to simulate the fuel cell system, and its different internal water conditions. The three internal water conditions that are explored are the normal, flooding, and drying condition. The fuel cell is modelled using the Randle's circuit, and the Randle's circuit values were obtained from [26], whereby the Randle circuit parameter were obtained from a practical fuel cell system using a square current perturbation method. The simulation that follows will be using the Randle's circuit used in [26] shown in Table 6-1, these are the same values that will be used for the practical emulated fuel cell system with the two dc-dc converter built. In [26] 99.99% pure Hydrogen was used to supply the anode side of the fuel cell system whilst air was supplied to the cathode side. The flow rate and temperature of the water in the humidifier has been controlled by coolers and heaters, with the experimental control done using MATLAB xPC toolbox. As such, the next subsection states the temperature of water in the humidifiers, flow rate and pressure of each of the internal water operating conditions. The fuel cell stack parameters are shown in Table 10-1 in Appendix A Thereafter the modelling and interpretation of the models used are presented.

2.9.1 Normal condition

The humidifier temperature of hydrogen (H_2) and air was 55 °C and the stack temperature being 60 °C , with the same flow rate for both the air and Hydrogen being 2 L/min and 6 L/min respectively. The hydrogen relative humidity was 60% whilst 100% for the air, this was achieved by passing the air and hydrogen through a bubble-type humidifier. The back temperature was the atmospheric pressure.

2.9.2 Flooding condition

In the flooding condition, the flow rates and back pressure is the same as in the normal water condition, the difference is the stack temperature being 55 °C, whist the humidifier temperature for both hydrogen and air moved from 55 °C in normal internal water condition to 70 °C in flooding internal water condition. The changing of the internal water condition was achieved by manipulating the relative humidity of the fuel and oxidizer by changing the temperature in the humidifier.

2.9.3 Drying condition

Similar to the flooding condition, the flow rates and back pressure is the same as in the normal water condition, with the stack temperature being 55 °C. The humidifier temperature for both hydrogen and air moved from 55 °C in normal internal water condition to 30 °C in drying internal water condition.

2.9.4 Modelling of circuit impedance of the fuel cell

A range of fuel cell models can be derived depending on the objective to be reached. However, the integration of fuel cells in an electrical environment requires an understanding of its electrical model.

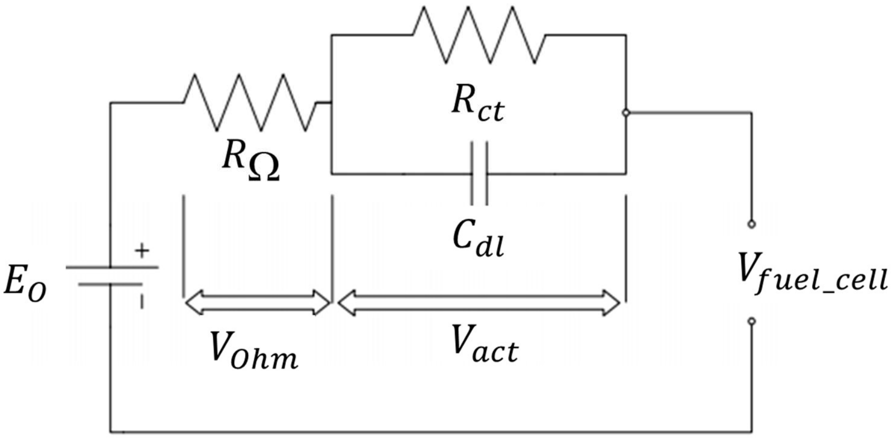

Fig. 2.12: Fuel cell emulation

The model used for fuel cell emulation must be precise, simple and must be able to predict and define the electrical behaviour in both static and dynamic conditions, and in this case, is a simple Randle circuit, shown in in Fig. 2.12, since this describes the input and output description of fuel cell in the realm of electrical environment.

i. Characterisation and simple modelling of fuel cells.

The polarization curve is normally presented as a sum of four terms: Theoretical open voltage (E_O), activation overvoltage (V_{act}), resistance overvoltage(V_{ohm}) and the concentration overvoltage(V_{conc}). The is shown by equation (2-22).

$$V_{fuel\_cell}=E_O - V_{ohm} - V_{act} - V_{conc} \tag{2-22}$$

Equation (2-22) is used to give the relationship between the polarization and the impedance model. Therefore, based on that, the fuel cell model needs to be precise and simple and be able to define the electrical behaviour in static and dynamic conditions. A DC source in series with an electrical impedance is used, whereby the electrical impedance is a Randle circuit, should be noted that the Randle circuit does not present the diffusion content.

The reasons for utilising passive impedance components to model the fuel cell system, i.e., a simple Randle circuit instead of a computer-controlled DC-DC embedded system that can also emulate a fuel cell system, are as follows [4] - [27]:

- Passive components are simple to connect and are readily available, also with the impedance tolerance specified by the manufacturer.

- Computer embedded emulated system does not accurately and readily provide impedance information.

2.9.5 Impact of water mismanagement on the parameters of the Randle's circuit.

The Randle circuit conditions values show the following changes.

Change 1: the transition from normal mode to drying mode shows a major increase in the series resistor (R_{Ω}) is observed as internal drying in the fuel cell system progress, and this is caused by the increase of the component's contact resistance and reduction in the conducting ions inside the electrolyte membrane. However, it should be noted that during this transition, there is no observed change in R_{ct} but C_{dl} is observed to have reduced by approximately 32% [26, 28].

Change 2: with the transition from drying mode to normal mode, the series resistor (R_{Ω}) value reverts to its initial condition magnitude. The parallel resistor (R_{ct}) is observed to have insignificant change or no change at all. The capacitor values are observed to increase from their initial magnitude [28].

Change 3: the transition from normal mode to flooding mode, series resistor(R_{Ω}) converges to a finite value after a slight change. This effect is due to the ion-conductivity of the polymer membrane, and R_{Ω} is observed to increase by a magnitude close to 10%, and at the same time, C_{dl} expands by a magnitude close to 17% [26, 28], [8].

2.10 Electrochemical characterization methods

Methods for electrochemical characterisation is usually performed by acquiring voltage and current data. Thereafter this information is used to understand the electrochemical dynamics of the electrochemical cell after analysis. The methods usually used for electrochemical characterization are the Polarization curve (PC), Current Interrupt (CI) and Electrochemical Impedance Spectroscopy (EIS). These methods assist with depicting information about the degradation and failure of the system. They also assist with understanding the power/performance losses. As such, they can be used to optimize the system performance and address the durability and cost of such systems.

2.10.1 Polarization Curve

The polarization curve is a plot of different current density loading against electrode potential (output voltage) for a specific electrode-electrolyte combination. This is the basic kinetic law for any electrochemical reaction.

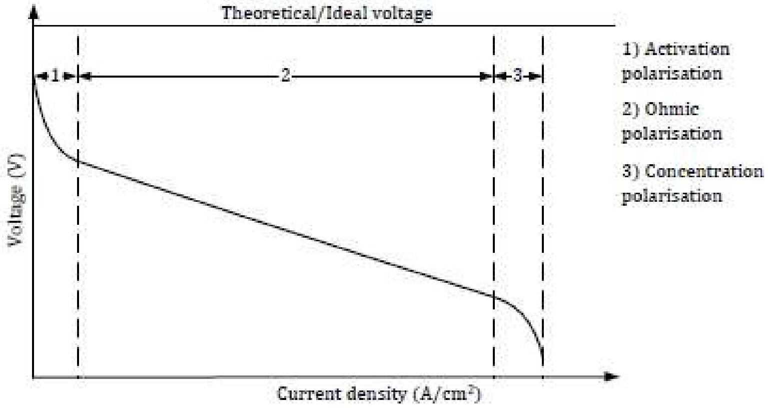

Fig. 2.13: PEMFC polarization curve

Fig. 2.13 shows a typical polarization curve of a PEMFC, this is usually determined after the open-circuit electrode potential of the test metal has reached steady-state values, and the time required to reach the steady state depends on the nature of the system. These are obtained with a potentiostat/galvanostat, which draws a fixed current from the fuel cell and measures the fuel cell output voltage [10]. There are three distinct regions of a fuel cell polarization curve, as described by equation 2.22. These are the activation polarization, ohmic losses and concentration polarizations. Activation polarization results in a potential drop at the lower power densities, and the ohmic losses decrease linearly at the moderate current densities. The concentration polarization is found at high densities where the potential decrease is no longer linear.

2.10.2 Current Interrupt

The current interrupt utilizes interrupting the current for a very short period interval and thus records the voltage response to measure the resistance in a fuel cell.

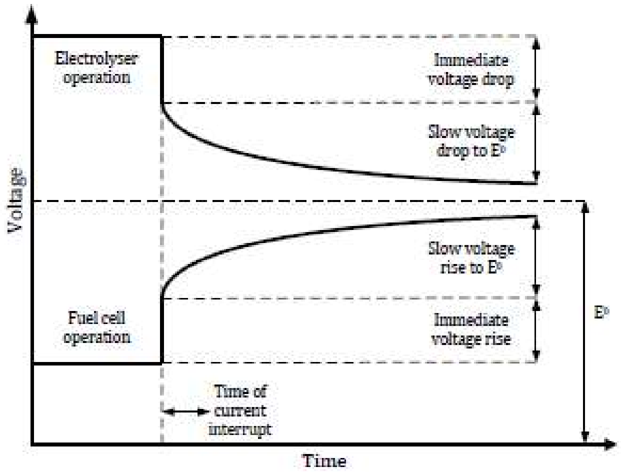

Fig. 2.14: Typical Current waveform

$$R_i = \frac{\Delta V_i}{\Delta I_i} \tag{2-23}$$

This technique takes advantage of that the simplest parameter that can be attained form any electrical circuit, ie. the dc resistance, described by equation above. The current interrupt response is similar to that of the resistor capacitive decay, thus a Thevenin circuit is the common circuit used to present the response. A drawback to this technique, is that its determined parameters don't give any information about the physiochemical property of the system [10] [29].

2.10.3 Electrochemical Impedance Spectroscopy

This technique exploits signals of different frequencies for system identification using the excitation-response relationship of an electrochemical system, as this can used in online, i.e. inject small ac signals into system of interest then measure the response for analysis [2]. This technique is explored in more detail in chapter 3.

2.11 Conclusion

In conclusion, this chapter reviewed, in detail, the chemical properties and electrical processes of fuel cell systems. It divided into the types of fuel cells, thermodynamics, Nernst and Butler-Volmer relationships, power generation and losses associated with the fuel cells. It then explored the fuel cell conditioning and the basic characteristics, emulation, fuel cell efficiency and converter applications. Based on a thorough review of the literature, impedance Spectroscopy shows advantages and applicability for online condition monitoring; as such, the next section explores Impedance Spectroscopy along with the signal associated with it.

Chapter 3

Impedance spectroscopy

3.1 Introduction

Impedance Spectroscopy (IS) is a frequency analysis technique utilised to acquire the electrochemical impedance (Nyquist plot) of an electrochemical cell as its frequency is varied. This technique exploits the excitation-response relationship of Linear Time-Invariant (LTI) systems [2]. The process for electrochemical systems is performed in two modes. These are galvanostatic and potentiostatic modes [5]. The potentiostatic mode is characterised by supplying the electrochemical cell with a voltage signal and, thereafter, measuring the current response. However, in the galvanostatic mode, it is the opposite [5]. As such, the electrochemical cell impedance is derived through equation (3-1) below.

$$Z(\omega) = \frac{V(\omega)}{I(\omega)} \tag{3-1}$$

The galvanostatic mode is used for a fuel cell system because it provides a high current and with low voltage. The impedance obtained using equation (3-1) is expressed through a Nyquist plot, as shown in Fig. 3.1 . The Nyquist plot is used to present the electrochemical (fuel cell) impedance, and this can be presented using the conventional Alternating Current Equivalent Electrical Circuit (AC EEC), as shown by Fig. 3.2, also better known as the Randles circuit as described in the previous chapter.

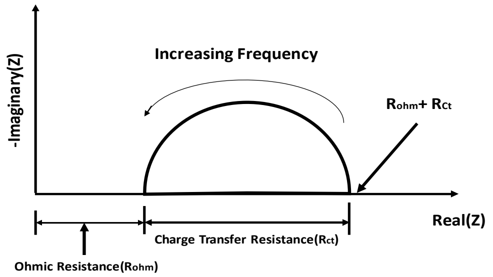

Fig. 3.1: Nyquist plot

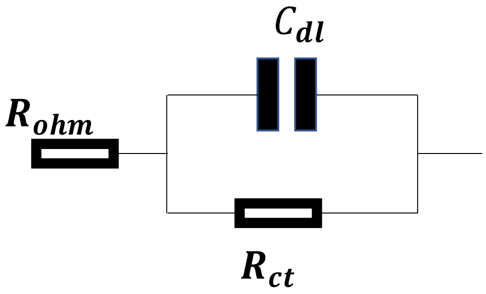

Fig. 3.2: Randle circuit

The Randle circuit is used to map the electrical impedance of the fuel cell to its chemical properties; this is denoted by the impedance response presenting the parameters. As such, R_{ohm} in Fig. 3.1 expresses the electronic and ionic resistance, whilst R_{ct} describes the activation losses (transfer resistance), and C_{dl} presents the electrolyte electrode parasitic capacitance [28].

3.2 Types of perturbation signals

3.2.1 Introduction

A perturbation signal is a signal created to characterise the behaviour of a system or Device Under Test (DUT) through perturbation, thereafter, studying the response of the system either in the time or frequency domain. The signal used for perturbation is chosen based on the estimation time, signal-to-noise ratio (SNR) and accuracy. There are two groups of characterising signals, these are single perturbation signals and broadband signals [30] [16].

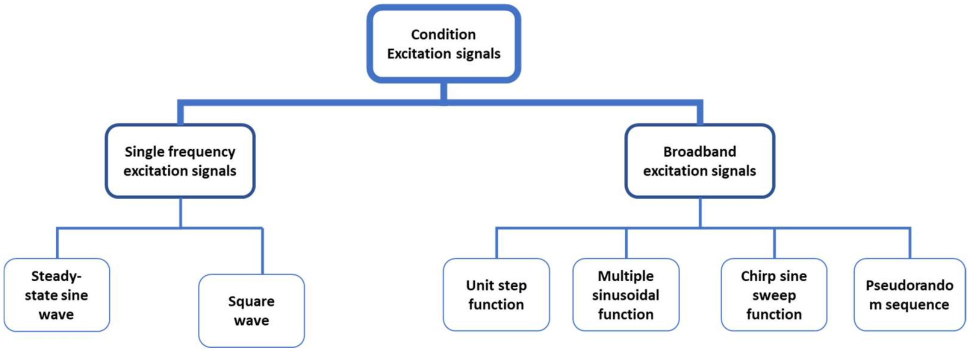

Fig. 3.3: Excitation signals for system identification

Fig. 3.3 shows the architecture of these categories. As such, this section will briefly summarize and discuss these signals, thereafter, discuss the PRBS and steady-state sine wave.

3.2.2 Broadband excitation signals

There is a range of injection signals that can potentially be used for system identification in an electrochemical system. As such, the selection of the perturbation signal is crucial, as the signal type has an effect on the estimation process used. This next section will briefly discuss the more commonly used ones as listed below [15] [30] [16]:

- Unit step function
- Sinusoidal signal
- Multi-sinusoidal signal
- Pseudo random binary sequence signal

i. Step function

This is used to determine a basic model of the system, and this is usually used for a system with large signal-to-noise ratios. The unit step function is presented by equation (3-2) below.

$$x(t) = \begin{cases} 0 & if\ t < 0 \\ x_0 & if\ t \geq 0 \end{cases} \tag{3-2}$$

$x(t)$ is the signal amplitude with time t . The unit step function can be used to determine the system's parameters, such as the overshoot, rise time and static gain, among other parameters [15].

ii. Multi-sinusoidal function

The multi-sine signal is a sum of single sinusoid frequencies, such as the time domain voltage signal can be given be defined by the Fourier series equation (3-3) below [30] [16].

$$x(t) = \sum_{k=1}^{n} a \sin(2\pi k f t + \emptyset_k) \tag{3-3}$$

n is the number of chosen frequency points and a is the excitation amplitude matrix; f is the frequency corresponding to k; and $\emptyset_k$ the phase of each frequency. One of the major disadvantages of the signal is its poor crest factor; as such, the signal undergoes multiple optimisations, namely, frequency, amplitude, and phase optimizations [28][29].

iii. Chirp sine sweep function

"Swept sine or Chirp signal, is a sinusoidal signal whose frequencies varies with time. This produces a near flat spectrum over the frequencies of interest" [15]. The standard non-parametric chirp signal can be described mathematically as (3-4) [31]:

$$p(t) = B \sin(2\pi f(t) t) \tag{3-4}$$

Whereby

$$f(t) = f_{min} + \left(\frac{f_{max} - f_{min}}{2T}\right) t \tag{3-5}$$

Where B is the amplitude, t is the simulation time. Where, $f(t)$ is the excitation frequency of the module; f_{min} is the minimum excitation frequency; and f_{max} is the maximum excitation frequency, and T the target time. The benefit of chirp signal is that it can be generated in short duration, whilst having a large bandwidth. The issue with this signal is that due to the poor signal-to-noise ratio (SNR) at low frequencies, the low impedance information is scattered. This is solved by implementing either the Short-Time Fourier transform (STFT), or wavelet transforms [30] [6].

iv. Pseudo-random binary sequence

This is a periodic and deterministic signal that can excite a linear range of frequencies. This method is easy to implement and is appropriate for current switching methods. As such, this section is discussed more in the following section, as it is a major part of this dissertation.

3.2.3 Single frequency excitation signals

These signals are characterized by having a single usable excitation frequency. This means that they do not have a $-3db$ cut-off frequency. They have a varying crest factor depending on the type; they do, however, possess the highest SNR because the signal's power is concentrated at its fundamental frequency. The major drawback of these signals is that they have the longest test time, especially for devices with wider excitation bandwidths. Some common single-frequency signals are discussed below.

i. Square wave

The square wave signal is desired as its spectrum has harmonic frequencies that are an integer multiple of the fundamental frequency of the square wave [31]. The Fourier series of the square wave is a sum of these harmonic frequencies, with different amplitudes [10].

ii. Steady-state sinusoids

This is the most common signal used for impedance spectroscopy because they are simple to implement, have a high SNR, and can be implemented on any device and with any excitation source [17]. This is discussed in more detail in section 3.3, since this technique is used in the project.

3.3 Steady-state sinusoids signal (EIS) configuration

This section entails the selection of the EIS frequencies, which will be used for both the simulation and the experimentation.

3.3.1 Signal injection

Galvanostactic mode is utilised in this project. As such, a dc current I is controlled, and a sinusoidal current ΔI is superimposed on it. This is shown by the equation (3-6) below:

$$\Delta I = I_{max} \sin(2\pi f t) \tag{3-6}$$

The superimposed sinusoidal current ΔI, with frequency f, when drawn by the fuel cell system, will result in a sinusoidal voltage response given by ΔV as described (3-7) below.

$$\Delta V = V_{max} \sin(2\pi f t + \theta) \tag{3-7}$$

This voltage response is around the DC voltage V, of the fuel cell system. The amplitude of this voltage response (V_{max}) and the phase angle (θ) depends on the frequency (f) perturbed and the impedance of the fuel cell system at the time of injection measurement. The impedance of the system is determined using (3-1).

3.3.2 Frequency selection

The chosen frequencies are based on a fundamental approach that allows a good resolution of presenting the impedance. These are the same frequencies that are used to do impedance estimation using the Frequency Response Analyser (FRA), which is the benchmark equipment detailed in section 6.3.As such, this allows the comparison of Broadband signal with the single perturbation EIS using the EIS, as such allows for a fair comparison. These frequency points are shown in Table 10-2 in Appendix A The total time taken for EIS measurements is 224.8 seconds. This is without any total recovery period, which will be considered in the practical experimentation to avoid overheating of the conductors.

3.3.3 Perturbation amplitude

The perturbation currents used were all 10% of the dc setpoint so that they do not affect the operating linearity of the fuel cell system. The number of cycles for lower frequencies which take a longer time to complete was set to a lower number of periods, and the analysis is shown in Appendix A

3.4 PRBS signal

3.4.1 Introduction

The previous sections show that dc-dc switch-mode converters can be utilized to facilitate EIS online without disrupting the system. However, this has its caveats, which is longer estimation time, due to each frequency point needing to be excited and measured individually. Whereas broadband technique eradicates the time delay by using a signal which has the frequencies contained within it. However, the trade-off is impedance estimation accuracy. As such, this section presents the proposed broadband signal called the PRBS signal. The PRBS signal is significant in that its frequency spectrum is similar to the frequency spectrum of white noise; yet different to white noise by that it is bandlimited. As a result, the PRBS signal contains multiple frequencies inside it that reduce the impedance estimation time when performing impendence spectroscopy.

3.4.2 The PRBS signal

A PRBS signal can be briefly described as a signal characterised by a combination of binary state series of sequence that forms a predetermined pattern. As such, the “pseudo” in PRBS implying the predetermined property, and “random” implies to the property of the signal not repeating its states within a single period. The duration at which it takes one state of the signal to move to another state, is dictated by the integer multiples of the minimum frequency within the signal [32].

3.4.3 Sequence generation

There is a range of PRBS signals, and these include the Maximum Length Sequence (MLS), quadratic residue codes, Hall sequence and twin prime sequences. Although, the MLS type is the most common way used to implement PRBS. This comes as a result that the MLS can easily be generated using Linear Feedback Shift Registers (LFSR) [1].

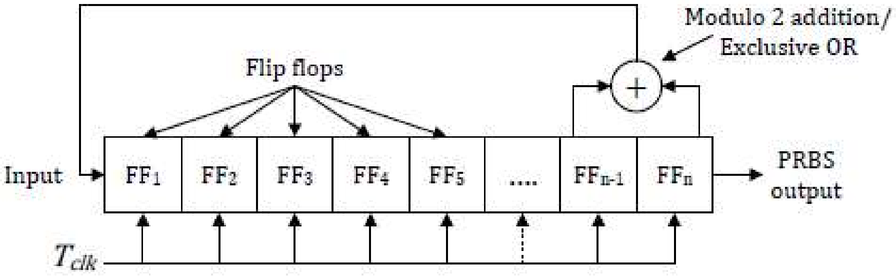

Fig. 3.4: LFSR used to produce the PRBS signal.

The MLS feedback has a requirement which is that the feedback should be taken from the correct register, as an incorrect register sequence will generate a sequence with a length less than the maximum length to be generated. The feedback configuration rule that dictates where the feedback should be taken when using LFSR for generating an *n* stage MLS is given in table below [1].

Table 3-1:LFSR configuration

Number of stages	Position of feedback connection
2	1,2
3	2,3
4	3,4
5	3,5
6	5,6
7	4,7
8	2,3,4,8
9	4,5,6,8
10	5,9

The table above shows the position where the feedback should be taken in order to produce an MLS PRBS signal. From the PRBS signal generated, it has a limited number of different possible terms which are restricted by (3-8) [33].

$$N = 2^n - 1 \tag{3-8}$$

Where N is the number of possible levels, n is greater than zero, presenting the number of state stages. The Maximum-Length-Binary Sequence (MLBS) is one type of a PRBS signal which is simpler to implement, this making it useful [1]. The MLBS signal type is preferred because it easily allow you to manipulate the spectral domain of the signal, hence used in most system identification applications. As such, the MLBS signal is considered in this research [1]. Another characteristic of the MLBS signal is that it differs from other PRBS signals by that it exhaust all bit patterns inside the sequence, with an exception of zero states, therefore an N sequence signal, the MLBS won't repeat its bit , it will only repeat its bits after N state has passed [1].

3.4.4 Autocorrelation

Some applications require the determining the level of similarity between signals, as such Correlation function are usually used to achieve this. Depending on the applications, including as in physical, technical or biological systems, these signals are used to either detect or measure phenomenon's [1] .

The correlation function can assist in through these distinct properties [1] :

- Can allow a measured signal to be analytical differentiated from a time shifted version of itself
- All measured signals can be easily differentiated from itself of time shifted version of itself or other measure signals.

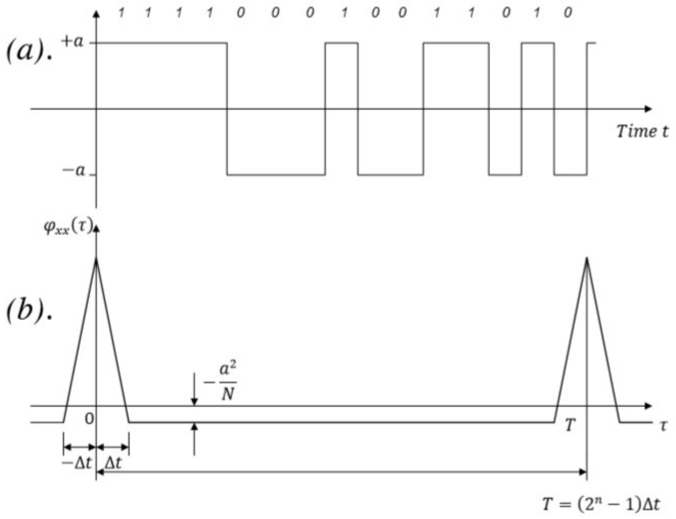

Fig. 3.5:(a) MLBS signal with N terms and (b) N term MLBS generic autocorrelation response

Fig. 3.5 depicts the characteristic of the MLBS signal, it portrays that the is no similarity on an MLBS signal for the first N terms. As such, the autocorrelation of the signal start to repeat after a single period [1]. It should be noted that the autocorrelation is simply the cross-correlation of the signal with itself, has it shows when repetition occurs. For this reason, autocorrelation can be used to find a specific periodic signal on a measured signal containing noisy signals [1].

3.4.5 Sequence properties

For a signal to be absolute PRBS, it has to meet specific properties; and these properties are [1]:

1. **Balance property**: In all the periods of the sequence, when the number of logic ones and logic zeros are subtracted from each other, the difference should not be more than 1.
2. **Run property**: "Among the runs of one, two three, etc. in the period half should be of length 1, a quarter of length 2, an eighth of length 3 etc. ", this implies that there should be as many of each run of logic one as logic zero states.
3. **Correlation property**: The cyclic shift of a sequence for any period of the sequence, must not have a difference of more than one when compared term by term.

3.4.6 PRBS signal bandwidth limitations

Due to the nature of the PRBS signal being a broadband bandlimited signal, it implies that it only contains energy at specific discrete frequencies and have a maximum defined frequency. These discrete frequencies are an integer multiple of the minimum frequency contained in the signal. This implies that the frequencies increase linearly inside the PRBS signal, and as such the minimum frequency contained with an MLBS signal is computed using equation (3-9) [1].

$$f_{min} = \frac{f_c}{N} = \frac{1}{N\Delta t} \tag{3-9}$$

Whereby f_c is the clock frequency, Δt is the clock period. The Wiener-Khintchine theorem is used to derive the maximum frequency within the PRBS signal. The Wiener-Khintchine theorem [1] states that a "the Fourier transform of the corresponding autocorrelation function is the power spectral density of a wide sense stationary random process" [1]. This theorem is depicted by Fig. 3.6 whereby the maximum useful frequency within the signal can be computed using equation (3-10) [1].

$$\Phi_{xx}(\omega) = 2\int_0^T \varphi_{xx}(\tau)\ \cos(\omega\tau)d\tau \tag{3-10}$$

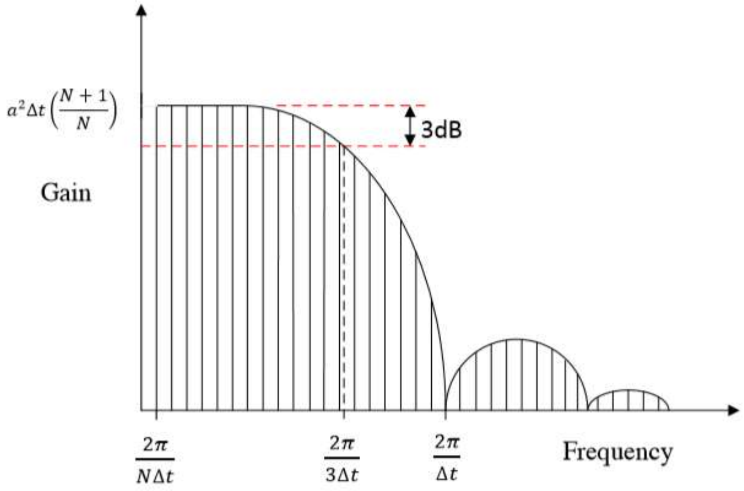

Fig. 3.6: Illustration of PRBS usable band power spectrum (FFT)

The PRBS power spectrum is described by equation (3-11):

$$\Phi_{PRBS}(i) = a^2\,\frac{(N+1)}{N}\left(\frac{\sin(\frac{\pi i}{N})}{\frac{\pi i}{N}}\right)^2\ \ i = \pm1, \pm2, .. \tag{3-11}$$

As depicted in Fig. 3.6, there is a small portion of frequencies concentrated on the flat spectrum, as such all the frequencies below the – 3 dB point are attenuated, this imply that they are not useful for electrochemical impedance estimation. The key design parameters for PRBS to select the signal properties are the number of stages inside the signal and the fundamental clock frequency. Computation of the integral defined by equation (3-10) provides the upper bound where the useful frequencies are found in a PRBS signal, and this is described by (3-12) [33]:

$$f_{max} = \frac{1}{3\Delta t} = \frac{f_c}{3} \tag{3-12}$$

3.4.7 PRBS length selection

Increasing the bit-length of the PRBS signal results in an increase to the number of states, these in turn increase the signal injection estimation time and useful bandwidth.

This implies that when designing the PRBS signal for perturbation to an electrochemical system, the following parameters needs to be optimized.

- Frequencies of interest
- Signal injection time
- Bandwidth useful

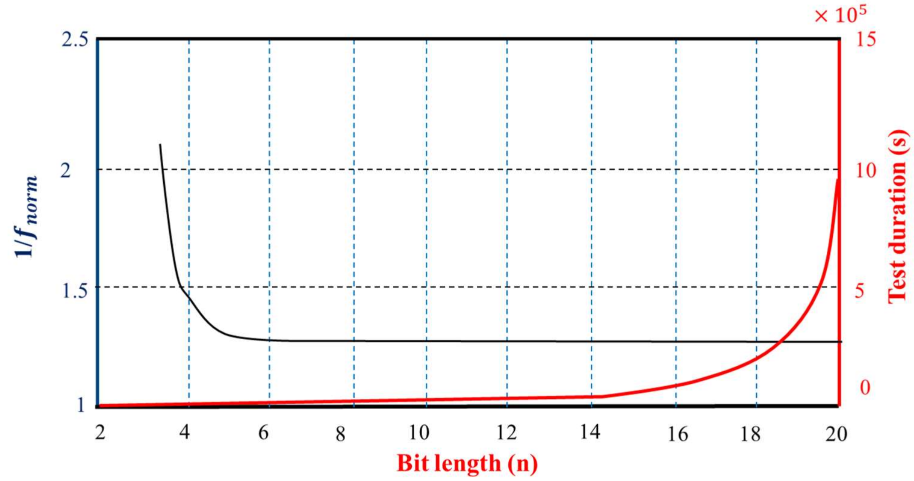

Fig. 3.7: The PRBS test duration with the normalised bandwidth for a specific length

As shown in Fig. 3.7, as the bit length of the PRBS increases, there are diminishing return trends observed, yet with an increase in the usable frequency for Impedance Spectroscopy. However, the disadvantage of the long sequence is the increase in the test time required to capture a complete sequence.

$$T_{max} = N \times T_c \tag{3-13}$$

The advantage of PRBS is that it is easy to implement on low power processing micro-controllers, which can easily output binary levels, which is different case with sinusoidal signals being continuous. Also, the PRBS signal has white-noise characteristics due to its broadband spectrum [4].

3.4.8 PRBS optimization and design

The frequencies of interests that cover the key internal dynamics of the fuel cell system are from 100 mHz to 10 kHz; as such, the injection signal selected must have a bandwidth wide enough to capture the start of the ohmic region. It is desired that the signal that is selected for PRBS excitation have shorter interval time and it is robust. Therefore, there is a need for a design resulting is shorter excitation time.

For the implementation of the PRBS signal, the fuel cell bandwidth (0.1-10KHz) is divided into two, i.e. the lower frequency spectrum and higher frequency spectrum, to avoid the increase in implementation time as explained in section 3.4.7(uses less memory, can be implemented on micro-controllers). A single signal which contains all the frequencies is also designed, but it has its associated disadvantages which are it demands a big size of computational space. However, it reduced test time.

Table 3-2: PRBS parameter values

Parameters	**Lower Spectrum**	**Higher spectrum**
Minimum frequency (f_{min}) in Hz	1.38	117.2
Clock frequency (f_c) in Hz	354	30 k
Maximum frequency (f_{max}) in Hz	118	10k
number of bits, n	8	8
Time for one period, T_{max} *in sec*	720m	8.5m

Table 3-2 shows the designed values when using two signals for injection, with the implementation time being less than a second when it is one period.

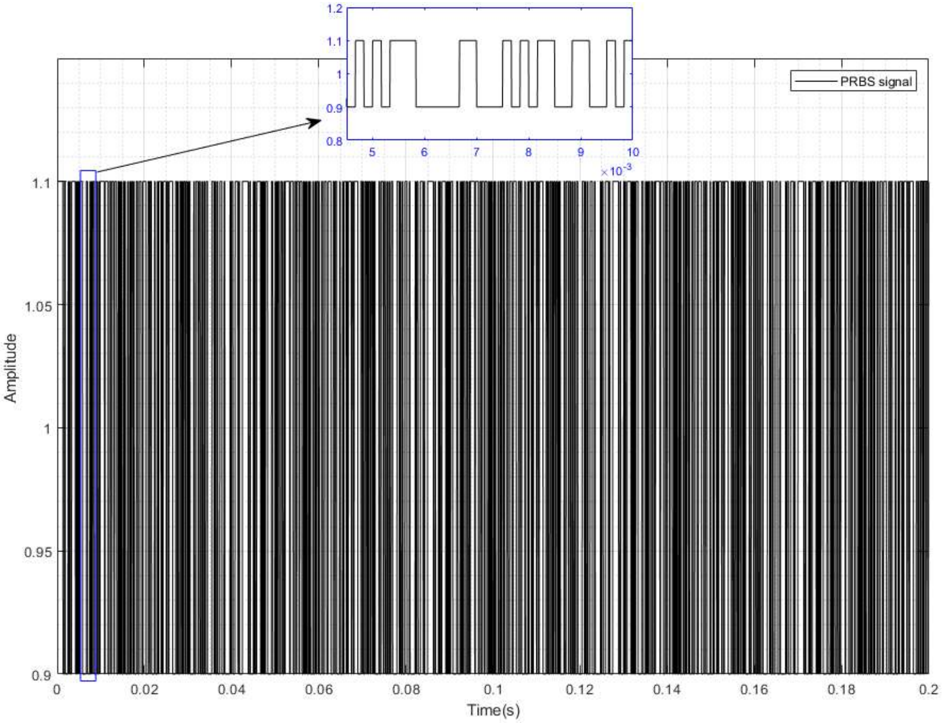

Fig. 3.8: PRBS signal waveform

Fig. 3.8 shows the waveform of the PRBS signal superimposed onto a dc signal of 1 A. This is the designed signal used for perturbation. If an electronic load was used, this is the input current which would have been desired.

3.5 Testing conditions for impedance spectroscopy measurements

The main assumption used is that the model is simplified as a purely impedance model, which is linear, which is not usually the case for a fuel cell system. Fuel cell systems are multi-physics systems dependent on their internal operating conditions, such as pressure, humidity and temperature. Also, the current is drawn to provide the corresponding output voltage on the polarization curve.

With these given conditions, the system can be linearized by approximating it to be linear and time invariant over a limited range. The EIS for the electrochemical systems in most applications is applied in galvanostatic mode; as such, it is important to choose an operating dc point that will allow the current to function in a linear region whilst transferring regulated power to the external circuit. [34].
This technique of inducing a linear region by choosing a specific point of drawing the current creates a pseud-linear relationship. An example of this pseudo-linearisation is expressed in Fig. 3.9

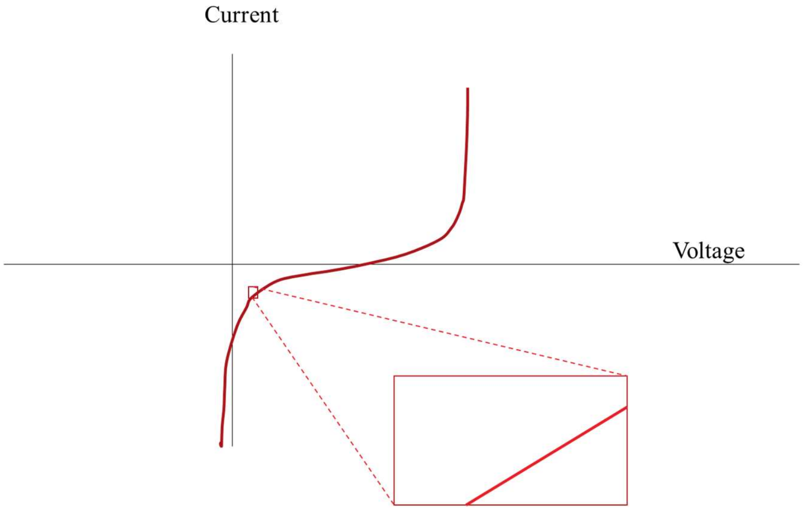

Fig. 3.9: Pseudo-linearity of a typical electrochemical system.

As depicted in Fig. 3.9, the current-voltage relationship is not linear, and when magnifying a point of the trajectory, the non-linear line when magnified appears as a straight line. As such, it would be assumed that whilst the electrochemical system is operating within this pseudo-linear magnified region, it can be regarded as a linear system. As such, this region constrains the range of signals or the range at which the drawn signal can fluctuate within, to consider the system as being linear [35].

The EIS application determines the maximum signal allowed, this infers that the excitation current and its respective voltage response are to be selected such that they have small amplitudes in comparison DC current and supplied mean voltage [36]. These, in essence, point to the three main conditions that need to be met to satisfy the Kramers-Kronig relationship [37]. These three main system conditions are causality, linearity and stability [38]. When these conditions are met, to derive a graphical model of the system, the assumption is that the impedance of the system at this operation point is linear and does not change [34]. This also assumes that the operating conditions are known and can be controlled since operating conditions such as temperature can affect the impedance at a particular operating point [39]. The system is also assumed to be time-invariant within the period that the measurements are taken [40]. Finally, it is essential that the injected signal contains sufficient power to provide enough Signal-to-Noise Ratio (SNR) without resulting the system into non-linearity [41].

3.6 Electrical equivalent circuits

Equivalent Electrical circuits (EEC) are utilized to represent the impedance of the electrochemical system. The EEC is usually presented by passive components such as the resistor, capacitor and inductors. Depending on the characteristic to be modelled, different resistor, capacitor, and inductor combinations (series/parallel or both) can be chosen. Since various combination of elements can be used, this section will focus on those relevant to fuel cell systems.

A simplified EEC model is represented by a simple RC electrical circuit, or RC in series with an inductor depending on the properties of the system, and the impedance values of these passive components are given by equations (3-14), (3-15) and (3-16) for resistor $\tilde{\Delta} z_r$, capacitor; $\tilde{\Delta} z_c$ and inductor $\tilde{\Delta} z_L$respectively.

$$\tilde{\Delta} z_r = r_s \Omega \tag{3-14}$$

$$\tilde{\Delta} z_c = \left(\frac{-j}{\omega_s c_s}\right) \Omega \tag{3-15}$$

$$\tilde{\Delta} z_L = (j \omega_s L_s) \Omega \tag{3-16}$$

Fig. 3.10 (a)-(d) shows the common combination along with their respective typical Nyquist plots. The total impedance of each combination is the resultant of every component's impedance. Fig. 3.10 (a) shows a series RL circuit, and using equations (3-14) and (3-16), the impedance can be determined, and for low frequencies, the impedance total is purely resistive, and as the frequency increases, the impedance converges to infinity. Fig. 3.10 (b) shows a series RC circuit, and using equations (3-14) and (3-16), the impedance can be determined, and for low frequencies, the impedance total is purely resistive, and as the frequency increases, the impedance converges to negative infinity. Fig. 3.10 (c) shows a parallel RC combination, and at low frequencies, it has pure resistance, whilst at high frequencies, the capacitor has a low impedance which is short-circuited as shown. Fig. 3.10 (d) shows a parallel RC combination in series with a pure resistor, and at low frequencies, it has pure resistance summation since the capacitor has infinite impedance; hence current only flows through the resistors; thus, the real axis intersection at the total resistive impedance of the network, whilst at high frequencies, the capacitor has low impedance(zero) which short-circuits the parallel resistor, as such only the intersection with the real axis [17].

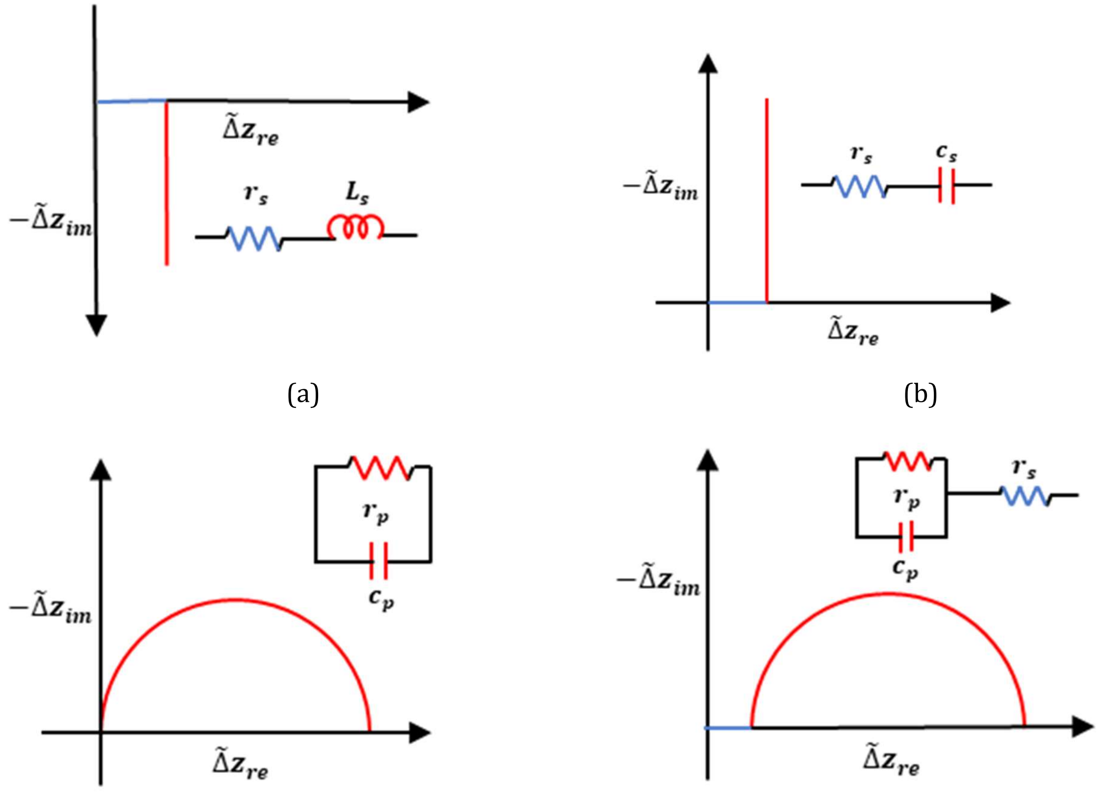

(a) (b)

(c) (d)

Fig. 3.10: EEC modelling from IS (a) series RL (b) series RC (c) parallel RC (d) series R-RC

3.7 Conclusions

This chapter reviewed impedance spectroscopy in detail as a linear characterization technique. It further developed the understanding of using a single sinusoid signal for injection along with it its respective parameter selection. i.e., the amplitude, phase, and signal frequency. Thereafter, the PRBS signal was described, its characteristics and design optimization for performing online condition monitoring along with the methodology to be adopted. The impedance spectroscopy consideration followed, then the modelling of fuel cell systems from the application of impedance spectroscopy.

Chapter 4

Simulation and implementation of impedance spectroscopy using a buck-boost converter

This chapter presents the design of the buck-boost converter while also developing the state-space model for the converter. The averaged linearized state-space model of the buck-boost converter is used for the small-signal analysis of the system, for controlling the output voltage to the specified tolerance range in the steady-state condition and, for injecting the EIS signal into the input source, i.e. the fuel cell system in this research.

Electrochemical impedance spectroscopy (EIS) of the modelled fuel cell circuit was performed theoretically to determine the impedance for different frequencies; the results obtained served as benchmark results before the EIS was performed using electrical circuits.

4.1 Buck-boost converter

The converter topology used is an inverting buck-boost converter; which only allows for the transfer of power in the forward direction, i.e., from the input voltage (fuel cell system) to the load. The converter topology is shown in Fig. 4.1. It minimizes the use of semiconductor devices to reduce power losses.

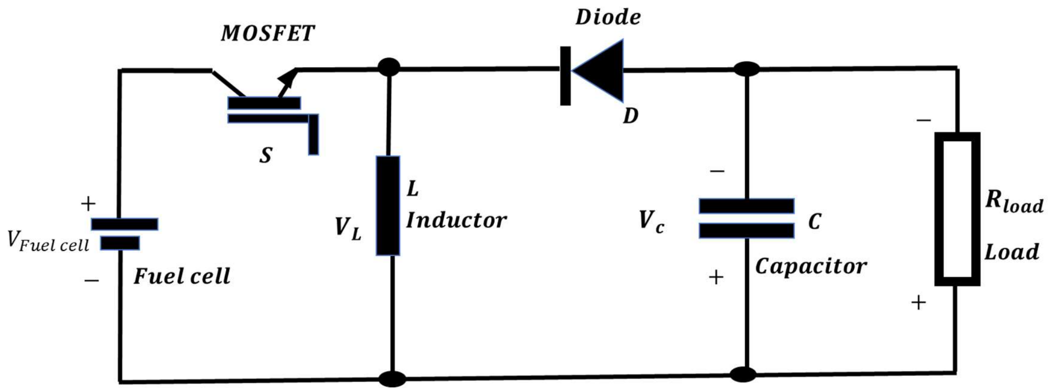

Fig. 4.1: Inverting buck-boost converter

The buck-boost converter above operates by varying the switching signal to the MOSFET switch, S, to determine the output voltage of the converter. The converter either boosts or bucks the input voltage of the fuel cell system by manipulating the duration the switch is kept on/off. The converter output load is modelled by a purely resistive load for simplification.

The complete analytical operation of the converter is detailed in the subsections below; equations are derived for component sizing and for relating the input voltage to the output voltage of the converter. For the analytical modelling of converter, some assumptions are made regarding the whole system for simplification. These assumptions are as follows:

- The voltage drop across the MOSFET switch, S and diode D, is negligible and considered to be ideal.
- The inductor is operating in the continuous current conduction mode.

It should be noted that the buck-boost converter, without adaptation of the above assumptions, is non-linear and time-variant (due to the semiconductors). The current flowing in the capacitor and the voltage drop across the inductor are governed by the below equations.

$$i_c(t) = C\frac{dV_c(t)}{dt} \tag{4-1}$$

$$V_L(t) = L\frac{di_L(t)}{dt} \tag{4-2}$$

4.1.1 Buck-boost converter when MOSFET switch S is on

When the MOSFET switch, S is closed (on), the diode D is reversed biased and acts as an open circuit. The inductor is directly connected to the fuel cell system, thus a voltage (V_L) is developed across the inductor. The inductor current (I_L) increases from zero, while the inductor voltage remains constant. The capacitor voltage (V_c) decreases during this transition because it is discharging through the load resistor (R_{load}). This configuration is illustrated in Fig. 4.2 below, where loop 2 is open.

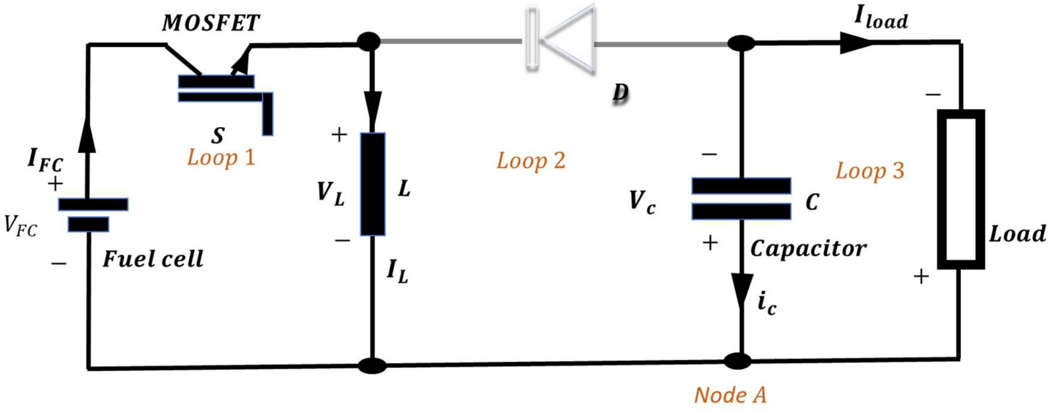

Fig. 4.2: Buck-boost converter when Switch S is ON

Kirchhoff's Voltage Law (for Loops 1 and 3) and Kirchhoff's Current Law (Node A) are performed.

$$V_L(t) = V_{FC}(t) = L\frac{di_L(t)}{dt} \tag{4-3}$$

$$0 = i_c(t) + \frac{V_c(t)}{R_{Load}} \tag{4-4}$$

$$V_o(t) = V_c(t) \tag{4-5}$$

4.1.2 Buck-boost converter when MOSFET switch S is off

When the MOSFET switch S is opened (off), the cell is isolated from the inductor. This phenomenon is illustrated in Fig. 4.3. Loop 1 is isolated; the diode is forward biased; the inductor voltage changes its polarity so that the inductor can oppose the change in current.

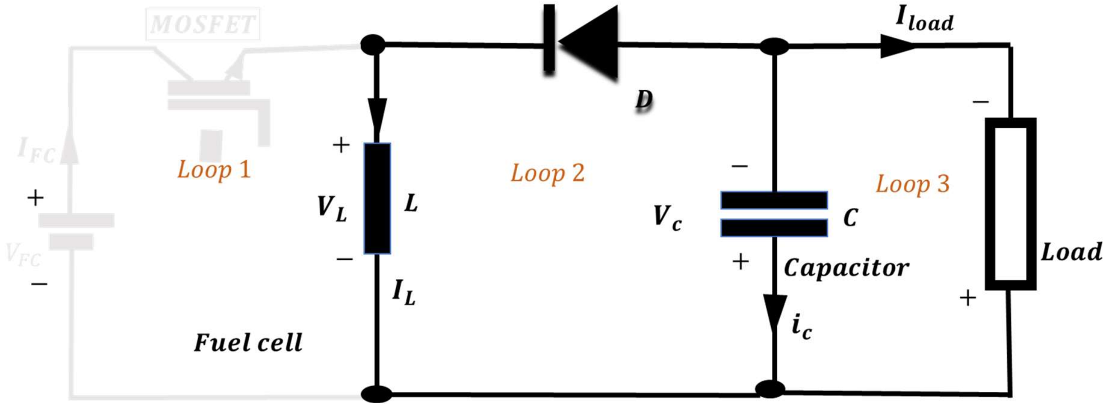

Fig. 4.3: Buck-boost converter when Switch S is OFF

Kirchhoff's Voltage Law (for Loops 2 and 3) and Kirchhoff's Current Law (Node A) are performed.

$$V_c(t) = V_L(t) = V_o(t) = L\frac{di_L(t)}{dt} \tag{4-6}$$

$$i_L(t) + i_c(t) + \frac{V_c(t)}{R_{load}} = 0 \tag{4-7}$$

4.1.3 Buck-boost converter overall operation under steady state

The buck-boost converter at start-up is transient [42]. However, this section focuses on the buck-boost operation at a steady state. The assumption of continuous conduction mode is presumed.

The average inductor current of the buck-boost converter can be computed using equations (4-3) and (4-7), as shown in the following section. The total duration can be presented by the switching period T_s and its on time DT_s where D is the duty cycle and represents the ratio of on time to switching period $(0 < D < 1)$. The percentage that the switch is off can be written as $(1 - D)T_s$. This is illustrated in Fig. 4.4 below.

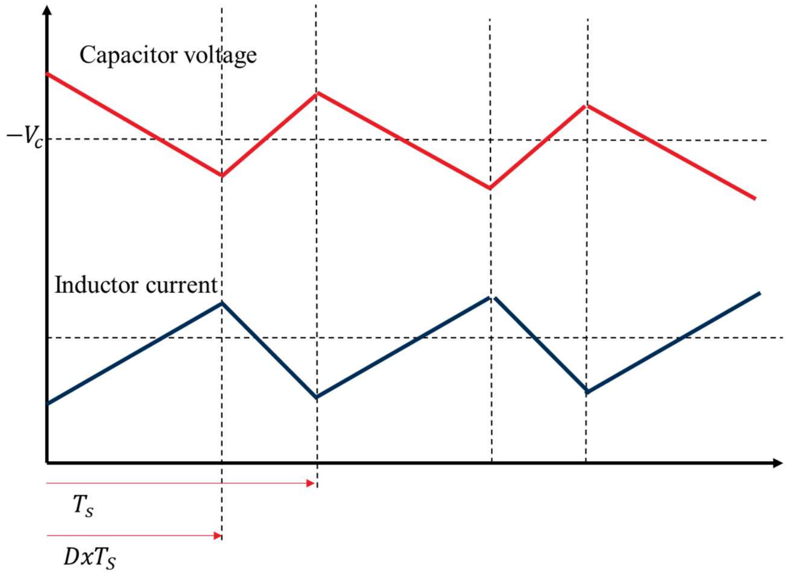

Fig. 4.4: Capacitor Voltage waveform and inductor current waveform for period Ts [43]

Inductor current when MOSFET switch S is closed (ON).

$$\frac{di_L(t)}{dt} = \frac{V_{FC(t)}}{L} \tag{4-8}$$

The rate of change of current is constant.

$$\frac{\Delta i_L(t)}{\Delta t} = \frac{\Delta i_L(t)}{DT_s} = \frac{V_{FC}(t)}{L} \tag{4-9}$$

$$\Delta i_{Lclosed}(t) = \frac{V_{FC}(t)DT_s}{L} \tag{4-10}$$

Inductor current when the MOSFET switch S is opened (OFF).

$$\frac{di_L(t)}{dt} = \frac{V_o(t)}{L} \tag{4-11}$$

The rate of change of current is constant.

$$\frac{\Delta i_L(t)}{\Delta t} = \frac{\Delta i_L(t)}{(1-D)T_s} = \frac{V_o(t)}{L} \tag{4-12}$$

$$\Delta i_L(t) = \frac{V_o(t)(1-D)}{L} \tag{4-13}$$

As a result, the averaged inductor current is computed as follows:

$$\Delta i_{Lclosed}(t) + \Delta i_{Lopened}(t) = 0 \tag{4-14}$$

$$\frac{V_{FC}(t)DT_s}{L} + \frac{V_o(t)(1-D)T_s}{L} = 0 \tag{4-15}$$

$$V_o(t) = -V_{FC}(t)\frac{D}{1-D} \tag{4-16}$$

$$\frac{V_o(t)}{V_{FC}(t)} = -\frac{D}{1-D} \tag{4-17}$$

Equation (4-17) relates output voltage to the input voltage on the fuel cell side. It also shows that the polarity of the output voltage is inversed in relation to the input voltage. The relationship is non-linear to the duty cycle.

4.2 Buck-boost state variable modelling of the buck-boost converter

As discussed in Section 4.1, the buck-boost converter is non-linear and time-variant because of the varying nature of the PWM switching and the properties of its semiconductor components. To effectively perform EIS on the buck-boost converter, given the possibility that there might be external disturbances experienced by the system (i.e. the combined dc-dc converter and fuel cell system), control is required. However, to apply linear control, a linear time-invariant model is required. [23] discusses and explores control for Linear-Time Invariant (LTI) systems. Initially, the system needs to be averaged to make it time-invariant. The quasi-linear model for it can then be subsequently found [44] [45]. Its s-domain transfer function can be utilized to determine the system's small-signal transfer function, which is shown in Fig. 4.5 below.

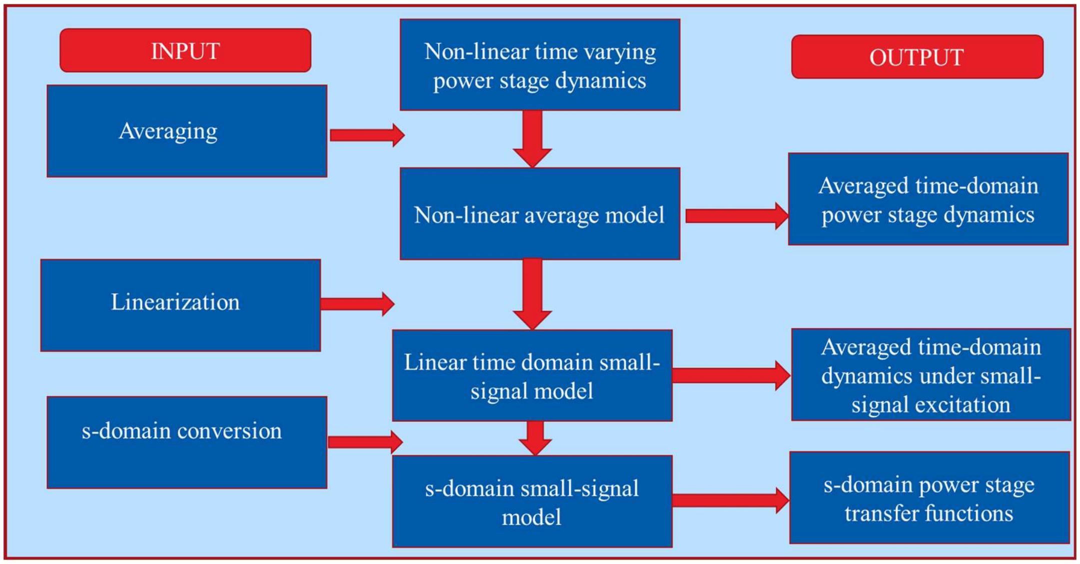

Fig. 4.5: Buck-boost converter modelling stages [45]

The stages are (1) State-space averaging, (2) Linearization around DC points and (3) S-domain conversion of the small-signal model.

4.2.1 State-space average modelling

State-space representation is a technique used to simplify a complex system. It uses a set of variables that model the internal dynamics of the system which are called state-space variables [46]. The state-space equation is expressed below [47].

$$\dot{x}(t) = Ax(t) + Bu(t) \tag{4-18}$$

$$y(t) = Cx(t) + Du(t) \tag{4-19}$$

Where $u(t)$ is the system input vector, $x(t)$ is the system state vector. In this computation, $\dot{x}(t)$ is a derivative of the state vector and $y(t)$ is the output vector. The matrices A, B, C, D, on the other hand, describe the system's dynamic behavior [18].

The state-vector dimension can be determined by the number of storage elements in the electrical circuit. In this case, it is the inductor and capacitor. $\dot{x}(t)$ is therefore expressed by the equation below, where $x_1(t), x_2(t)$ are mapped as $i_L(t),\ V_c(t)$ respectively.

$$x\dot{(t)} = \begin{bmatrix} \frac{di_L(t)}{dt} \\ \frac{dv_C(t)}{dt} \end{bmatrix} \tag{4-20}$$

The operation of the buck-boost converter is time-variant and non-linear because of the switching components and the diodes volt drop [46], [47].
The state-space equation for the buck-boost converter during the on and off mode is as follows.

$$\dot{x}(t) = A_1 x(t) + B_1 u(t) \text{ for } dT_s \tag{4-21}$$

$$\dot{x}(t) = A_2 x(t) + B_2 u(t) \text{ during } (1-d)T_s \tag{4-22}$$

By averaging out the system, the final average matrix A and B are as follows [46]:

$$A_{average} = A_1 d + A_2(1-d) \tag{4-23}$$

$$B_{average} = B_1 d + B_2(1-d) \tag{4-24}$$

$$\dot{x}_{Average}(t) = A_{Average} x(t) + B_{Average} u(t) \text{for total period } T_s \tag{4-25}$$

During dT_S. The switch is turned on

Converting the above equations into the matrix form gives:

$$\begin{bmatrix} \frac{di_L(t)}{dt} \\ \frac{dv_C(t)}{dt} \end{bmatrix} = \begin{bmatrix} 0 & 0 \\ 0 & -\frac{1}{R_{load}C} \end{bmatrix} \begin{bmatrix} I_L \\ V_C \end{bmatrix} + \begin{bmatrix} \frac{1}{L} \\ 0 \end{bmatrix} V_{FC} \tag{4-26}$$

When the switch is turned off:

$$\begin{bmatrix} \frac{di_L(t)}{dt} \\ \frac{dv_C(t)}{dt} \end{bmatrix} = \begin{bmatrix} 0 & \frac{1}{L} \\ -\frac{1}{C} & -\frac{1}{R_{load}C} \end{bmatrix} \begin{bmatrix} I_L \\ V_C \end{bmatrix} + \begin{bmatrix} 0 \\ 0 \end{bmatrix} V_{FC} \tag{4-27}$$

Converting the above equations into matrix form gives the computations of the average models.

$$A_{average} = \begin{bmatrix} 0 & 0 \\ 0 & -\frac{1}{R_{load}C} \end{bmatrix} d + \begin{bmatrix} 0 & \frac{1}{L} \\ -\frac{1}{C} & -\frac{1}{R_{load}C} \end{bmatrix} (1-d) \tag{4-28}$$

$$A_{average} = \begin{bmatrix} 0 & \frac{1-d}{C} \\ -\frac{(1-d)}{C} & -\frac{1}{R_{load}C} \end{bmatrix} \tag{4-29}$$

$$B_{average=} \begin{bmatrix} \frac{1}{L} \\ 0 \end{bmatrix} d + \begin{bmatrix} 0 \\ 0 \end{bmatrix} (1-d) \tag{4-30}$$

$$B_{average=} \begin{bmatrix} \frac{d}{L} \\ 0 \end{bmatrix} \tag{4-31}$$

Average state-space model:

$$\begin{bmatrix} \frac{di_L(t)}{dt} \\ \frac{dv_C(t)}{dt} \end{bmatrix} = \begin{bmatrix} 0 & \frac{1-d}{C} \\ -\frac{(1-d)}{C} & -\frac{1}{R_{load}C} \end{bmatrix} \begin{bmatrix} I_L \\ V_C \end{bmatrix} + \begin{bmatrix} \frac{d}{L} \\ 0 \end{bmatrix} V_{FC} \tag{4-32}$$

4.2.2 State-space average model linearization

The averaged state-space model is now time-invariant but still non-linear. A non-linear average model can be linearized into a small-signal model [46], [48], [49], [50]. The system is assumed to have a very small input and thus can be regarded as pseudo-linear, i.e. operating around a small linear point. This linearization is achieved by assuming that the buck-boost converter state-space variables $(u(t), x(t),)$ $d(t)$ are composed of a DC and AC component as shown below.

$$u(t) = U(t) + \tilde{u}(t) \tag{4-33}$$

$$x(t) = X(t) + \tilde{x}(t) \tag{4-34}$$

$$d(t) = D(t) + \tilde{d}(t) \tag{4-35}$$

The above equations (4-33), (4-34),(4-35) are computed into the averaged state-space equation (4-32) [46] before the buck-boost converter parameters are substituted to give the equation below.

$$\begin{aligned}\dot{X}(t) + \dot{\tilde{x}}(t) = {} & [A_{on}[D(t) + \tilde{d}(t)] + A_{off}[1 - D(t) - \tilde{d}(t)]][X(t) + \tilde{x}(t)] \\ & + \left[B_{on}[D(t) + \tilde{d}(t)] + B_{off}[1 - D(t) - \tilde{d}(t)]\right][U(t) + \tilde{u}(t)]\end{aligned} \tag{4-36}$$

Assumptions made are [46]:

- DC components in the model have known variables, and they can be computed when knowing the buck-boost converter components.
- The system (buck-boost converter) is analyzed under steady-state; therefore, this results in $\dot{X}(t) \approx 0$.
- Second-order terms have a small magnitude and can therefore be ignored (second-order terms are products of $\tilde{u}(t), \tilde{x}(t), \tilde{d}(t)$).
- The input $u(t)$, which is the fuel cell voltage in the case of the buck-boost converter is assumed to be composed of the DC component only, ignoring the ac perturbation ($\tilde{u}(t) \approx 0$).

This simplifies equation (4-32) to the equation below:

$$\dot{\tilde{x}}(t) = A\tilde{x}(t) + [[A_{on} - A_{off}]X(t) + [A_{on} - A_{off}]U(t)]\, \tilde{d}(t) \tag{4-37}$$

The above equation
(4-32) is the average linear small-signal model of the buck-boost converter before parameter substitution.

4.2.3 State-Space S-domain conversion of the small-signal model.

The small-signal equation described by equation
(4-32) is both Time-Invariant and Linear (LTI); therefore, a transfer function that can be controlled using linear control may now be implemented. Thus, the Laplace transform equation
(4-32) is computed below.

$$s\tilde{x}(s) = A\tilde{x}(s) + [[A_{on} - A_{off}]X(s) + [A_{on} - A_{off}]U(s)]\, \tilde{d}(s) \tag{4-38}$$

This is simplified to:

$$\tilde{x}(s) = [sI - A]^{-1}[\big[[A_{on} - A_{off}]X(s) + [A_{on} - A_{off}]U(s)\big]\,\tilde{d}(s)] \tag{4-39}$$

When substituting the buck-boost parameter variables, a pair of equations is found, which relates the capacitor voltage and inductor current to the perturbation duty cycle, as shown below.

$$G_{Vc}(s) = \frac{\widetilde{v_C}(s)}{\tilde{d}(s)} = \frac{-\left[\frac{(V_{FC} - V_C)(1 - D)}{LC}\right] + s\frac{I_L}{C}}{s^2 + \frac{s}{R_{load}C} + \frac{(1 - D)^2}{LC}} \tag{4-40}$$

$$G_{i_L}(s) = \frac{\widetilde{i_L}(s)}{\tilde{d}(s)} = \frac{\frac{(V_{FC} - V_C)}{L}s + \frac{(V_{FC} - V_C)}{R_{load}C} + \frac{(1 - D)I_L}{LC}}{s^2 + \frac{s}{R_{load}C} + \frac{(1 - D)^2}{LC}} \tag{4-41}$$

The equation is used for the control of the capacitor voltage (i.e. output voltage), and the equation is used to perform EIS by determining the duty cycle required to inject a current into the fuel cell system.

4.3 Components selection

4.3.1 Input and output voltage

A single fuel cell produces a typical voltage of $0.7 - 0.8\,V$. To increase the output voltage provided by the fuel cell system, the cells can be connected in series. In this case, it was assumed that the fuel cells each produce a minimum typical voltage of $0.6\,V$, and 6 fuel cells provide a combined voltage in the range of $4.2 - 4.5\,V$.

$$V_{FC-min} = 4.2\,V \text{ and } V_{FC-max} = 4.5\,V \tag{4-42}$$

This $V_{FC-m} = 4.2\,V$ from the fuel cell is required to provide $9\,V$ ($V_{out} = 9\,V$) to an output load, with an output power of $30.15\,W$. Thus, a resistor of $2.68\,\Omega$ would ideally act as an ideal constant current load sink of $3.2\,A$.

The switching frequency chosen for this simulation is $F_{sw} = 100\,kHz$. It is a higher switching frequency than usual, which implies a higher degree of switching losses, however this sufficient to perform EIS since the bandwidth of interest is from $0.1\,Hz$ to $10\,kHz$. Then using equation (4-17) the DC-biased duty cycle is $D = 0.67$.

4.3.2 Inductor:

The minimum inductance required to ensure the converter operates in CCM, is determined using(4-43) [45].

$$L_{min} = \frac{R_{load}(1-D)^2}{2f} \tag{4-43}$$

With the specified load resistor, frequency and duty cycle, $L_{min} = 1.45926\mu H$. The chosen inductor was $L = 444\mu H$, since it provided better ripple cancellation.

4.3.3 Capacitor:

The minimum capacitance to be used is chosen using equation (4-44) [45], which is calculated based on the specified load resistor, frequency, duty cycle and output voltage ripple of less than 5%. This is the capacitor value taken into consideration to perform the simulations and the practical experimentation.

$$C_{min} = \frac{D}{(\frac{\Delta V_o}{V_o})R_{load}f} \tag{4-44}$$

As such, the calculated C_{min} is 50 μF. The chosen capacitor is $C = 470\ \mu F$. However, it should be noted that a larger capacitor will assist in reducing the ripple across the load caused by EIS.

4.4 Open loop current injection

Perturbating the inductor current with an ac sinusoidal signal of a specific frequency and amplitude , requires that the relationship between the duty cycle and amplitude of the sinusoid be determined. Therefore, as mentioned before, equation (4-45) is used to relate the inductor ac sinusoidal signal, along with its associated ac sinusoidal duty cycle and the injected frequency, given that the converter DC values are known (can easily be determined). The equation used for EIS injection is shown below. The Laplace transform is analysed for the frequency domain by substituting $s = j\omega$, Whereby $\omega = 2\pi f$, with f being the associated frequency.

$$\tilde{d}(f) = \tilde{i_L}(f) \cdot \frac{(2\pi fj)^2 + \frac{2\pi fj}{R_{load}C} + \frac{(1-D)^2}{LC}}{\frac{2\pi fj(V_{FC}-V_C)}{L} + \frac{(V_{FC}-V_C)}{R_{load}C} + \frac{(1-D)I_L}{LC}} \tag{4-45}$$

For injecting an ac sinusoidal signal of amplitude $\tilde{i_L}(f) = 1\ A$ with a frequency of 100 Hz, with the buck-boost converter parameters:

$$R_{load} = 2.68,\ V_{FC} = 4.5, V_c = 9, I_L = 10, D = 0.67, f = 100\ Hz.$$

The duty cycle amplitude is as below.

$$\tilde{d}(f) = 0.07845158503\angle 2.6488°@100Hz$$

4.5 Buck-boost simulations and discussions

The converter system for the fuel cell was designed and simulated in MATLAB Simulink. The converter was used to facilitate power transfer whilst estimating its impedance using online EIS and PRBS. The Randle circuit, as shown in Fig. 3.2 with parameters listed in Table 6-1used to represent the fuel cell [7].

The fuel cell's bandwidth, spanning from 0.1 Hz to 10 kHz was considered since this bandwidth covers the dynamics presented by the Randle circuit model [3] [51]. The benchmark results are obtained from extracting the impedance response for the Randle circuit representing each condition as stipulated in Table 6-1.

4.5.1 Buck-boost open loop results with and without the emulated fuel cell system

The buck-boost converter was firstly simulated with an ideal dc voltage source, and then the emulated fuel cell system (dc source with Randle circuit model). This is done to observe the changes in the input voltage, input current, inductor current, output current and output voltage.

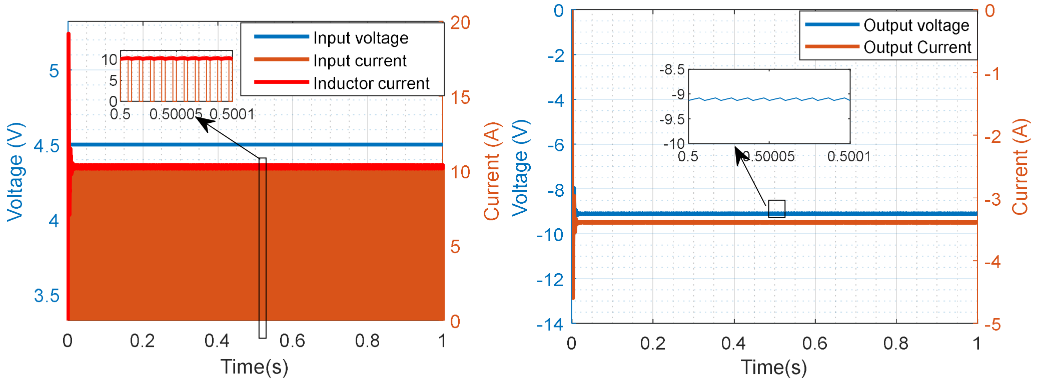

(a) (b)

Fig. 4.6: Buck-boost converter measured signals (a) Input current, voltage, and inductor current (b) the output voltage and output current

Fig. 4.6(a) above shows the input current, voltage and inductor current of the buck-boost converter. In this condition, the fuel cell is modelled to have negligible internal impedance, as such input current, inductor current and the input voltage are as designed, i.e., it draws an inductor current of 10 A, input voltage of 4.5 V with the input current, discontinuous , varying between 10A and 0 A (i.e. waveform is identical to inductor current when it ramps up during t_{on}). Fig. 4.6(b) shows the output voltage and current for the ideal case. The output voltage is $-9\ V$ and the output current is $-3.4\ A$. This is a result that an inverting buck-boost topology is used.

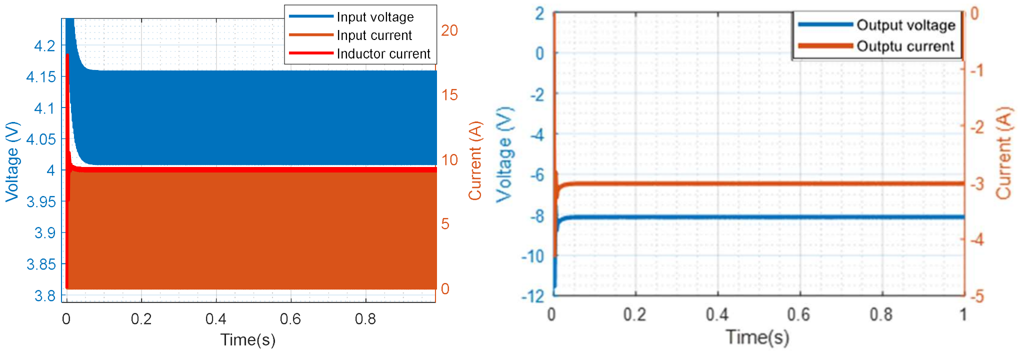

(a) (b)

Fig. 4.7: Buck-boost converter measured signal (a) input voltage, current and inductor current (b)output voltage and output current.

Fig. 4.7(a) shows the input current, voltage and inductor current of the buck-boost converter when emulating the fuel cell at the input. Fig. 4.7(b) shows the output voltage and current, where both the signals are of opposite polarity to the input voltage and current. It can be observed that the input voltage, current and inductor current of the buck-boost converter are different from those in Fig. 4.6, and the magnitudes have decreased.

With the input voltage being approximately $4.1\ V$, the inductor current drawn is approximately $9.7\ A$, and the input current is discontinuous, varying between $9.7\ A$ and $0\ A$, with an increase in ripple current. The observed output voltage is $-8\ A$, and the measured current is approximately $-3A$. This implies that for different operating conditions (Randle circuits), different input/output currents and voltages, and inductor currents will be observed in comparison to the ideal case. Thereby demonstrating the need for DC power control before Impedance Spectroscopy is performed.

4.5.2 Buck-boost open-loop EIS results with and without the emulated fuel cell system.

The effects of performing EIS on the converter are being investigated before the converter has any form of DC power control.

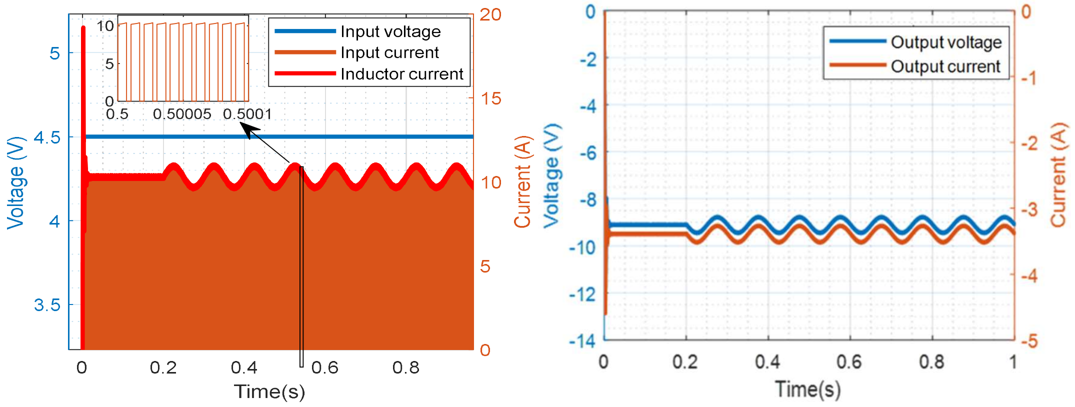

(a) (b)

Fig. 4.8: Buck-boost converter measured signal (a) Input current, voltage, and inductor current converter (b) the output voltage and output current

Fig. 4.8(a) shows the input current, voltage, and inductor current of the buck-boost converter when the converter has an ideal dc source. Fig. 4.8(b) shows the output voltage and current, when EIS is implemented. The input ac perturbation (for impedance spectroscopy) is designed to have a peak-to-peak magnitude that is 10 % of its DC value. The amplitude is determined by using the amplitude equation derived for the buck-boost converter, which is equation (4-45), when performed in open loop. This shows the effectiveness of the derived perturbation equation using the small-signal linearized modelled system equations. Since the inductor is perturbed, the current has an amplitude of 1 A.

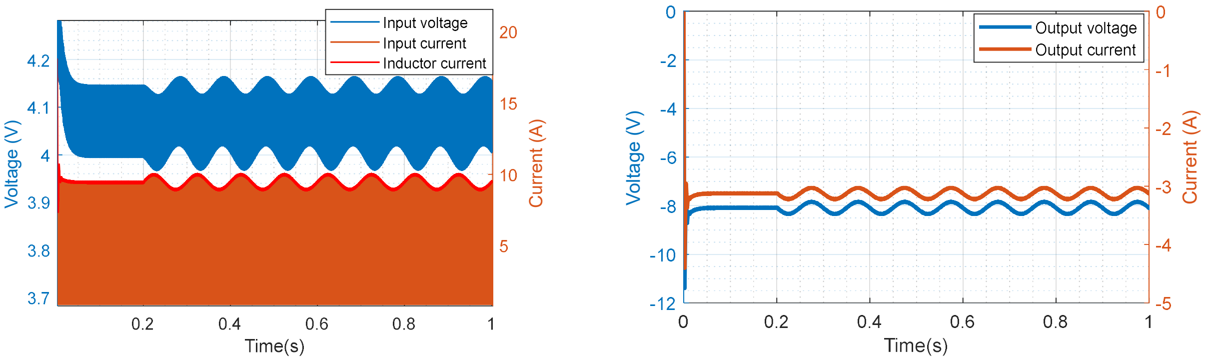

(a) (b)

Fig. 4.9: Buck-boost converter measured signal (a) Input current, voltage, and inductor current (b) the output voltage and output current

Fig. 4.9 (a) shows the input current, voltage, and inductor current of the buck-boost converter when the converter has the emulated fuel cell system. Fig. 4.9(b) shows the output voltage and current, and this is when EIS is implemented. The ac perturbation signal is no longer 10 % of its DC value, the DC voltage is inductor current is 9.5 A whilst the ac amplitude is 0.6 A. This shows that the perturbation signal is not as initially designed, and this motivated the need for ac control as well.

4.5.3 Buck-boost open-loop PRBS results with and without the emulated fuel cell system.

The effects of performing PRBS on the converter is to be investigated before implementing DC power control, as done in section 4.5.2.

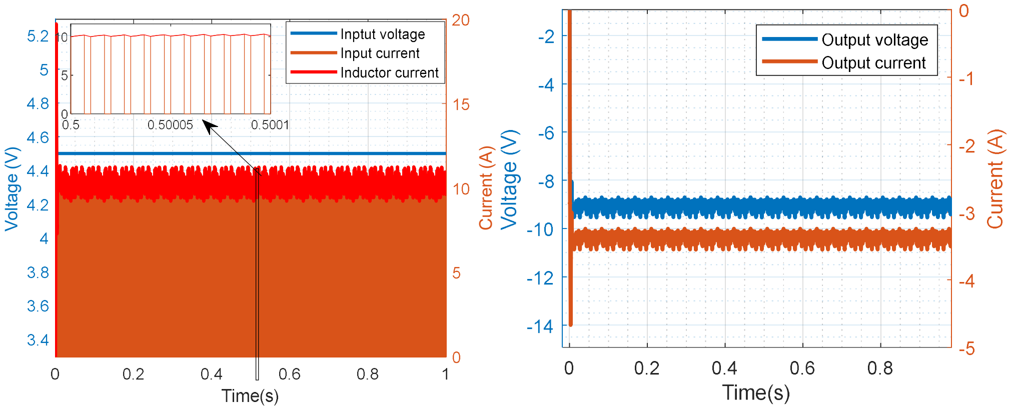

(a) (b)

Fig. 4.10: Buck-boost converter measured signal (a) Input current, voltage, and inductor current (b) the output voltage and output current

Fig. 4.10(a) shows the input current, voltage, and inductor current of the buck-boost converter when the converter has no emulated fuel cell system. Fig. 4.10(b) shows the output voltage and current when PRBS is implemented. The input voltage and current, inductor current, and output voltage and current are designed with the ac signal (impedance spectroscopy) being 10 % of the DC. In the ac (spectroscopy) signal, the amplitude is determined by using the amplitude equation derived for the buck-boost converter, when performed in an open loop. This shows the effectiveness of the estimated derived perturbation equation, using the small-signal linearized modelled systems equations.

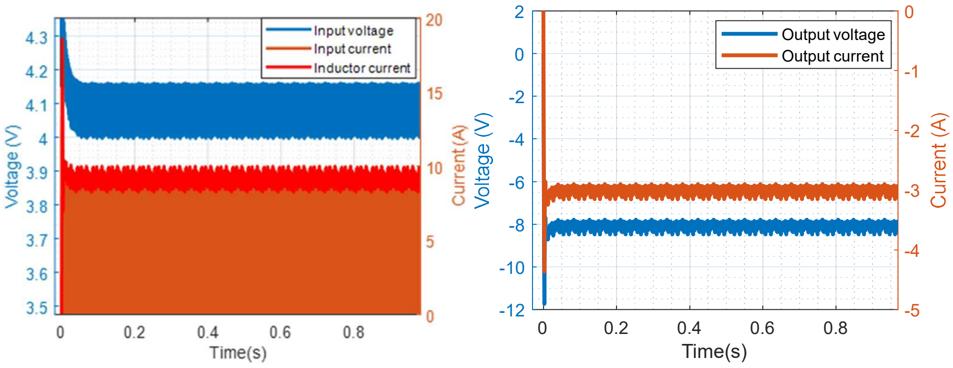

(a) (b)

Fig. 4.11: Buck-boost converter measured signal (a) Input current, voltage, and inductor current converter (b) the output voltage and output current.

Fig. 4.11 (a) The input current, voltage, and inductor current of the buck-boost converter when the converter has an emulated fuel cell system. Fig. 4.11 (b) the output voltage and current when PRBS is implemented.

A modelled fuel cell system is used, and the input voltage and current, inductor current, and output voltage and current are designed with the ac signal (impedance spectroscopy) being 10 % of the DC. In the ac (spectroscopy) signal, the amplitude is determined by using the amplitude equation derived for the buck-boost converter**,** when performed in an open loop. This shows that the perturbation AC is no longer 10% as initially designed, it is rather 6% of the new dc current, and this motivated the need for ac control as well.

4.6 Design of the controllers for the buck-boost converter

Fig. 4.12 shows the overall configuration of the buck-boost converter. In this section, the controllers for both the inductor current (inner loop) and outer output voltage (outer loop) are discussed. Two methods are considered for the inner control loop, given the additional requirements for perturbation of the ac signal, after which one is selected. The ac perturbation signal is added to I_{ref}, to achieve condition monitoring.

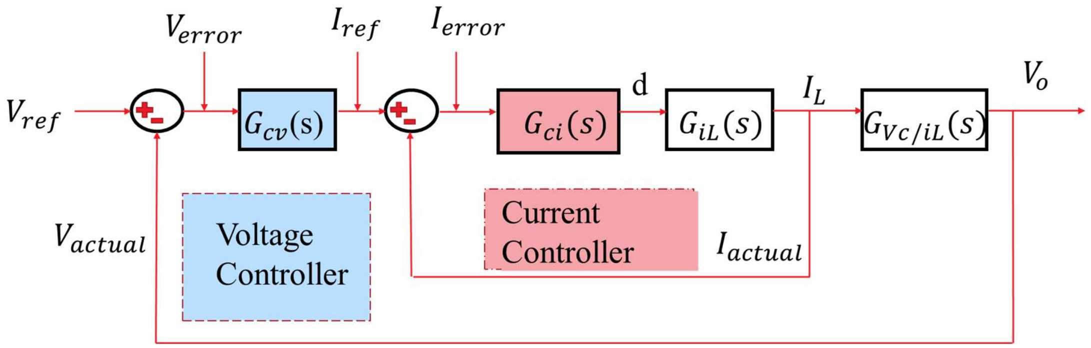

Fig. 4.12: Controller implementation overview.

4.6.1 Current loop controller

The current controller was designed using the current loop-derived transfer function (4-41) from section 4.2.3.

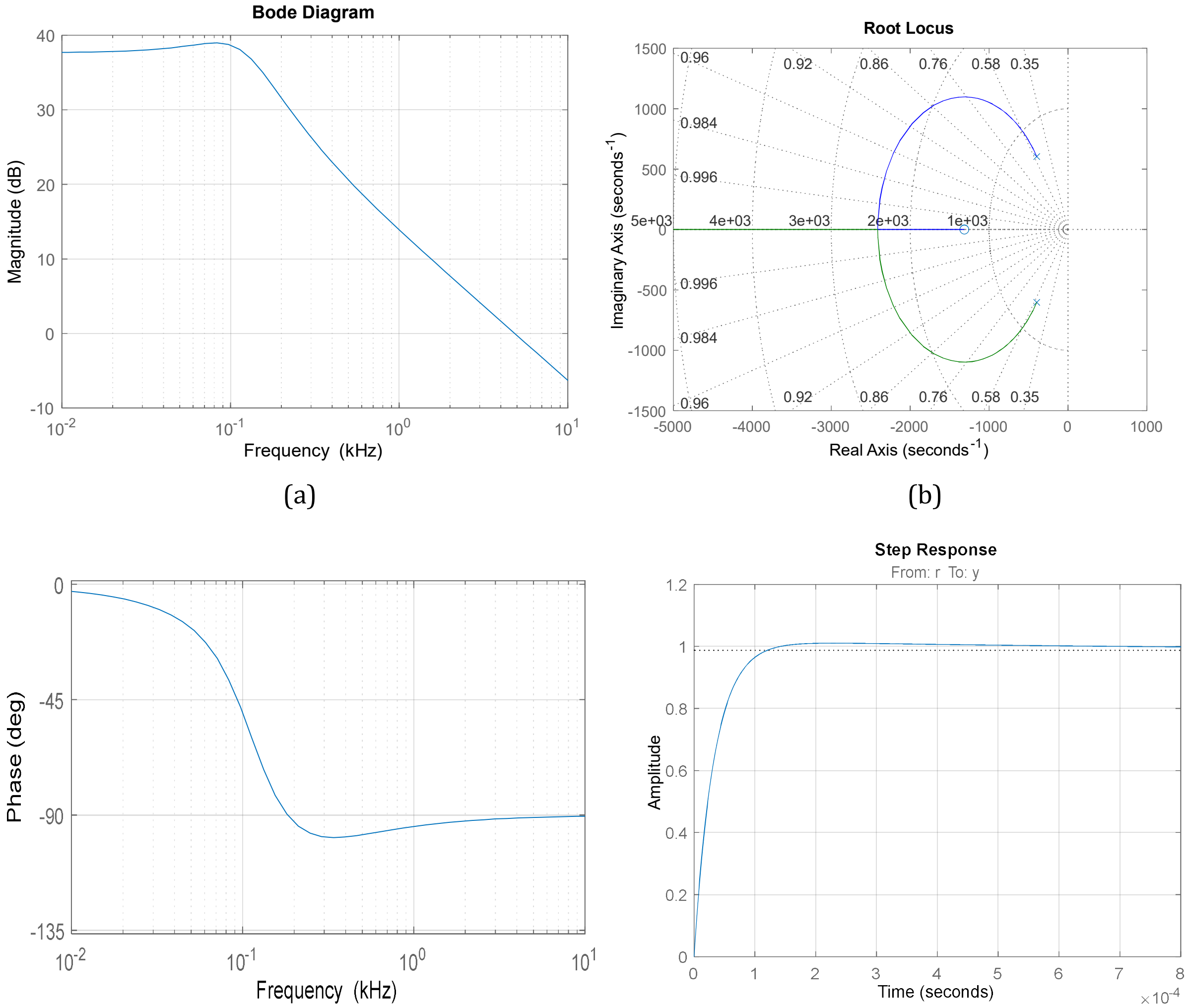

(a)

(b)

(c) (d)

Fig. 4.13: The inner current loop (a) bode magnitude (b) root locus (c) bode phase (d) time response

Fig. 4.13 shows the open loop response of the inner current loop of the buck-boost converter. The open loop system response currently has an overshoot of 2.36%. Fig. 4.14 shows the control loop configuration with its controller and transfer function.

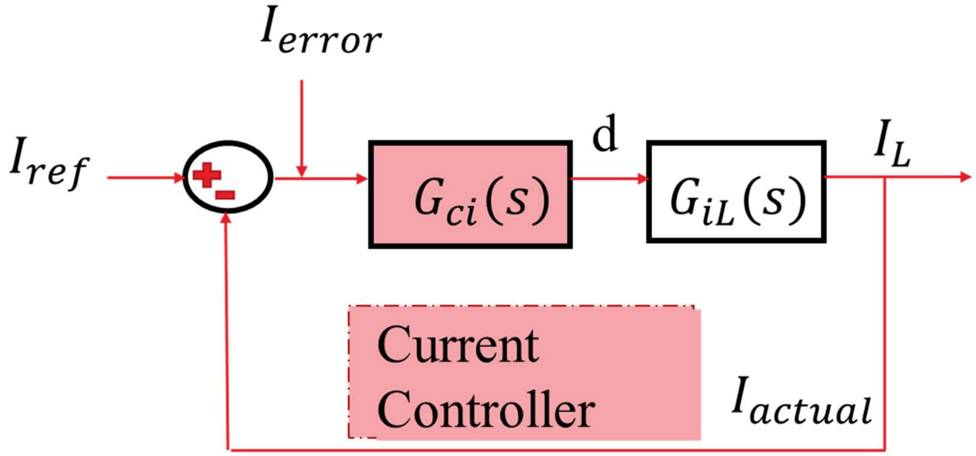

Fig. 4.14:Inner current loop with $G_{ci}(s)$representing the controller and I_{error} the error signal

i. PI compensator

The first step and priority of this PI current controller, G_{ci} (s), is to ideally achieve a zero-state error $e(s)$; as such, the first action was to add an integrator (the integrator, however, adds phase at dc frequency). The controller design and tuning is achieved using the MATLAB control system package, thus shown in Fig. 4.13 (d) is the closed loop unit step response of the system in Fig. 4.14 with a unity controller ($G(s) = 1$). The inner current loop system is currently stable, due to the placement of poles on the left side of the imaginary axis, as shown in the root locus plot in Fig. 4.13 (b). Fig. 4.13 (d) shows that the step response is bounded and converging to unity. Thus, this time domain behaviour response confirms stability.

$$\lim_{s\to 0} e(s) = \lim_{s\to 0}\left(\frac{1}{1+G.P} * Id^*\right) \tag{4-46}$$

In most designs, the priority would be to have the closed loop system have zero steady-state error.
As such, for a zero steady-state error and to ensure equation (4-46) converges to zero when s tends to zero for a given step input, $G(s)$ needs to have an integrator. The addition of this integrator introduces a pole at zero, which can be stabilized by the integrator gain in $G_1(s)$ and a proportional controller to

control the overshoot. Fig. 4.15 shows the system properties when the zero-steady state error is achieved and minimal overshoot.

As seen in Fig. 4.15, this is a stable system with closed-loop poles on the negative real axis. The settling time response seen in Fig. 4.15 (d) (right) is approximately 0.07 s which can be considered fast, and it satisfies the zero steady-state error requirement; these form a Proportional + Integral Controller (PI) of the form shown by equation (4-46) below.

$$G_{ci}(s) = K_p + \frac{K_i}{s} = \frac{K_p\left(s + \frac{K_i}{K_p}\right)}{s} \tag{4-47}$$

Whereby K_i is the integrator gain and K_p is the proportional gain. The system in Fig. 4.15 was designed and tuned using the PI controller method.

$$G_{ci}(s) = \frac{0.035(s + 1891.42)}{s} \tag{4-48}$$

Whereby K_p and K_i were calculated to be 0.035 and 66.21, respectively.

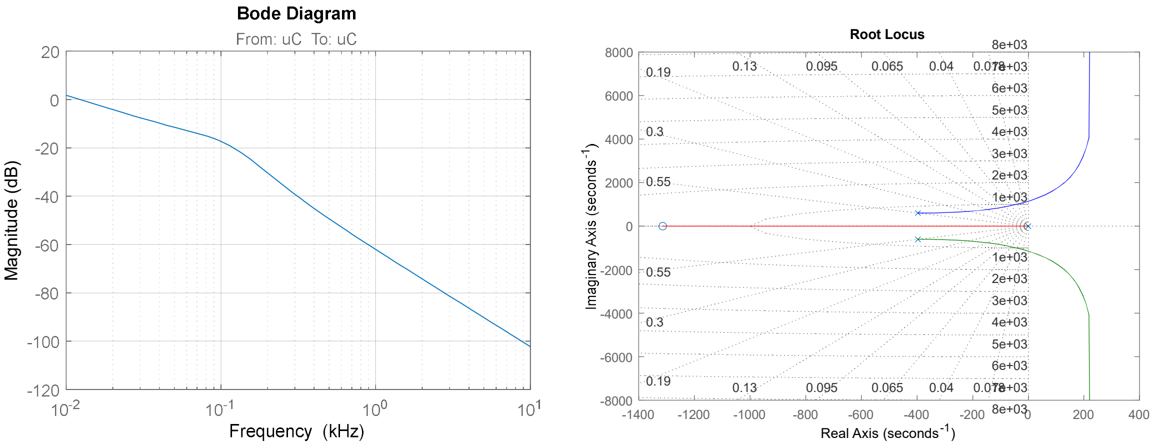

(a) (b)

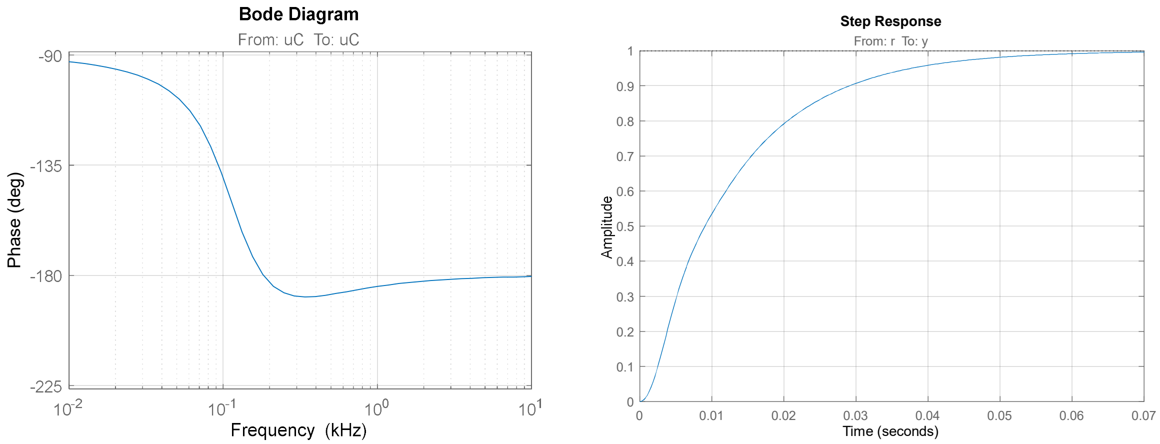

(c) (d)

Fig. 4.15: The inner current loop (a) bode magnitude (b) root locus (c) bode phase (d) time response

Fig. 4.15 (a) and Fig. 4.15 (c) show the magnitude and phase of the system, respectively. This shows that the system with this control currently attenuates ac signals less than 100 Hz.

This controller would be ideal for power transfer only. However, not good enough for impedance spectroscopy.

ii. Lead-lag compensator

Due to the limitations brought about by the PI control method, in terms of bandwidth, the lead-lag compensator was designed and used to increase the bandwidth. The lead was used to improve the frequency response whilst maintaining systems stability, and the lag was used to reduce the steady-state errors. The lead-lag compensator is shown in equation(4-49).

$$G_{ci}(s) = 590.54\frac{(s+69.84)(s+706.6)}{(s+1325)(s+2.2e^{4})} \tag{4-49}$$

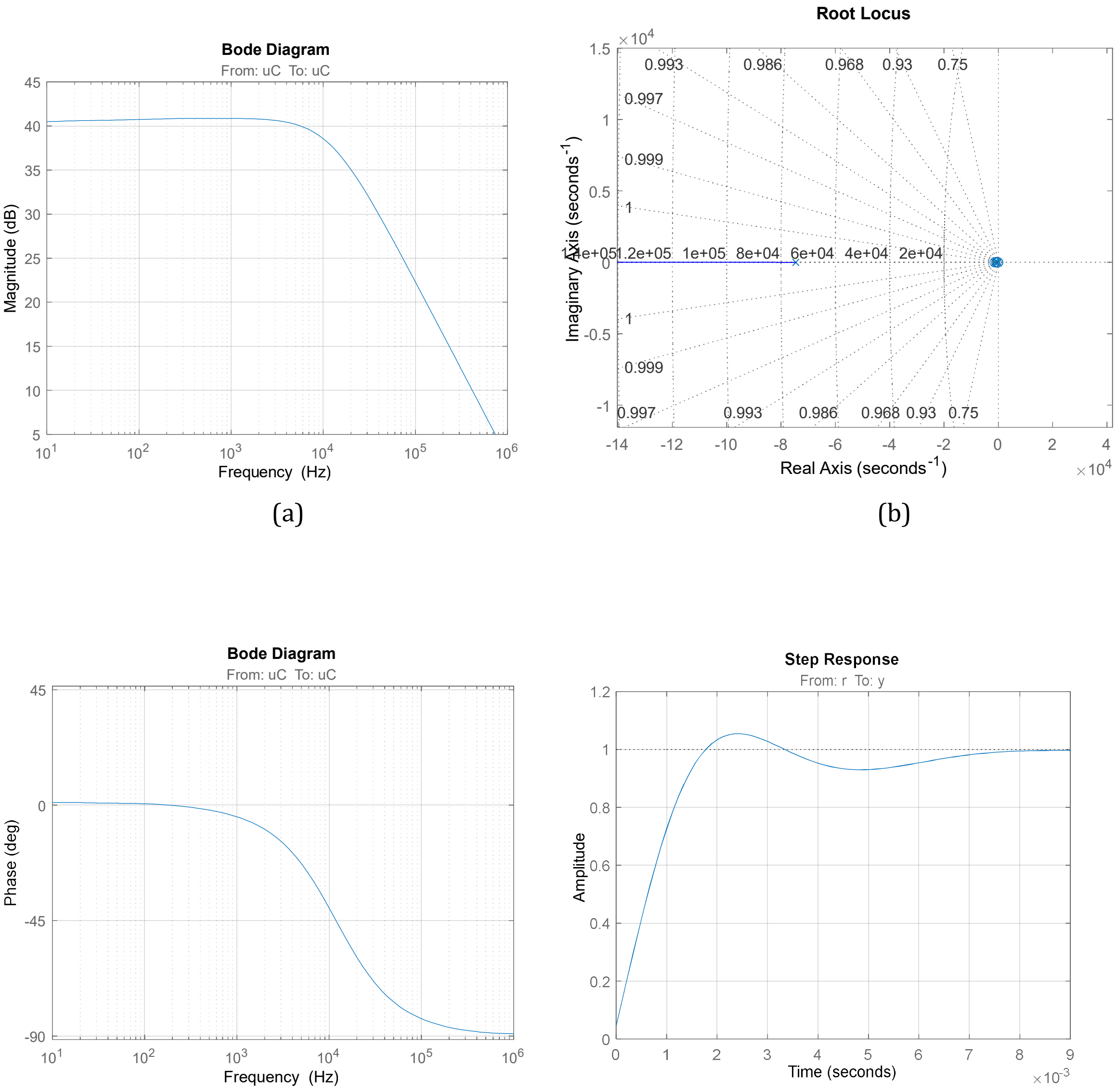

(a) (b)

(c) (d)

Fig. 4.16: The inner current loop (a) bode magnitude (b) root locus (c) bode phase (d) time response

Fig. 4.16 (a) and Fig. 4.16 (c) shows the magnitude and phase, with the magnitude plot showing that the controlled inner loop allows ac signals of up to $10kHz$. The bandwidth requirement for impedance spectroscopy is reached, however the steady-state error is not necessarily zero. It is evident that it is less than 5%, which is sufficient for the system since current ripple is expected. Fig. 4.16 (b) shows that the lead-lag compensator has all its poles on the left of the imaginary axis, and Fig. 4.16 (d) shows the unit step response is bounded, with an overshoot of less than 8%. The steady-state error is less than 2% with the phase margin at approximately 90°, and high gain margin. The system's settling time is less than 80 ms.

4.6.2 Voltage loop controller

This section presents the design for the voltage controller.

For the design, the following assumptions will be made:

- The inner loop satisfies the($< 10\%$) steady-state error requirement
- The inner loop has a faster settling time than the outer voltage loop (at least 10 times faster)
- And the inner loop tracks the input current to the tolerated values ($< 5\%$)

The voltage control loop is shown in Fig. 4.17, whereby the inner current loop has been simplified into a transfer function described by unity gain. The system in Fig. 4.17 portrays the input-output voltage of the system. The main parameter, in this case, is the output voltage, implying a controller needs to be designed to manipulate the output voltage response of the system.

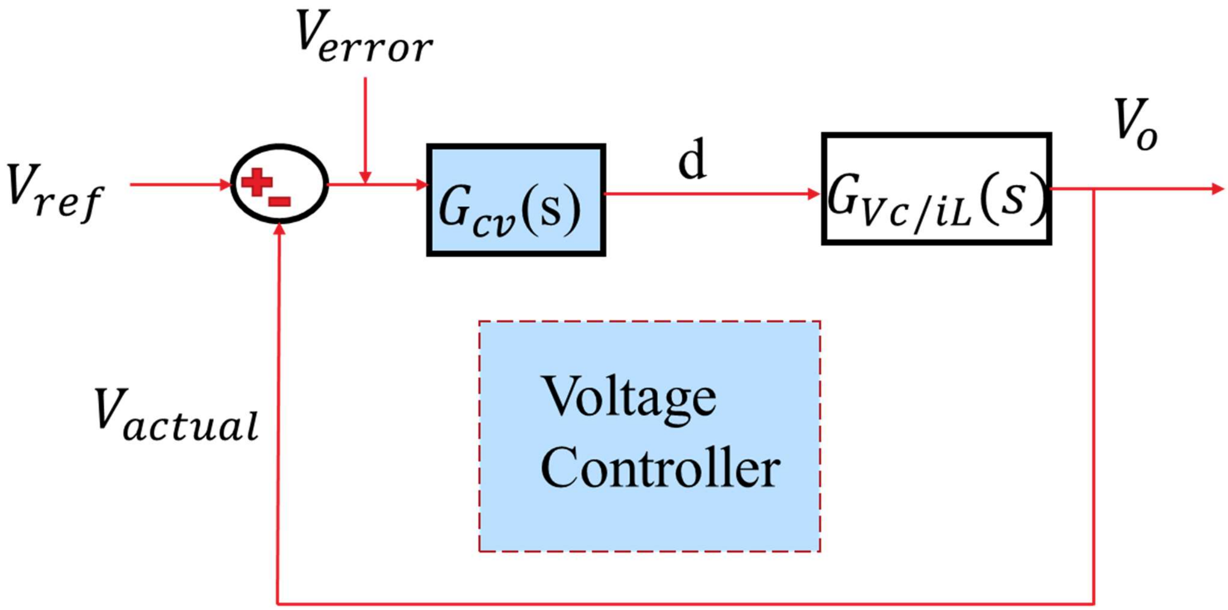

Fig. 4.17: Voltage Control loop where G_{CV} is the controller and V_{error} the error signal

Similar to the current loop when pursuing PI compensation, the first step of the voltage loop compensator will be an addition of an integrator. The need for an integral controller is to meet the zero steady-state error described by equation (4-50) for a step input (voltage).

$$\lim_{s\to 0} e(s) = \lim_{s\to 0}\left(\frac{1}{1+L} * v^*\right) \tag{4-50}$$

Where L represents the closed loop path shown in Fig. 4.17, the inclusion of a simple unity controller affects the system's behaviour in the manner shown in Fig. 4.18.

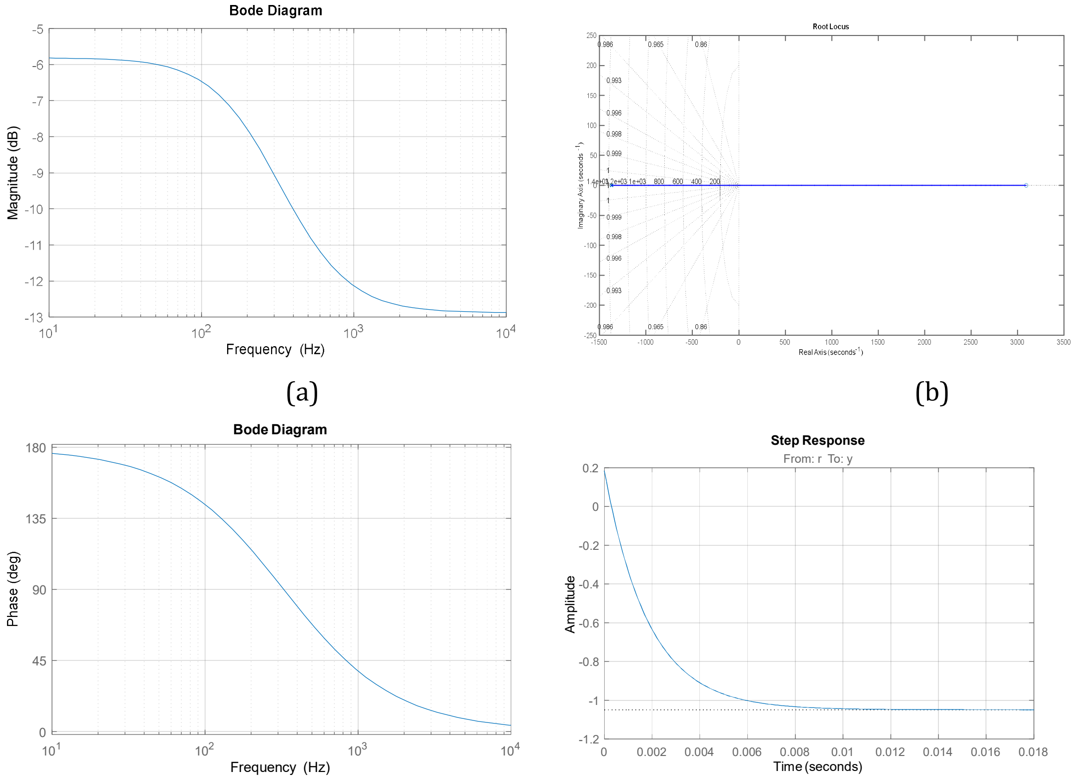

(a) (b)

(c) (d)

Fig. 4.18: The inner current loop (a) bode magnitude (b) root locus (c) bode phase (d) time response

As seen in Fig. 4.18(b), the root locus has a line that is located in both halves (RHS and LHS) of the imaginary axis, implying that the system can be unstable depending on the gain. Fig. 4.18(d) shows that the system is currently bounded and converging to approximately −1.1. Using the same method presented by equation (4-46), an optimized PI compensator was designed, the desired response depicted in Fig. 4.19 was achieved.

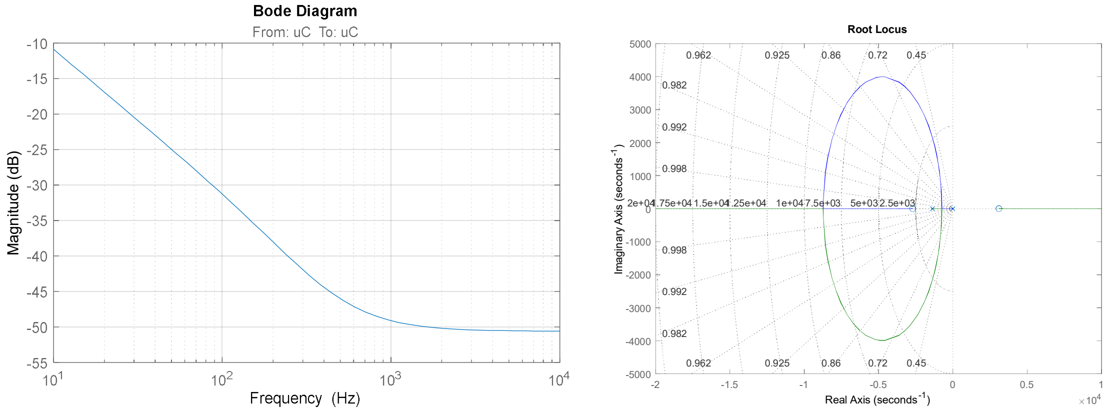

(a) (b)

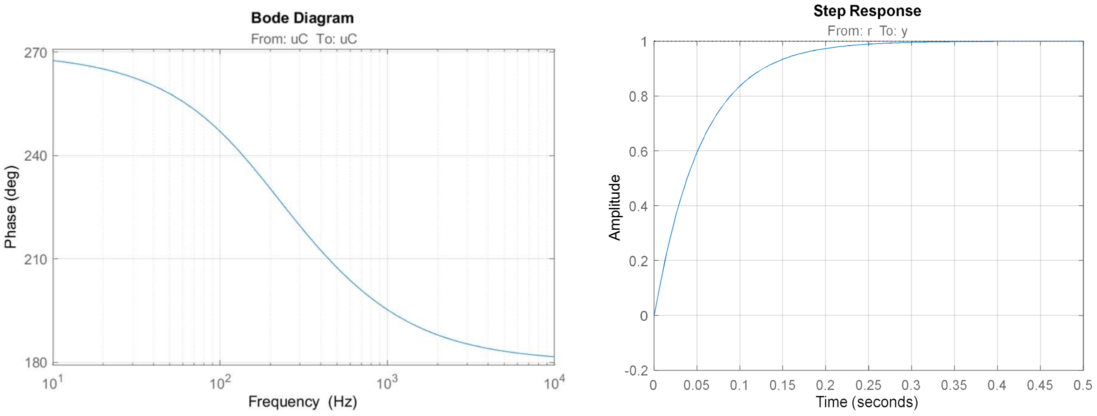

(c)

(d)

Fig. 4.19: The inner current loop (a) bode magnitude (b) root locus (c) bode phase (d) time response

For system portrayed in Fig. 4.18, the compensator was designed as described by equation (4-51). Whereby K_p and K_i were calculated as -0.013015 and 35.15 respectively.

$$G(s) = \frac{-0.013015(s + 2701)}{s} \tag{4-51}$$

Controller (4-51) achieves the function of ensuring stability of the system, whilst maintaining zero-error steady state condition. From the root locus in Fig. 4.19(c), closed loop poles are all on the LHS thereby indicating stability. Furthermore, the time domain behaviour has a fast response time and no oscillations. Fig. 4.19(a) and Fig. 4.19(c), the phase margin is approximately 89°. The gain margin is at 50.6 dB and settling at around 500ms. This meets the systems requirements since the inner loop is at least 20 times the outer loop.

4.6.3 Buck-boost converter closed-loop DC signals

The buck-boost control double-loop strategy was configured onto the simulated converter, and the signals were recorded. The Simulink diagrams added to Appendix E

The buck-boost converter was simulated with the designed controller, without any impedance spectroscopy signal injection. The following results were recorded.

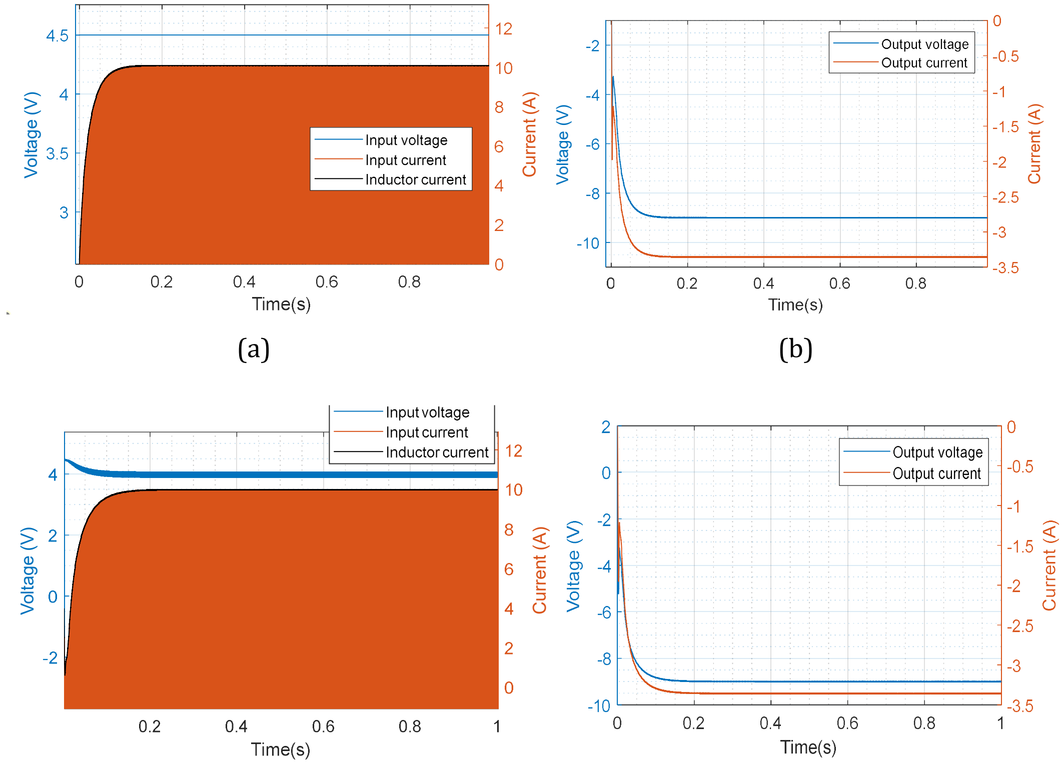

(a) (b)

(c) (d)

Fig. 4.20: Buck-boost converter's DC controlled signals without current perturbation (a)(c) Input current, voltage, and inductor current (b)(d) output voltage and output current

Fig. 4.20(a) & (b) show the input and output signals without Randles circuit and Fig. 4.20 (c) & (d) with Randles circuit. This shows that the control achieves DC control with DC inductor current of 10A and output current and output voltage of $-3.5A$ and $-9V$ respectively for with and without the Randle circuit.

4.6.4 Buck-boost converter closed loop EIS signal results

The buck-boost converter was then injected with the EIS, and the results are presented in Fig. 4.21.

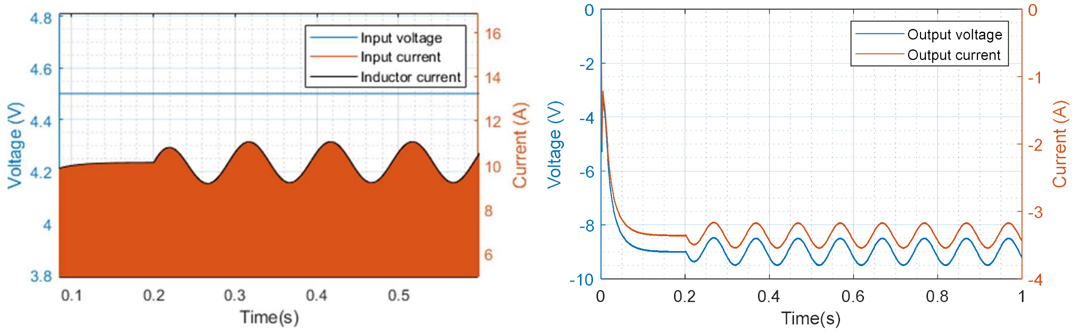

(a) (b)

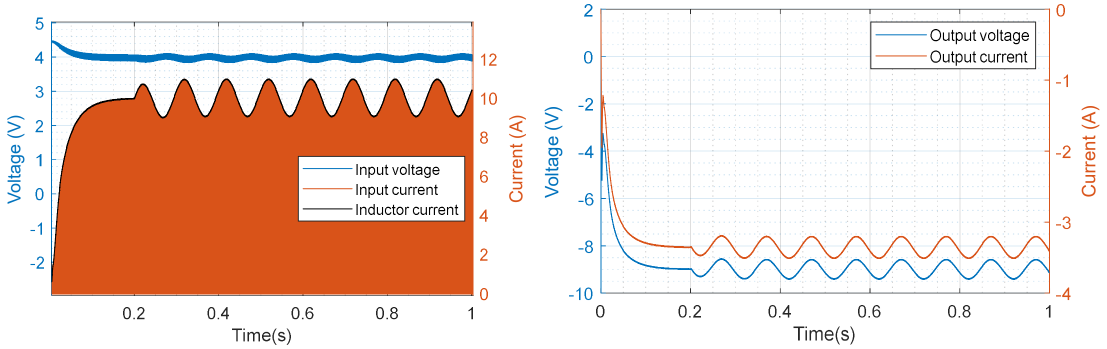

(c) (d)

Fig. 4.21: Buck-boost converter measured (a)(c) input voltage, current and inductor current(b)(d) output voltage and current

Fig. 4.21 (a) without the Randle circuit and (c) with the Randle circuit shows the input current, voltage, and inductor current of the buck-boost converter Fig. 4.21(b) without Randle circuit and (d) with the Randle circuits shows the output voltage and output current. This shows that the control achieves DC control with DC inductor current of 10A and output current and output voltage of $-3.5A$ and $-9V$ respectively whilst maintaining the desired injected ac sinusoidal inductor input current with an amplitude of 1A. This shows that the controller archives the desired input/inductor current and output voltage.

4.6.5 Buck-boost converter closed loop PRBS signal results

The buck-boost converter was then injected with the PRBS, and the results are presented in Fig. 4.22.

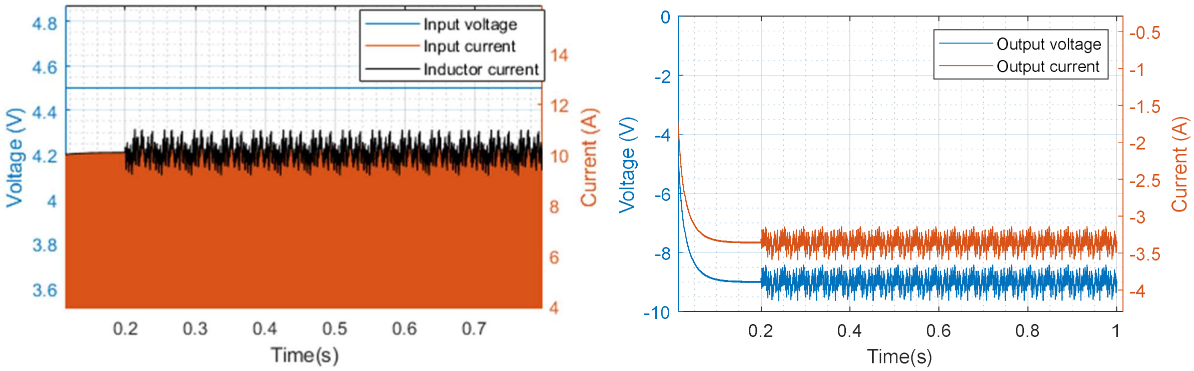

(a) (b)

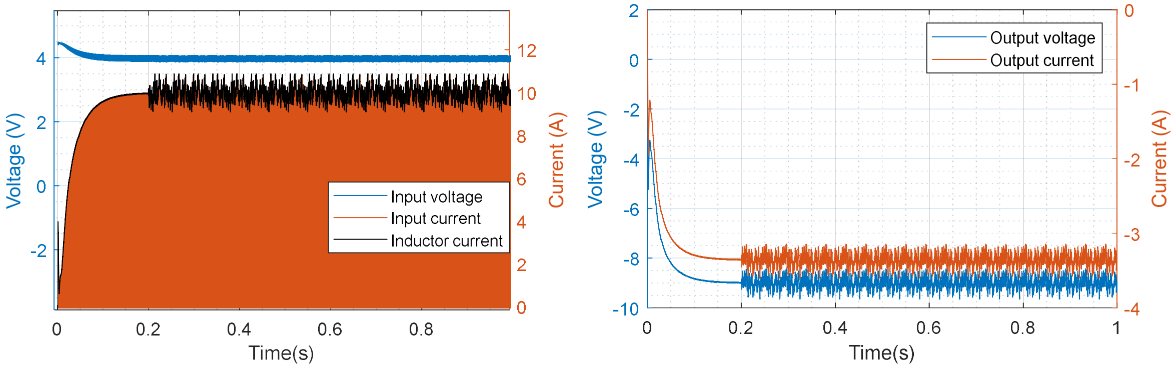

(c) (d)

Fig. 4.22: Buck-boost converter measured (a)(c) input voltage, current and inductor current(b)(d) output voltage and current

Fig. 4.22(a) without the Randle circuit and (c) with the Randle circuit shows the input current, voltage, and inductor current of the buck-boost converter Fig. 4.22(b) without Randle circuit and (d) with the Randle circuits shows the output voltage and output current. This shows the effectiveness of control with and without the Randle circuits, that the control achieves DC control with DC inductor current of 10A and output current and output voltage of $-3.3A$ and $-9V$ respectively whilst maintaining the desired ac injected PRBS inductor input current with an amplitude of 1A.

4.7 Buck-boost impedance results

This section presents the simulation impedance estimation results that are acquired from the modelled (Randle circuit) normal, flooding, and drying state of the fuel cell system. The signals were designed such they respect the linearity of the converter; also, the double loop control strategy assisted with controlling the drawn inductor current to the desired value of 10 A. The theoretical fuel cell system impedance results were compared to the results obtained from the PRBS and EIS.

Fig. 4.23 both the EIS and PRBS impedance estimation results are presented, and they both adequately estimate the theoretical impedance results, even though the sampling frequency was kept as minimal as possible at $2MHz$. As such, these plots will act as a benchmark as to what type of plot(estimation) results to obtain from the experimental results.

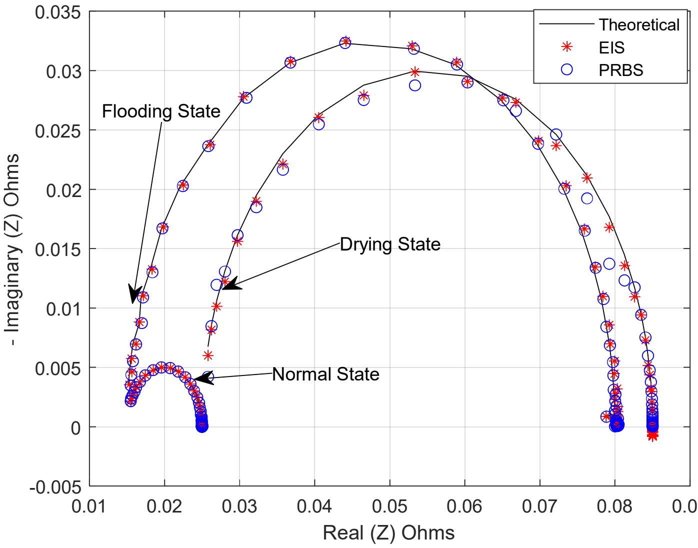

Fig. 4.23: Fuel Cell impedance estimation according to different internal water conditions-Nyquist

Fig. 4.23 shows the simulation estimated impedance result for all the different internal water internal statuses depicted by the model Randle circuit. These plots show the distinction and the effective use in using Impedance Spectroscopy to differentiate between the three internal water management conditions.

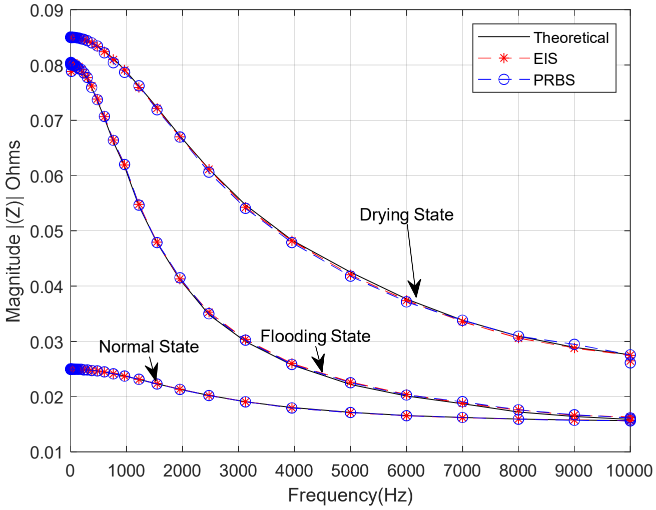

Fig. 4.24: Fuel Cell impedance estimation according to different internal water conditions-Magnitude

Fig. 4.24 shows the magnitude of the estimated water. For lower frequencies, the normal flooding and drying condition have an estimated impedance of approximately $25\,m\Omega$, $80\,m\Omega$ and $90\,m\Omega$ respectively. For higher frequencies up to $10kHz$ the normal, flooding and drying have an estimated impedance of approximately $15\,m\Omega$, $15\,m\Omega$ and $30\,m\Omega$.

4.8 Error results

The error analysis for the impedance results were computed using the least squares formula to check deviation. The simulation impedance error was obtained for all the operating conditions. Table 4-1 shows the maximum impedance error for the buck-boost converter when both the EIS and PRBS were injected. The error percentage results are below 5%.

Table 4-1: Impedance maximum average error of EIS and PRBS against theoretical results

Condition	**EIS maximum percentage error**	**PRBS maximum percentage error**
Normal	**1.7**	**1.7**
Drying	**1.2**	**1.9**
Flooding	**1**	**1**

Table 4-2 shows the average impedance error for the buck-boost converter when both the EIS and PRBS were injected.

Table 4-2: Impedance average estimation error of EIS and PRBS against theoretical results

Condition	**EIS maximum percentage error**	**PRBS maximum percentage error**
Normal	**0.126**	**0.131**
Drying	**0.169**	**0.27**
Flooding	**0.60**	**0.53**

The average error percentage results are below 1%. The electronic load impedance extraction section in Appendix B shows that there is an error that is associated with the sampling frequency chosen, this result from that the sampling frequency is limited based on the PC used for simulation.

4.9 Conclusions

This chapter presented the use of a buck-boost DC-DC converter for power transfer and online condition monitoring of a fuel cell system. The converter is modelled by its average linearized small-signal model. The proposed scheme was simulated to verify its suitability for EIS and PRBS implementation in comparison to its theoretical results. The results for both PRBS and EIS are in close proximity to the benchmark theoretical results. These results have demonstrated the feasibility of using PRBS for online internal water fault detection of the fuel cell with a shorter impedance estimation time, which is 5 times less than the EIS time, also with an error of less than 5% to the benchmark theoretical results of the buck-boost converter.

Chapter 5

Simulation and implementation of impedance spectroscopy using a boost converter

This chapter entails detailed analytical, state-space (dynamic) modelling of the boost converter, it follows the same sequence followed for the buck-boost converter. From boost modelling, component selection to impedance results.

5.1 Boost converter

The converter topology used is a unidirectional boost converter; this only allows the transfer of power in the forward direction, i.e. from the input voltage (fuel cell) to the load. The converter topology is shown.

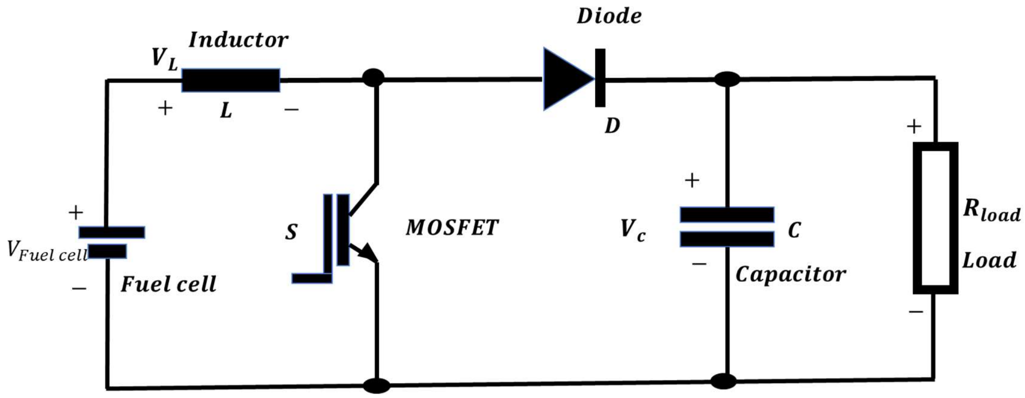

Fig. 5.1: Boost Converter

The boost converter, like the buck-boost converter, operates by varying the MOSFET switch, *S*, to determine the output voltage of the converter. The boost converter, unlike the buck-boost converter that can either boost or buck the input fuel cell voltage, only steps up the voltage. This is also achieved by manipulating the duration of the on time of the switch. The output is modelled as a constant purely resistive load for simplicity.

The complete analytical operation of the converter is detailed in the subsections below. Equations are derived for component sizing and for relating the input voltage to the output voltage of the converter.

For analytical modelling of the converter, some assumptions are made regarding the whole system for simplification as in the buck-boost converter. These assumptions are as follows:

- The voltage across the MOSFET switch, S and diode D is negligible and considered to be ideal.
- The inductor is operating in the continuous current conduction mode.

It should be noted that the boost converter without adaptation of the above assumptions is non-linear and time-variant (due to the semiconductors). The current flowing in the capacitor and the voltage drop across the inductor is governed by the equations below.

$$i_c(t) = C\frac{dV_c(t)}{dt} \tag{5-1}$$

$$V_L(t) = L\frac{di_L(t)}{dt} \tag{5-2}$$

5.1.1 Boost converter when MOSFET switch *S* is ON

When the MOSFET switch, S is closed (ON), the diode D is reversed biased and acts as an open circuit. The inductor is directly connected to the fuel cell system, thus a voltage (V_L) is impressed across it causing the inductor current (I_L) to rise. The capacitor voltage (V_c) decreases during this transition because it is discharging through the load resistor (R_{load}). This configuration is shown in Fig. 5.2, whereby loop 2 is open.

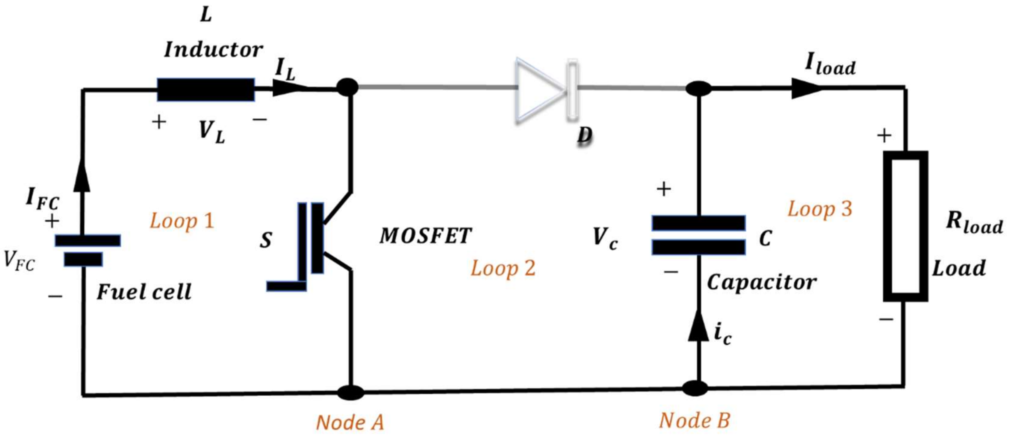

Fig. 5.2: Boost converter when Switch S is ON

Kirchhoff's voltage law (for loops 1 and 3) and Kirchhoff's current law (node B) are performed.

$$V_L(t) = V_{FC}(t) = L\frac{di_L(t)}{dt} \tag{5-3}$$

$$0 = i_c(t) - \frac{V_c(t)}{R_{Load}} \tag{5-4}$$

$$V_o(t) = V_c(t) \tag{5-5}$$

5.1.2 Boost converter when MOSFET switch *S* is off

When the MOSFET switch S is opened (off), the fuel cell system is connected to the inductor and external load; this is shown in Fig. 5.3. The diode is forward biased, and the inductor voltage changes its polarity so that the inductor can oppose the change in current.

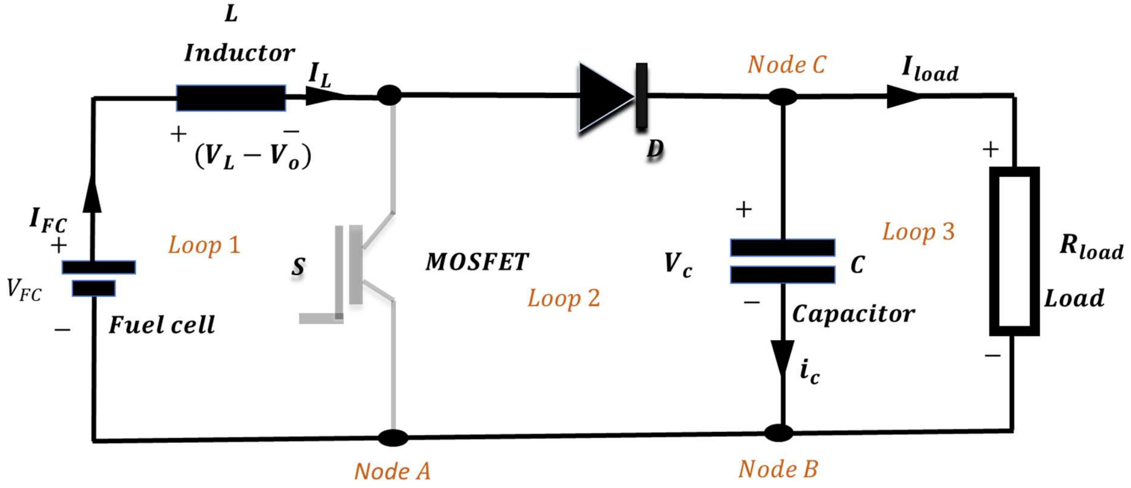

Fig. 5.3: Boost Converter when Switch S is OFF

Kirchhoff's voltage law (for loops 1/2 and 3) and Kirchhoff's current law (node C) are performed.

$$V_L(t) = V_{FC}(t) - V_o(t) = L\frac{d_{iL}(t)}{dt} \tag{5-6}$$

$$i_L(t) - i_c(t) - \frac{V_c(t)}{R_{load}} = 0 \tag{5-7}$$

5.1.3 Boost converter overall operation under steady state

Assuming steady state operation, while in continuous conduction mode, the average current and voltage in an ideal inductor and capacitor, respectively, are zero.

The average current in the inductor in the boost converter can be simplified using equations (5-3) and (5-7) as follows:

The total duration can be presented by the switching period T_s, and for the time it is on D is the percentage the switch S is ON ($0 < D < 1$). The percentage of the switch is off can be written as $(1 - D)T_s$. This is illustrated in Fig. 5.4 below.

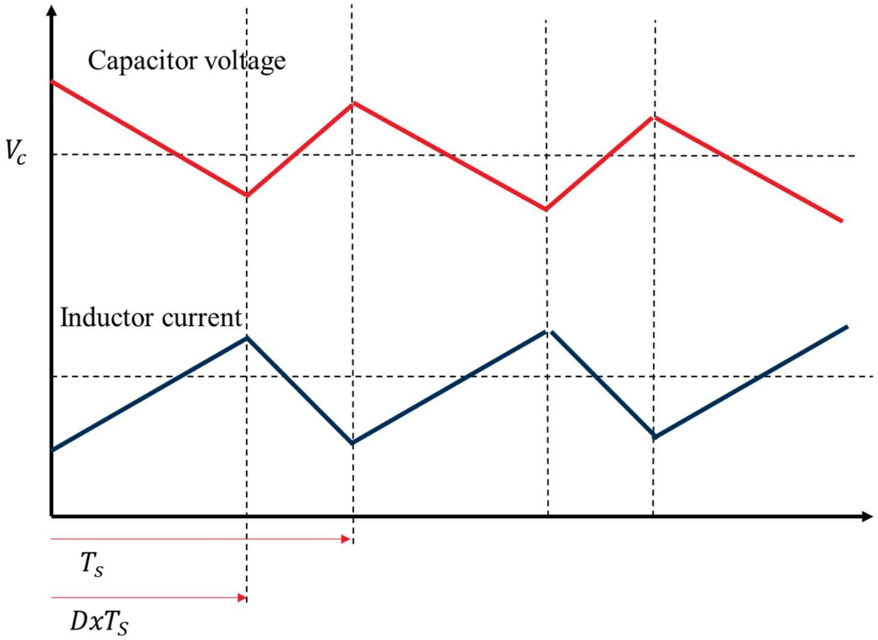

Fig. 5.4: Capacitor Voltage and inductor current for period Ts [43]

Inductor current when MOSFET switch S is closed (ON).

$$\frac{d_{iL}(t)}{dt} = \frac{V_{FC}(t)}{L} \tag{5-8}$$

The rate of change of current is constant.

$$\frac{\Delta i_L(t)}{\Delta t} = \frac{\Delta i_L(t)}{DT_s} = \frac{V_{FC}(t)}{L} \tag{5-9}$$

$$\Delta i_{Lclosed}(t) = \frac{V_{FC}(t)DT_s}{L} \tag{5-10}$$

Inductor current when MOSFET switch S open (OFF).

$$\frac{d_{iL}(t)}{dt} = \frac{V_{FC}(t) - V_o(t)}{L} \tag{5-11}$$

The rate of change of current is constant.

$$\frac{\Delta i_L(t)}{\Delta t} = \frac{\Delta i_L(t)}{(1-D)T_s} = \frac{V_{FC}(t) - V_o(t)}{L} \tag{5-12}$$

$$\Delta i_L(t) = \frac{(V_{FC}(t) - V_o(t))(1-D)}{L} \tag{5-13}$$

As a result, the averaged inductor current is computed as follows:

$$\Delta i_{Lclosed}(t) + \Delta i_{Lopened}(t) = 0 \tag{5-14}$$

$$\frac{V_{FC}(t)DT_s}{L} + \frac{V_{FC}(t) - V_o(t)(1-D)T_s}{L} = 0 \tag{5-15}$$

$$V_o(t) = -V_{FC}(t)\frac{1}{1-D} \tag{5-16}$$

$$\frac{V_o(t)}{V_{FC}(t)} = \frac{1}{1-D} \tag{5-17}$$

Equation (5-16) relates output voltage to the input voltage on the fuel cell side, and it also shows that the output voltage is not inverting as is the case in the buck-boost.

5.2 Boost State variable modelling of the boost converter

As discussed in section 5.1, the boost converter is non-linear and time-invariant due to the varying nature of the PWM switching and the semiconductor properties.

The stages are:

- State-space averaging,
- Linearization around DC points and
- S-domain conversion of the small-signal model.

5.2.1 State-space average modelling

The same derivation that was done for the buck-boost converter [47] is repeated for the boost converter. The state-space equations are summarized below.

$$A_{average} = \begin{bmatrix} 0 & \frac{1-d}{C} \\ -\frac{(1-d)}{C} & -\frac{1}{R_{load}C} \end{bmatrix} \tag{5-18}$$

$$B_{average=}\begin{bmatrix}\dfrac{d}{L}\\0\end{bmatrix}\tag{5-19}$$

The result and average-space model.
Average state-space model:

$$\begin{bmatrix}\dfrac{di_L(t)}{dt}\\\dfrac{dv_C(t)}{dt}\end{bmatrix}=\begin{bmatrix}0 & -\dfrac{(1-d)}{L}\\\dfrac{(1-d)}{C} & -\dfrac{1}{R_{load}C}\end{bmatrix}\begin{bmatrix}I_L\\V_C\end{bmatrix}+\begin{bmatrix}\dfrac{1}{L}\\0\end{bmatrix}V_{FC}\tag{5-20}$$

5.2.2 State-space average model linearization

The averaged state-space model is now time-invariant but non-linear. A non-linear average model can be linearized into a small-signal model [46] [48] as in [15] [49] [50]. The system is assumed to have a very small input, and thus can be regarded as pseudo-linear, i.e., operating around a small linear point. This linearization is achieved by assuming that the boost converter state-space variables $(u(t), x(t),)$ $d(t)$ are composed of a DC and AC component as shown below.

$$u(t)=U(t)+\tilde{u}(t)\tag{5-21}$$

$$x(t)=X(t)+\tilde{x}(t)\tag{5-22}$$

$$d(t)=D(t)+\tilde{d}(t)\tag{5-23}$$

The above equations (5-21), (5-22), and (5-23) are computed into the averaged state-space equation [46] before the boost converter parameters are substituted to give the equation below.

$$\begin{aligned}\dot{X}(t)+\dot{\tilde{x}}(t)=&[A_{on}\left[D(t)+\tilde{d}(t)\right]+A_{off}\left[1-D(t)-\tilde{d}(t)\right]][X(t)+\tilde{x}(t)]\\&+\left[B_{on}\left[D(t)+\tilde{d}(t)\right]+B_{off}\left[D(t)+\tilde{d}(t)\right]\right][U(t)+\tilde{u}(t)]\end{aligned}\tag{5-24}$$

Assumptions made are [46], as in the case of the buck-boost converter:

- DC components in the model have known variables, and they can be computed when knowing the boost converter components.
- The system (boost converter) is analyzed under steady state; therefore, this results in $\dot{X}(t)\approx 0$.

- Second-order terms have a small magnitude and can therefore be ignored (second-order terms are products of $\tilde{u}(t), \tilde{x}(t), \tilde{d}(t)$).
- The input $u(t)$, which is the fuel cell voltage in the case of the boost converter is assumed to be composed of the DC component only, ignoring the ac perturbation ($\tilde{u}(t) \approx 0$).

This simplifies equation (5-24) to the equation below:

$$\dot{\tilde{x}}(t) = A\tilde{x}(t) + [\left[A_{on} - A_{off}\right]X(t) + \left[A_{on} - A_{off}\right]U(t)]\,\tilde{d}(t) \tag{5-25}$$

The above equation is the average linear small-signal model of the boost converter before the parameter substitution.

5.2.3 State-space S-domain conversion of the small-signal model

The small-signal equation described by equation (5-25) is both time-invariant and linear; therefore, a transfer function that can be controlled using linear control can be implemented on it. Thus, the Laplace Transform of equation (5-25) is computed below.

$$\begin{bmatrix} \tilde{\imath}_L(s) \\ \tilde{v}_C(s) \end{bmatrix} = \frac{1}{s^2 + \left(\frac{1}{R_{LOAD}C}\right)s + \frac{(1-D)^2}{CL}} \begin{bmatrix} s + \frac{1}{R_{LOAD}C} & -\frac{(1-D)}{L} \\ \frac{(1-D)}{C} & s \end{bmatrix} \begin{bmatrix} \frac{1}{L}V_c \\ -\frac{1}{C}I_L \end{bmatrix} \tilde{d}(s) \tag{5-26}$$

$$s\tilde{x}(s) = A\tilde{x}(s) + [\left[A_{on} - A_{off}\right]X(s) + \left[A_{on} - A_{off}\right]U(s)]\,\tilde{d}(s) \tag{5-27}$$

This is simplified to:

$$\tilde{x}(s) = [sI - A]^{-1}[\left[\left[A_{on} - A_{off}\right]X(s) + \left[A_{on} - A_{off}\right]U(s)\right]\tilde{d}(s)] \tag{5-28}$$

When substituting the boost parameter variables, a pair of equations is found, which relates capacitor voltage and inductor current to the perturbation duty cycle, as shown below.

$$G_{Vc} = \frac{\tilde{v}_C(s)}{\tilde{d}(s)} = \frac{-\frac{1}{C}I_L s + V_c\frac{(1-D)}{LC}}{s^2 + \left(\frac{1}{R_{LOAD}C}\right)s + \frac{(1-D)^2}{LC}} \tag{5-29}$$

$$G_{i_L}(s) = \frac{\widetilde{i_L}(s)}{\tilde{d}(s)} = \frac{\frac{1}{L}V_c s + \frac{V_c}{R_{LOAD}LC} + \frac{(1-D)}{LC}I_L}{s^2 + \frac{s}{R_{LOAD}C} + \frac{(1-D)^2}{LC}} \tag{5-30}$$

For the application of injecting perturbations into the fuel cell, the inductor current to duty cycle relationship must be known, which is equation (5-30).

Equation (5-29) is used for the control of the capacitor voltage, and equation (5-30) is used to perform EIS, by determining the duty cycle required to inject a current inside the fuel cell system [52] [53] [54] [55].

5.3 Component selection

5.3.1 Input and output voltage

As stated in section 4.3, the 6 fuel cells provide a combined voltage in the range of $4.2 - 4.5\ V$.

$$V_{FC-min} = 4.2V \ and \ V_{FC-max} = 4.5V \tag{5-31}$$

This $V_{FC-mi} \ = 4.2V$ from the fuel cell is required to provide 9 V ($V_{out} = 9\ V$) to an output load, with an output power of 45 W. Thus, a resistor of 2 Ω would ideally act as an ideal constant current load sink of 5 A. The switching frequency chosen for this simulation is $F_{sw} = 100\ kHz$, the DC-biased duty cycle is $D = 0.5$.

5.3.2 Inductor

The inductor ripple current is computed by the selection of the inductor (along with the switching frequency). This relationship, i.e., the ripple current (ΔI_L) is given by the equation below.

$$\Delta I_L = \frac{V_{IN}D}{Lf_{sw}} \tag{5-32}$$

The reduction of ripple current is important for two reasons. The first is such that the inductor operate in CCM, and the second is to reduce the ripple waveform in the current of the fuel cell as the impedance spectroscopy signals are modulated onto the inductor current. The inductor ripple current was chosen to be $\Delta I_L = 1A$. The value of the required inductor was calculated by rearranging the equation above.

$$L = \frac{V_{IN}D}{\Delta I_L f_{sw} V_{out}} \tag{5-33}$$

CCM needs the inductor current to be always above 0. The point where the inductor current is half of the inductor current ripple is defined as the boundary point between discontinuous conduction mode (DCM) and CCM. This boundary point occurs when $I_L = \frac{\Delta I_L}{2}$.

$$I_L = \frac{V_{IN}D}{2LfsV_{out}} \tag{5-34}$$

$L_{min} = 0.125\ uH$, however, the same inductor used for the buck-boost converter of $L = 444\ uH$ is used, as this value is very large and will reduce current ripple.

5.3.3 Capacitor

Similar to the buck-boost converter, the next component that needed to be added was the output filter capacitor, this is to minimise the voltage ripple on the voltage bus when the converter is operating in boost mode. The value was chosen using the following equation.

$$C_{OUT(min)} = \frac{I_{OUT(max) \times D}}{f_s \times \Delta V_{out}} \tag{5-35}$$

The maximum current that will be delivered to the external load is $3.2\ A$ at a duty cycle of 0.5. The voltage ripple chosen is $1\ V$. This results in an output filter capacitor value of $C_{OUT(min)} = 25uF$. The chosen C value used is $470\ uF$ as it is very large and will efficiently regulate the output voltage.

5.4 Open loop current injection

Similar to the buck-boost converter, the amplitude of the ac sinusoidal duty cycle was determined. Conversely equation

(5-30) is used to relate the inductor ac sinusoidal signal, along with its associated ac sinusoidal duty cycle and the equation used for EIS injection is shown below.

$$\tilde{d}(f) = \tilde{\iota_L}(f) \cdot \frac{(2\pi f j)^2 + \frac{2\pi f j}{R_{load}C} + \frac{(1-D)^2}{LC}}{\frac{1}{L}V_c s + \frac{V_c}{R_{LOAD}LC} + \frac{(1-D)}{LC}I_L} \tag{5-36}$$

For injecting an ac sinusoidal signal of amplitude $\tilde{\iota_L}(f) = 1\ A$ with a frequency of $100Hz$, and boost converter parameters:

$R_{load} = 2$, $V_{FC} = 4.5, V_c = 9, I_l = 10, D = 0.5, f = 100Hz$. The duty cycle amplitude is as below.

$$\tilde{d}(f) = 0.0113017\angle 1.29029177°@100Hz$$

5.5 Boost converter simulations and discussion

The converter system for the fuel cell was designed and simulated in MATLAB Simulink. The converter was used to facilitate power transfer whilst estimating its impedance using online EIS and PRBS. The Randle circuit, as shown in Figure 2 with parameters listed in Table I, was used to represent the fuel cell [7]. The fuel cell's bandwidth, spanning from 0.1 Hz to 10 kHz, was considered since this bandwidth covers the dynamics presented by a Randle circuit model [3] [51]. The benchmark results are presented by extracting the impedance response for the Randle circuit representing each condition as stipulated in Table 6-1.

5.5.1 Boost converter open loop results with and without the emulated fuel cell system

The boost converter, similar to the buck-boost converter, was simulated in an open loop, and the output and input voltage and current are present as below.

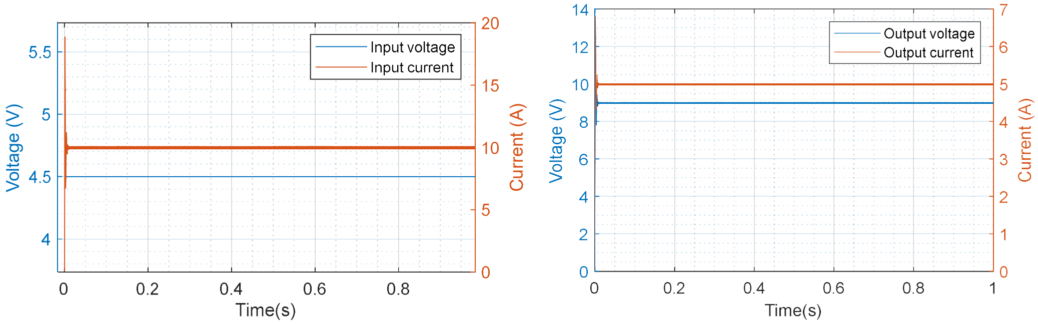

(a) (b)

Fig. 5.5:Boost converters measured signals (a) input current and input voltage (b) the output voltage and output current

Fig. 5.5(a) above shows the input current and the voltage of the boost converter with an ideal dc voltage source as its input. As such, the current input current and voltage are designed with an input voltage of 4.5 V and input current of 10 A.

Fig. 5.5 (b) shows the output voltage and current for this case where its values are as expected.

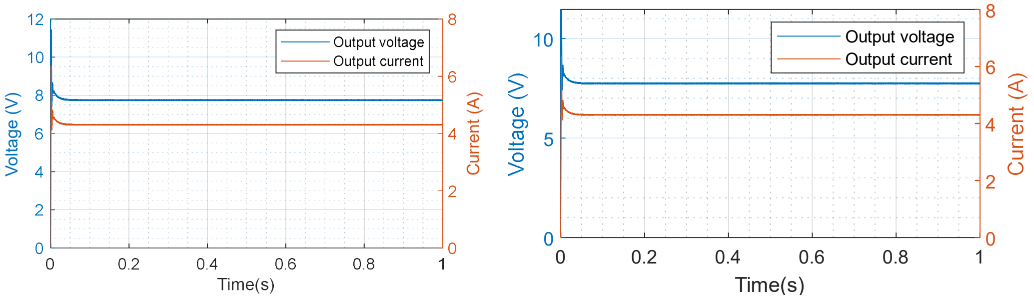

(a)

(b)

Fig. 5.6: Boost measured converters signal (a) input voltage, current (b)output voltage and output current.

Fig. 5.6 (a) shows the input current, voltage, and inductor current of the boost converter when the input has the Randles equivalent circuit. Fig. 5.6 (b) shows the output voltage and current. It can be observed that the input voltage, current and inductor current of the boost converter are different from those in Fig. 5.5(a), and the magnitudes have decreased. Like for the buck-boost converter, this is used for justifying the DC power control before considering implementation of impedance spectroscopy.

5.5.2 Boost open-loop EIS results with and without the emulated fuel cell system.

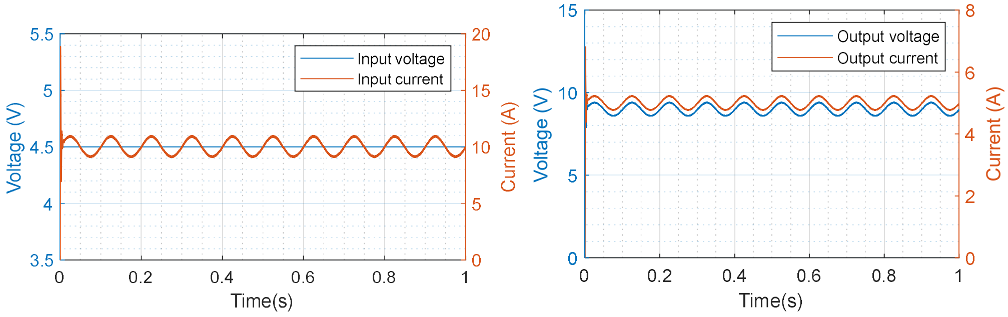

(a)

(b

Fig. 5.7: Boost converter's (a) Input current, voltage (b) the output voltage and output current

Fig. 5.7(a) shows the input current and voltage of the boost converter when the converter has no integrated fuel cell system. Fig. 5.7 (b) shows the output voltage and current when EIS is implemented. An ideal converter is assumed, and the input voltage and current, inductor current, and output voltage and current are designed with the ac signal (impedance spectroscopy) being 10 % of the DC signal. In the ac (spectroscopy) signal, the amplitude is determined by using the amplitude equation derived for the boost converter in section 5.4 when performed in an open loop. This shows the effectiveness of the derived perturbation equation using the small-signal linearized modelled systems equations.

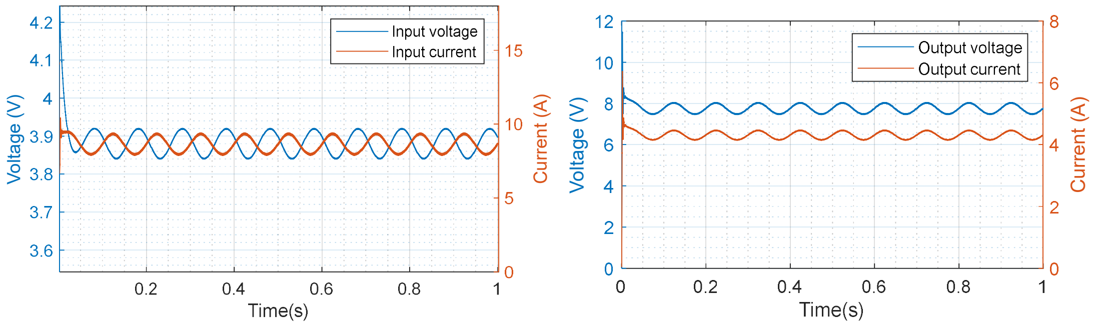

(a) (b)

Fig. 5.8: Boost converter's (a) Input current, voltage and inductor current of the boost converter (b) the output voltage and output current

Fig. 5.8 (a) shows the input current and voltage current of the boost converter when the converter has an integrated fuel cell system. Fig. 5.8 (b) shows the output voltage and current when EIS is injected. The input voltage and current, inductor current, and output voltage and current are designed with the ac signal (impedance spectroscopy) being 10 % of the DC signal. In the ac (spectroscopy) signal, the amplitude is determined by using the amplitude equation derived for the boost converter section 5.4 when performed in an open loop. This shows that the perturbation AC is no longer 10% as initially designed, and this motivated the need for ac control as well.

5.5.3 Boost open-loop PRBS results with and without the emulated fuel cell system.

The same process performed for EIS in section 5.5.2 is reported for the PRBS signals, and the observed signals are recorded below.

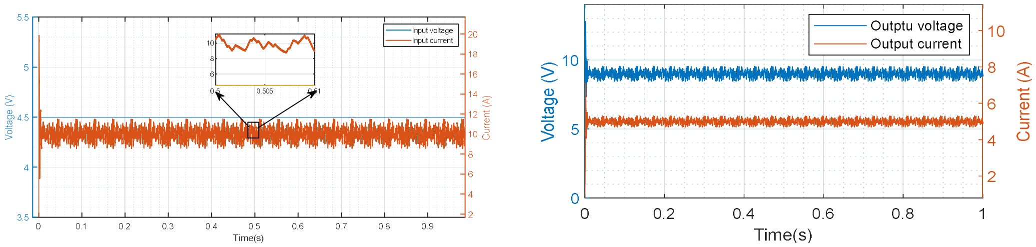

(a) (b)

Fig. 5.9: Boost converter's (a) Input current and voltage c (b) the output voltage and output current

Fig. 5.9 (a) shows the input current and voltage of the boost converter when the converter has no fuel cell integration. Fig. 5.9 (b) shows the output voltage and current when PRBS is implemented. An ideal fuel cell system is assumed, and the input voltage and current, inductor current, and output voltage and current are designed with the ac signal (impedance spectroscopy) being 10 % of the DC current. In the ac (spectroscopy) signal, the amplitude is determined by using the average amplitude estimation derived for the boost converter, when performed in an open loop. This shows the effectiveness of the estimated derived perturbation equation, using the small-signal linearized modelled systems equations.

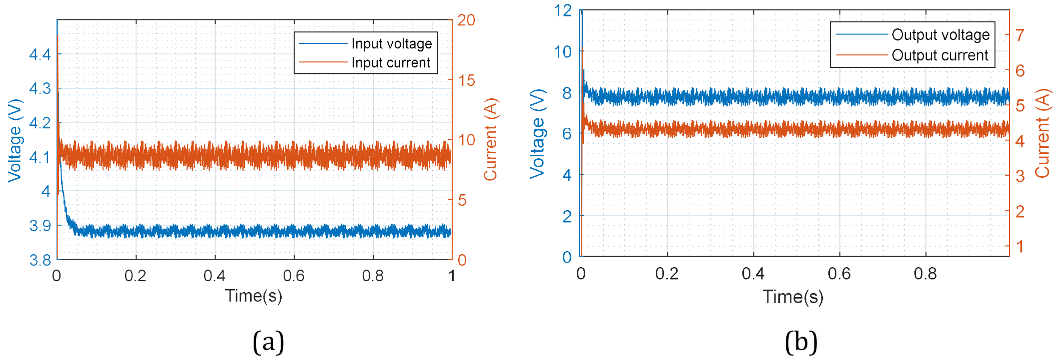

(a) (b)

Fig. 5.10: boost converter's (a) Input current and voltage (b) the output voltage and output current

Fig. 5.10(a) shows the input current, voltage, and inductor current of the boost converter when the converter has a fuel cell integration. Fig. 5.10 (b) shows the output voltage and current when PRBS is implemented. A fuel cell system is integrated, and the input voltage and current, inductor current, and output voltage and current are designed with the ac signal (impedance spectroscopy) being 10 % of the DC current. In the ac (spectroscopy) signal, the amplitude is determined by using the average amplitude estimation equation derived for the boost converter, when performed in an open loop. This shows that the perturbation AC is no longer 10% as initially designed, and this motivated the need for ac control as well, similar to the buck-boost section.

5.6 Boost converter control

As mentioned before, a lead-lag controller is used for the inner control loop to increase the bandwidth so as to implement impedance spectroscopy. This section details the controller design using the root locus technique. This requirement to be met to achieve optimized performance are as follows [23]:

- Steady state error (±10%)
- Faster system response (for the inner loop compared to the outer loop)
- Optimized tracking

The root locus method is used for optimal compensator design, whereby an optimal controller will be designed; this will be done to have all the close loop poles on the LHS of the real plane [21]. Starting with the inner current loop, a lead-lag controller was designed using the same process as in the buck-boost controller design.

5.6.1 Current loop controller

Fig. 5.11 shows the inner loop systems' properties before compensation.

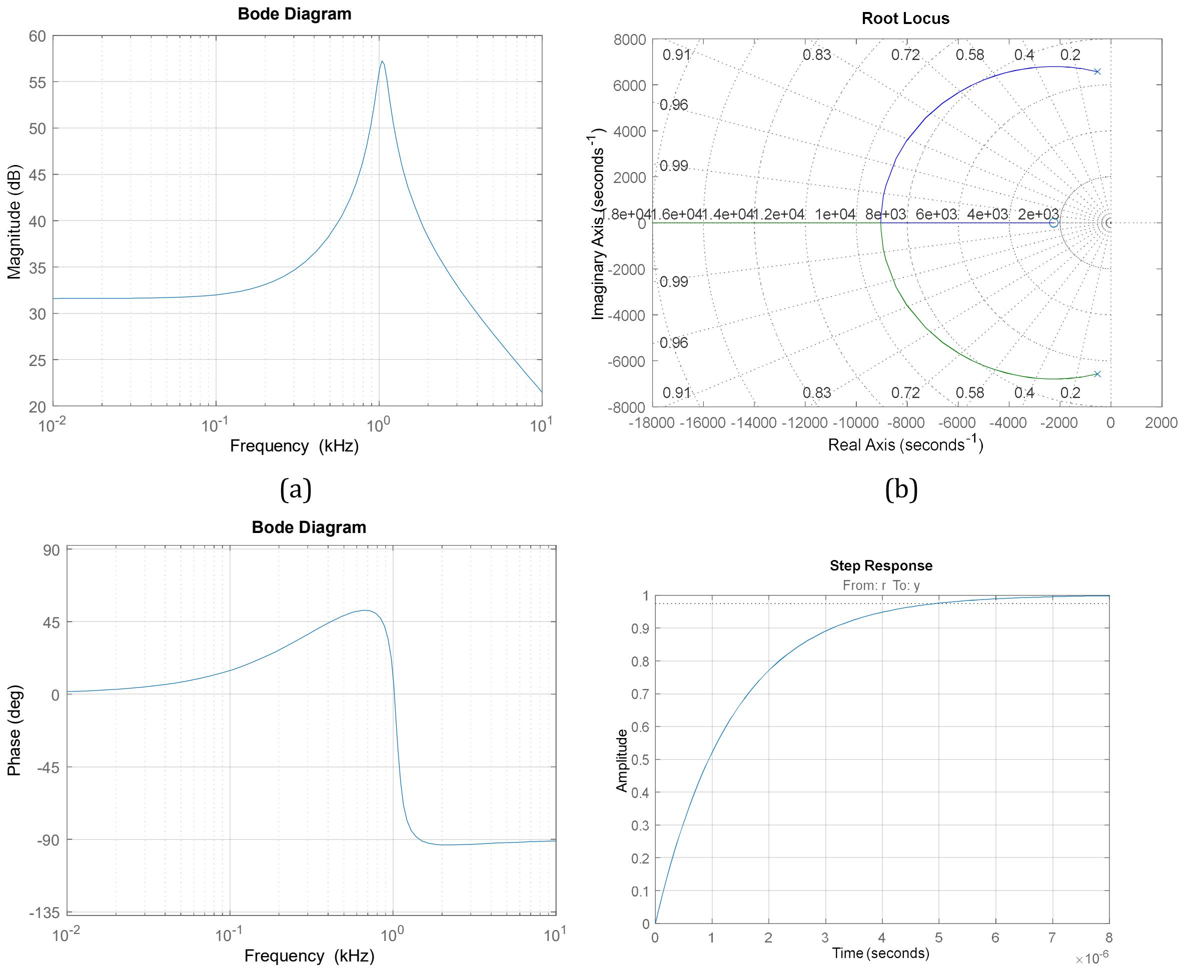

(a) (b)

(c) (d)

Fig. 5.11:Boost converters inner loop (a) bode magnitude (b) root locus (c) bode phase (d) time response

Fig. 5.11 is the system's uncompensated properties from the current loop-derived transfer function from section 5.2.3. Fig. 5.11(a) and Fig. 5.11(c) show the magnitude and phase, whereas the gain margin is infinity and the phase margin is 89°. With selling time less than 8us and steady state less than 3%. The control loop with the modelled plant is described in Fig. 5.12 below [21].

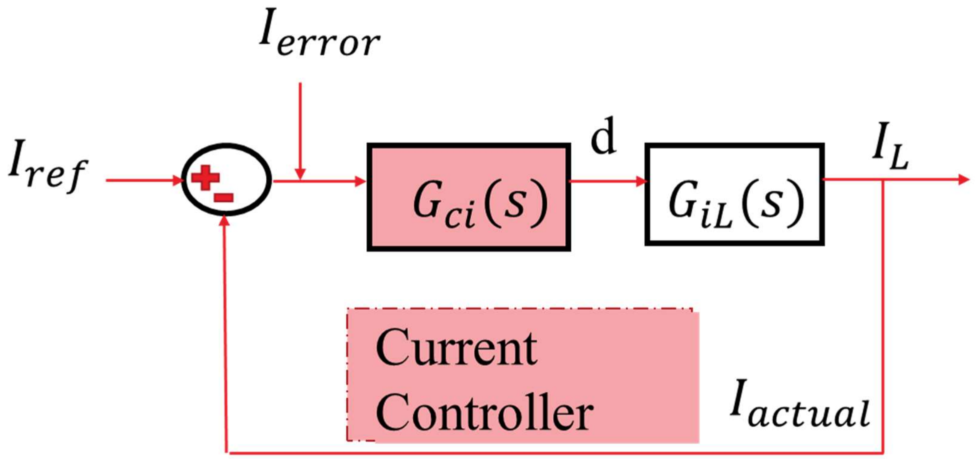

Fig. 5.12: Current Control loop with $G_{ci}(s)$ being the controller

Thus a lead-lag compensator for the system was designed with its visual presentation in Fig. 5.13.

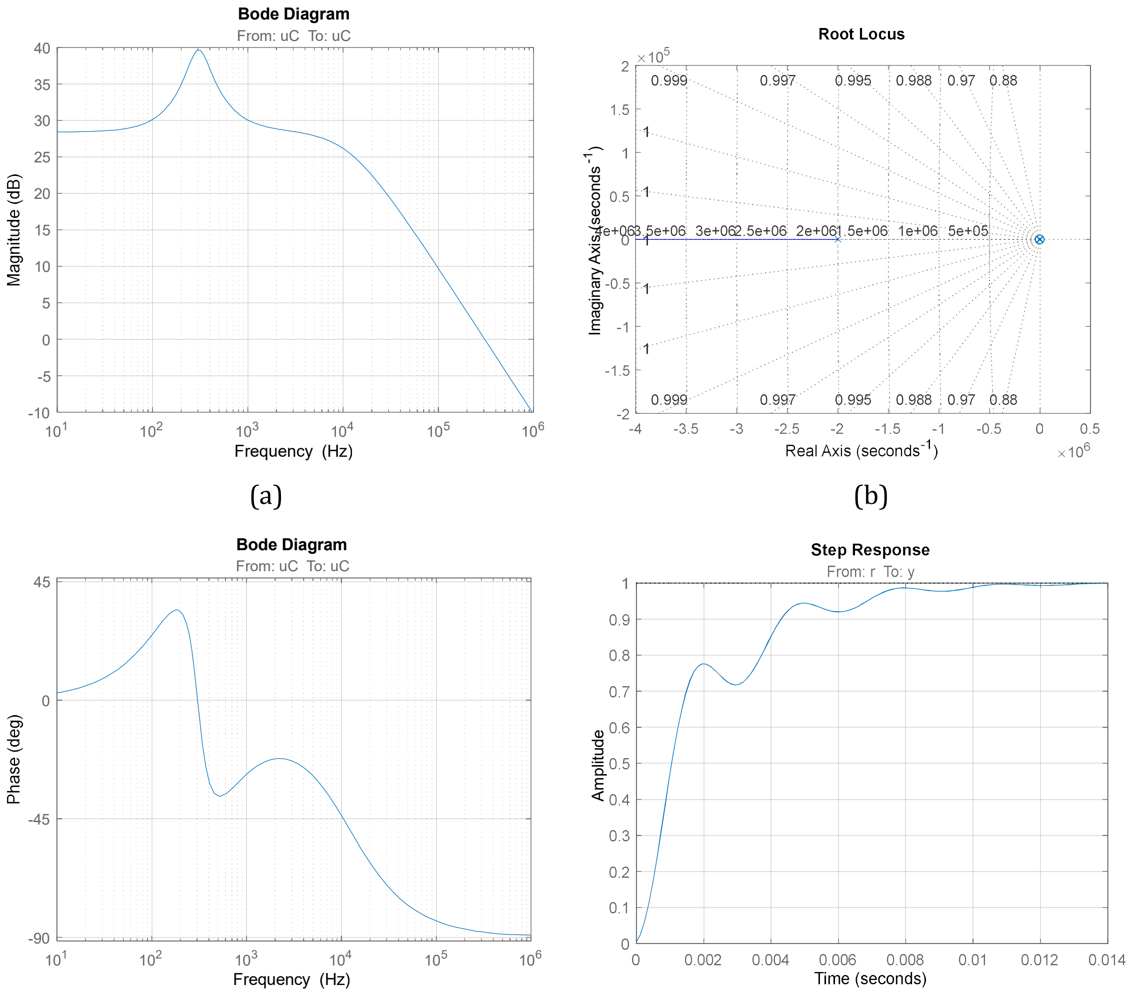

(a) (b)

(c) (d)

Fig. 5.13:Boost converters inner loop (a) bode magnitude (b) root locus (c) bode phase (d) time response

Fig. 5.13 shows the boost converters compensated system properties. The controller was used to achieve a settling time of less than $14ms$ as shown by Fig. 5.13(d). Fig. 5.13(a) and Fig. 5.13(c) shows the magnitude and phase of the system, with the phase margin being 92.7° and infinity gain margin. The system achieves the desired bandwidth. However, there is a trade-off of the peak at around 100 Hz, this means sinusoidal currents around this point will be amplified however this won't impact impedance spectroscopy, as the peak can be accounted for during implementation. Fig. 5.13(b) shows that all poles are on the LHS, showing stability.

5.6.2 Voltage loop controller

A PI controller is utilized for the voltage control loop. The following section presents the steps taken to design the voltage controller. The following assumptions will be made:

- The inner loop satisfies the ($\pm 10\%$) steady-state error requirement
- The inner loop has a faster settling time than the outer voltage loop (at least 20 times faster)
- And the inner loop tracks the input current to the tolerated values (5%)

The voltage loop is as shown in Fig. 5.14, whereby the inner current loop has been simplified into a transfer function described by unity, assuming the current control is within the desired range.
The system in Fig. 5.14 depicts the input and output voltage of the system. The main parameter in this case, is the output voltage, implying a compensator needs to be designed to manipulate the output voltage response of the system.

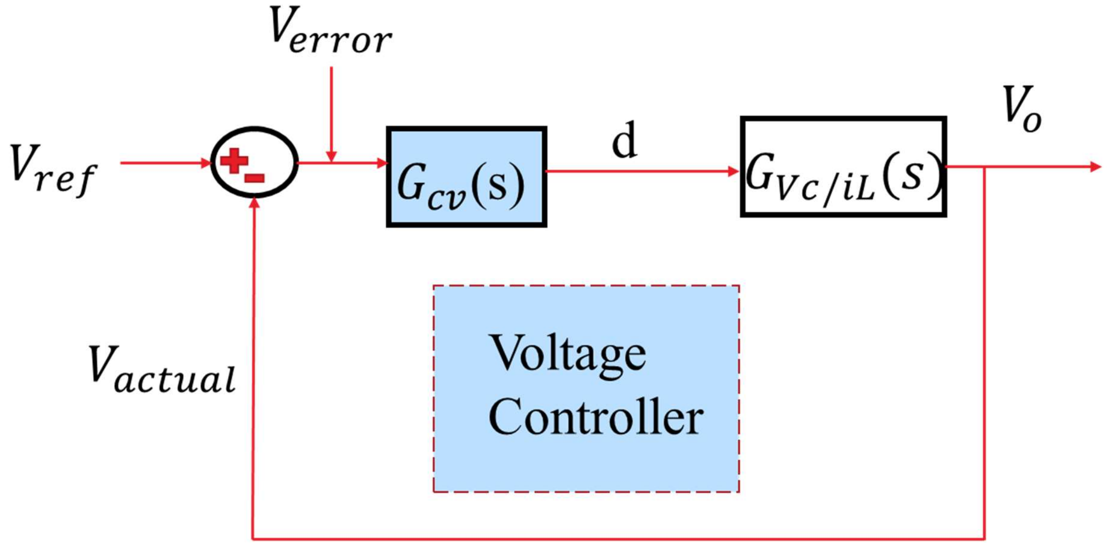

Fig. 5.14: Voltage control loop with $G_{cv}(s)$ being the controller

Similar to the current loop, the first step of the voltage loop controller will be adding an integrator eliminate steady-state error. The closed loop path shown in Fig. 5.14 has its system properties shown in

Fig. 5.15 when there is a unity gain. The use of simple feedback, with the unity controller, influences the voltage system behaviour in the manner shown in Fig. 5.15.

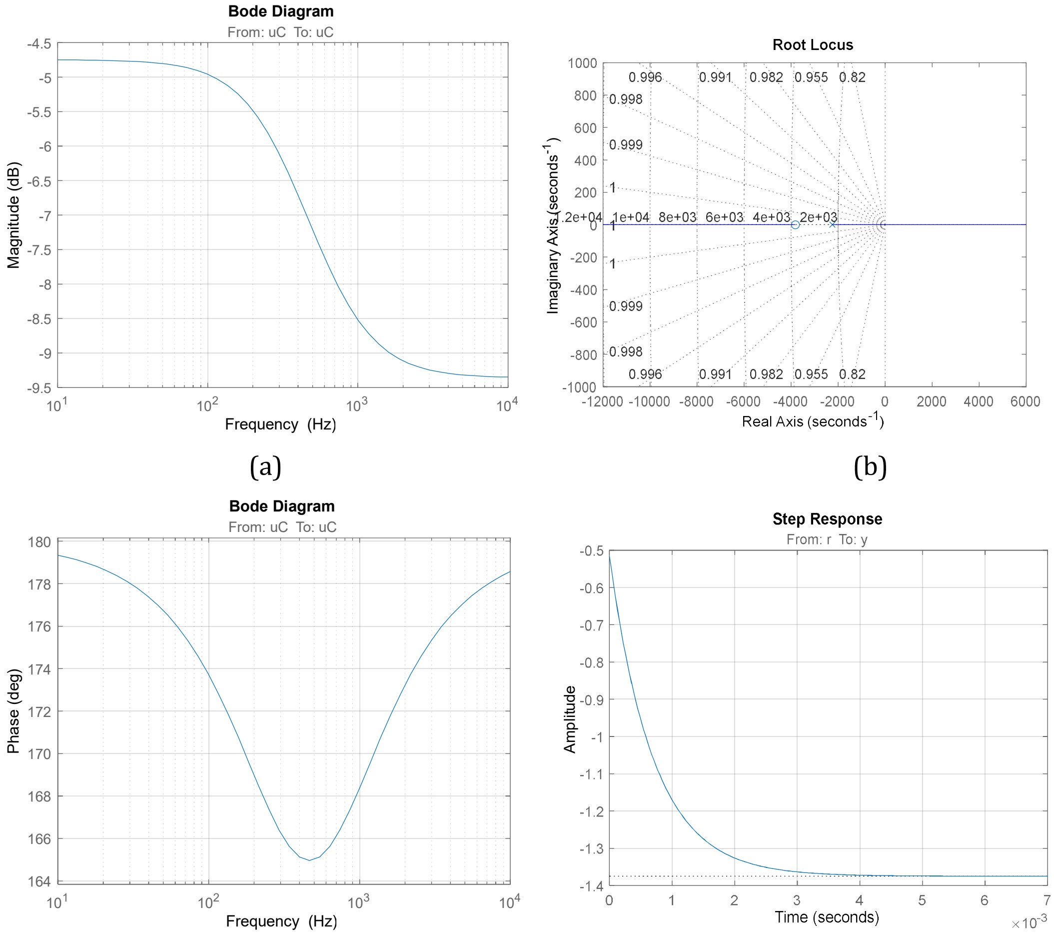

(a) (b)

(c) (d)

Fig. 5.15:Boost converters inner loop (a) bode magnitude (b) root locus (c) bode phase (d) time response

As seen in Fig. 5.15(b), the root locus has a line that spans into the RHS, meaning it can be unstable given a certain range of gains. Fig. 5.15(d) unit step response shows that the system is currently not tracking, thus has an error and the settling time is less than $7ms$. Fig. 5.15(a) and Fig. 5.15(c) shows the magnitude and phase, with the gain margin being 4.75 dB and phase margin of infinity. Using the same structure proposed in the buck-boost section 4.6.2, a controller was designed, the desired response is depicted in Fig. 5.16.

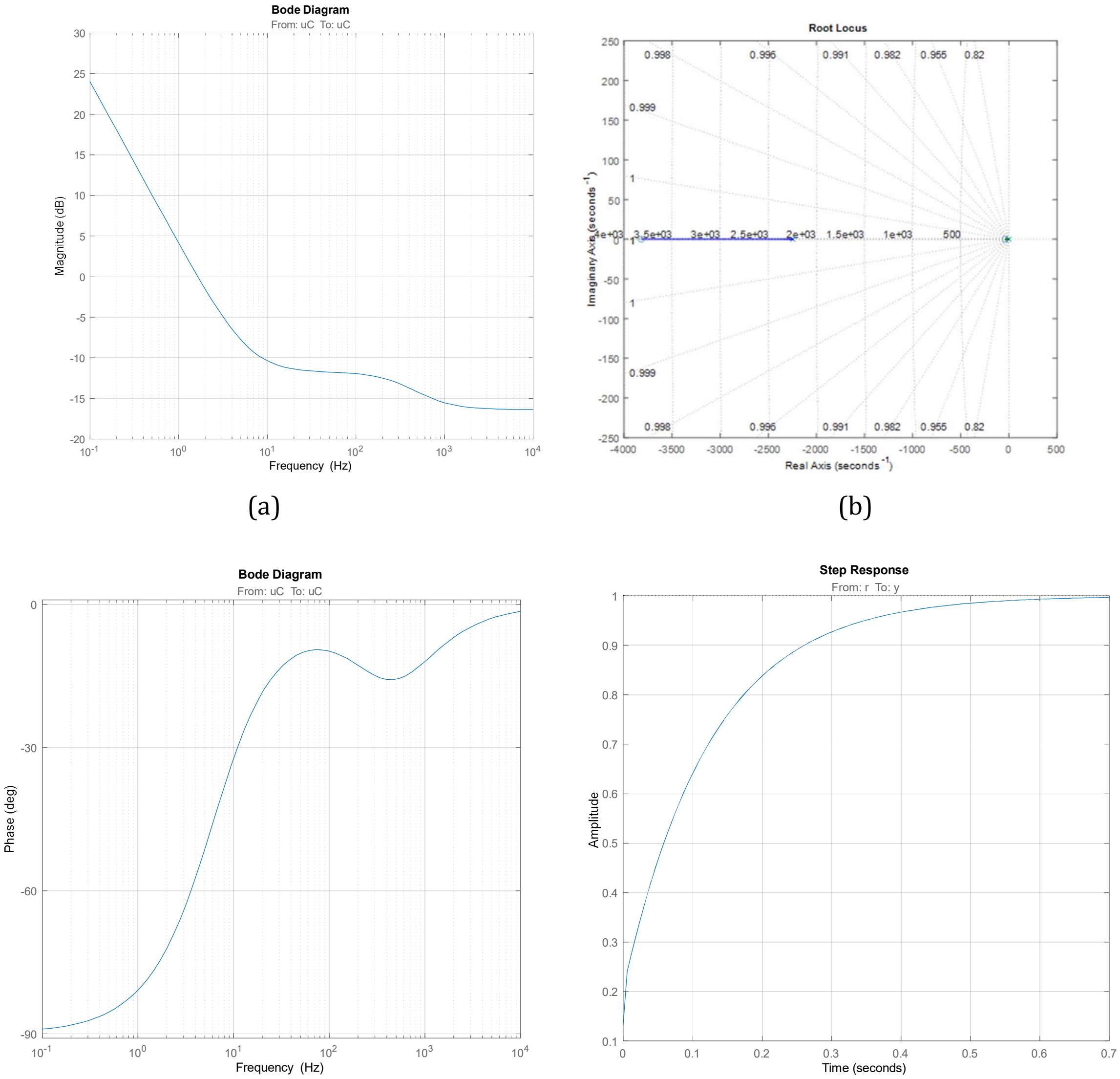

(a) (b)

Fig. 5.16:Boost converters inner loop (a) bode magnitude (b) root locus (c) bode phase (d) time response

For system portrayed in Fig. 5.16, the controller was tuned as shown by equation (5-37), Whereby K_p and K_i were calculated as 0.038805 and 1.8188 respectively.

$$G(s) = \frac{-0.44606(s + 38.72)}{s} \tag{5-37}$$

The controller described by (5-37) stabilizes the system and maintains the zero-error steady state requirement. Fig. 5.16(b) shows the root locus that all the closed loop poles are on the LHS. In addition, Fig. 5.16(d) shows that time domain behaviour has a fast response time and no oscillations. The settling time is less than $700ms$, steady-state error less than 1%. Fig. 5.16(a) and (c) i.e. the magnitude plot and phase plot show the phase margin at around 105° and gain margin of infinity. The controllers meet the systems requirement for the implementation of impedance spectroscopy.

5.6.3 Boost converters-controlled Impedance results

The boost converter was simulated, with the designed controller, without any impedance spectroscopy signal injection. The following results were recorded.

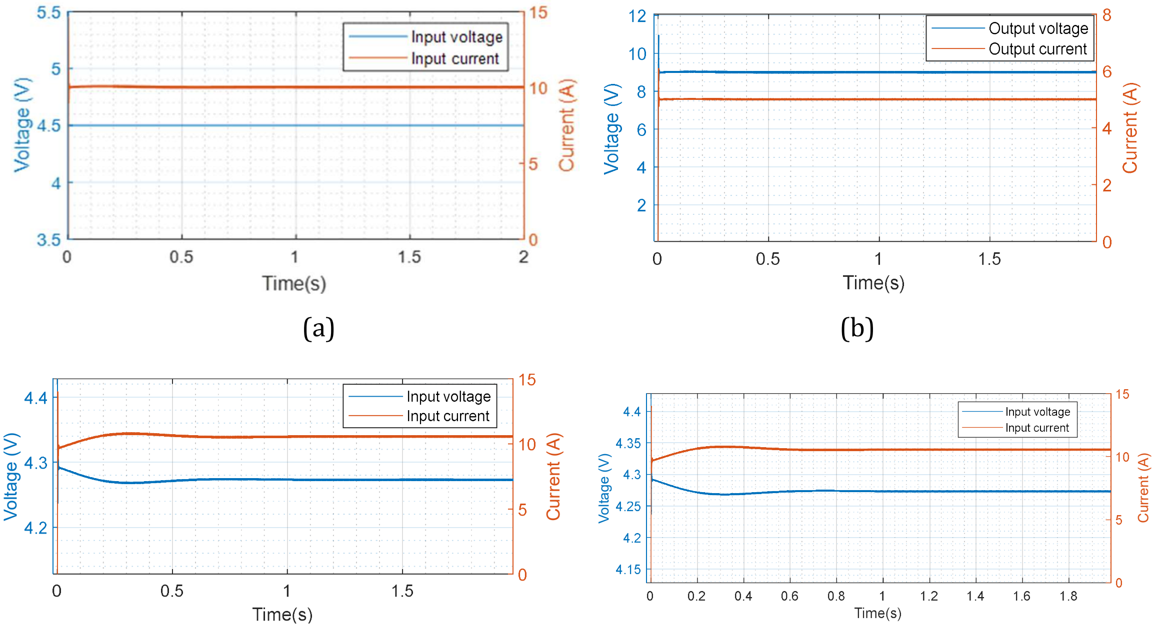

(a) (b)

(c) (d)

Fig. 5.17: Boost converter's DC controlled signals without current perturbation (a) Input current and voltage (b) the output voltage and output current (c)input voltage and current(d)output voltage and current with an emulated fuel cell system.

Fig. 5.17 (a) shows the input current and voltage of the boost converter without the emulated fuel system, and Fig. 5.17 (c) shows the output voltage and current without the fuel cell system. Fig. 5.17 (b) shows the input voltage and current with the emulated fuel cell system, and Fig. 5.17 (d) shows the output voltage and output current with the emulated fuel cell system. This shows the effectiveness of control with and without the emulated fuel cell system. This shows that the control achieves DC control with DC inductor current of 10 A and, output current and output voltage of 5 A and 9 V respectively for when the converter is sourced from a pure dc source and an emulated fuel cell system. This shows that the control achieves DC control.

5.6.4 Boost converter closed loop EIS signal results

The boost converter was then injected with the EIS, and the results are presented in Fig. 5.18.

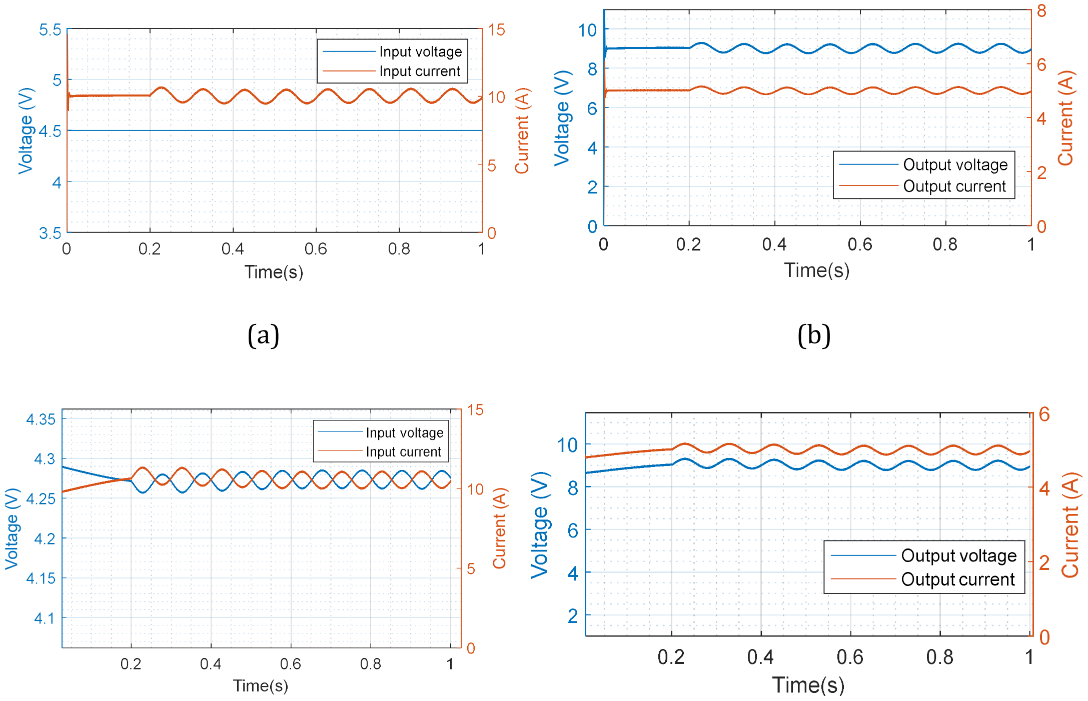

(a) (b)

(c) (d)

Fig. 5.18: Boost converter measured (a)(c) input voltage, current and inductor current(b)(d) output voltage and current

Fig. 5.18 (a) without the Randle circuit and (c) with the Randle circuit shows the input current, voltage, and inductor current of the boost converter. Fig. 5.18 (b) without the Randle circuit and (d) with the Randle circuits shows the output voltage and output current. This shows the effectiveness of control with and without the Randle circuits. This shows that the control achieves DC control with DC inductor current of 10 A and, output current an output voltage of 5 A and 9 V respectively whilst maintaining the desired injected ac sinusoidal inductor input current with an amplitude of 1 A. This shows that the controller archives the desired input/inductor current and output voltage. This shows that the controller archives the desired input/inductor current and output voltage.

5.6.5 Boost converter closed loop PRBS signal results

The boost converter was then injected with the PRBS, and the results are presented in Fig. 5.19.

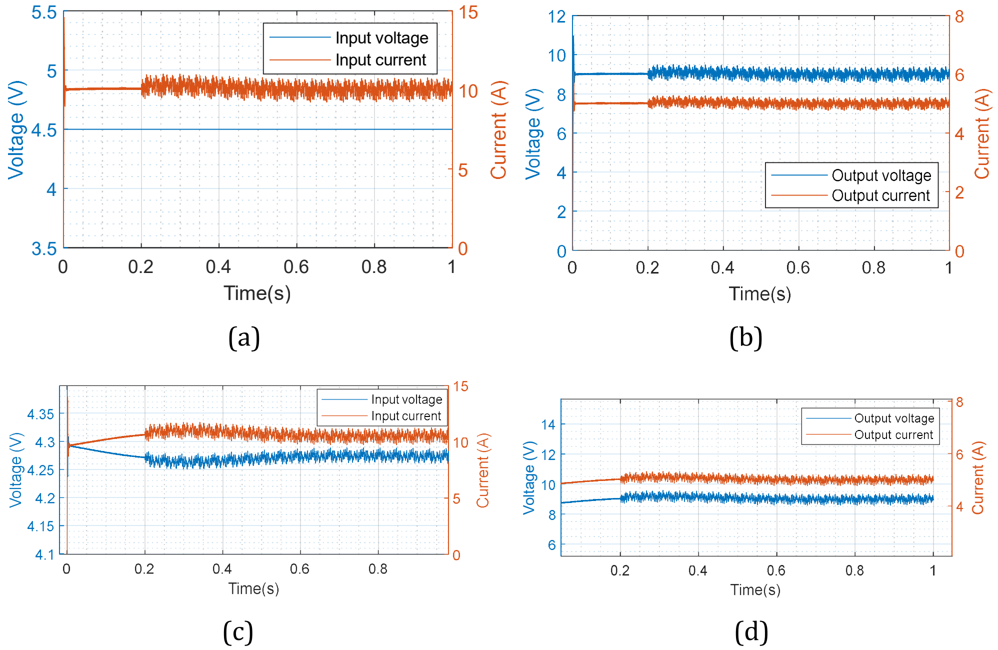

(a) (b)

(c) (d)

Fig. 5.19: Boost converter's dc-controlled signal with current perturbation (a)(c) input voltage, current and inductor current(b)(d) output voltage and current

Fig. 5.19 (a) without the Randle circuit and (c) with the Randle circuit shows the input current, voltage, and inductor current of the boost converter Fig. 5.19 (b) without the Randle circuit and (d) with the Randle circuits shows the output voltage and output current. This shows the effectiveness of control with and without the Randle circuits. This shows that the control achieves DC control with DC inductor current of 10A and output current and output voltage of 5 A and 9 V respectively whilst maintaining the desired ac injected PRBS inductor input current with an amplitude of 1 A. This shows that the controller archives the desired input/inductor current and output voltage. This shows that the controller archives the desired input/inductor current and output voltage. This shows that the controller archives the desired input/inductor current and output voltage.

5.7 Boost impedance results

This section presents the simulation impedance estimation results that are acquired from the modelled (Randle circuit) normal, flooding, and drying state of the fuel cell system. The signals were designed such they respect the linearity of the converter; also, the double loop control strategy assisted with controlling the drawn inductor current to the desired value of 10 A. The theoretical fuel cell system impedance results were compared to the results obtained from the PRBS and EIS.

.

Fig. 5.20 both the EIS and PRBS impedance estimation results are presented, and they both adequately estimate the theoretical impedance results, even though the sampling frequency was kept as to a maximum value of 2 MHz. As such, these plots will act as a benchmark as to what type of plot (estimation) results to obtain from the experimental results.

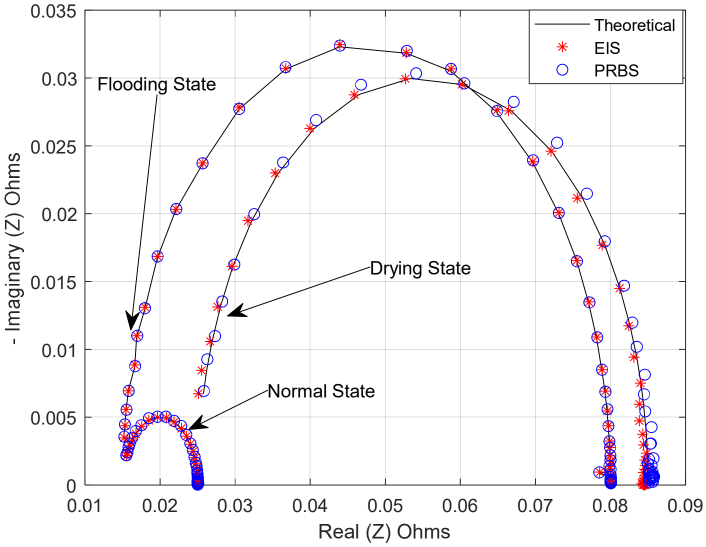

Fig. 5.20: Fuel cell impedance estimation according to different internal water conditions-Nyquist

Fig. 5.20 shows the simulated impedance results for all the different internal water internal statuses depicted by the Randle's equivalent circuit. These plots show the distinction and the effective use in using impedance spectroscopy to differentiate between the three internal water management conditions.

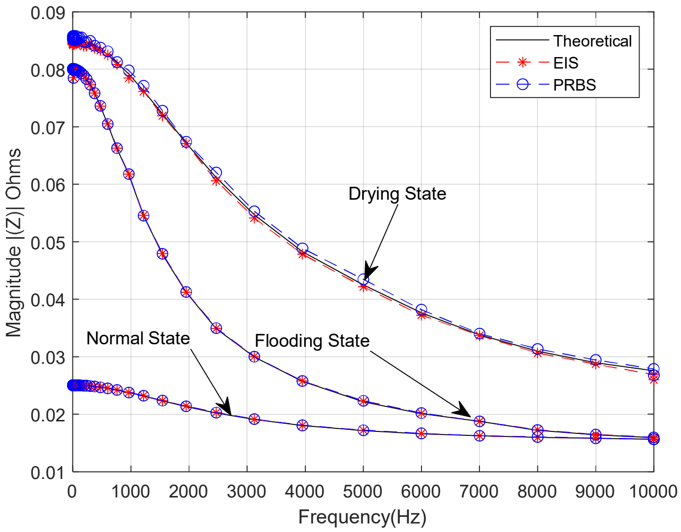

Fig. 5.21: Fuel Cell impedance estimation according to different internal water conditions-Magnitude

Fig. 5.21 shows the magnitude of the estimated water internal condition, for lower frequencies from 1 Hz, the normal, flooding and drying condition have an estimated impedance of approximately 25 $m\Omega$, 80 $m\Omega$ and 90 $m\Omega$ respectively. For higher frequencies up to 10 kHz the normal, flooding and drying have an estimated impedance of approximately 15 $m\Omega$, 15 $m\Omega$ and 30 $m\Omega$.

5.8 Error results

The error analyses for the impedance results were computed using the least square formula to check deviation. The simulation impedance error was obtained for all the operating conditions. Table 5-1 shows the maximum impedance error for the boost converter when both the EIS and PRBS were injected. The error percentage results are below 5%.

Table 5-1: Impedance maximum average error of EIS and PRBS against theoretical results

Condition	**EIS maximum percentage error**	**PRBS maximum percentage error**
Normal	0.5	2
Drying	1.5	1.5
Flooding	0.6	2.2

Table 5-2 shows the average impedance error for the boost converter when both the EIS and PRBS were injected.

Table 5-2: Impedance average estimation error of EIS and PRBS against theoretical results

Condition	**EIS maximum percentage error**	**PRBS maximum percentage error**
Normal	$\mathbf{0.2}$	$\mathbf{0.15}$
Drying	$\mathbf{0.61}$	$\mathbf{0.67}$
Flooding	$\mathbf{0.13}$	$\mathbf{0.14}$

The average error percentage results are below 1%, this is in correspondence to the error results obtained for the buck-boost converter. The error was not expected to be zero, as the electronic load impedance extraction section in the Appendix B shows that there is an error that is associated with the sampling frequency chosen

5.9 Conclusions

This chapter, similar to chapter 4, presented the use of the boost DC-DC converter for power transfer and online condition monitoring of a fuel cell. The converter was modelled by its average linearized small-signal model. The proposed scheme implemented was simulated to verify its suitability for EIS and PRBS implementation in comparison to theoretical results. The results for both PRBS and EIS are in close proximity to the theoretical results in chapter 4 for the boost converter. These results have demonstrated the feasibility of using PRBS for online internal water fault detection of the fuel cell with a shorter impedance estimation time as for the buck-boost converter, with the signal being 5 times lesser than the EIS time, also with an error of less than 5% to the benchmark theoretical results of the boost converter.

Chapter 6

Experimental setup

6.1 Introduction

This chapter presents the experimental setup used to implement the systems described in section 2.9. Section 6.2 firstly discusses the emulation of the fuel cell, the procedure used for impedance estimation, and thereafter presents the FRA and how it is used to obtain the benchmark results from the emulated Randle circuits. Thereafter it presents the converters and circuits used for signal generation and acquisition.

6.2 Fuel cell system emulation

6.2.1 Fuel cell emulation

The fuel cell will be emulated using a dc power supply in series with Randle's equivalent circuit, as mentioned before. The characteristics of the fuel cell are shown in Fig. 6.1, this shows the different health condition of the fuel cell system, which are normal case, flooded and the dry case. The fuel cell supplies the load, and its output power can range from $0 - 100\,W$. For a buck-boost converter, for normal conditions the power delivery is 30 W from the fuel cell, this corresponds to an input voltage of 4.5 V and input current of 6.7 A, whereas for the boost converter this input power and current characteristic corresponds to a voltage of 4.5 V and current of 10 A. The difference between the two dc-dc converter topologies used is the power drawn. The dc operating point would need to be considered when using a practical PEMFC.

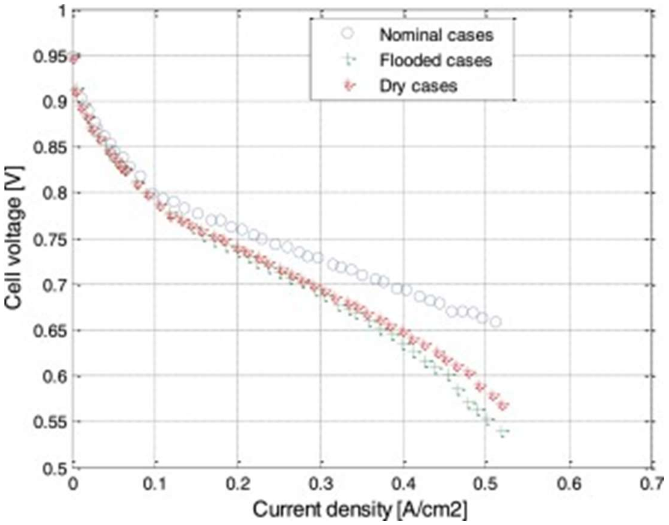

Fig. 6.1: Voltage-current characteristic [26]

The electrical impedance estimation procedure followed the step outline below:

- A superposition of a small amplitude signal, meeting Kramer's Kronig rule, is imposed on top of a direct current (or voltage) drawn from the fuel cell stack. The ac signal is swept across a range of selected frequencies. The DC component of the current drawn in the fuel cell stack corresponds to the point of operation on the polarization curve.
- Measurement of the amplitude and phase shift of the sinusoidal component of the voltage response of the fuel cell.
- The calculation of the complex impedance by ratio division of the voltage to current for a range of frequencies, and the dc frequency components are eliminated.

Fig. 6.2 shows the Randle circuit constructed for easy connection, with the resistor and capacitor values being those in Table 6-1.

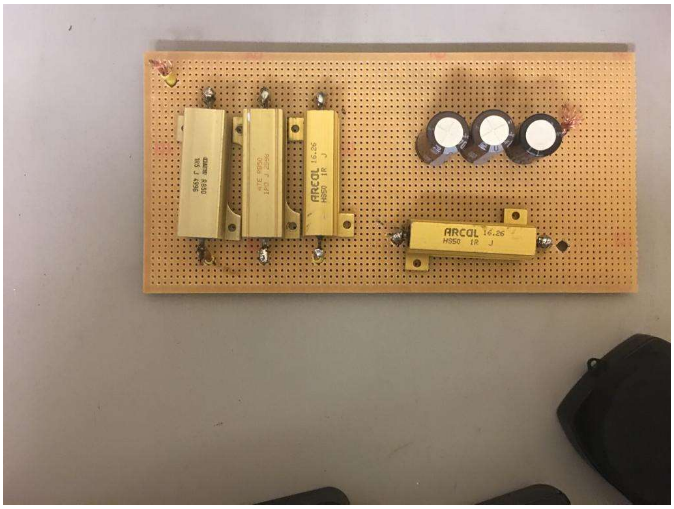

Fig. 6.2: Emulated cells

Table 6-1: Fuel cell emulation parameters

Operation condition	$R_{\Omega}(m\Omega)$	$R_{ct}(m\Omega)$	$C_{dl}(mF)$
Normal	15.9	5.59	222.9
Drying	27.8	55.8	148.5
Flooding	14.9	63.4	262.6

Table 6-1 shows the Randle circuit values used as the benchmark results; these are obtained from [26]. Whereby the parameters of the fuel cell stack is determined using square current perturbation. [26] used a PEMFC stack with an active area of 25 cm^2, and an operating open-circuit voltage of 4.5 V which consists of 5 cells in series. The power bandwidth is $0\ W - 75\ W$, with a maximum current density of $1\ A/cm^2$. The impedance estimation of the electrical equivalent circuit was performed using the least squares method, with the estimation current being in the range of 5 A to 20 A.

A natural concern would be-what effect does the wire-wound resistor have on the final result for higher frequencies-it should be noted that the wire-wound wound resistor would have impact on the current drawn, and voltage response measured, and this could have been demonstrated by doing parameter determination of the Randle's circuit(passive values), and checking how the values compare to those in Table 6-1, thus the inductance and power losses brought about by the wire-wound resistor and connecting wires would be quantified, however, the experimental result of this dissertation, acknowledges that the resistive and inductive/capacitive components used do have tolerance with respect to their nominal values. The given tolerance values are also not exact given the handling, storage and aging of the components, rather the final result focuses on benchmarking the accuracy of the converters developed against the FRA, as such whether the components used are susceptible to losses or inductances or other effects, this does not affect the error analysis bought by the use of the converters against the FRA.

6.3 Frequency Response Analyser

6.3.1 Introduction

The purpose of this study is to quantify the performance of the two BIS signals, in performing impedance spectroscopy, i.e., EIS and PRBS. The two signals are used to attain the impedance information; thereafter, benchmarked against impedance information from the Frequency Response Analyzer (FRA). The equipment used for the analysis and to attain these benchmark results is Auto lab 302N Potentiostat/Galvanostat (PGSTAT302N) and the FRA, which is manipulated through the NOVA software through a PC. This industry-grade commercial equipment has high accuracy and is mostly used to attain impedance results. The process of impedance estimation is similar to when other equipment is used; however, for ease of reference when repeating the process followed in this research, this section presents the methodology followed, the probes setup and considerations in the laboratory. The FRA setup is discussed, followed by the performance results obtained.

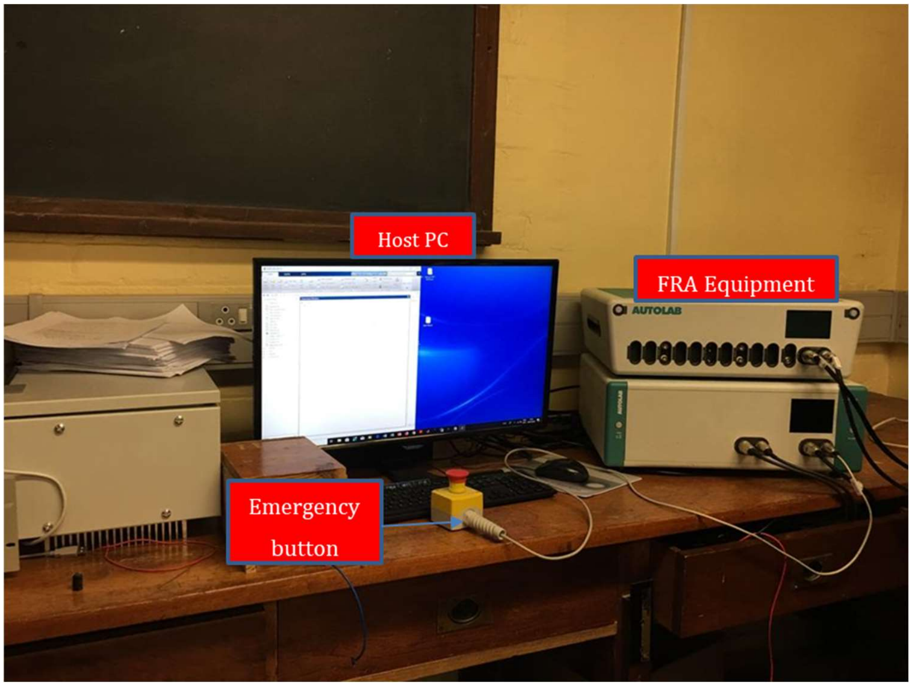

Fig. 6.3: **FRA hardware setup**

The experimental setup is shown in Fig. 6.3**.** Prior to taking the benchmark experimental results, the setup required calibration. The following section presents the calibration performed for the FRA, the electrode configuration, information about the Potentiostat/Galvanostat (PGSTAT) and the FRA. In addition, information on the current booster and the voltage multiplier will be provided.

6.3.2 Calibration

When the FRA2-Autolab PGSTAT320N experiences a change or is re-installed in a new laboratory, before being integrated with the Nova software to take experimental results, it requires calibration [56]. The calibration needs the determination of the factor values of parameters called $C1$ and $C2$ [56]. The user manual [56] describes how $C1$ and $C2$ are calibrated independently, and the calibrations setups are named:

- Calibration of PGSTAT's $C1$
- Calibration of PGSTAT's $C2$

The calibration of $C1$ and $C2$ necessity is the following items:

- Calibration dummy cell
- Faraday's cage

6.3.3 Frequency Response Analyzer hardware outline.

The following section presents the different components specific to the FRA equipment, and their modes of operation.

i. Connection of PGSTAT Electrodes

Four electrodes are utilised by the Metrohm Auto lab PGSTAT, with two of these electrodes used for transmitting current i.e., working electrode and counter electrode. The remaining two probes are used to reference and to measure either the voltage or current. The green probe not accounted for is the ground connection.

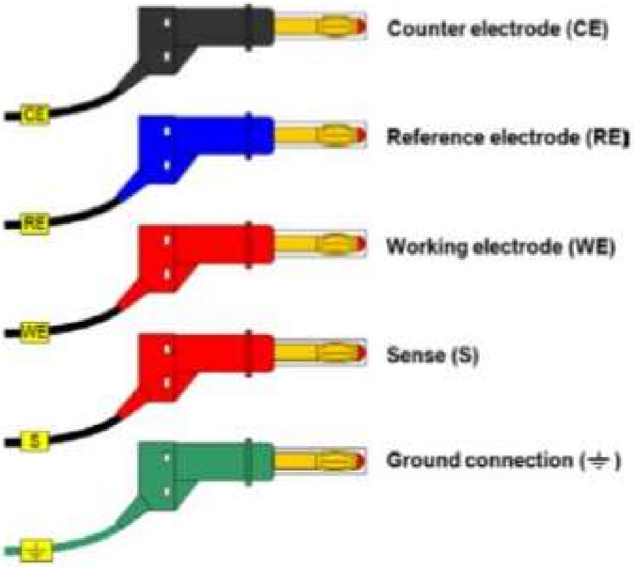

Fig. 6.4: Colour code of the PGSTAT electrodes [56].

Fig. 6.4 depicts the probes colours with its respective functions, thus depicts distinctive colour probes and their associated functions, with the ground included as being the green coloured probe. Fig. 6.5 depicts the configuration setup used for taking experimental results.

The green probe, i.e., ground connection is connected to the faraday's cage, and the reference electrode is short-circuited to the counter electrode, whilst the working electrode is directly connected to the reference electrode.

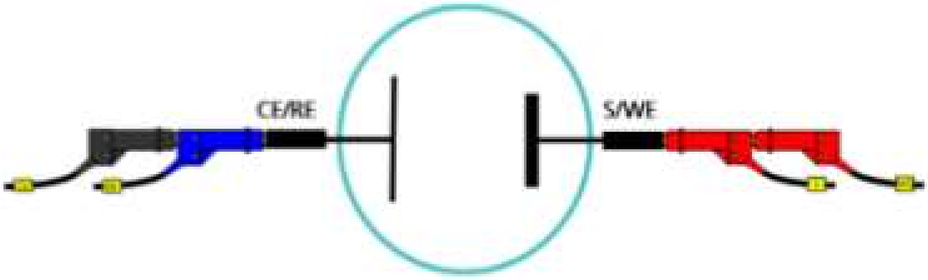

Fig. 6.5: Electrode configuration used to perform IS [57].

ii. Potentiostat/Galvanostat (PGSTAT)

PGSTAT is intergarated to the Fresponse Anaylser which is the FRA32M module utilised to perform EIS. The PGSTAT used is the PGSTAT302N, and it has an absolute compliance voltage of $30\,V$. The PGSTAT302N has a voltage range of $\pm 10\,V$ with a frequency bandwidth of up to $1\,MHz$. This has a maximum current handling capability of $2\,A$, and the current precision is up to $10\,nA$. The $1\,MHz$ bandwidth is divided into three modes of operation i.e., high speed mode, high stability mode and Ultra-high-speed mode. The Ultra-high-speed mode is utilised for frequencies from 125 kHz to 1.25 Mhz, and high-speed mode responsible for 10 kHz to 125kHz with the high-speed mode used in this research, utilized for frequencies lower than 10 kHz

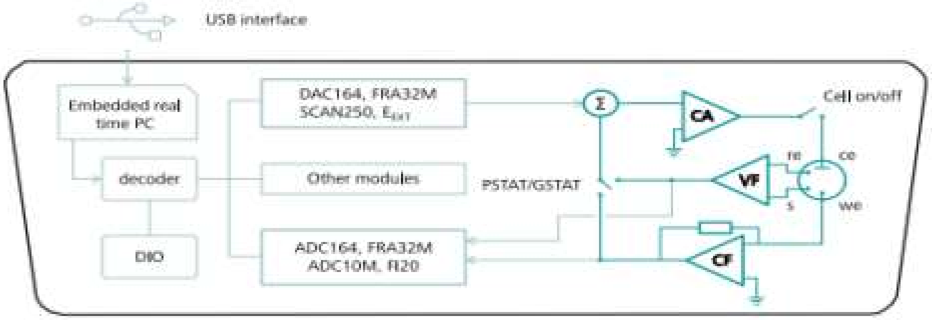

Fig. 6.6: Autolab Potentiostat/Galvanosta outline [56]

Fig. 6.6 shows the autolab schematic. This research utilized potentiostatic mode implementing EIS. Due to the FRA32M module caveats, the FRA has curve fitting tool which only allows signals in the range configuration of 1,5,15 Sine [56]. It should be noted that the range of the FRA32M module is from 10 μHz to 32 MHz [56].

6.4 Overall setup of converters

The overview of experimental setup is shown in Fig. 6.7. The National Instruments (NI-USB 6366 device) was used to inject (. i.e. produce control signal) and acquire the PRBS and EIS measured. The emulated fuel cell system, explained in the fuel cell section, was used in series with the dc power supply when the fuel cell system was connected.

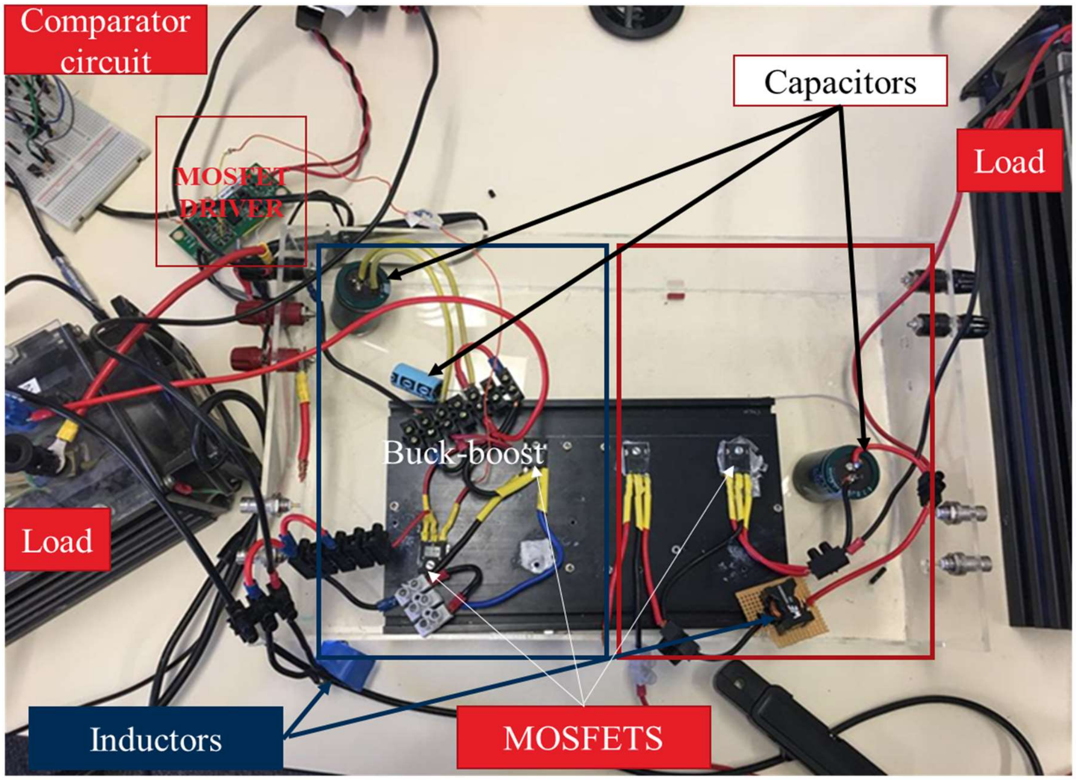

Fig. 6.7: Converter lab setup utilized

As observed in Fig. 6.7, layout inductance is apparent on the converters built, and as such a natural concern would be what effect does these have on the final results, more especially at higher frequencies. The stray inductance and resistance in the cables do have influence on the impedance results, but due to their consistence across all the tests, and since this is a comparative study, the effects are negated once comparisons are deduced

The purpose of the experimental results is to benchmark the converter accuracy against the FRA results, as such as means to minimise the effect of the connection wires and passive components used, the point at which the voltage response and current perturbated was measured at the Randle's circuit, was kept consistent for both the FRA and the converters as such this minimised the effect the other components have on the analysis of the Randle's circuit impedance. The effect would have been a major concern if the experimental results were used to do parameter determination of the Randle's circuit (i.e. of passive components used), rather the final results only compare and benchmark the capability of the converters against the FRA given that the same system under test is used.

Fig. 6.8 depicts a simplified block diagram between electrical components. The galvanostatic mode was used for both the EIS and BIS excitation, with the NI-USB6366 utilized for signal for acquiring and outputting signals. LabVIEW was used to output the PWM signals via the NI-USB 6366.

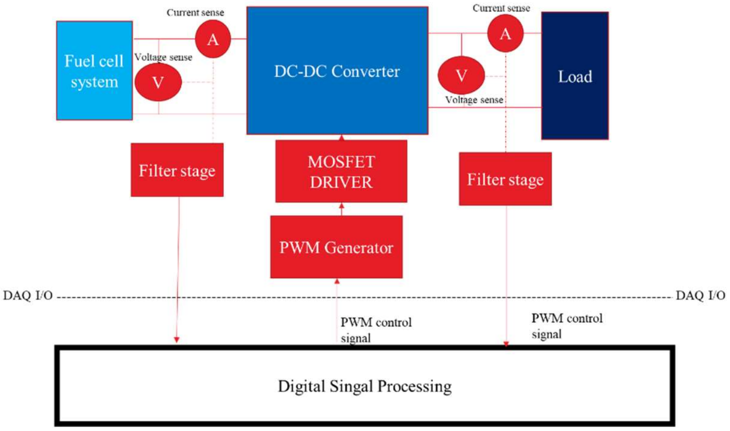

Fig. 6.8: The hardware connection over for online monitoring [6].

The Fast Fourier Transform spectral analysis with synchronous detection were utilized to measure the excitation and voltage response. The MATLAB/SIMULINK software was used to do digital signal processing, with the connection wires kept as much as possible, to reduce stray inductances and ohmic losses.

6.5 DC power supply

Fig. 6.9 illustrates the dc power supply utilized to emulate a fuel cell when integrated to a Randle circuit. This power supply was chosen since it has high output precision with low noise interference, as well as a very dynamic current-voltage characteristic curve.

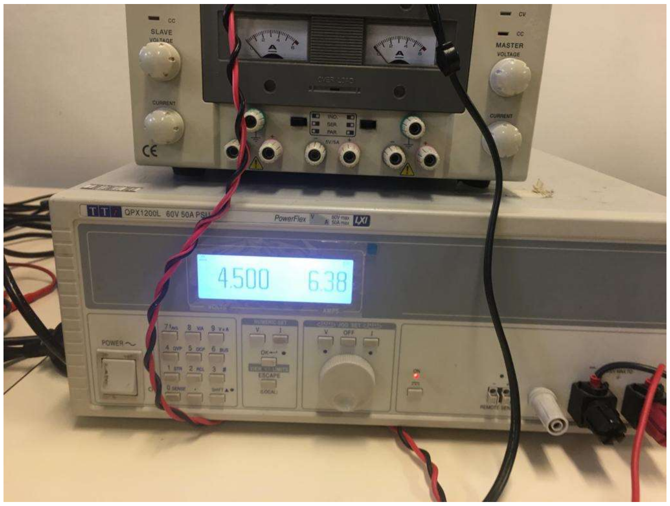

Fig. 6.9: The QPX1200SP DC power supply

6.5.1 Power envelope

Fig. 6.10 depicts the power characteristic of the dc power supply used. The dc power supply follows the blue shaded envelop shown in Fig. 6.10. The dc power supply can produce a voltage of up to $60\,V$ for currents from $0\,A$ to $20\,A$. Then the dc power supply follows an exponential curve from $20\,A$ at a maximum voltage of $60\,V$ and then start decaying to $50\,A$ at a maximum voltage of $20\,V$ [58].

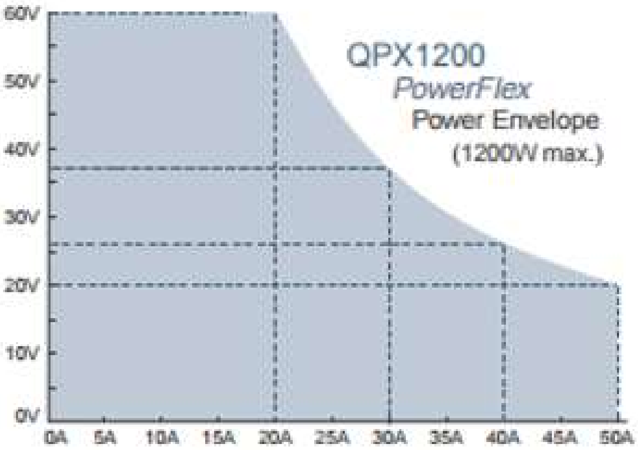

Fig. 6.10: The QPX 1200SP power supply power envelope [58]

6.5.2 Output specifications and settings

As mentioned above, the dc power supply QPX1200SP voltage and current range's is from $0-60\,V$ and $0-50\,A$ respectively. This device has the capability of automatically switching between constant voltage and constant current mode, with its current setting having a resolution of up to $10\,mA$, and a voltage resolution of up to $1\,mV$ [58]. It should also be noted that the voltage has a setting accuracy of

0.1%/±2 mV whilst the current setting accuracy is 0.3% /±20 mA [58].

6.5.3 Overvoltage and overcurrent protection

The dc power supply has two settable protection modes, which are the Overvoltage (OVP) and the Overcurrent (OCP) mode. The OVP is operational for output voltages ranging from 2 V to 65 V, allowing incremental step values with a resolution of 100 mV. The OCP is configurable for currents in the range from 2 A to 55 A , and with a resolution of 100 mA. The current when operating was set to a maximum value of 25 A, which is defined using the conductors current rating, it was only increased for instances where the converter performance characteristics were recorded when varying the converter duty cycle to a maximum. The dc power supply would shut down when the output current exceeds 25 A. The OVP was set to 10 V, which was to allow the converter to fluctuate around the 4.5 V chosen without omitting the power supply characteristics or being constrained.

6.6 Data generation and acquisition

Data generation and acquisition were achieved using the National Instruments (NI-USB 6366) DAQ, and this is shown in Fig. 6.11.

Fig. 6.11: The National Instruments (Ni-USB 6366) DAQ

The DAQ was used in both converter topology configurations to generate the control signal from the host computer (through LabVIEW) to the converters input duty cycle control signal, then was further used to acquire output signals from each converter topology (input voltage, input current/inductor current, output voltage and current) to the host PC interfacing through LabVIEW and MATLAB/Simulink for Digital signal processing. The NI-USB 6366 contains eight analogue inputs, with each channel having the capability of being used in a grounded source or floating source configuration. For experimental data acquisition all the channel pins were configured as the ground source configuration.

6.6.1 Sampling rate

The sampling rate was constrained by the sampling rate of the NI-USB DAQ, which has a maximum sampling rate of $2Ms/s$ per channel, with $50ppm$ being the timing accuracy with and $10ns$ being the timing resolution. Thus, the same sampling frequency was used for both the generation and acquisition of the signals. For each signal frequency, perturbated into the fuel cell system, the Nyquist theorem was observed and satisfied. Equation (6-1) shows how the sampling frequency had to be specified each time following the equation.

$$F_S = frequency\ xsamples \leq 2Msamples/s \tag{6-1}$$

As such, to inject a signal with a frequency less than $4kHz$, 500 samples or lower would be selected.

6.7 MOSFETS and diodes and conductors

IGBTs have higher power handling capability, as such A MOSFET was chosen over an IGBT because the designed buck-boost and boost converters are meant to be fast as possible with lower voltage high current capability. MOSFER IRFP 2907 can allow a drain current of $209\ A$ to pass through it with a maximum drain voltage of $75\ V$, which accommodates the circuit operating conditions. The MOSFET was attached to a heat sink to protect it from overheating when in operation.

The biasing diode chosen is the IRFP 2907 MOSFET, biased as a diode since both the boost and the buck-boost converter will be drawing a current of more than $5\ A$ from the emulated fuel cell system, as such a biasing diode with high current rating was chosen.

Table 6-2 MOSFET time characteristics

t_r	190ns
t_f	130ns
$t_{d(on)}$	130ns
$t_{d(off)}$	23ns

MOSFET used has an internal body diode characterised by forward voltage drop of 1.3 V. A MOSFET cannot produce a perfect square wave, and there is a slope associated with turning the MOSFET on and off, known as the t_r and t_f time. There is also a turn-on and turn-off delay given by $t_{d(on)}$ and $t_{d(off)}$ respectively. These values are shown in Table 6-2 [15], and they meet experimental requirements.

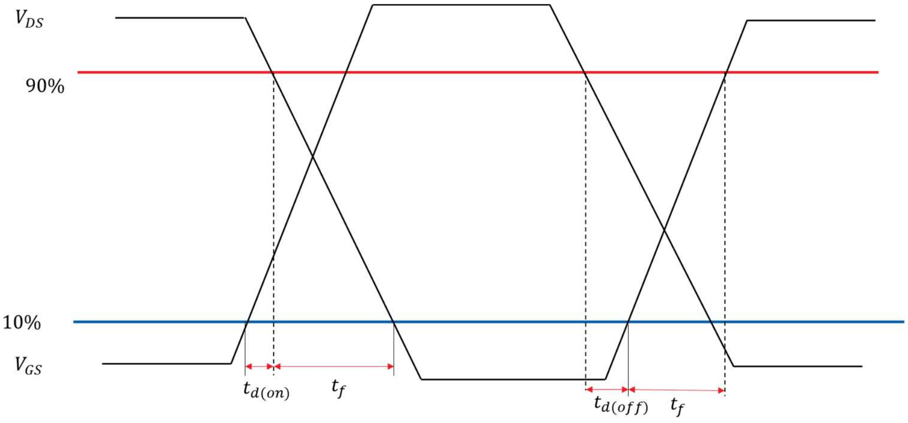

Fig. 6.12 Switching time waveforms [15]

Fig. 6.12 shows the switching overlap, which contribute to switching losses.

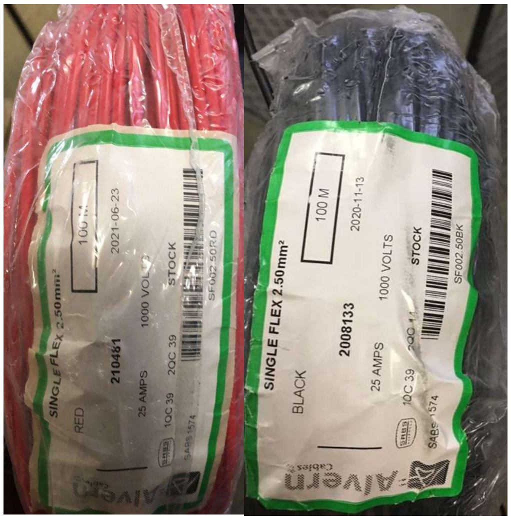

Fig. 6.13: Conductors used

Fig. 6.13 shows the conductors used, the current rating of these wires is 25 A, with a maximum voltage of 1000 V. These wires were chosen because they have a current rating of approximately 2.5 times the input drawn current.

6.8 Drive circuitry

The drive circuit, as in [15], is responsible for converting the PWM signal to a level required to switch the MOSFET, as shown in the figure below. This PWM generation is achieved by taking in the duty cycle signal and then converting it to PWM using a PWM generator, as this section details the overall design and construction of the drive circuitry.

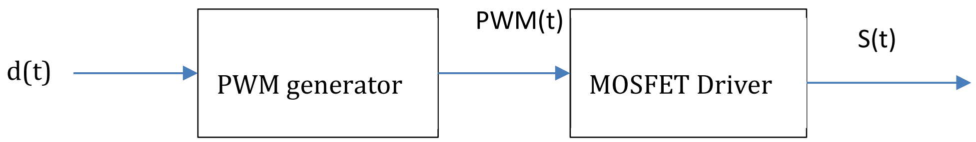

Fig. 6.14:PWM generation

6.8.1 PWM generation

Two options were considered for the generation of the PWM signal, these were the analogue and digital option. Each option has it caveats and advantages. The digital option is advantageous for signal like PRBS, or a square wave that have binary output nature (two levels), as they can easily be produced by micro-controller. The digital option is also advantageous by that it allows for high sample rate depending on the micro-controller used.

In the other case, the analogue option is advantageous by that it favours the output of analogue signal like sinusoids or chirp signal without any external filtering. The analogue option was chosen, since a micro-controller was not the main device chosen, also producing the PWM on an external dedicated circuit simplifies the system design. The PWM signal was produced by comparing a triangular waveform produced by EXAR microchip called XR-8038A to the duty cycle from the DAQ. Fig. 6.15 depicts the schematic of the microchip responsible for producing the triangular wave.

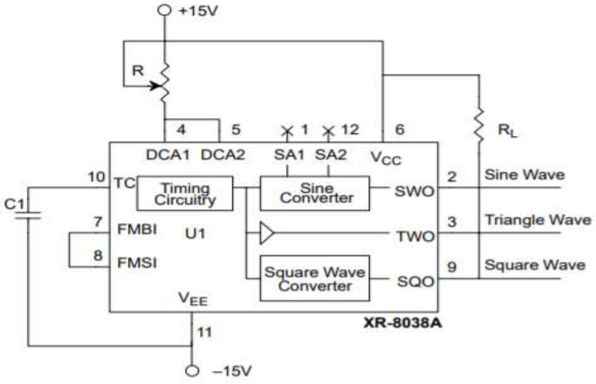

Fig. 6.15: Circuit used to generate the Saw tooth [43]

The timing is set by adjusting R and C. The timing is given by the following equation:

$$f_{SW} = 100\ kHz = 0.15/RC \tag{6-2}$$

Therefore, RC would need to

$$RC = \frac{0.15}{100000} = 7.5\ \times 10^{6} \tag{6-3}$$

Therefore $C = 10nF$ and $R = 750\ \Omega$ were chosen. The PWM signal was generated by producing a triangle signal from the microchip and comparing it to a dc reference voltage which is the duty cycle waveform, and the comparator used is the LM311.

6.8.2 MOSFET driver

The MOSFET driver is the part responsible for translating the produced PWM waveform into the MOSFET. The design consideration for the MOSFET component is that the drive high voltage needs to be greater than the source.

The MOSFET gate driver used is the UCC20520EVM-286 evaluation board from Texas Instruments. The driver circuit is attached in Appendix C This board comprises the UCC20520 isolated dual gate with a bandwidth of up to 5 MHz, with optimized in-class propagation delay and pulse width distortion [59]. The board has optimized switching performance and protection capability due to its integrated components.

The MOSFET gate Driver Module has these features:

- Integrated programming trimmer potentiometer
- Can draw or supply current in the range from 4 A to 6 A
- The board can allow up to 25 V in VDDA/VDDB, with a range of $3 - 18\ V$ power supply range for VCCI

More details about the module capabilities and use are described in [59].

Hardware configuration:

1. The VCCIN connector was connected to a 5 V power supply.
2. An additional 12 V power supply was connected to $VDDAIN$ (with the positive terminal to VDDAIN and the negative terminal to $GNDA$).
3. Function generator/PWM generated waveform was connected to pin $JINA$ and the ground to $TP14$.
4. The driver output to the MOSFET/oscilloscope (for illustration purposes) was connected between V_GA and $GNDA$.

6.8.3 Minimum MOSFET gate resistance

The MOSFET gate current can be calculated by (6-4):

$$I_G = \frac{Q_G}{t_{transistion}} \tag{6-4}$$

Where Q_G is the gate charge and $t_{transistion}$ being the transition time, this is computed by adding the rise time (t_r) and the delay time (t_{delay}).

For MOSFET IRFP2907, $Q_G = 410nC$, t_r=190ns and t_{delay}=153ns.

$$I_G = \frac{Q_G}{t_{transistion}} \tag{6-5}$$

$I_G = 1.195\ A$, the MOSFET driver provides a gate voltage of 12 V; thus, from KCL, the gate resistance is computed as follows:

$$R_G = \frac{V_G}{I_G} \tag{6-6}$$

This results in $R_G = 10.03\ \Omega$, the power dissipated by the resistor is affected by the frequency of the current drawn through the resistor. As such, the influence of the frequency is explored to find the maximum and minimum boundaries of the gate resistor power dissipation, and the gate resistor power dissipation is calculated using equations (6-7) and (6-8) as follows:

$$P_{dissipation} = {I_{rms}}^2 R_G \tag{6-7}$$

And I_{rms} given as:

$$I_{rms} = I_G \sqrt{2 \times \frac{t_{transition}}{T}}; \tag{6-8}$$

Where $T = \frac{1}{F_s}$; thereby resulting in $I_{rms} = 0.312$ and $P_{dissipation} = 0.983$W.

6.9 Current and voltage measurements

Currents and voltages need to be measured for two reasons, converter voltage control as well as impedance measurements. The signals needing to be measured include: the output voltage and current V_c and I_L, inductor current I_L and fuel cell input voltage V_{fc}.

6.9.1 Current measurement

Pintech PT-350 current probes were selected to measure the inductor current and output current, and it comes with its adapter to supply it.

Fig. 6.16: Pintech PT-350 current probe

The current probes are shown in Fig. 6.16. This has an accuracy of $1\%(\pm 5mV)$ and band with of $DC - 50MHz$

6.9.2 Voltage measurement

The Tektronix P5200a voltage probe was used to measure the input voltage and output voltage.

Fig. 6.17: Tektronix P5200a voltage probe.

This was the voltage probe used for all voltage measurements, and there are several of these available in the laboratory.

6.9.3 Filters

As stated earlier on, switch mode dc-dc converters have noise due to the switching of the converter. However, for EIS analysis, the injected voltage and current of the fuel cell need to be as accurate as possible in order to effectively estimate the impedance of the fuel cell system for online condition monitoring. As such, this section designs the filter used for the measured voltage and current for EIS analysis, as was done by [13] [15].

An ideal filter would filter or eliminate all the frequencies outside the specified region; however, due to practical limitations, each filter type has its caveats which are explored below [60].

Table 6-3: Advantages and disadvantages of different filter types [60]

Filter Type	Butterworth	Bessel	Chebyshev
Advantage	• Flat passband region	• Linear phase in the passband	• Steeper roll-off.
Disadvantage	• Slightly non-linear in phase • Gentle gradient in the "knee" region	• Amplification is not flat • Gentle gradient in the "knee" region	• Ripples in the passband region • Phase is not linear. Worse than Butterworth

Due to the flat passband band nature of the Butterworth, it was chosen as the filter of choice; this is to mitigate any attenuation of the injected signal and to ensure that the injected signal and response signal is measured as accurately as possible. The filter chosen is the Sallen-Key active low pass filter, as shown below [60] [61]:

$$H_{LP}(f) = \frac{\frac{K}{R_1R_2C_1C_2}}{S^2 + S\left(\frac{1}{R_1C_1} + \frac{1}{R_2C_1} + \frac{1-K}{R_2C_2}\right) + \frac{1}{R_1R_2C_1C_2}} \tag{6-9}$$

$$H_{LP}(S) = \frac{b}{S^2 + aS + b} \tag{6-10}$$

$$H_{LP}(S) = \frac{(\omega_p)^2}{S^2 + \frac{\omega_p}{Q_p}S + (\omega_p)^2} \tag{6-11}$$

ω_p is the frequency corresponding to the peak. The DC gain is given by K, and $(\omega_p)^2 = \frac{1}{R_1 R_2 C_1 C_2}$, $\omega_p = \sqrt{b}$, where $Q_p = \frac{\sqrt{b}}{a}$ From this, let $R = R_1 = R_2,\ C = C_1 = C_2,$ and $\omega_p = {}^{1}/_{RC}$ [61].

Fig. 6.18 depicts the second order Sallen key filter, this filter type main benefit is that it can easily be modified to have unity gain, and its order can be increased by cascading it to other unity Sallen key filters [61] [62].

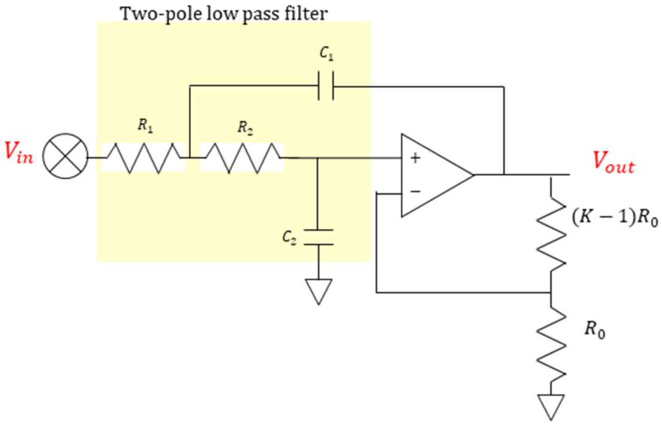

Fig. 6.18:Basic Sallen-key LPF

Equation (6-9),(6-10) and (6-11) were utilized to compute appropriate capacitor and resistor values for the filter, as shown in Fig. 6.19 [61].

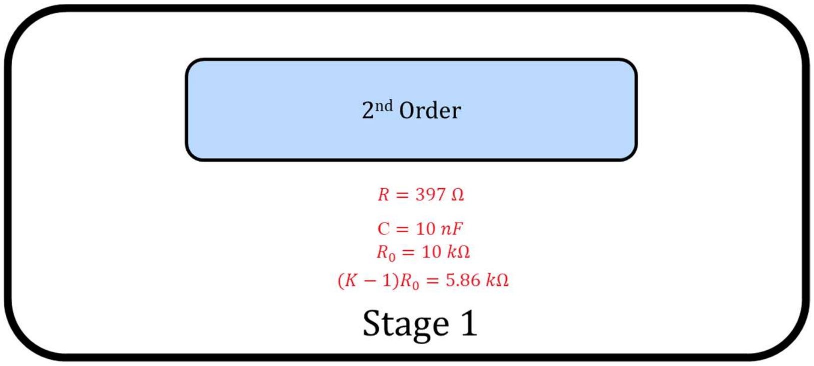

Fig. 6.19: Sallen-key parameters

These values were simulated in LTspice, with the schematic shown in Fig. 6.20.

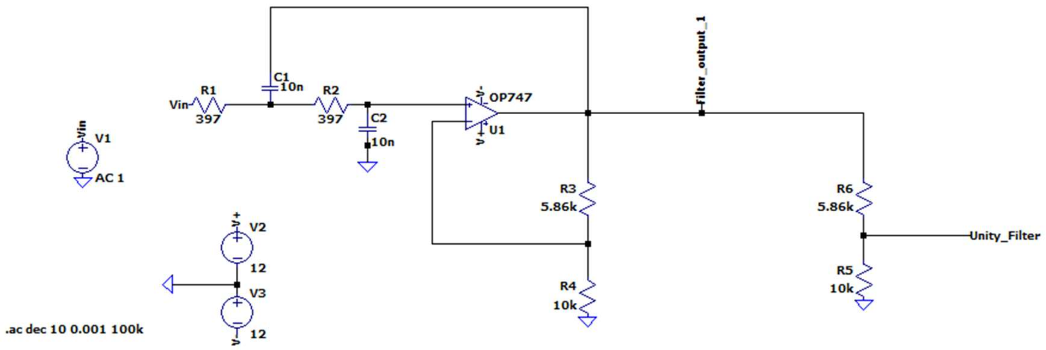

Fig. 6.20: LTSPICE of unity active low pass filter (Sallen-key configuration)

The cut-off frequency was chosen to be 40 kHz, and the gain from the Floyd table is $K = 1.586$. This results in the low pass transfer function below given by equation (6-12) before the gain is scaled to unity.

$$H_{LP}(f) = -\frac{1.586}{-(\frac{f}{2\pi.40000})^2 + \frac{jf}{(1.414)2\pi.40000} + 1} \tag{6-12}$$

The voltage bode response are presented in Fig. 6.21. The red line is the 2nd order filter's phase and magnitude response before it is scaled to a unity gain, and the blue line is the output response of the 2nd order filter after being scaled to unity.

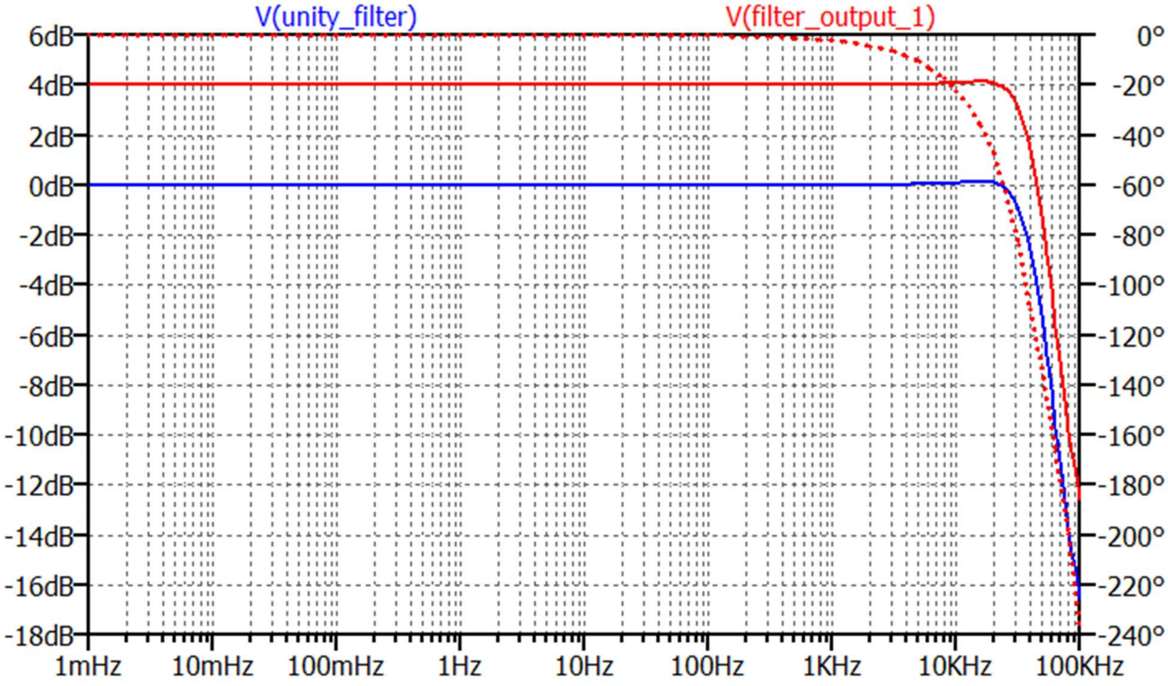

Fig. 6.21: Phase and Magnitude response of Sallen-key low pass filter

From this, the order of the filter can be increased by cascading the filter with a first order unity low pass filter.

6.10 Conclusions

This section detailed the practical fuel cell emulation using the components in the lab, it further describes the FRA used as the benchmark equipment. The dc-dc converter built; the filtering circuits used along with the drive circuits. The results obtained from this hardware setup is presented in the next chapters.

Chapter 7

Boost converter experimental results and discussion

7.1 Boost converter open-loop experimental results

This chapter presents the results for the normal emulated fuel cell system to avoid redundancy as the other operating conditions have similar signals measured. The measured signals were acquired using the National Instruments USB NI-6366 and viewed with LabVIEW and MATLAB.

The following section presents the measured results of the converter for incremental changes, which are:

(1) Boost converter DC-DC open loop results without an emulated fuel cell system, to show the associated converter losses.

(2) Boost converter DC-DC open loop EIS and PRBS results with the emulated fuel cell system

(3) Boost converter DC-DC closed loop EIS and PRBS results with the emulated fuel cell system.

7.1.1 Boost converter DC-DC power open-loop results without an emulated fuel cell system

The output voltage and current were tested using an input voltage of 4.5 V and constant load resistor of 2 Ω, and this is consistent with the designed values and the simulation results. It should be noted that the wires and the inductors introduced some resistance which has resulted in minor differences between the simulation and experimental results, and the difference between simulated and experimental results are presented in chapter 9.

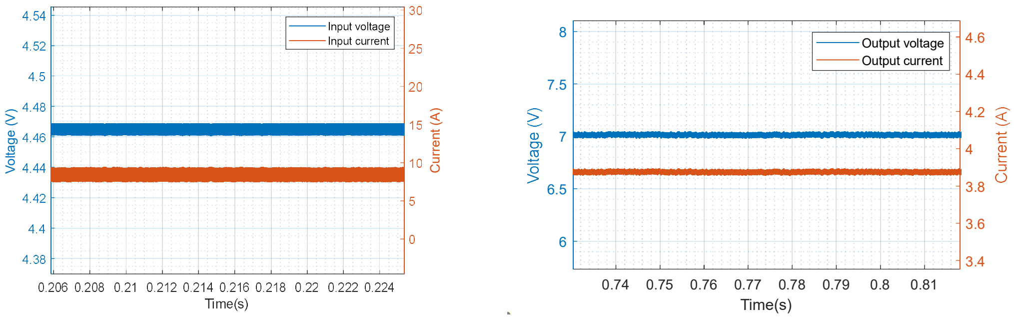

(a) (b)

Fig. 7.1: DC-DC measured signals of the boost converter (a) input current and voltage (b) output voltage and output current

Fig. 7.1(a) shows the input current and voltage of the boost converter, these are the characteristics of the boost converter without the inclusion of the emulated fuel cell, connected to the DC source (DC power supply). Fig. 7.1(b) shows the output voltage and current of the boost converter, without the emulated fuel cell system. The measured voltage and current are lower than the designed values used in the simulation results, and this is due to the parasitic elements of the inductor and the equivalent series resistor of the output capacitor, as well as the connecting wires and voltage drop across the diode and MOSFET switch. These values are shown in Table 7-1, with the comparison to the designed simulation values.

Table 7-1: Boost converter performance comparison between the expected and actual boost parameters

Converter parameter	$V_{in}(V)$	$I_{in}(A)$	$P_{in}(W)$	$V_{out}(\mathrm{V})$	$I_{out}(\mathrm{A})$	$P_{out}(W)$
Simulation values	4.5	10	45	9	5	45
Actual values	4.47	7.2	32.2	6.92	3.82	26.4

Table 7-1 shows that there is a difference between the designed values and the actual measured values, with the voltage gain being 1.547 instead of the designed value of 2, and a power efficiency of 81.9%. The desired input current was $10A$, however $7.2A$ was drawn. Consequently, the duty cycle of the boost converter was varied to determine the corresponding duty cycle that will allow for this input current. The input current had a ripple of $1.978A$ which was 27.5% of the input current, and the output voltage ripple was $0.065V$ which is less than 5% of the output voltage. The converter's duty cycle was varied in steps of 0.1 from 0.1 to 0.7, and the converter parameters were recorded.

Table 7-2: boost converters varied duty cycle for DC power supply

Duty cycle	$V_{in}(V)$	$I_{in}(A)$	$P_{in}(W)$	$V_{out}(V)$	$I_{out}(\mathrm{A})$	$P_{out}(W)$
0.1	4.49	2.15	9.67	4.02	2.26	9.10
0.2	4.48	2.78	12.5	4.55	2.47	11.2
0.3	4.48	4.05	18.1	5.18	2.83	14.7
0.4	4.47	5.44	24.3	5.99	3.27	19.6
0.5	4.46	7.21	32.2	6.91	3.80	26.3
0.6	4.45	10.8	48.5	8.05	4.45	35.8
0.7	4.42	16.8	74.6	9.29	5.13	47.7

Table 7-2 shows that the input current increased from $2.153A$ to 16.48 as the duty cycle was increased, however, it should be noted, to achieve an input current of $10A$ the duty cycle needs to be between 0.5

and 0.6. From Table 7-2 it is noted that the converter without the emulated fuel cell (with its associated losses considered), can achieve the desired input current with the modification of the duty cycle.

7.1.2 Boost converter DC-DC open loop results with an emulated fuel cell system

The emulated fuel cell system was used as the source of the boost converter, and parameters were selected such that they emulate the normal operating conditions of the fuel cell system. With the source being the emulated fuel cell system (i.e., Randle circuit in series with the dc power supply), the input and output signals were measured.

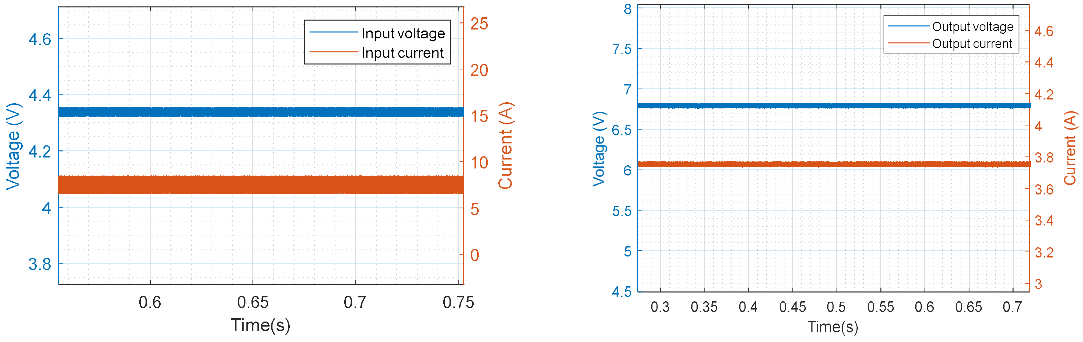

(a) (b)

Fig. 7.2: DC-DC measures signals of the boost converter sourced from fuel cell system (a) input voltage and input current (b) output voltage and output current.

Fig. 7.2 (a) shows the input current and voltage and Fig. 7.2 (b) shows the output voltage and current - it can be observed that the input voltage and current of the boost converter are different from those in Fig. 7.1(a), and the magnitudes have decreased. The reason for this decrease is because the emulated fuel cell system has a voltage drop across it due to the Randle circuit impedance and this reduces the effective input voltage boosted by the boost converter.

Table 7-3: Boost converter performance comparison between the expected and actual boost parameters

Converter parameter	$V_{in}(V)$	$I_{in}(A)$	$P_{in}(W)$	$V_{out}(\mathrm{V})$	$I_{out}(\mathrm{A})$	$P_{out}(W)$
Simulation values	4.5	10	45	9	5	45
Actual values	4.33	6.92	30.0	6.48	3.55	23.0

Table 7-3 shows the actual values with respect to the simulated/desired results. The efficiency of the converter when sourced from the emulated normal fuel cell system was 76.6%. The effective gain voltage gain of the converter was 1.49. The ripple current was 2.074A which results in a 29.9%, ripple in reference to the input current and the capacitor ripple was less than 10% of the output voltage.

As discussed in the boost converter simulation chapter 5. For different operating conditions (fuel cell systems internal water conditions) different input currents, voltages, output currents and voltage and inductor currents were observed. Table 7-1 and Table 7-3 shows how the actual boost converter measured values differ from the simulation values. This was the case whether the converter was sourced with a simple DC power supply or the emulated fuel cell system.

Table 7-4: boost converters varied duty cycle for emulated fuel cell system

Duty cycle	$V_{in}(V)$	$I_{in}(A)$	$P_{in}(W)$	$V_{out}(V)$	$I_{out}(A)$	$P_{out}(W)$
0.1	4.44	2.47	11.0	3.97	2.18	8.69
0.2	4.42	3.05	13.5	4.53	2.49	11.3
0.3	4.41	4.32	19.1	5.15	2.84	14.6
0.4	4.38	5.01	21.9	5.91	3.24	19.1
0.5	4.33	6.93	30.7	6.28	3.69	23.2
0.6	4.262	9.73	41.5	7.25	4.53	32.16
0.7	4.14	147	60.8	9.03	4.93	44.5

Table 7-4 shows the boost converters values when its duty cycle was varied whilst sourced from the emulated fuel cell system. As in Table 7-2, the input current of 10A was between a duty cycle of 0.6 to 0.7. This further motivated the need for DC power control before impedance spectroscopy was performed, since the Kramers-Kronig's condition must be maintained.

7.1.3 Boost converter DC-DC open loop EIS results with the emulated fuel cell system

Fig. 7.3 (a) below shows the input and output voltage and current of the boost converter when the emulated fuel cell system is connected. It should be noted that this was different from Fig. 7.2 (a), where the input voltage was constant; in this scenario, it was a sinusoidal waveform, since sinusoidal current is drawn from the emulated fuel cell system.

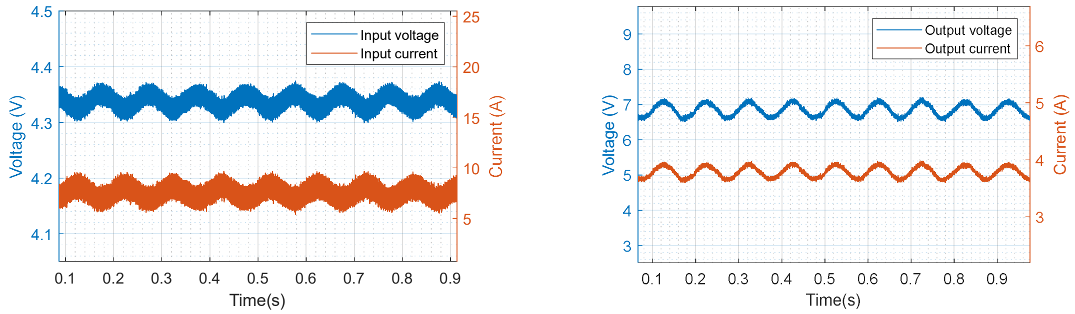

(a) (b)

Fig. 7.3: DC-DC boost converters EIS perturbed with Randle circuit (a) input voltage and current (b) output voltage and current

As can be seen in Fig. 7.3 (a), the $10Hz$ perturbated drawn current is not as designed in the simulation chapter. The input current was supposed to be 10A. However, the current measured is around 7A, and the AC perturbed current was not 1A. As such there was the need for both DC and AC control, confirming the simulation results. The input voltage and current sinusoidal signals were also out of phase, with the phase shift determined by the impedance of the normal condition Randle circuit. Also, in Fig. 7.3 (b), both the output voltage and current were in phase, as they were measured for the load resistor.

7.1.4 Boost converter DC-DC open loop results with an emulated fuel cell system with PRBS

Fig. 7.4 shows the input and output voltages and current when the emulated fuel cell is connected. This is different from in section 7.1.2 by that the converter was now perturbed with the source being the emulated normal condition fuel cell system.

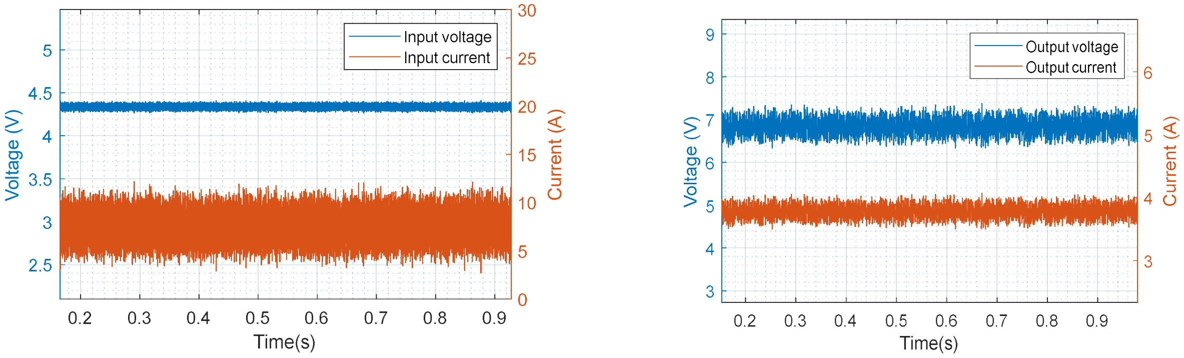

(a) (b)

Fig. 7.4: DC-DC boost converters PRBS perturbed with a Randle circuit (a) input voltage and current (b) output voltage and current

Fig. 7.4 (a) shows the input voltage and current. The AC current amplitude was not as desired, both the DC and AC signal components don't have the desired designed simulation values and as such, there was a need for control of both components. In Fig. 7.4 (b), both the output voltage and current were in phase, as they were measured across the load resistor.

7.2 Boost converter closed-loop experimental results

Section 7.1 showed the experimental results in open loop with justification for DC and AC control demonstrated. In this section, the boost converter was controlled using the controller designed in the control section, for both the DC power supply and emulated fuel cell system, with and without perturbation presented, following the same format as in the simulation section for the boost converter.

7.2.1 Boost converter DC-DC closed loop EIS perturbation results with a DC power supply and an emulated fuel cell system

This section shows the input and output voltage when the EIS signal was perturbed into the fuel cell system and a DC power supply.

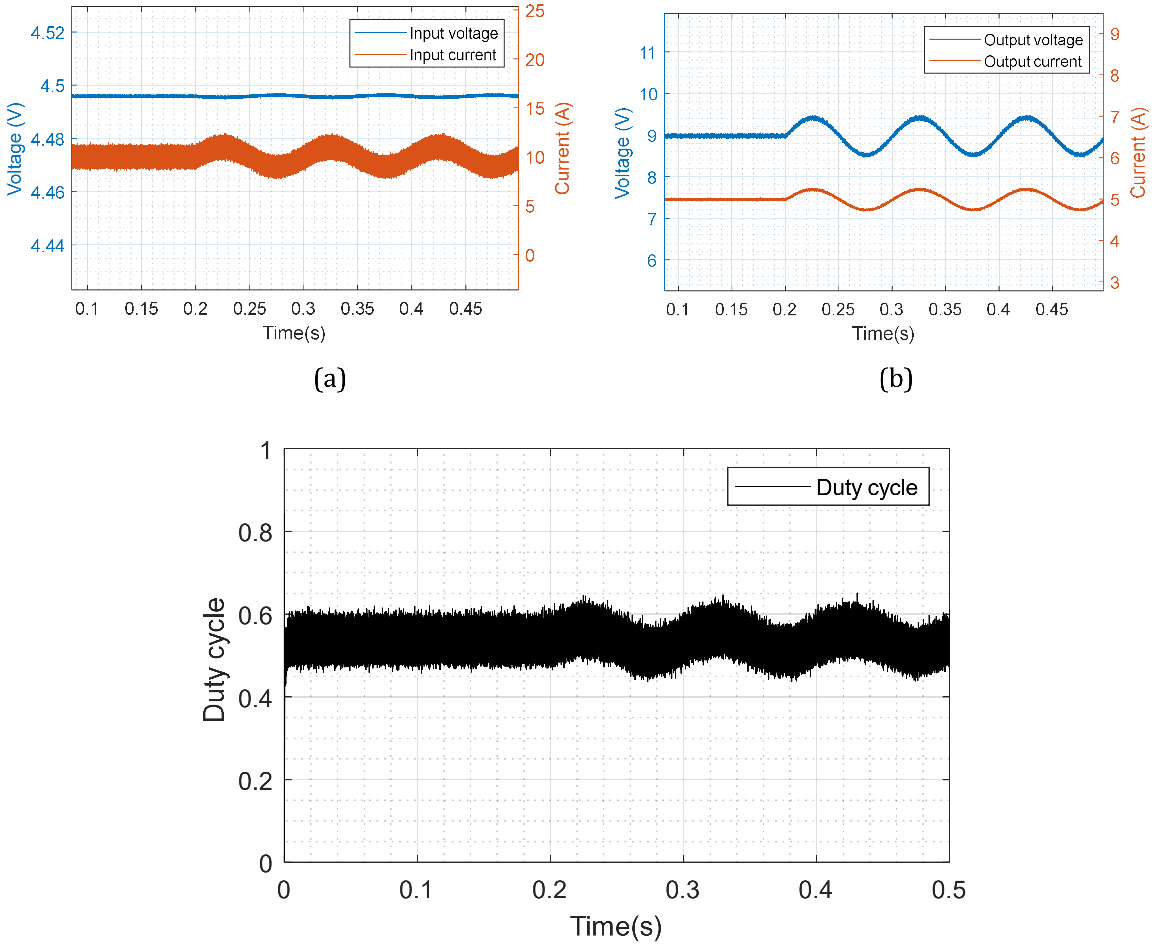

(a) (b)

(c)

Fig. 7.5: boost converter's DC power supply EIS perturbed (a) input voltage and current (b) output voltage and current (c) control duty cycle

Fig. 7.5 shows all the controlled conditions when the converter is EIS perturbed when sourced from a DC source. The converter was controlled, with the EIS signal perturbed at 0.2 seconds after the signals have reached a steady state, the control meets the desired condition of a DC input current of approximately 10 A and an AC input current of 1 A.

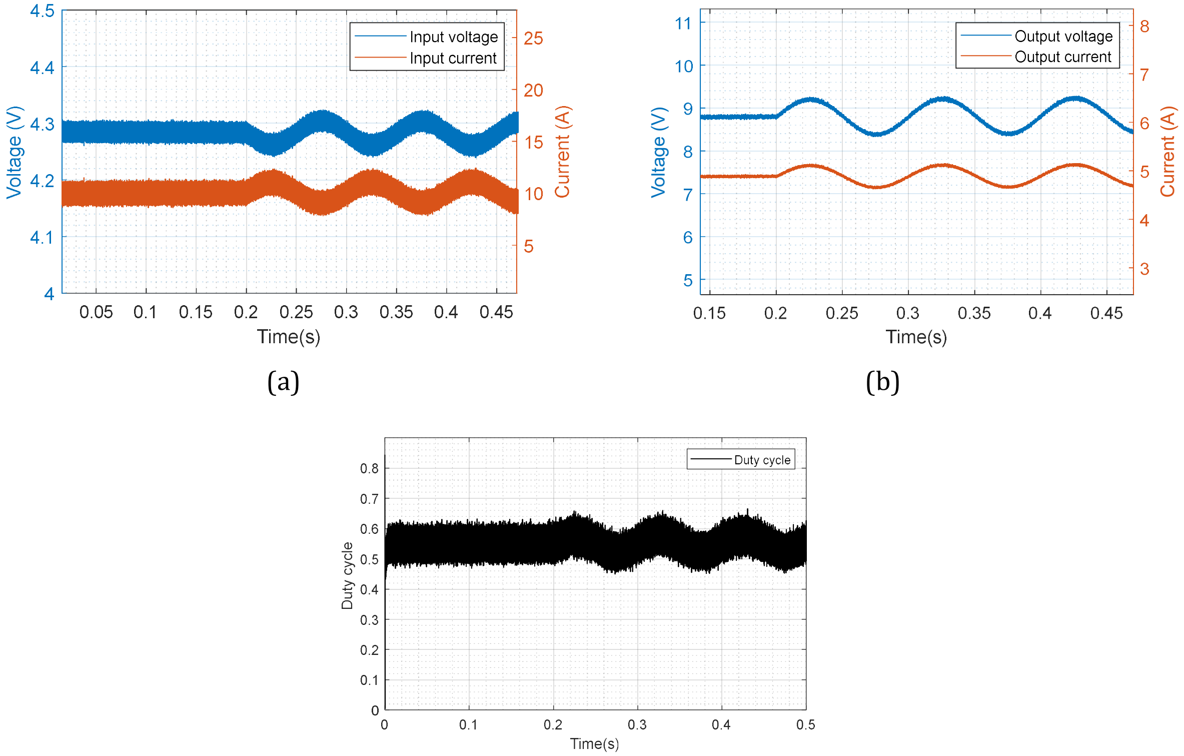

(a)

(b)

Fig. 7.6: Boost converter's emulated fuel cell system EIS perturbed (a) input voltage and current (b) output voltage and current (c) control duty cycle

Fig. 7.6(a)-(c) shows all the controlled conditions when the converter is EIS perturbed when sourced from an emulated fuel cell system. The converter was controlled, and the EIS signal was perturbed at 0.2 seconds once the signals are steady. The controller strategy meets the designed condition of a DC input current of $10A$ and an AC input current of $1A$. Regardless of the decrease in input DC voltage from when the DC power supply is replaced with the emulated Randle circuit, the control meets the control requirements, and these are a DC input current of $10A$, with an AC perturbed signal, with an amplitude of $1A$, and the capacitor output voltage of $9V$. Fig. 7.6(c) shows that the duty cycle varies between 0.5 and 0.68, which is different from Fig. 7.5 (c), where the duty cycle varies from 0.48 to 0.62.

7.2.2 Boost converter DC-DC closed loop results with and without a Randle circuit with PRBS

The double loop controlled boosted converter was also tested with the PRBS signal, as in Section 7.2.1, and the signals were measured and presented in Fig. 7.8 and Fig. 7.8.

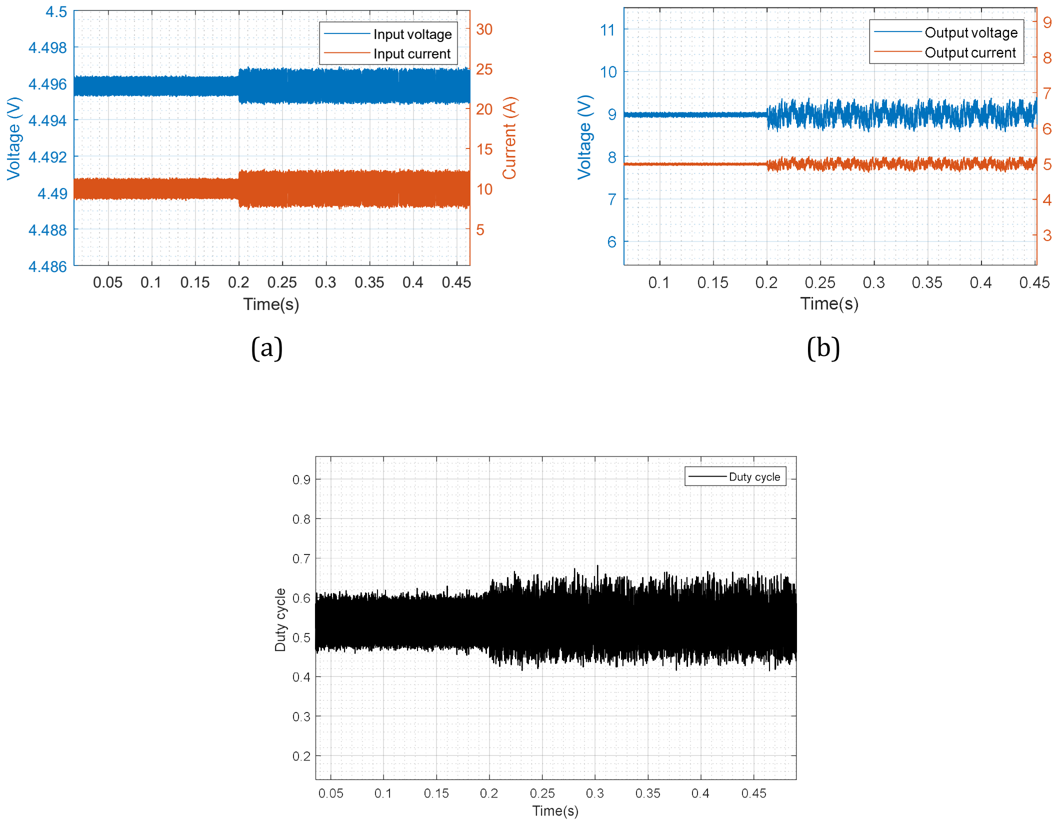

(a)

(b)

(c)

Fig. 7.7: boost converter's DC power supply PRBS perturbed (a) input voltage and current (b) output voltage and current (c) control duty cycle

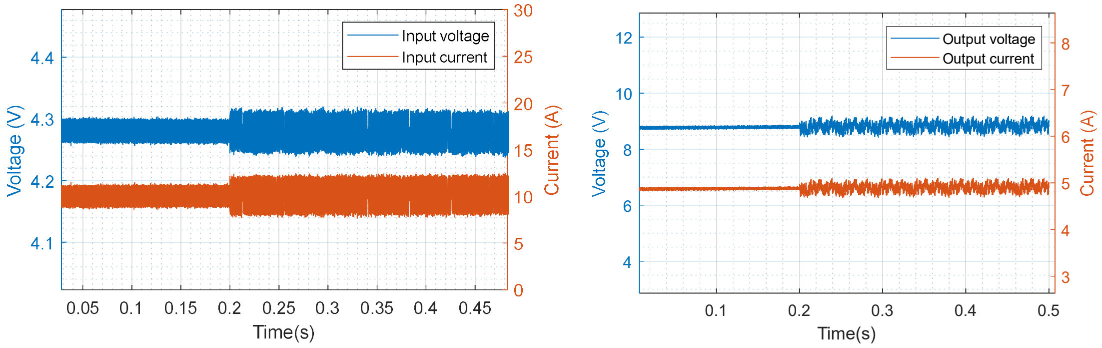

(c)

(d)

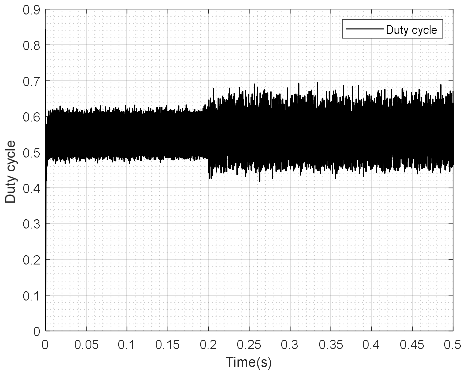

(c)

Fig. 7.8: boost converter's emulated fuel cell system PRBS perturbed (a) input voltage and current (b) output voltage and current (c) control duty cycle

The converter was tested with the perturbed PRBS signal when sourced from a DC source in Fig. 7.7, and when sourced from the emulated fuel cell system in Fig. 7.8, the PRBS in both scenarios was injected at a time stamp of 0.2 seconds once the converter system has settled. Similar to Section 7.2.1 the input DC voltage dropped from $4.48V$ in Fig. 7.8(a) to $4.28V$ in Fig. 7.8 (a), and this does not affect the PRBS amplitude signal of $1A$. Both the DC and AC controlled signals meet the desired specifications, and the signal processing for impedance estimation was done from these measured, controlled signals, whereby the impedance estimation results are presented in 7.3.

7.3 Boost converter Impedance results

The experimental impedance results acquired for normal, flooding and dry states, will be presented and discussed in this section.

A high perturbation amplitude maximizes the signal-to-noise ratio (SNR) but results in a deviation of the linearity conditions of Kramer-Kroning's, as such 10% ac signal to the dc signal was chosen. The boost converter was built as specified in the design section, and the respective input and output voltage, current and power were measured as shown in sections 7.1 and 7.2 where the signals are analysed.

For the three operating conditions normal, flooding and drying, the impedance was extracted: using the PRBS and EIS. These results are benchmarked against those of the Frequency Response Analyzer.

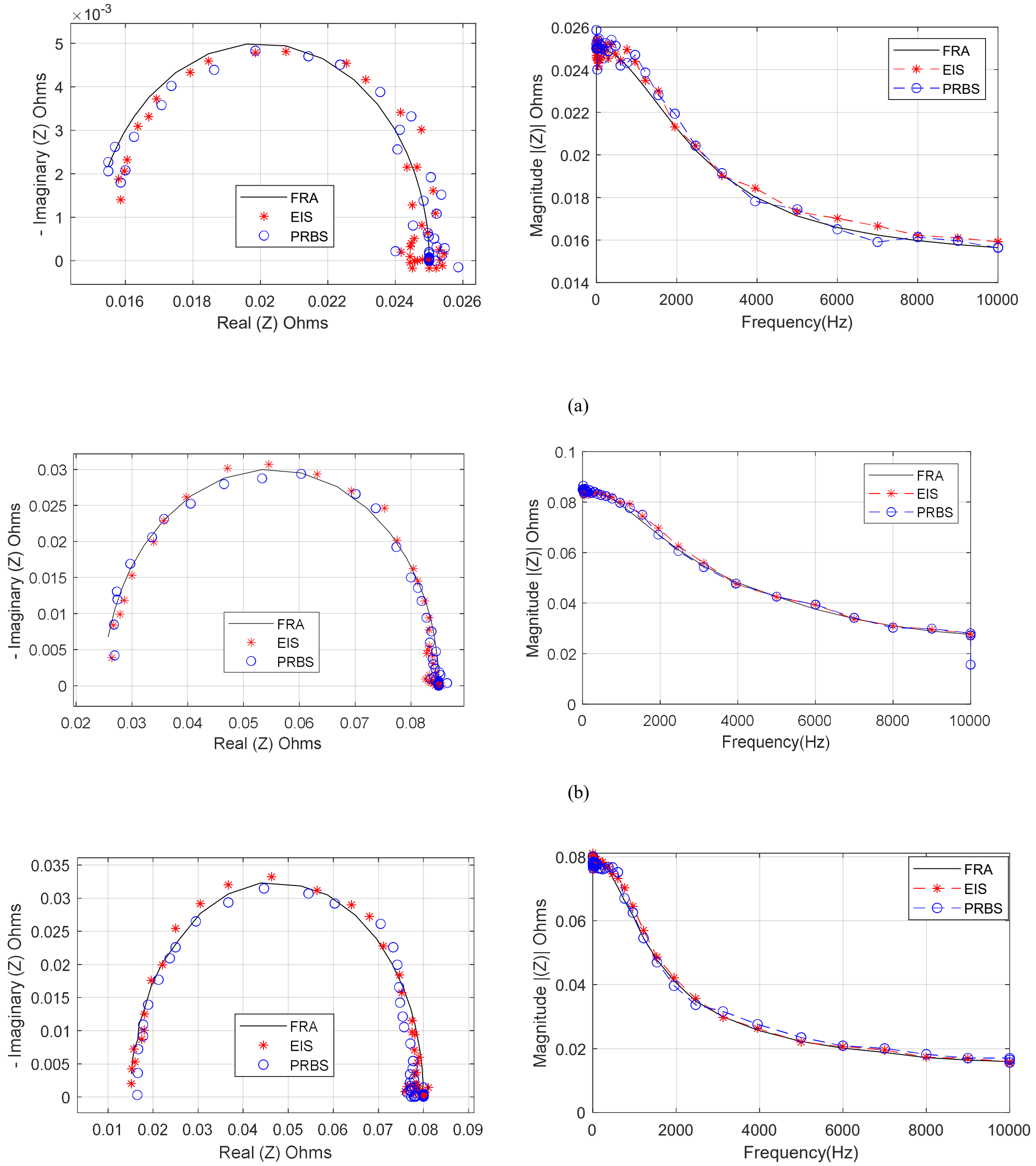

(a)

(b)

(c)

Fig. 7.9: Fuel Cell impedance estimation-Nyquist(left) and Magnitude(right) (a) normal conditions (b) drying (c) flooding.

As shown in Fig. 7.9(a)-(c), both the EIS and PRBS results adequately estimate the impedance curve from the Frequency Response Analyzer, however, for all conditions the EIS results were closer to the Frequency Response Analyzer results compared to the PRBS results. The higher frequencies for both the EIS and PRBS results were more accurate compared to the lower frequencies, however, this was as a result of, in EIS, an increase in the number of periods perturbed (more than 10 periods), For PRBS, the same period is used for both the lower spectrum and higher spectrum signal, since the signal contains all frequencies needed. The impedance estimation errors are quantified in Table 7-5.

Table 7-5: Impedance maximum estimation error of EIS and PRBS against FRA results

Condition	**EIS maximum percentage error**	**PRBS maximum percentage error**
Normal	**3.65**	**4.95**
Drying	**4.51**	**4.71**
Flooding	**6.19**	**7.26**

Table 7-5 shows that the PRBS has the maximum impedance error for most operation conditions, and this was consistent with the simulation results performed for Randle circuits. However, these errors were slightly greater than those of the simulations as they were affected by switching noise, switching dead-time and the tolerance of the passive components.

Table 7-6: Impedance average estimation error of EIS and PRBS against FRA results

Condition	**EIS average percentage error**	**PRBS average percentage error**
Normal	1.157	0.8522
Drying	1.07	0.79
Flooding	1.71	2.85

Table 7-6 shows the average percentage error, and both the EIS and PRBS percentage error were below 5%, with the largest error deviation being 2.85% for the PRBS signal, which was consistent with the maximum percentage error.

For lower frequencies, the DC supply varied slightly, even when a decoupling capacitor was added in parallel to the DC supply, and this variation was observed for the measured input voltage. This contributed to lower frequencies of the perturbed signals having significant errors. Although the error was larger for PRBS, the measurement time was significantly reduced in comparison to EIS, as shown in Table 7-7.

Table 7-7:Parameters for measurement and performance validation

	EIS	**PRBS**
Amplitude	$1A$	$1A$
Bandwidth	$1Hz - 10kHz$	$1.46Hz - 10kHz$
N	$-$	255
Measurement time	$25s$	$8\ s$

Fig. 7.10 shows the impedance plots for the different operating conditions (normal, drying and flooding) on a single figure to illustrate the difference in traces.

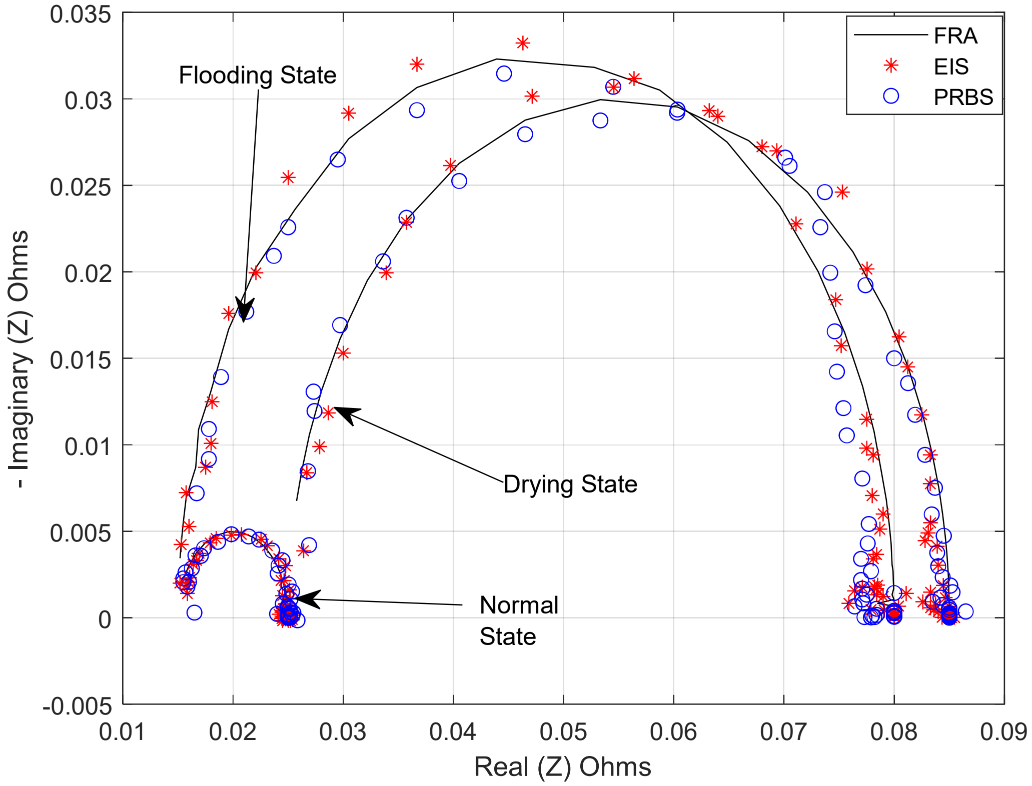

Fig. 7.10: Fuel Cell impedance estimation according to different internal water conditions-Nyquist

The magnitude of the impedance were all plotted in Fig. 7.11; the purpose of these plots was to show a different perspective in an attempt to easily identify the three internal water management conditions.

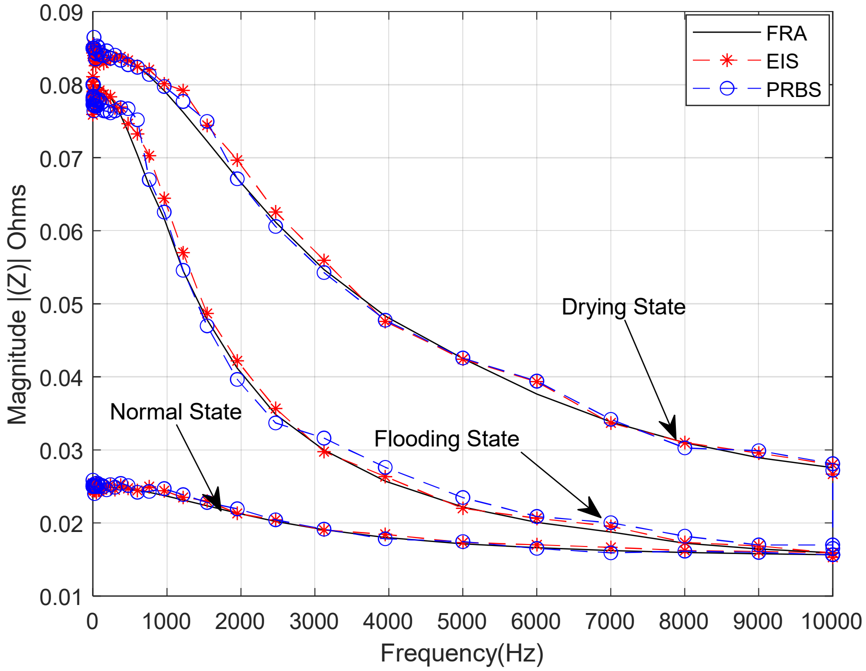

Fig. 7.11: Fuel Cell impedance estimation according to different internal water conditions-Magnitude

As shown in Fig. 7.11, for the normal state at low frequencies, the impedance was approximately 25 $m\Omega$, whereas the other two states were approximately 80 $m\Omega$. However, as the frequencies increased towards $10kHz$, the flooding state converged with the normal state around 15 $m\Omega$, whilst the drying state converged at around 30 $m\Omega$ s for high frequencies. These plots show how the different internal water management scenarios may be distinguished.

7.4 Conclusions

This chapter presented the use of a boost DC-DC converter for power transfer and online condition monitoring of a fuel cell. The converter is modelled by its average linearized small-signal model. The proposed scheme implemented was simulated to verify its suitability for EIS and PRBS implementation in comparison to theoretical results. The results for both PRBS and EIS were in close proximity to the theoretical results. This section presents the same process experimentally to validate the applicability of the boost converter for impedance determination. The experimental results provided further information on the open loop signals, closed loop signals and presentation of the controlled EIS and PBRS signal, in conjunction with error analysis. These results have demonstrated the feasibility of using PRBS for online internal water fault detection of the fuel cell with a shorter impedance estimation time, which is 5 times lesser than the EIS time, also with an error of less than 10% to the FRA benchmark results for the boost converter.

Chapter 8

Buck-boost converter experimental results and discussion

8.1 Introduction

This section presents the experimental results of the buck-boost converter, following the same sequence as done for the boost converter, however summarized. The input current to the buck-boost converter is discontinuous which differs to that of boost converter. Following this observation, this section explores the features associated with this discontinuity in relation to impedance extraction and the associated switching harmonics that it possesses.

8.2 Buck-boost open loop experimental results

The buck-boost converter was tested in an open loop, and its results are presented in the sections that follow. Since the input current of the buck-boost converter is discontinuous, it is analysed differently from the inductor current which is continuous.

8.2.1 Buck-boost converters DC-DC power open loop results without the emulated fuel cell system

The buck-boost converter was tested in open loop, and the results were measured with the designed parameters from the simulation and the designed controller.

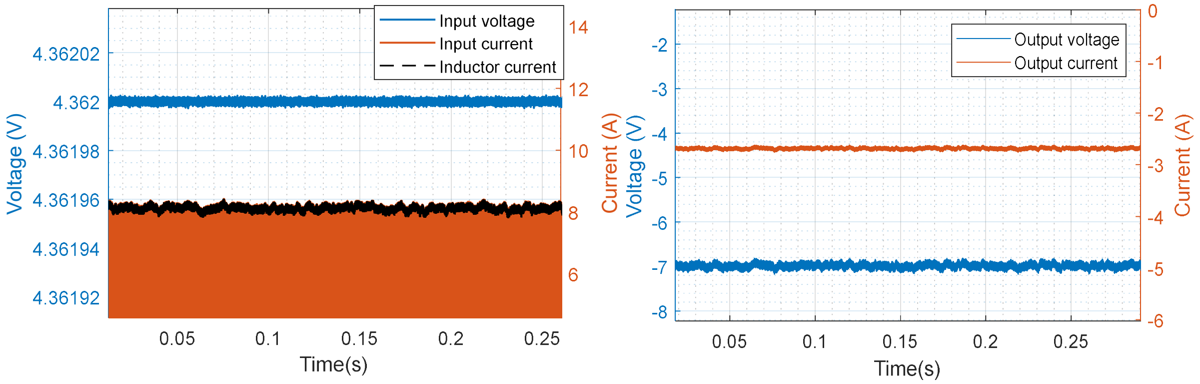

(a) (b)

Fig. 8.1: measured signals (a) Input current, voltage, and inductor current of the buck-boost converter and (b) the output voltage and output current for the buck-boost converter.

Fig. 8.1(a) shows the converters values when the converter is sourced from the DC power supply. The DC power supply voltage value fluctuates due to the input current being discontinuous, as a result, a decoupling capacitor was added to stabilise the DC power supply voltage. The inductor current is continuous whilst the input current varies from zero to the inductor current value. Fig. 8.1(b) shows the output voltage and current being negative as this is an inverting buck-boost converter. These values are shown in Table 8-1 in comparison to the simulation values.

Table 8-1: Buck-boost converters experimental values

Converter parameter	$V_{in}(V)$	I_{in}(A)	I_L(A)	P_{in}(W)	V_{out} (V)	I_{out}(A)	P_{out}(W)
Simulation values	4.5	6.7	10	30.15	9	3.35	30.15
Actual values	4.362	5.092	7.9	22.21	7.03	2.7	18.9

The buck-boost converter voltage gain is 1.61, and the power efficiency in relation to the simulated results is 62.6%. Table 8-2 shows the buck-boost converter results when the duty cycle of the converter is varied. Table 8-2 shows that as the duty cycle is increased from 0.3 to 0.8 the input current can reach 17 A, and the output voltage can increase up to 9.2 V.The input voltage as the duty cycle is increase it drops up to 3.9 V. This is as a result of the diode and MOSFET switch voltage drop, and the wiring losses.

Table 8-2: boost converters varied duty cycle for DC power supply

$Duty\ cycle$	$V_{in}(V)$	$I_{in}(A)$	I_L(A)	$P_{in}(W)$	$V_{out}(V)$	I_{out}(A)	$P_{out}(W)$
0.3	4.48	$8.03e-1$	1.19	3.597	1.508	$5.64e-1$	0.850
0.4	4.413	1.531	2.29	6.756	2.53	$9.412e-1$	2.38
0.5	4.392	2.735	4.08	12.01	3.66	1.365	7.147
0.6	4.354	4.91	7.32	21.38	5.23	1.953	10.21
0.7	4.267	9.017	13.45	38.48	7.254	2.71	19.65
0.8	3.905	17.26	25.76	67.4	9.282	3.44	33.8

8.2.2 Buck-boost converter DC-DC open loop results with an emulated fuel cell system

The emulated fuel cell system was then connected to the buck-boost converter, whereby the results will be presented and discussed. The input and output voltages exhibited a behaviour similar to the boost converter experimental results.

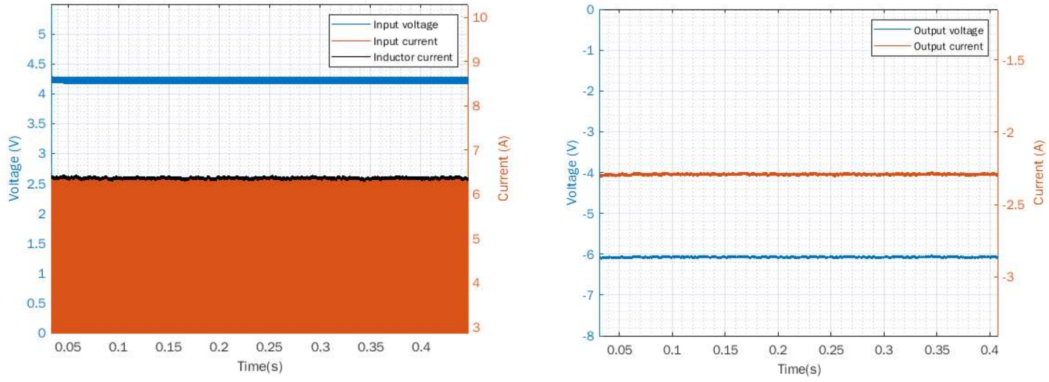

(a) (b)

Fig. 8.2: Buck-boost converter's (a) input voltage, current and inductor current (b)output voltage and output current.

Fig. 8.2(a) shows the inductor current at $6.2A$, and the input voltage varying between zero and the inductor current level. Fig. 8.2(b) shows the inverted output current and voltage, and this voltage was different from section Fig. 8.1(b) as this had decreased in magnitude from -7.9 to $-6.27V$. The power efficiency of the buck-boost converters was not like one of the boost converters, this might be due to the switching losses, also the two converters were not designed to deliver the same amount of power, rather they were designed to deliver the same input current and output voltage hence the difference in power performance characteristics.

Table 8-3: Buck-boost converters experimental values

Converter parameter	$V_{in}(V)$	I_{in}(A)	I_L(A)	P_{in}(W)	V_{out} (V)	I_{out}(A)	P_{out}(W)
Simulation values	4.5	6.7	10	30.15	9	3.35	30.15
Actual values	4.12	4.36	6.2	17.93	6.27	2.23	13.9

Table 8-4: buck-boost converters varied duty cycle for emulated fuel cell system

Duty cycle	$V_{in}(V)$	I_{in}(A)	I_L(A)	$P_{in}(W)$	$V_{out}(V)$	I_{out}(A)	$P_{out}(W)$
0.3	4.46	0.68	1.02	3.03	1.49	$7.12e-1$	1.07
0.4	4.40	1.25	1.88	5.53	2.41	1.08	2.62
0.5	4.32	2.1	3.14	9.09	3.57	1.58	5.63
0.6	4.21	3.74	5.58	15.74	4.66	2.32	10.81
0.7	3.94	6.75	10.08	26.61	6.20	3.03	18.78
0.8	3.66	12.66	18.90	46.35	8.88	3.79	33.63
0.9	2.33	21.9	32.69	51.03	9.03	3.24	29.26

The buck-boost only boosts when the duty cycle is greater than 0.5. For values less than 0.5, the output voltage was reduced. Due to the losses and voltage drops across the diode and MOSFET, the voltage for a duty cycle less than 0.3 was very small, and as a result was not recorded. For a duty cycle greater than

0.8, the input inductor current was greater than 25A, as such the buck-boost was used for a short period at a duty cycle of 0.9, which was beyond the maximum current of the conductors used, as described in the hardware setup chapter. Table 8-4 shows that the voltage reaches an output voltage of 9 V, for a duty cycle closer to 0.9. The input current of 10A was found at a duty cycle closer to 0.7, consequently the converter with the given performance, shows the feasibility of reaching the desired characteristic with proper control.

8.2.3 Buck-boost converter DC-DC open loop EIS results without the emulated fuel cell system

The buck-boost converter was then tested with the perturbation of the EIS signal. This was done when the source was the DC power supply and when the source was the emulated fuel cell system.

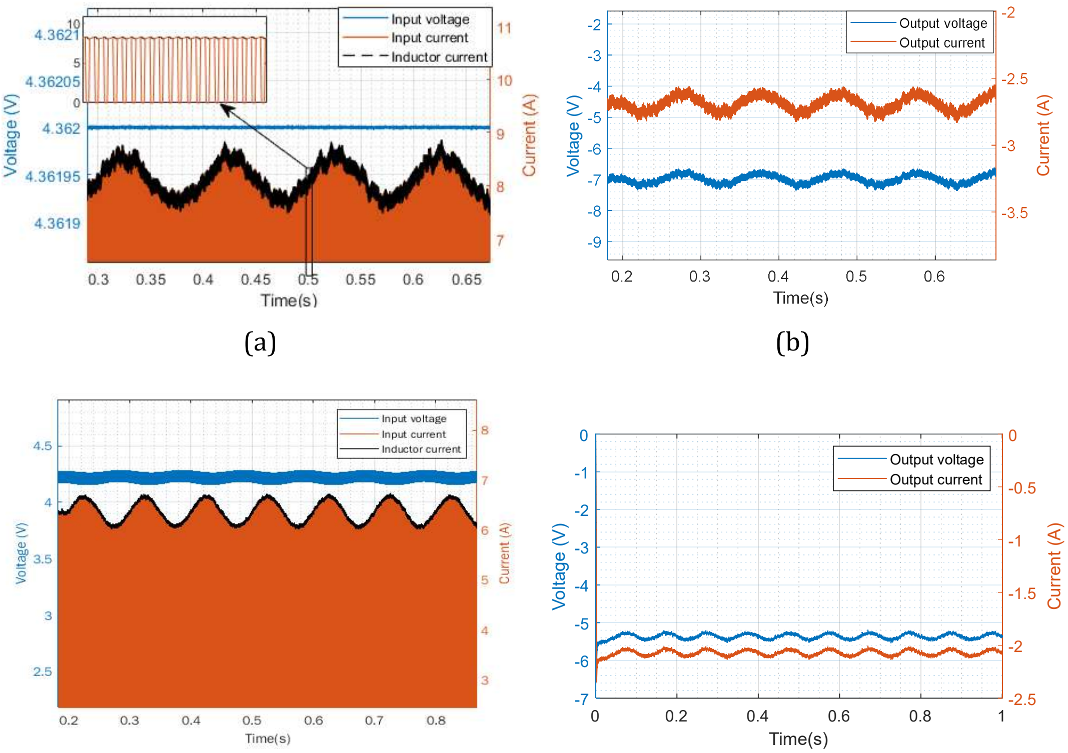

(a) (b)

(c) (d)

Fig. 8.3: Buck-boost converter's (a) Input current, voltage, and inductor current of the buck-boost converter (b) the output voltage and output current

Fig. 8.3(a) shows the input voltage, input current and inductor current. This was magnified to show the discontinuous nature of the input current, which was different from the boost converter, whereby the input current and the inductor current were the same. Fig. 8.3(b) shows the output voltage and current with the inverted signals, and in contrast to the input voltage being discontinuous, the output current and voltage were continuous. Fig. 8.3(c) shows the input results for buck-boost converter when the source was the emulated fuel cell system. There was a higher input voltage drop across the fuel cell system, this was as expected in comparison to the simulation results in section 5.5. In Fig. 8.3(d) the output voltage and current were lower in comparison to Fig. 8.3(b); this was as expected from observation in the simulation in section 5.5, due to the internal impedance brought by the emulated fuel cell system, and as such the EIS amplitude was not 1A as designed, which further signals the need for control.

8.2.4 Buck-boost converter DC-DC open loop PRBS results with and without the emulated fuel cell system

The buck-boost converter was tested with and without the emulated fuel cell, with the perturbation signal being the PRBS signal.

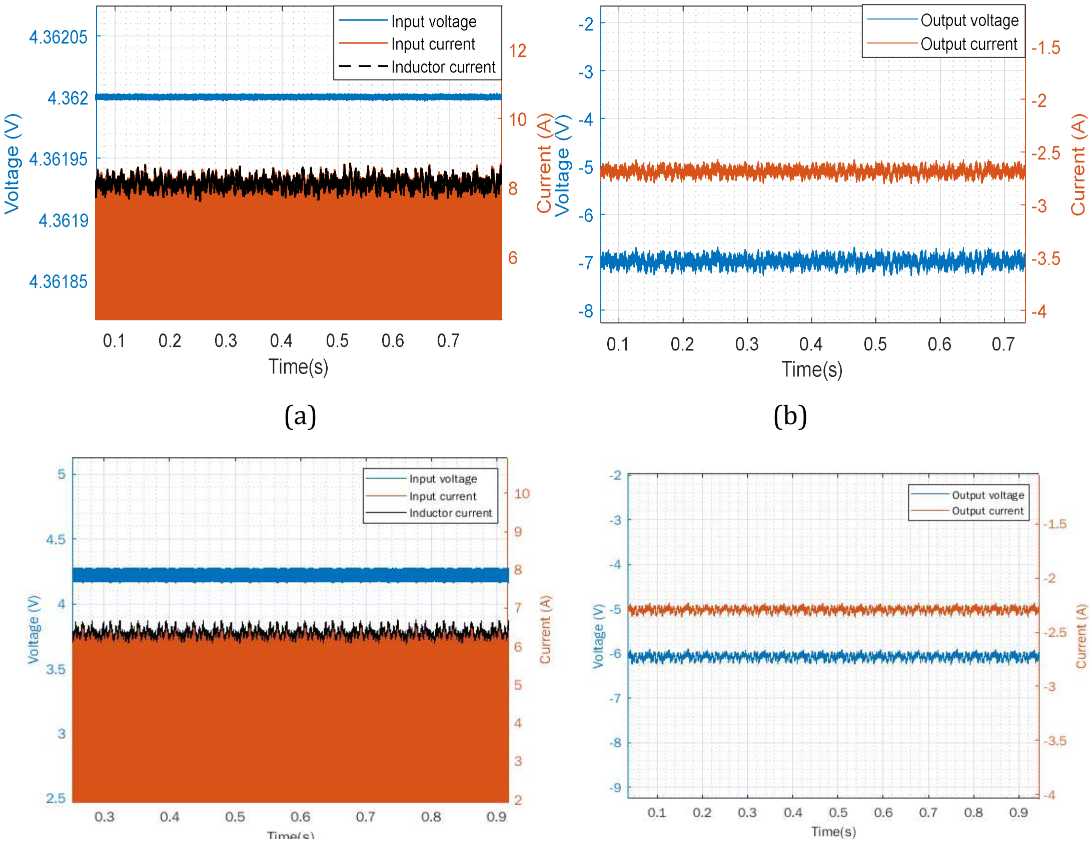

(a) (b)

(c) (d)

Fig. 8.4: buck-boost converter's (a) Input current, voltage, and inductor current of the buck-boost converter (b) the output voltage and output current

Fig. 8.4(a) and Fig. 8.4(b) show the open loop PRBS injection input and output signals respectively without the emulated fuel cell system. Fig. 8.4(c) shows the PRBS injection input signals and Fig. 8.4(d) shows the open loop PRBS injection output signals with an emulated fuel cell system. Similar to the simulation results in section 5.5, the experimental results were shown for the PRBS injection, and similar characteristics to the EIS perturbation were observed. The duty cycle equation derived in the simulation results section seems to be ineffective for open-loop injection, and as a result, the next section proposes and employs the closed-loop injection.

8.3 Buck-boost converter closed-loop experimental results

8.3.1 Buck-boost converter DC-DC closed loop with and without an emulated fuel cell system EIS injection

This section shows the input and output voltages and currents when the EIS signal is injected into the fuel cell system and DC power supply. The buck-boost converter was tested with the double loop control configuration as done for the boost converter.

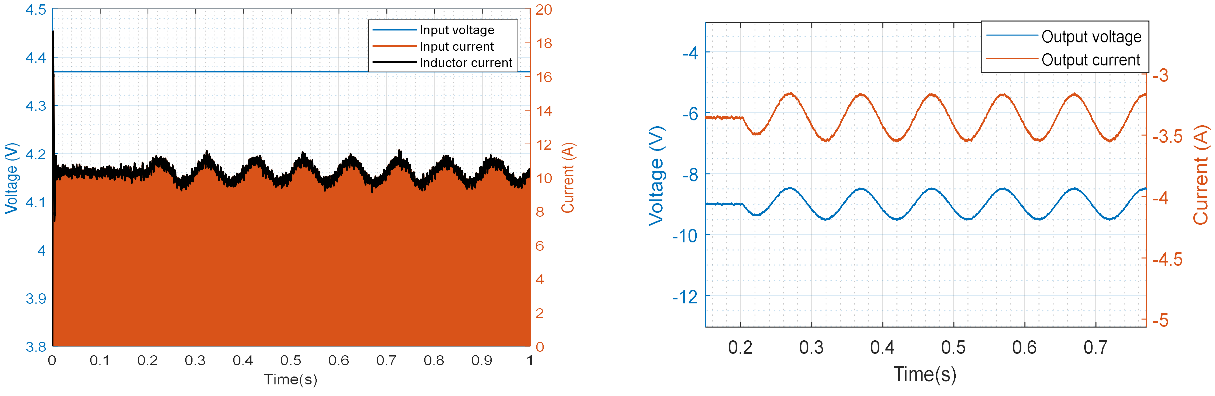

(a) (b)

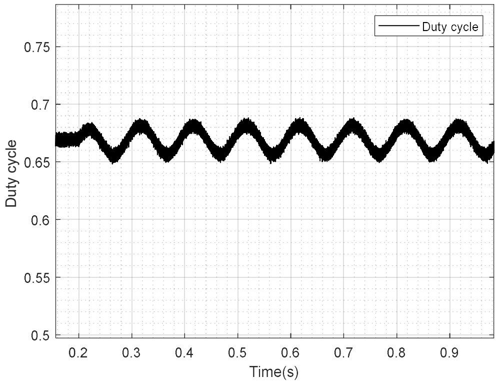

(c)

Fig. 8.5: Buck-boost converter's (a) Input current, voltage, and inductor current (b) the output voltage and output current (c) control duty cycle

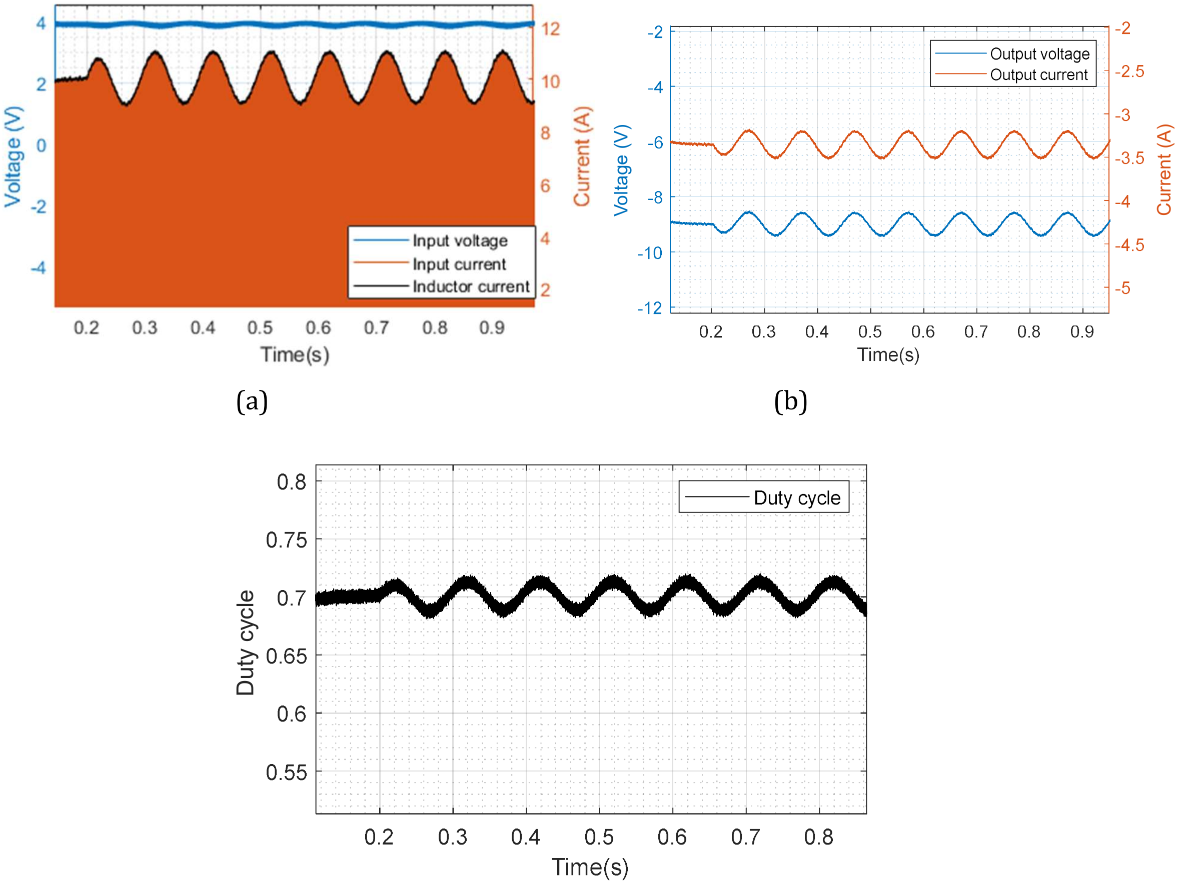

(a)

(b)

(c)

Fig. 8.6: buck-boost converter's (a) Input current, voltage, and inductor current (b) the output voltage and output current (c) control duty cycle

Fig. 8.5 and Fig 8.6 shows the results for the two cases when the converter is EIS perturbed from a DC source and Randle's circuit. The converter is controlled, and the EIS signal is perturbed 0.2 seconds after the signals have reached a steady state, the control meets the desired condition of a DC inductor input current of $10A$, with an AC perturbed signal, with an amplitude of $1A$, and the capacitor output voltage of $9V$ for both cases. The only difference being the decrease in input DC voltage from when the DC power supply was replaced with the emulated Randle circuit.

Fig. 8.6 (c) shows that the duty cycle varied between 0.66 and 0.74 which was different from Fig. 8.5 (c) where the duty cycle varied from 0.65 to 0.68.

8.3.2 Buck-boost converter DC-DC closed loop without and with an emulated fuel cell system with PRBS injection

The double loop control of the boost converter was also tested with the PRBS signal, for a buck-boost converter as in Section 7.2.1 and the signals were measured and presented by Fig. 8.7 and Fig. 8.8.

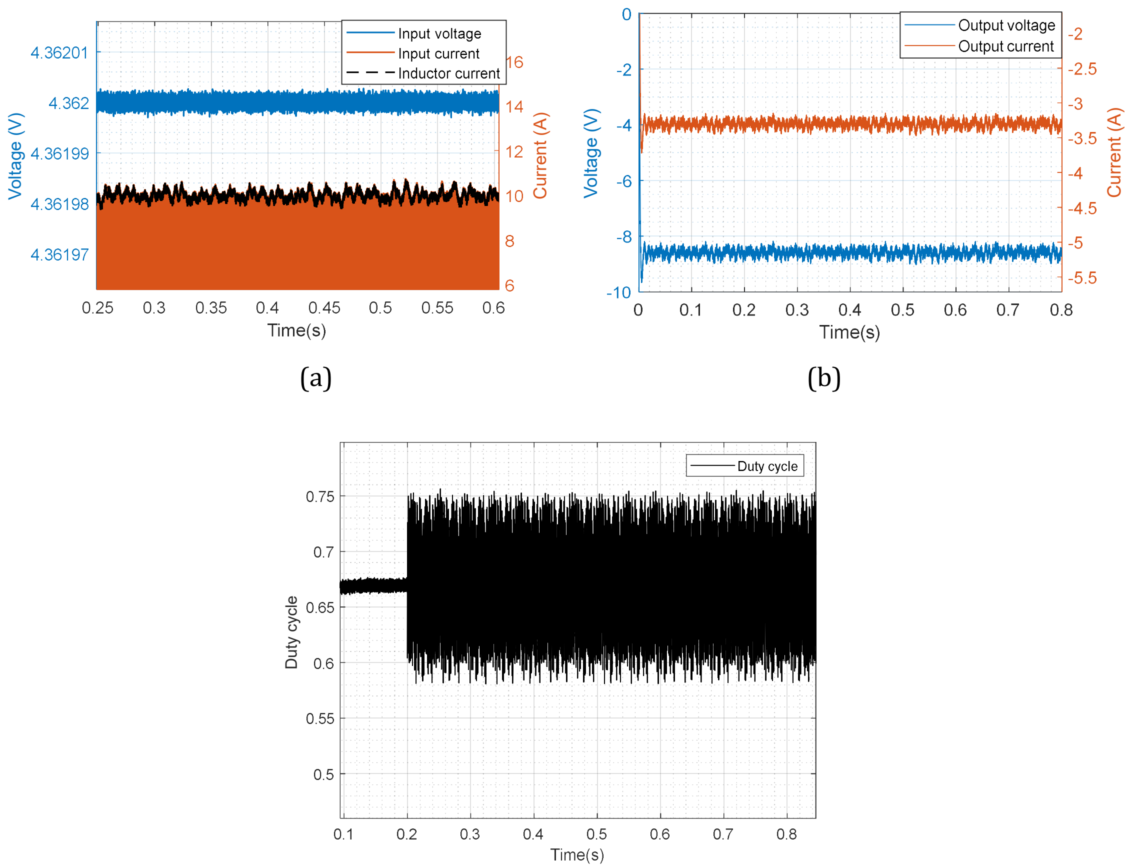

(a) (b)

(c)

Fig. 8.7: buck-boost converter's (a) Input current, voltage, and inductor current (b) the output voltage and output current (c) duty cycle

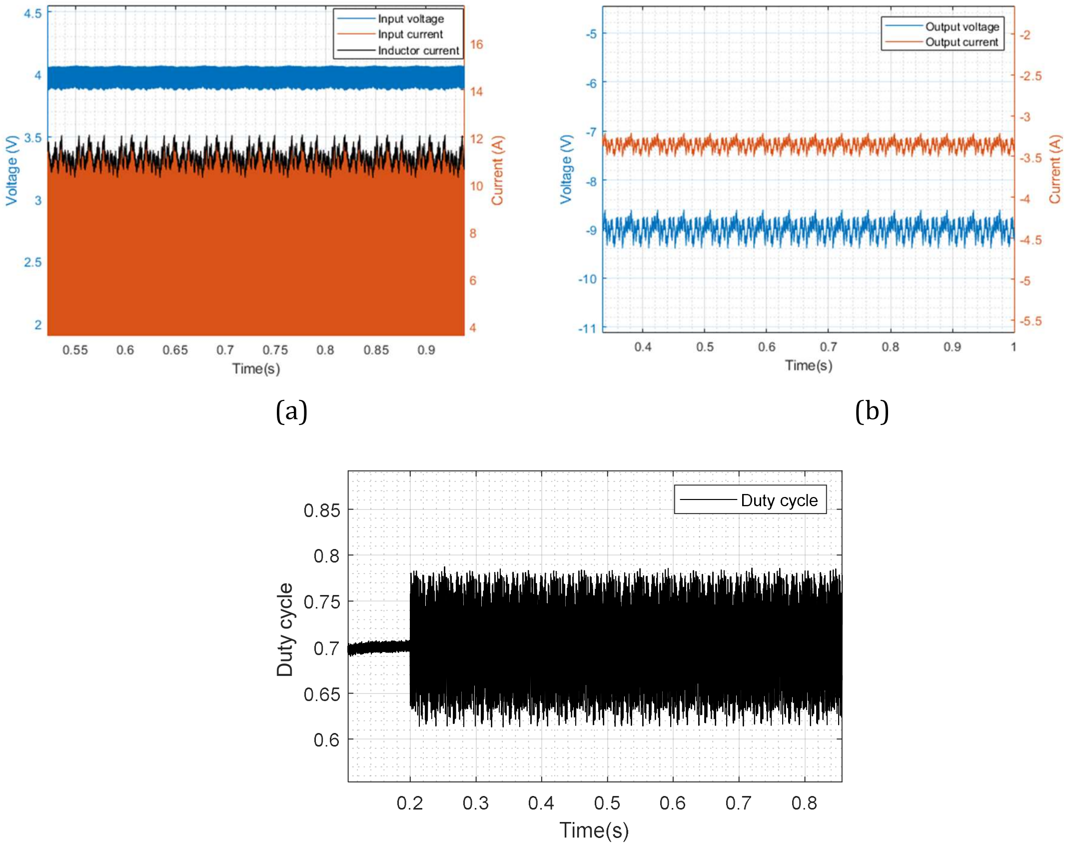

(a) (b)

(c)

Fig. 8.8: buck-boost converter's (a) Input current, voltage, and inductor current (b) the output voltage and output current (c) duty cycle

The converter was tested with the perturbed PRBS signal when sourced from a DC source in Fig. 8.7 and when sourced from the emulated fuel cell system in Fig. 8.8. The PRBS in both scenarios was injected at a time stamp of 0.2 seconds once the converter system has settled. Similar to Section 7.2.1 the input DC voltage dropped from 4.36V in Fig. 7.8(a) to 4.1 V in Fig. 7.8 (a), and this does not affect the PRBS amplitude signal of 1A. Both the DC and AC controlled signals met the desired specifications, and the signal processing for impedance estimation was done from these measured controlled signals, whereby the impedance estimation results are present in Fig. 8.9.

8.4 Buck-boost converter impedance results

The impedance extraction was then performed for the EIS and PRBS signals in closed loop control. Similar to the boost converter, the impedance estimation was done for the three operating conditions, and the respective Nyquist plots are described in Fig. 8.9.

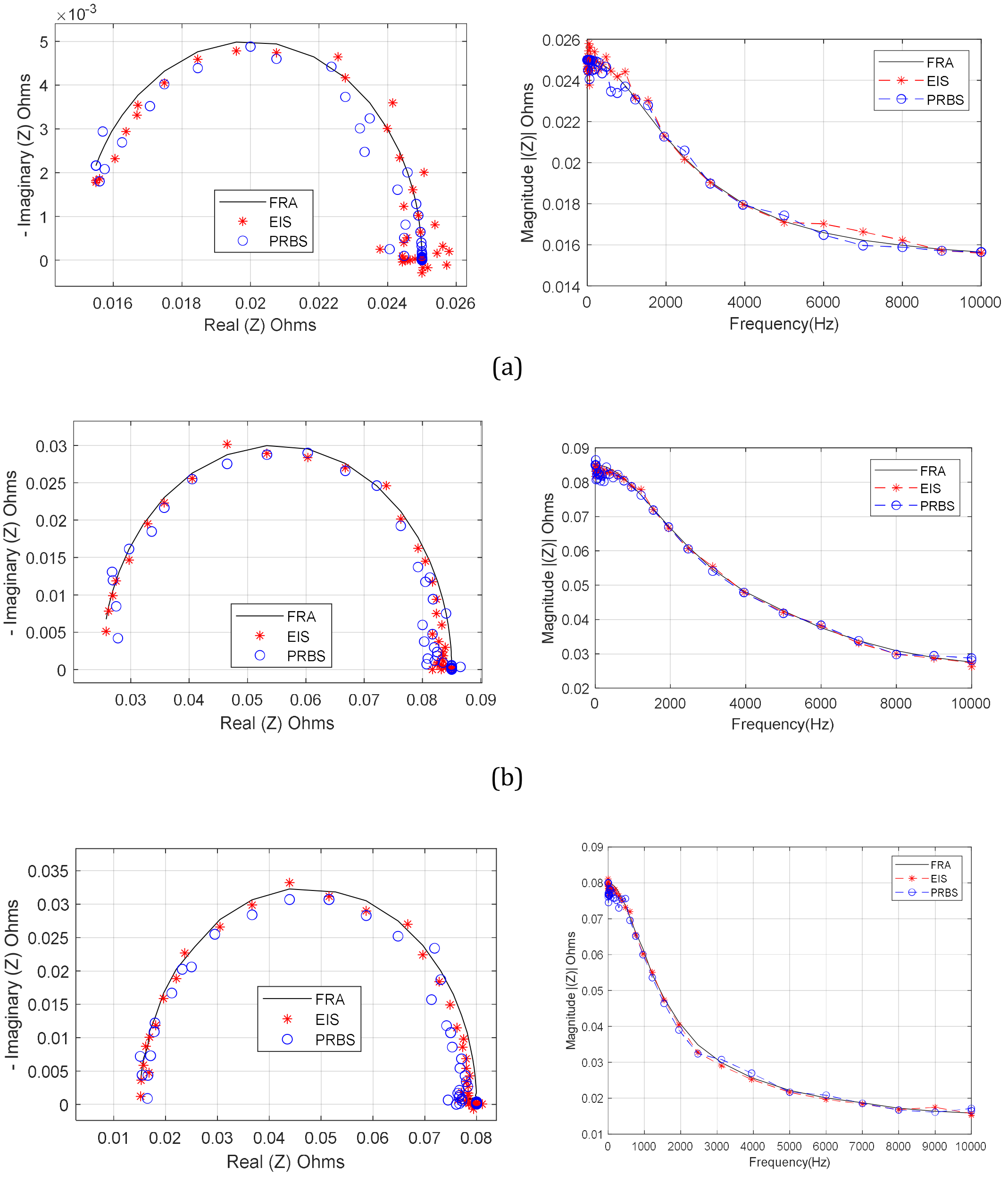

(a)

(b)

(c)

Fig. 8.9: Fuel Cell impedance estimation (a) normal conditions (b) drying (c) flooding.

Fig. 8.9(a) shows the difference in the impedance estimated between FRA, EIS and PRBS results. This variation is more comparable to the boost converters variations. It was expected that the buck-boost converter switching harmonics would compromise the efficacy of the PRBS signal when using the buck-boost converter in comparison to the boost converter. The variations between FRA, EIS and PRBS in Fig. 8.9 (b) and Fig. 8.9(c) are minimal compared to Fig. 8.9(a). The maximum errors for each operating condition are shown in Table 8-5.

Table 8-5: Impedance maximum estimation error of EIS and PRBS against FRA results

Condition	EIS maximum percentage error	PRBS maximum percentage error
Normal	3.07	4.76
Drying	6.82	5.82
Flooding	6.36	7.93

As in the boost converter, the estimation time associated with PRBS was less compared to EIS (where it takes five times longer to perform EIS). Fig. 8.10 shows the Nyquist trace lines for each operating condition. The buck-boost converter PRBS results had a higher maximum error value compared to the EIS signal.

Table 8-6: Impedance average estimation error of EIS and PRBS against FRA results

Condition	EIS average percentage error	PRBS average percentage error
Normal	1.03	0.59
Drying	1.15	1.47
Flooding	1.61	2.7

Table 8-6 shows the average error results for the buck-boost converter, with all the percentage errors being below 5%. The buck-boost converter PRBS results were expected to be lower compared to those obtained by the EIS signal. This was expected since the buck-boost converter has discontinuous input current, which can easily emulate the varying square wave nature of the PRBS signal. However only the normal operating condition was lower, else for the other operating conditions, the PRBS was lower than the EIS. The buck-boost converters discontinuity was shown to increase the error in comparison to the boost converter, which corresponds to the maximum error results in Table 8-5.

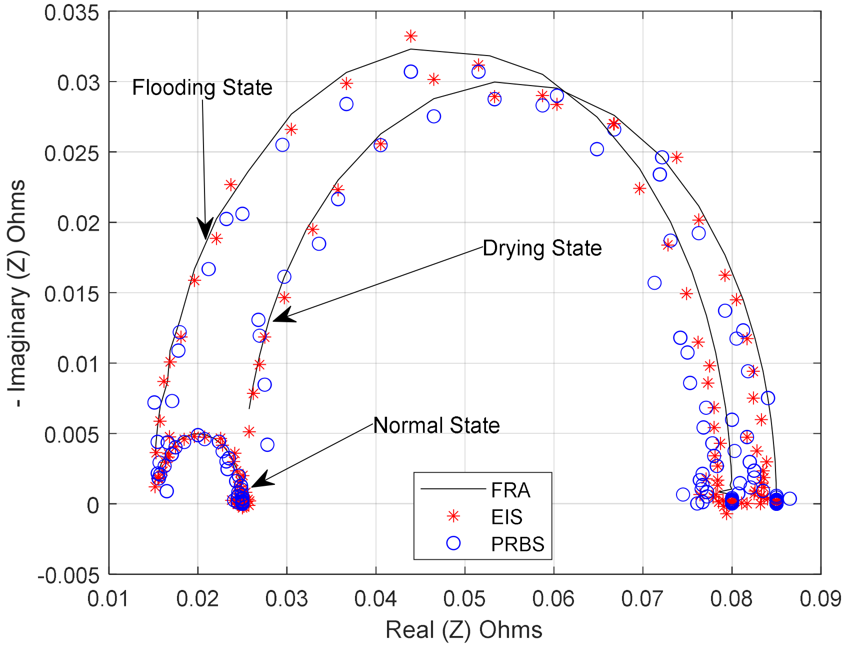

Fig. 8.10: Fuel Cell impedance estimation according to different internal water conditions

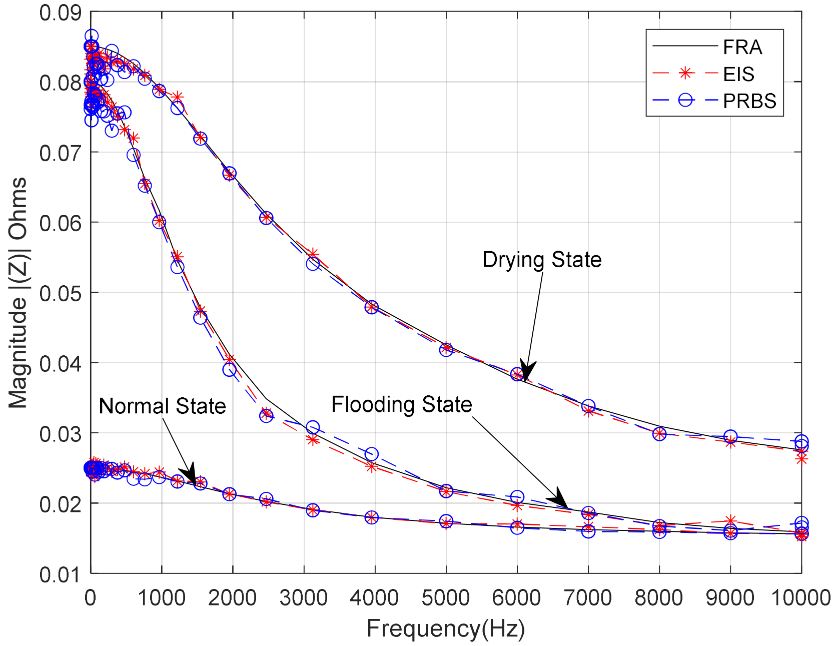

Fig. 8.11: Fuel Cell impedance estimation according to different internal water conditions-Magnitude

Fig. 8.11 shows the magnitude of the impedance for the different internal water internal conditions depicted by the Randle circuit. These plots were similar to those plotted for the simulation results.

8.5 Conclusions

This section presented the open loop-, the closed loop-experimental results and impedance estimation results when the converter is biased (as designed in chapter 4 when simulated). The format used, in the simulation of the buck-boost converter was followed in this section, and it was investigated whether the switching harmonics and discontinuous nature of the buck-boost converter input current would contribute to the efficiency of the PRBS signal when using the buck-boost converter in comparison to the boost converter. However, it was observed that there was no advantage brought about by the harmonics and discontinuous input current, given the procedure used in the dissertation.

Chapter 9

Boost and buck-boost converter comparison

9.1 Simulation comparisons between boost and buck-boost

This section outlines the comparison of the impedance results and error analysis of each converter when performing IS through EIS and PRBS. These simulation results were obtained using MATLAB and Simulink with the design and simulation of each DC-DC converter system and interface with the fuel cell system described in the simulations of the boost and buck-boost chapter.

9.1.1 Impedance results

Each operating condition was set up, and both the boost and buck-boost converter were connected to the set up, operating condition Randle circuit, and both the EIS and PRBS signal were injected.

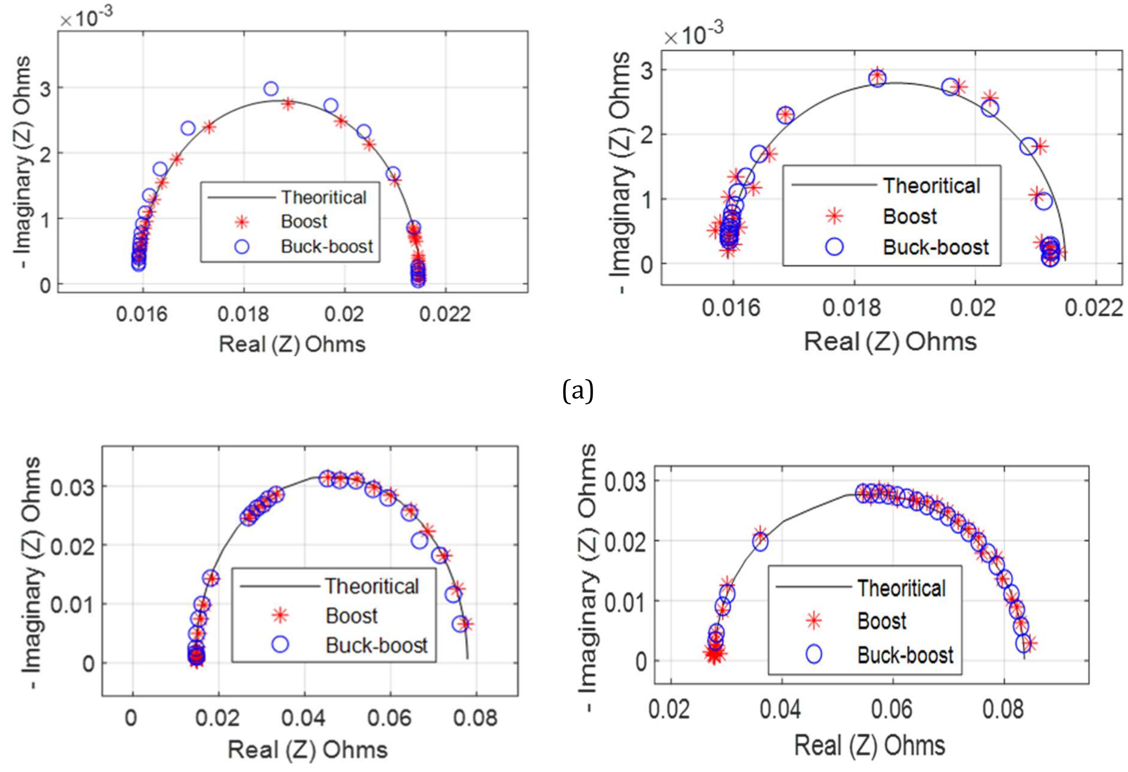

(a)

(b)

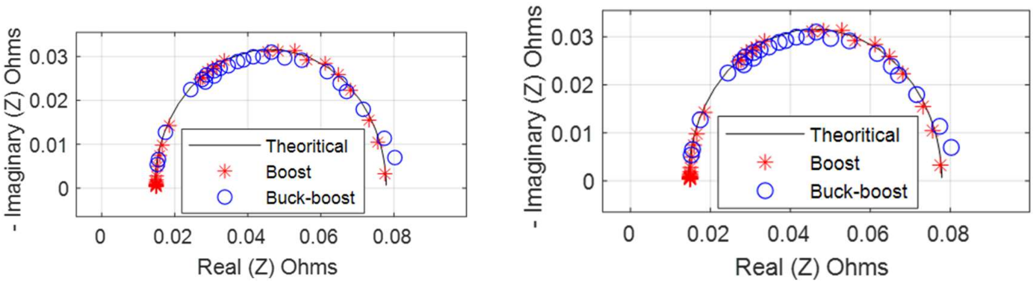

(c)

Fig. 9.1: Fuel Cell impedance estimation using EIS (left) and PRBS(right) (a) normal conditions (b) drying (c) flooding

Fig. 9.1 (a), (b) and (c)-left shows the Nyquist plot for the single sinusoid method, where both the buck-boost and boost converter results adequately estimate the theoretical results using EIS. Both the converters adequately estimated the theoretical results, however for the flooding condition, the buck-boost converter had a greater deviation for lower frequencies. This could be attributed to the discontinuous nature of the buck-boost converter. The buck-boost converters input current varied from 10 A to 0 A, and this contradicts with the Kramer's Kronings condition. The results used are feasible when using an emulated fuel cell system, which consists of passive components that do not change their behaviour with drastic current change. Fig. 9.1 (a), (b) and (c)-right shows the Nyquist plot for impedance estimation of the fuel cell. However, the boost converter results were closer to the theoretical results compared to those of the buck-boost converter, this was observed more in the normal and flooding operation, even though the buck-boost converters input current was discontinuous, as opposed to the continuous input current of the boost converter, where the input current was the same as the inductor current.

9.1.2 Error analysis

The maximum error for the estimated impedance is present in Table 9-1, when using the EIS signal.

Table 9-1: Impedance estimation error of EIS against the theoretical results

Condition	Buck-boost converter maximum percentage error	Boost converter maximum percentage error
Normal	1.7	0.5
Drying	1.2	1.5
Flooding	1	0.6

Table 9-1 shows that the boost converter had a lower estimation deviation than the buck-boost converter. The buck-boost converter was expected to have higher errors towards the lower frequencies spectrum, however, the maximum error was found towards the center of the spectrum; this was attributed to the filtering capability of the converter. Table 9-2 shows the impedance estimation error when a PRBS signal is used.

Table 9-2: Impedance estimation error of PRBS against the theoretical results

Condition	Buck-boost converter maximum percentage error	Boost converter maximum percentage error
Normal	1.7	2
Drying	1.9	1.5
Flooding	1	2.2

Corresponding to the Nyquist impedance plots, the normal and flooding state of the fuel cell when perturbed with a PRBS signal was greater when compared to the EIS errors, and this was observed more towards the lower frequencies.

9.2 Experimental comparisons between boost and buck-boost

This section presents the comparison of the buck-boost converter and the boost converter impedance estimation results when using the EIS and PRBS signals, respectively. These results were obtained using the same procedure as described in the hardware setup section, which was subsequently used in the boost and buck-boost experimental results section.

9.2.1 Impedance results

Each operating condition was set up, and both the boost and buck-boost converter were connected to the set up operating condition Randle circuit, and both the EIS and PRBS signal were perturbed.

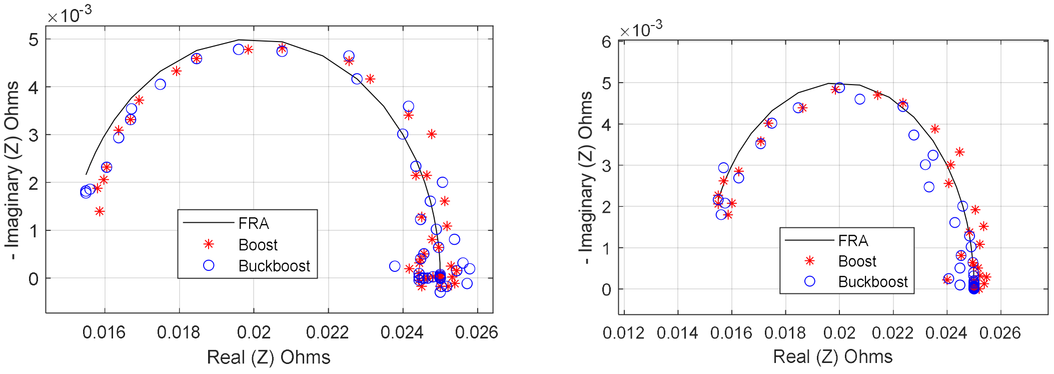

(a)

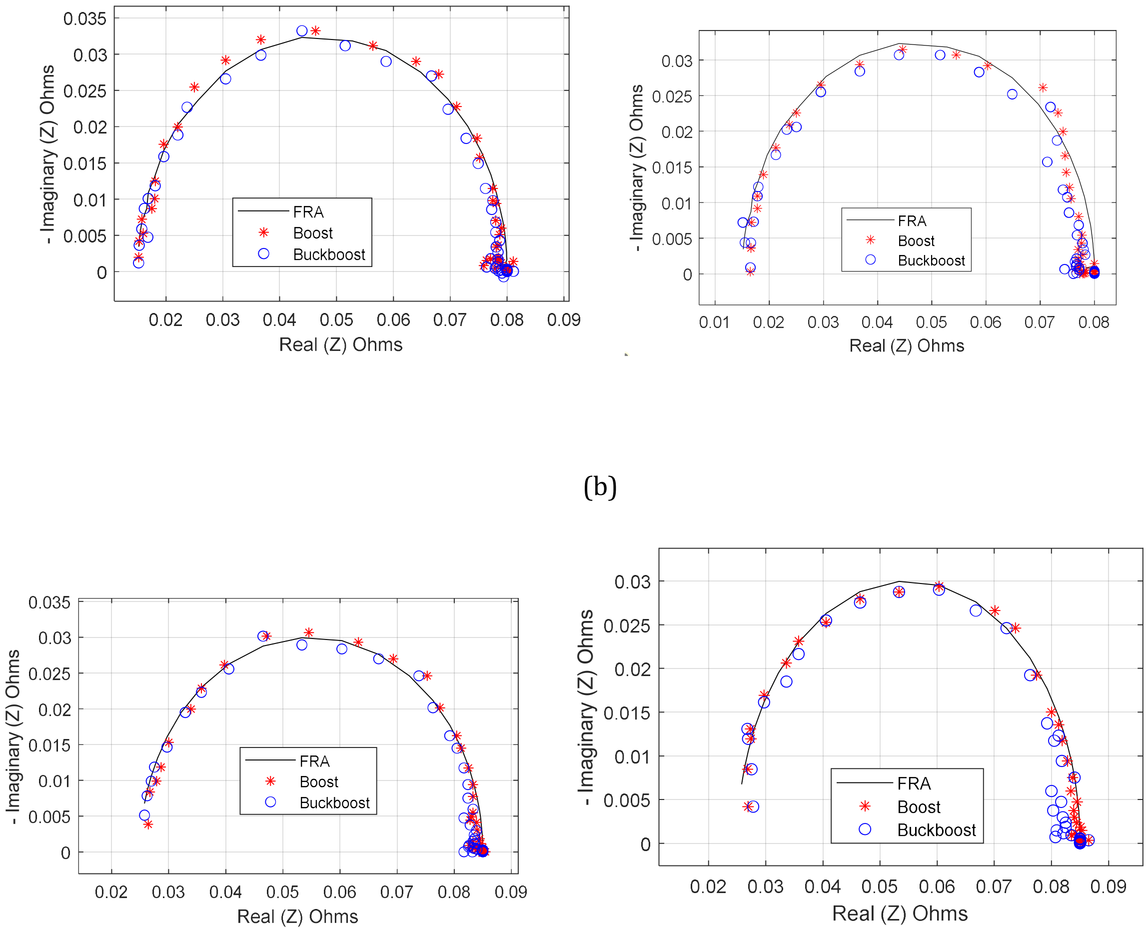

(b)

(c)

Fig. 9.2 :Fuel Cell impedance estimation using EIS (left) and PRBS (right) (a) normal conditions (b) flooding (c) drying

The figures on the left of Fig. 9.2 shows Nyquist impedance plot for the EIS signal, whilst the figures on the right are for the PRBS signal; both for the boost and buck-boost converters. Both adequately estimate the Frequency Response Analyzer results when using PRBS and EIS signal. However, there was no directly measured impact brought about by the discontinuous nature of the buck-boost converter when using PRBS, as the switching harmonics were expected to be higher. Since low pass filters were used, it is deduced that their impact may be adequately suppressed, which is not typical in applications with high measurement sensitivity.

9.2.2 Error analysis

Impedance estimation error of PRBS against FRA results the maximum error for impedance estimation when using the EIS signal is presented in Table 9-3 below.

Table 9-3: Impedance maximum estimation error of EIS against FRA results

Condition	Buck-boost converter maximum percentage error	Boost converter maximum percentage error
Normal	3.65	3.07
Drying	4.51	6.82
Flooding	6.19	6.36

The maximum errors were mostly observed at the lower frequency spectrum. Many frequency points were used to resemble the full semi-circle as the FRA results. Even though the buck-boost converter had a discontinuous input current, the estimated impedance was very similar to the FRA results.

Table 9-4: Impedance maximum estimation error of PRBS against FRA results

Condition	Buck-boost converter maximum percentage error	Boost converter maximum percentage error
Normal	4.95	4.76
Drying	4.71	5.58
Flooding	7.26	7.93

The maximum error for impedance estimation when using the PRBS signal is presented in Table 9-4. The maximum errors were mostly observed at the lower frequency spectrum.

Table 9-5: Impedance average estimation error of EIS against FRA results

Condition	Buck-boost converter average percentage error	Boost converter average percentage error
Normal	1.03	1.157
Drying	1.15	1.07
Flooding	1.61	1.71

Table 9-6: Impedance average estimation error of EIS against FRA results

Condition	Buck-boost converter average percentage error	Boost converter average percentage error
Normal	0.59	0.85
Drying	1.47	0.79
Flooding	2.7	2.85

Table 9-6 shows the average error results for the two converters; this shows that the average impedance error was less than 5 %.

9.3 Conclusions

This section presented the comparisons of the two converters when performing impedance spectroscopy for each signal i.e., EIS and PRBS. It was noted that the discontinuous nature of the buck-boost converter does not contribute towards impedance spectroscopy, mostly when using the PRBS signal (which was also continuous), rather it affects the linearity of the source fuel cell. This was minimised on the emulated fuel cell system since it was emulated using passive components, that a drastic change in their drawn current does not instantly change their impedance information.

Chapter 10

Closure

10.1 Conclusions

As a result of the discussions in the previous sections, the following conclusions were drawn.

10.1.1 Satisfactory use of the emulated PEMFC system as the device under test

Given that the PEMFC system was emulated. The impedance estimation results achieved were satisfactory due to that, the impedance estimation results acquired from the FRA using the emulated Randle circuit fuel cell system corresponded to the theoretical and simulation estimated impedance results. Even though they were slight deviations between the FRA results and simulation results, this was expected as the passive resistors and capacitors have a tolerance associated with them. In addition, the connecting wires have non-negligible equivalent series impedance.

10.1.2 Satisfactory use of impedance spectroscopy as a characterization technique

Impedance spectroscopy as a characterization technique is efficient, and this was shown by the Nyquist plot and magnitude plot of the impedance estimated results. The magnitude plot can distinguish between the three water internal conditions i.e., normal, drying and flooding condition. This was deduced by looking at the magnitudes of the plots at the boundaries of the bandwidth (i.e. start and end frequency), whereby the magnitudes of the Nyquist plot converge to a certain predetermine benchmark value.

10.1.3 Single sinusoid signal as an analogue broadband excitation signal

The single sinusoid technique had been used as an injection technique; however, it was further explored and used to perform impedance spectroscopy on both the boost and buck-boost converter. It was used in both the boost and buck-boost converter where the converter specifications (the input/inductor current, input voltage and output voltage) are similar in order to compare the accuracy of these two converter topologies when utilising this converter. The signal gave satisfactory results closer to the FRA bench result, which was within a reasonable range.

10.1.4 Pseudo-Random Binary Sequence signal adequate use as a digital excitation signal

The PRBS signal was chosen for investigation due to its binary digital nature. It was as explored, as this signal has the potential of being generated by a low-cost micro-controller. The use of the signal comes with the advantage of reducing the impedance estimation time of the single sinusoid injection to at least a quarter. The PRBS signal was satisfactory in performing Impedance spectroscopy for the two converter topologies as the estimated impedance results obtained were close to the FRA benchmark results.

10.1.5 Satisfactory use of the buck-boost converter as an excitation source

The buck-boost converter was considered as an excitation source; due to that, some applications require both stepping up and stepping down. In addition, it was chosen for investigation due to the input current of the converter being discontinuous and as such, resembled a digital signal and its induced switching harmonics. The effects of this discontinuous input current and voltage were investigated to determine how they affect impedance analysis when operated with a PRBS signal (which is a binary digital signal).

As such, it was observed that the switching harmonics associated with this signal were minimised when impedance analysis was performed, as adequate filtering of the signal was done before being sampled. The discontinuous nature of the input current of the buck-boost converter was affecting the power supply to the extent that a decoupling capacitor was introduced at the input (i.e. the output of the power supply), given the non-linearity of a fuel cell system. The use of this converter topology is not recommended. However, given that this study was done using passive components, which are not affected by the discontinuity of the current drawn through it, the results obtained using this converter was satisfactory and within a range close to the results obtained using the boost converter.

10.1.6 Satisfactory use of the boost converter as an excitation source

The boost converter was chosen for its continuous input current and boosting nature as it is commonly used in PEMFC systems applications. The closed loop boost converter experimental results were satisfactory, as the signal was within the defined specifications, and the impedance estimated results were within a reasonable range.

10.1.7 Satisfactory double nested loop performance

A double loop strategy was proposed and presented for the two DC-DC converter topologies, i.e., boost and buck-boost converter. The double loop control strategy was used to facilitate the power transfer for the converters at steady-state and to achieve the implementation of Impedance spectroscopy using the two signals of analysis (EIS and PRBS). The double loop strategy performed well in these two conditions (during power transfer and Impedance spectroscopy implementation). The two converter's open loop results were presented whilst performing power transfer only, thereafter when performing Impedance spectroscopy (for when the emulated PEMFC system was connected and not connected to the converters). The open-loop experimental results showed the associated voltage drops on the input voltage, input current, output voltage and output current. In addition, the open-loop experimental results showed that the design specifications were not met in this configuration, resulting in the need for closed-loop control. Both the simulation and experimental results in a closed loop showed that the design specification at steady-state error were met, and the specified range bounded output voltage was met within the set range of specifications.

10.1.8 Digital signal processing of impedance information

The signal acquired from the two converters, i.e., the boost and buck-boost converter, were analysed using the Fast Fourier Transform (FFT). The FFT was satisfactory in obtaining the impedance information, as this was first done in simulations, and the results were similar to the theoretical results. When done using the experimental signals, the results were satisfactory when compared to the FRA benchmark results. The signal used for analysis was first filtered and then analysed, and there were minor deviations due to the equivalent series resistor in connecting wires and some noise within the analysed bandwidth, however, the deviations were within a reasonable range of less than 10%.

10.1.9 Online condition monitoring system

This work proposed the use of DC-DC converter topologies for power transfer and online condition monitoring of a fuel cell system. The converters were modelled by their average linearized small-signal model. The proposed scheme was implemented in simulation and practical experimentation to verify its feasibility and suitability for EIS and PRBS implementation, then compared to the theoretical results. Thereafter the experimental results were compared to the FRA results. The results for both PRBS and EIS are close approximations to the theoretical results using the two converter topologies along with the experimental results to the FRA results, and this shows the practical application in condition monitoring. The buck-boost converter switching harmonics and discontinuity when performing online condition monitoring was observed to have minimal impact on the estimated impedance with adequate filtering.

The buck-boost converter's discontinuous current was observed to have some effect when performing online condition monitoring through impedance spectroscopy, this is because it affects the Kramer Kronig's requirement, and this is suspected of having a negative influence when applied on a practical non-linear system.

10.2 Recommendations

Based on the conclusions drawn, the following conclusions are deduced for future work.

10.2.1 Input voltage

The input voltage of 4.5 V was easily affected by the MOSFET, diode voltage drops, and the equivalent series resistor found within the connecting wires. As such, to emulate a PEMFC system with a higher power rating and output voltage of the PEMFC, depending on the availability of the impedance information and overplorization voltage curve (if both information is available), a PEMFC system with a higher input voltage would be ideal.

10.2.2 Inclusion of capacitance equivalent series resistance in converter modelling and design

The consideration of capacitive equivalent series resistances and equivalent series resistance of the inductor and conducting wires is recommended to get a better intuition in the expected power losses and voltage gain at the output of the converters. The experimental results showed that the knowledge of the switching frequencies alone is not sufficient to account for the power losses observed at the output of the two converters.

10.2.3 Converter construction

Building the circuit on PCB has the advantage of reducing the power losses associated with the connecting wires, and this can assist in improving the efficiency of the converter topology. However, this depends on the budget of the project - and having the passive components be used in advance will aid with the design, as this will allow the designer to design the PCB such that the components with different physical dimensions can be easily soldered without any modification or mistakes. The current capability of the PCB should be considered as well, as fuel cell systems draw large currents.

10.2.4 Converter control strategy

The implementation of a PI/lead-lag compensator can be further expanded by using the QFT to control the converter topology to achieve the set specifications. Any advanced technique used is recommended-depending on the skills of the designer. The designed controller should be able to use the double loop strategy (or a strategy that controls both the input and output of the converter) for more than one operating point of the converter. This would be advantageous in industrial applications as there is more than one operating point required, as some systems are used in extreme varying ambient conditions.

10.2.5 Cuk converter investigation when performing impedance spectroscopy

Given that the Cuk converter can be regarded as a buck-boost converter with a low ripple current, that is continuous, the analysis of this converter using the double-loop strategy is recommended, as the input current is not discontinuous. Consequently, when sourced to a non-linear source such as a PEMFC system, the effect of the converter on the linearity will be minimised. The consideration of this converter will only introduce complexity when finding the small-signal linearized equations, as it has more than one capacitor and inductor. However, the control will be similar to the one used for the boost and buck-boost converter.

10.2.6 Practical use of a PEMFC

An emulated fuel cell system using Randle’s circuit was used, and this was due to there was no access to the chemical engineering laboratory due to the pandemic. As such, it is recommended to use a practical fuel cell system to measure the effects the of the two converters on the fuel cell system, mostly the buck-boost converter since it has a discontinuous input current that may affect the linearity of the fuel cell system, thereafter, measure how the impedance estimation measures between an emulated fuel cell system and a practical one.

References

[1] J. H. P. van der Merwe, “Characterisation of a proton exchange membrane electrolyser using electrochemical impedance spectroscopy,” North-West University, Potchefstroom Campus, 2012.

[2] IEA, “The Future of Hydrogen,” 2019.

[3] M. H. a. T. A. O. Bethoux, “A new on-line state-of-health monitoring technique dedicated to PEM fuel cell,” in *2009 35th Annual Conference of IEEE Industrial Electronics*, Porto, 2009.

[4] A. J. Bard and L. R. Faulkner, Electrochemical Methods Fundamentals and Applications, vol. 2nd ed, John Wiley & Sons, Inc, 2001.

[5] J. Zhang, PEM Fuel Cell Electrocatalysts and Catalyst Layers Fundamentals and, Springer, 2008.

[6] F. A. Aroge, “Impedance Spectroscopy Techniques for Condition Monitoring of Polymer Electrolyte Membrane Fuel Cells,” OpenUCT, 2018.

[7] Y. -z. Yuan, H. Wang, C. Song and J. Zhang, Electrochemical Impedance spectroscopy in PEM Fuel Cells, Springer, 2010.

[8] C. A. Martinson, “Characterisation of proton exhcange membrane electrolyser using the current interrupt method,” North-West University, Potchefstroom, 2012.

[9] R. O'HAYRE, C. SUK-WON, W. SUK-WON and F. B. PRINZ, FUEL CELL FUNDAMENTALS, 3rd ed., WILEY, 2016.

[10] F. A. AROGE and P. S. Barendse, “Impedance Spectroscopy Techniques for Condition Monitoring of Polymer Electrolyte Membrane Fuel Cells,” OpenUCT, Cape Town, 2018.

[11] J. H. Wee, “Applications of proton exchange membrane fuel cell systems,” *Renew. Sustain. Energy Rev,* vol. 11(18), pp. 1720-1738, 2006.

[12] “PEM Fuel Cells: Theory and Practice,” *Academic Press,* 2012.

[13] R. Koch and A. Jossen, “Impedance Spectroscopy for Battery Monitoring with Switched Mode Amplifiers,” in *16th International Power Electronics and Motion Control Conference and Exposition* , Antalya,Turkey, 2014.

[14] W. Huang and J. A. A. Qahouq, “An Online Battery Impedance Measurement Method Using DC–DC Power Converter Control,” *IEEE TRANSACTIONS ON INDUSTRIAL ELECTRONICS,* vol. 61, no. 11, pp. 5987-5995, 2014.

[15] S. Moore, “Online Condition Monitoring of Lithium Ion Batteries by Performing Impedance Spectroscopy Using a DC-DC Converter,” OpenUCT, Cape Town, 2018.

[16] A. Waligo and P. Barendse, “A Comparison of the Different Broadband Impedance Measurement Techniques for Lithium-Ion Batteries,” Cape Town, 2016.

[17] C. d. Beer, P. S. Barendse and P. Pillay, “Fuel Cell Condition Monitoring Using Optimized Broadband Impedance Spectroscopy,” *IEEE TRANSACTIONS ON INDUSTRIAL ELECTRONICS,,* vol. 62, no. 8, pp. 5306- 5316, 2015.

[18] N. Mohan, W. Undeland and W. P. Robbins, Power Electronics,Converters,Applications,andDesign, John Wiley & Sons, INC, 2003.

[19] Z. Liao and X. Ruan, “Control Strategy of Bi-directional DC-DC Converter for a Novel Stand-alone Photovoltaic Power System,” in *IEEE Vehicle Power and Propulsion Conference (VPPC)*, Harbin, China, 2008.

[20] R. W. Erickson, “DC-DC Power Converters”.*Wiley Encyclopedia of Electrical and Electronics Engineering.*

[21] K. Ogata, Modern Control Engineering, Pearson.

[22] M. Braae, Control Theory for Electrical Engineers, Cape Town: UCT Press, 1994.

[23] K. Ogata, Modern Control Engineering, New Jersey: Prentice Hall, 2010.

[24] F. G. Franklin, D. J. Powell and A. Emami-Naeini, Feedback Control of DynamicSystems, Prentice Hall, 2002.

[25] N. S. Nise, Control Systems Engineering, Wiley, 2015.

[26] D. Shin, S. Yoo and Y.-H. Lee, “On-line Water Contents Diagnosis of PEMFC Based on Measurements,” *International Journal of Precision Engineering and Manufacturing-Green Technology ,* pp. 1085-1093, 2020.

[27] M. S. B. Yahia , H. Allagui and A. Mami, “The Identification of Randles Impedance Model Parameters of a PEM Fuel Cell by the Least Square Method,” *International Journal of Advanced Computer Science and Applications,* vol. 8, no. 8, pp. 345-354, 2017.

[28] S. Mahlangu and P. Barendse, “Online Condition Monitoring of Fuel Cells (FC) by Implementing Electrical Impedance Spectroscopy using a Switch-Mode DC-DC Converter,” in *2021 IEEE Energy Conversion Congress and Exposition (ECCE)*, Vancouver, 2021.

[29] M. S. A.-I. S. S. K. K. Daniel-Ioan Stroe, “Generalized Characterization Methodology for Performance Modelling of Lithium-Ion Batteries,” *MDPI Batteries,* vol. 2, no. 37, 2016.

[30] D. A. Howey, V. Y. Paul D.Mitcheson, G. K.Offer and N. P.Brandon, “Online Measurement of Battery Impedance Using Motor Controller Excitation,” *IEEE Transactions on vehicular technology,* vol. 63, no. 6, pp. 2557-2566, 2014.

[31] R. Nazer, V.Cattin, P.Granjon, M. Montaru and M. Ranieri, “Broadband Identification of Battery Electrical Impedance for HEVs,” *IEEE Transactions on vehicular technology,* vol. 62, no. 7, pp. 2896-2905, 2013.

[32]] R. Klein et al,, “ "Electrochemical model based observer design for a lithium-ion battery,",” *IEEE Trans. Control Syst. Technol,* Vols. 289-301, p. 21, 2013.

[33] A.J. Fairweather et al, ““Battery parameter identification with Pseudo Random Binary Sequence excitation (PRBS)",” *Journal of Power Sources ,* vol. 196, p. 9398– 9406, 2011.

[34] R. Koch and A. Jossen,, ““Impedance Spectroscopy for Battery Monitoring with Switched Mode Amplifiers,”,” *in 16th International Power Electronics and Motion Control Antalya,Turkey,,* 2014.

[35] Gamry, ““Basics of Electrochemical Impedance Spectroscopy,”,” Gamry Instruments, [Online]. Available: https://www.gamry.com/application-notes/EIS/basics-ofelectrochemical-impedance-spectroscopy/. . [Accessed July 2019].

[36] D. Depernet, O. Ba and A. Berthon, ““Online impedance spectroscopy of lead acid batteries for storage management of a standalone power plant,”,” *Journal of Power Sources ,* vol. 219, pp. 65-74,, 2012.

[37] J. Giner-Sanz and V. P.-H. E.M. Ortega,, “Optimization of the Perturbation Amplitude for Impedance Measurements in a Commerical PEM Fuel Cell Using Total Harmonic Distortion,”,” *Fuel Cells,* vol. 16, no. 4, pp. 469-479, 2016.

[38] C. d. Beer, P. S. Barendse and P. Pillay, ““Fuel Cell Condition Monitoring Using Optimized Broadband Impedance Spectroscopy,”,” *IEEE TRANSACTIONS ON INDUSTRIAL ELECTRONICS,* vol. 62, no. 8, pp. 5306- 5316, 2015.

[39] W. Huang and J. A. A. Qahouq , ““An Online Battery Impedance Measurement Method Using DC–DC Power Converter Control,”,” *IEEE TRANSACTIONS ON INDUSTRIAL ELECTRONICS,* vol. 61, no. 11, pp. 5987-5995, 2014.

[40] D. Depernet, O. Ba and A. Berthon,, ““Online impedance spectroscopy of lead acid batteries for storage management of a standalone power plant,”,” *Journal of Power Sources,* vol. 219, pp. 65-74, 2012.

[41] D. A. Howey, V. Y. Paul D.Mitcheson et al, “"Online Measurement of Battery Impedance Using Motor Controller Excitation,”,” *IEEE Transactions on vehicular technology,* vol. 63, no. 6, pp. 2557-2566, 2014.

[42] H. M. Mahery and E. Babaei, “Mathematical modeling of buck–boost dc–dc converter and investigation,” *Electrical Power and Energy Systems,* vol. 44, pp. 949-963, 2013.

[43] S. Moore and P. Barendse, “Online Condition Monitoring of Lithium ion Batteries by Performing Impedance Spectroscopy Using a DC-DC Converter,” OpenUCT, Cape Town, 2018.

[44] H. AbdEl-Gawad and V. Sood, “Small-Signal Analysis of Boost Converter, including Parasitics, operating in CCM,” in *2014 6th IEEE Power India International Conference (PIICON)*, Delhi, 2014.

[45] O. Alao and P. Barendse, “Online condition monitoring of Lithium-ion and Lead acid batteries for renewable energy applications,” OpenUCT, Cape Town, 2018.

[46] N. Mohan, T. M. UNDELAND and W. P. ROBBINS , Power Electronics.Converters ,Applications,and Design, NEW YORK: John Wiley & Sons, INC, 2003.

[47] G. N. Love, “Small signal modelling of power electronic converters, for the study of time-domain waveforms, harmonic domain spectra, and control interactions,” University of Canterbury,, Christchurch, New Zealand., 2007.

[48] M. S. Hassan and A. A. Elbaset, “Small-Signal MATLAB/Simulink Model of DC-DC Buck Converter using State-Space Averaging Method,” in *17th International Middle-East Power System Conferennce (MEPCON'15)*, Mansoura, 2015.

[49] C. Fleischer, W. Waag, H.-M. Heyn and D. U. Sauer, “On-line adaptive battery impedance parameter and state estimation considering physical principles in reduced order equivalent circuit battery models: Part 1. Requirements, critical review of methods and modeling,,” *Journal of Power Sources,* vol. 260, pp. 276-291, 2014.

[50] T.-T. Nguyen, V.-L. Tran and W. Choi, “Development of the intelligent charger with battery State-Of-Health estimation using online impedance spectroscopy,” in *2014 IEEE 23rd International Symposium on Industrial Electronics (ISIE)*, Istanbul, 2014.

[51] N. Fouquet, C. Doulet, G. Dauphin-Tanguy and B. Ould-Bouamama, “Model based PEM fuel cell state-of-health monitoring via ac impedance measurements,” *Journal of Power Sources 159,* pp. 905-913, 2006.

[52] C. Fu, “Digitally Controlled Average Current,” ARIZONA STATE UNIVERSITY, ARIZONA, 2011.

[53] Y. Y. Phyo and T. L. Naing, “Implementation the Average Input Current Mode Control of Tw0-Phase Interleaved Boost Converter Using Low-Cost Microcontroller,” *World Academy of Science, Engineering and Technology, Internaltional Journal of Electronics and Communication Engineering,* vol. 12, no. 10, 2018.

[54] K.-T. Wan, “Advanced current-mode control techniques for DC-DC power electronic converters,” Missouri University of Science and Technology, 2009.

[55] D. K. Saini, “True-Average Current-Mode Control of DC-DC Power Converters: Analysis, Design, and Characterization,” Wright State University, 2018.

[56] Metrohm Autolab , ““NOVA Autolab User Manual."”.

[57] Auto lab Application Note BAT01, , ““High Voltage Measurements: Characterization of NiMH Batteries with Autolab PGSTAT302N in Combination with Voltage Multiplier,”,” Metrohm Autolab B.V.

[58] Thurlby Thandar Instruments Ltd, “QPX1200 DC power supply”.

[59] T. INSTRUMENTS, “Using the UCC21520EVM-286, UCC20520EVM-286,UCC21521CEVM-286, and UCC21530EVM-286,” TEXASN INSTRUMENTS, 2019.

[60] J. Karki, “Active Low-Pass Filter Design,” Texas Instruments- AAP precision Anlag, Dallas, Texas, 2002.

[61] T. L. Floyd, Electronic Devices Conventinal Current Version, Ninh Edition ed., Pearson.

[62] P. Horowitz and W. Hill, THE ART OF ELECTRONICS, 3rd ed., Cambridge University Press, 2015.

[63] National Instruments, “NI 6366 X series data acquisition,” National Instruments.

[64] J. D. Kramer and C. Jacky, “How to write biblos,” vol. 1, no. 1, 2006.

[65] H.-S. Park, M.-h. Shin, T.-H. Eom, C.-Y. Won, S.-D. Kang and T.-H. Min, “A development of the detection unit of Fuel cell impedance,” in *2017 IEEE 3rd International Future Energy Electronics Conference and ECCE Asia (IFEEC 2017 - ECCE Asia),*, Kaohsiung, 2017.

[66] A. Debenjak, J. Petrovcic, P. Boskoski, B. Musizza and D. Juricic, “Fuel Cell Condition Monitoring System Based on Interconnected DC-DC Converter and Voltage Monitor,” *IEEE Transactions on Industrial Electronics,* vol. 62, no. 8, pp. 5293-5305, 2015.

[67] J. Karki, “Analysis of the Sallen-Key Architecture,” July 2002. [Online]. Available: http://www.ti.com.cn/cn/lit/an/sloa024b/sloa024b.pdf. [Accessed 3 December 2017].

[68] N. A. Chaturvedi et al, “ "Algorithms for advanced battery-management systems,",” *IEEE Control Systems,* vol. 30, pp. 49-68,, 2010.

[69] M. Chen and G. A. Rincon-Mora, “ "Accurate electrical battery model capable of predicting,” " *IEEE Trans. Energy Convers,* vol. 21, pp. 504-511, 2006.

[70] M. Pedram and Q. Wu,, “ "Design considerations for battery-powered electronics,",” *in Proceedings of the 36th Annual ACM/IEEE Design Automation Conference,,* pp. 861-866., 1999.

[71] C. Chiasserini and R. R. Rao, “ "Energy efficient battery management,",” *IEEE J. Select. Areas Commun,* vol. 19, pp. 1235-1245, 2001.

[72] D. Andre et al, “ "Characterization of high-power lithium-ion batteries by electrochemical impedance spectroscopy. II: Modelling,",” *J. Power Sources,* Vols. 196,(12), pp. 5349-5356.

[73] M. Charkhgard and M. Farrokhi, “"State-of-charge estimation for lithium-ion batteries using neural networks and EKF,",” *IEEE Trans. Ind. Electron,* Vols. vol. 57, (12), , pp. 4178-4187, 2010.

[74] H. He, R. Xiong and J. Fan, , “"Evaluation of lithium-ion battery equivalent circuit models for state of charge estimation by an experimental approach,",” *Energies,* Vols. vol. 4, (4), pp. 582-598, 2011.

[75] Yu, J, “Health Degradation Detection and Monitoring of Lithium-Ion Battery Based on Adaptive Learning Method,” *IEEE Journals & Magazine.*

[76] D. A. Jäger-Waldau, “‘Importance of operating & maintenance costs (OMCs) relative to overall cost and other cost drivers for PV plants,” in *Conférence Technical Programme Chairman*.

[77] I. E. Agency, “SNAPSHOT OF THE GLOBAL PV MARKETS IN 2019,” INTERNATIONAL ENERGY AGENCY PHOTOVOLTAIC POWER SYSTEMS PROGRAMME, 2019.

[78] D. Depernet, O. Ba and A. Berthon, “Online impedance spectroscopy of lead acid batteries for storage management of a standalone power plant,” *Journal of Power Sources,* vol. 219, pp. 65-74, 2012.

Appendices

Appendix A Tables

Table 10-1: Fuel cell stack specifications

Description	Specification
Type of stack	$PEMFC$
Membrane electrode assembly	$Gore\ MEA(M815)$
Active area	$25\ cm^2$
Open-circuit voltage	$4.5\ V$
Quantity of cells	5
Power bandwidth	$0\ W - 75\ W$
Maximum current density	$1\ A/cm^2$

Table 10-2: perturbated frequencies, associated periods and sampling frequencies

Frequency Point	Frequency (Hz)	Cycle Count	Sample Frequency (Hz)	Time(s)
1	10000	100	100000	0.010
2	9999	98	99990	0.010
3	9000	96	90000	0.011
4	8000	94	80000	0.012
5	7000	92	70000	0.013
6	6000	90	60000	0.015
7	5000	88	50000	0.018
8	3952	86	39520	0.022
9	3123.7	84	31237	0.027
10	2469	82	24690	0.033
11	1951.5	80	19515	0.041
12	1542.5	78	15425	0.051
13	1219.2	76	12192	0.062
14	963.63	74	9636.3	0.077
15	761.65	72	7616.5	0.095
16	602.01	70	6020.1	0.116
17	475.83	68	4758.3	0.143
18	376.1	66	3761	0.175
19	297.27	64	2972.7	0.215
20	234.96	62	2349.6	0.264
21	185.72	60	1857.2	0.323
22	146.79	58	1467.9	0.395
23	116.02	56	1160.2	0.483
24	91.705	54	917.05	0.589
25	72.484	52	724.84	0.717
26	57.292	50	572.92	0.873
27	45.283	48	452.83	1.060
28	35.792	46	357.92	1.285
29	28.29	44	282.9	1.555
30	22.361	42	223.61	1.878
31	17.674	40	176.74	2.263
32	13.97	38	139.7	2.720
33	11.042	36	110.42	3.260
34	8.7273	34	87.273	3.896
35	6.8981	32	68.981	4.639
36	5.4523	30	54.523	5.502
37	4.3095	28	43.095	6.497
38	3.4062	26	34.062	7.633
39	2.6923	24	26.923	8.914
40	2.128	22	21.28	10.338
41	1.682	20	16.82	11.891
42	1.3294	18	13.294	13.540
43	1.0508	16	10.508	15.226
44	0.83055	14	8.3055	16.856
45	0.65647	12	6.5647	18.280
46	0.51887	10	5.1887	19.273
47	0.41012	8	4.1012	19.506
48	0.32416	6	3.2416	18.509
49	0.25622	4	2.5622	15.612
50	0.20251	2	2.0251	9.876
Total time(s)				224.800

Appendix B Simulation results of electrochemical impedance spectroscopy

This section entails the simulation of Electrochemical Impendence Spectroscopy, and a simplified Randle circuit shown in Fig. 10.1 below is used to model the fuel cell Impedance as in [10].

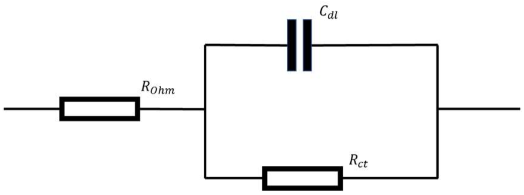

Fig. 10.1: Simplified Randle circuit

And the Randle circuit parameters are as shown in Table 10-3 below.

Parameter	Value
R_{ohm}	0.5 Ω
R_{ct}	4.7 Ω
C_{dl}	2.2uF

Table 10-3:The Randle circuit parameters

Three sets of EIS results obtained in different settings are presented in this section, these are:

- The theoretical impedance of the Randle circuit(calculated).
- Randle circuit Impedance results were obtained using an electronic load, which draws current from the Randle model.

The procedure used to obtain these three sets of results is also going to be used in practical implementation. The Theoretical results will act as the benchmark test, and in practical application, these results correspond to the Frequency Response Analyzer (FRA) results, the frequency Response Analyzer (FRA) is reliable and gives the most accurate results, since it performs advanced Fourier transform.

Then the simulation results obtained from the electronic load correspond to the practical results which will be obtained using a Practical Programmable electronic Load. The purpose of including the electronic load results is to act as a filter (intermediate stage) to show the deviations introduced by the computation of impedance results using the Fast Fourier Transform.

B.1 Theoretical results

The Theoretical results were computed using the derived equation below,

$$Z_{total} = R_{ohm} + \frac{R_{ct}}{1 + 2\pi f R_{ct} C_{dl}} \tag{10-1}$$

Where f is the frequency investigated in the fuel cell, which is varied. These results are plotted in a Nyquist plot shown below.

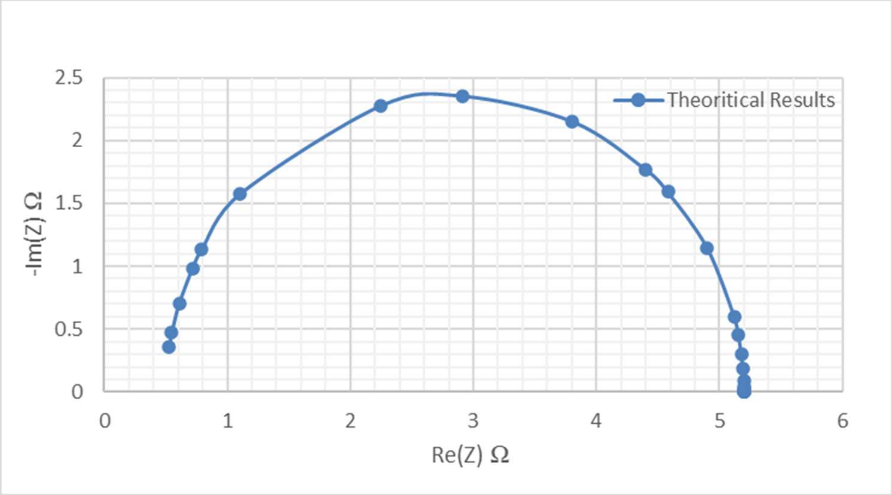

Fig. 10.2:Nyquist of the Randle circuit

When resistor R_{ohm} in the Randle, the circuit is short-circuited. The new Nyquist plot is shown in Fig. 10.3 below.

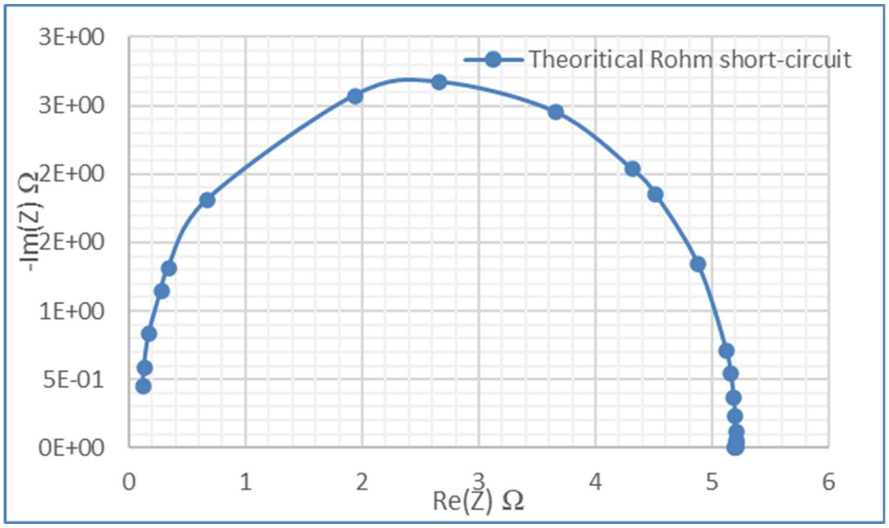

Fig. 10.3:Rohm short-circuited (Theoretical)

The Short-circuited R_{ohm} the Nyquist plot is like the complete simplified Randle circuit however it is only shifted to the left.

B.2 Electronic load results

The EIS results were obtained using the circuit shown in Fig. 10.4 below.

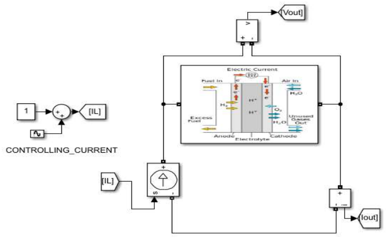

Fig. 10.4:Electronic load configuration

The fuel cell model is perturbated with a DC-biased current of 1A, and different signals of different frequencies are to be added to the DC. A design decision had to be made, regarding the number of periods of each frequency to perturb the fuel cell and the magnitude of the AC sinusoidal amplitude which were to be used.

The design considerations are that when many cycles of each sinusoidal signal were to be used, the trade-off would be that the whole EIS process would take a longer. Moreover, a selection of the appropriate AC sinusoidal amplitude is required. In the practical sense, the fuel cell needs to be operated in a linear region and drawing large amplitude AC Sinusoidal Currents may discharge the fuel cell at a faster rate. The first investigation performed was to inject the Randle circuit with an AC sinusoidal signal of Amplitude 0.05A, With the second case having double the number of cycles as the first signal. The resulting Nyquist plot is shown below.

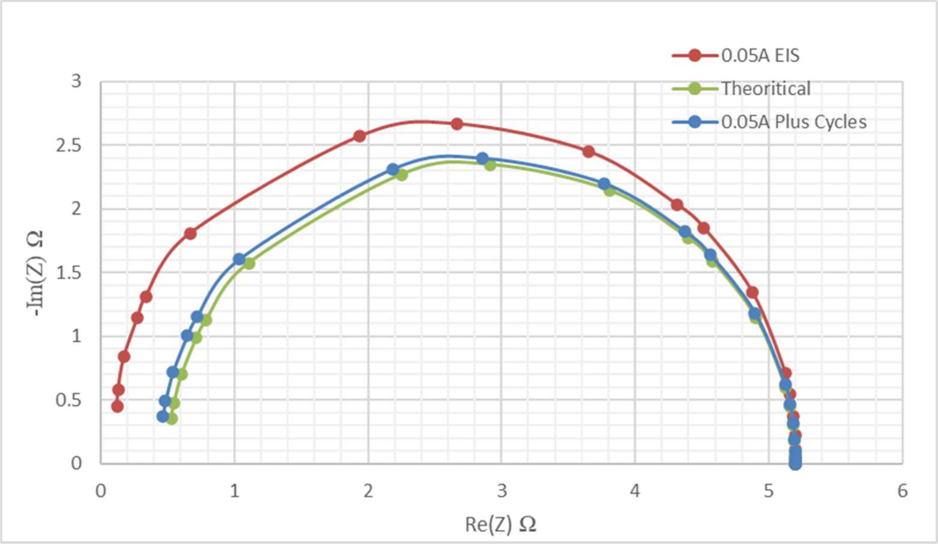

Fig. 10.5: Nyquist of the Randle circuit for different cycles

This shows that you needed to increase the number of periods to increase the accuracy of your impedance estimation.

Appendix C Datasheets

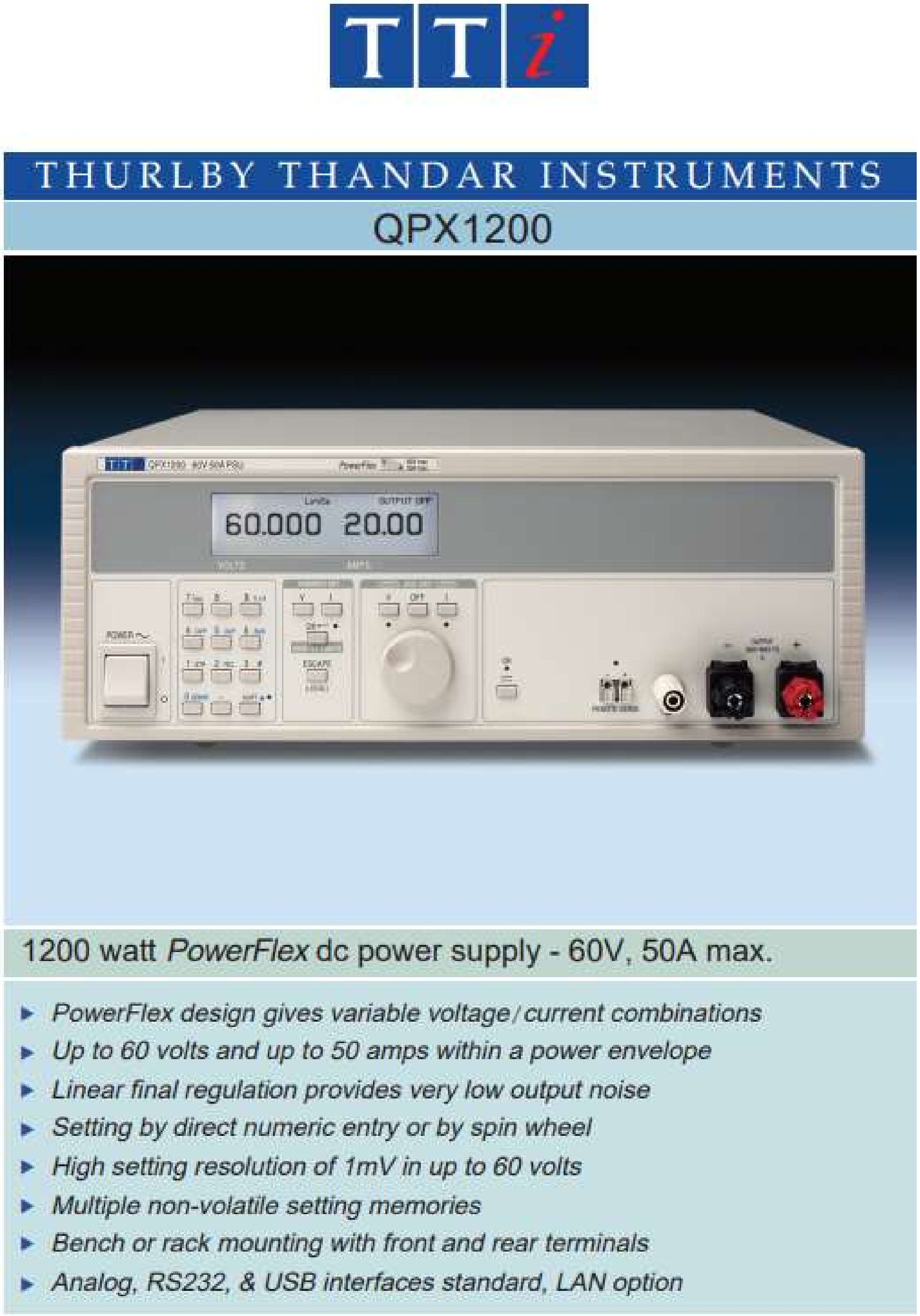

THURLBY THANDAR INSTRUMENTS

QPX1200

1200 watt *PowerFlex* dc power supply - 60V, 50A max.

- *PowerFlex design gives variable voltage/current combinations*
- *Up to 60 volts and up to 50 amps within a power envelope*
- *Linear final regulation provides very low output noise*
- *Setting by direct numeric entry or by spin wheel*
- *High setting resolution of 1mV in up to 60 volts*
- *Multiple non-volatile setting memories*
- *Bench or rack mounting with front and rear terminals*
- *Analog, RS232, & USB interfaces standard, LAN option*

Fig. 10.6 10.7: Specifications for the QPX 1200L power supply [58]

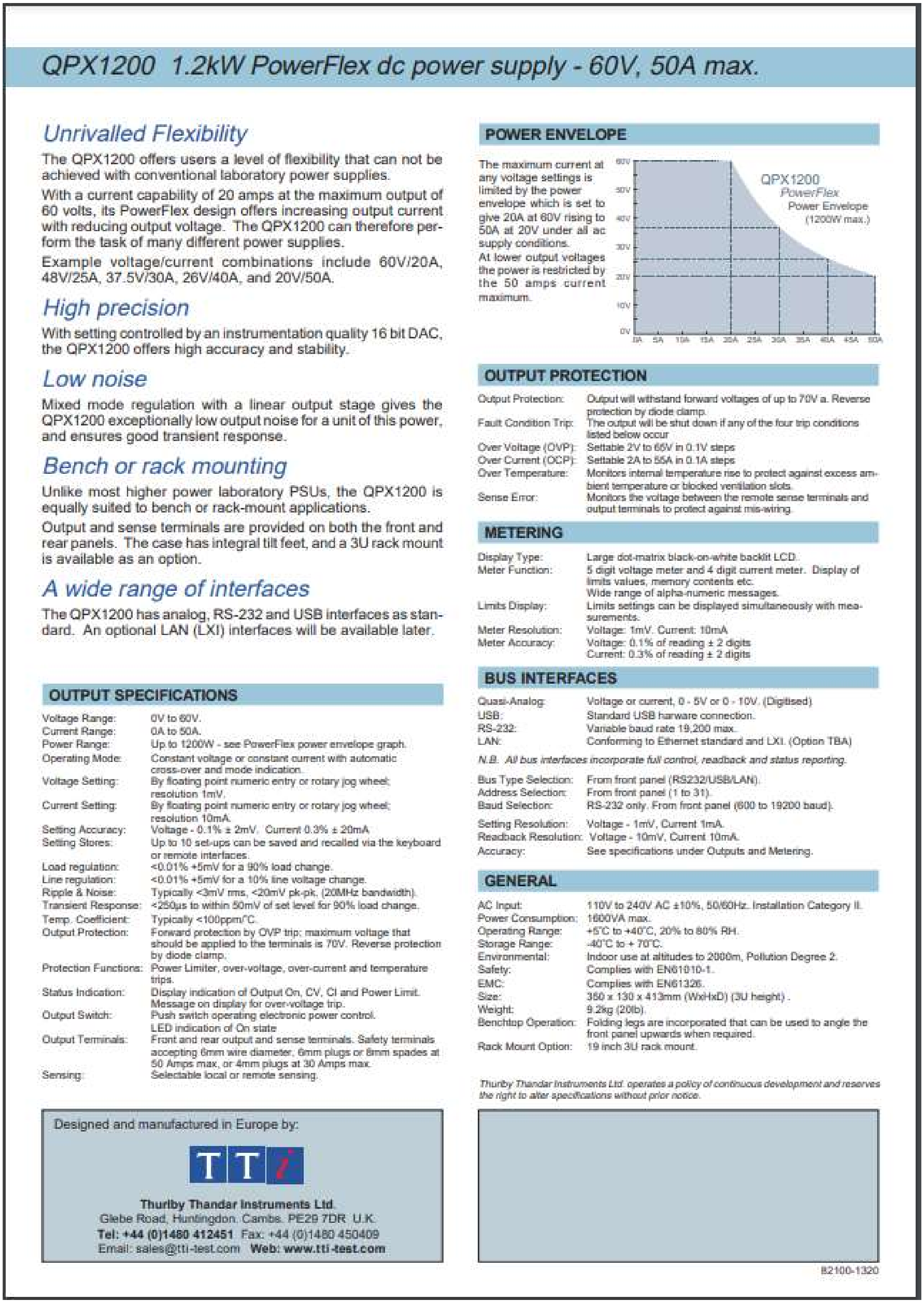

QPX1200 1.2kW PowerFlex dc power supply - 60V, 50A max.

Unrivalled Flexibility

The QPX1200 offers users a level of flexibility that can not be achieved with conventional laboratory power supplies.

With a current capability of 20 amps at the maximum output of 60 volts, its PowerFlex design offers increasing output current with reducing output voltage. The QPX1200 can therefore perform the task of many different power supplies.

Example voltage/current combinations include 60V/20A, 48V/25A, 37.5V/30A, 26V/40A, and 20V/50A.

High precision

With setting controlled by an instrumentation quality 16 bit DAC, the QPX1200 offers high accuracy and stability.

Low noise

Mixed mode regulation with a linear output stage gives the QPX1200 exceptionally low output noise for a unit of this power, and ensures good transient response.

Bench or rack mounting

Unlike most higher power laboratory PSUs, the QPX1200 is equally suited to bench or rack-mount applications.

Output and sense terminals are provided on both the front and rear panels. The case has integral tilt feet, and a 3U rack mount is available as an option.

A wide range of interfaces

The QPX1200 has analog, RS-232 and USB interfaces as standard. An optional LAN (LXI) interfaces will be available later.

OUTPUT SPECIFICATIONS

Voltage Range:	0V to 60V.
Current Range:	0A to 50A.
Power Range:	Up to 1200W - see PowerFlex power envelope graph.
Operating Mode:	Constant voltage or constant current with automatic cross-over and mode indication.
Voltage Setting:	By floating point numeric entry or rotary jog wheel; resolution 1mV.
Current Setting:	By floating point numeric entry or rotary jog wheel; resolution 10mA.
Setting Accuracy:	Voltage - 0.1% ± 2mV. Current 0.3% ± 20mA
Setting Stores:	Up to 10 set-ups can be saved and recalled via the keyboard or remote interfaces.
Load regulation:	<0.01% +5mV for a 90% load change.
Line regulation:	<0.01% +5mV for a 10% line voltage change.
Ripple & Noise:	Typically <3mV rms, <20mV pk-pk, (20MHz bandwidth).
Transient Response:	<250μs to within 50mV of set level for 90% load change.
Temp. Coefficient:	Typically <100ppm/°C.
Output Protection:	Forward protection by OVP trip; maximum voltage that should be applied to the terminals is 70V. Reverse protection by diode clamp.
Protection Functions:	Power Limiter, over-voltage, over-current and temperature trips.
Status Indication:	Display indication of Output On, CV, CI and Power Limit. Message on display for over-voltage trip.
Output Switch:	Push switch operating electronic power control. LED indication of On state
Output Terminals:	Front and rear output and sense terminals. Safety terminals accepting 6mm wire diameter, 6mm plugs or 8mm spades at 50 Amps max, or 4mm plugs at 30 Amps max.
Sensing:	Selectable local or remote sensing.

Designed and manufactured in Europe by:

TTi

Thurlby Thandar Instruments Ltd.
Glebe Road, Huntingdon. Cambs. PE29 7DR U.K.
Tel: +44 (0)1480 412451 Fax: +44 (0)1480 450409
Email: sales@tti-test.com **Web: www.tti-test.com**

POWER ENVELOPE

The maximum current at any voltage settings is limited by the power envelope which is set to give 20A at 60V rising to 50A at 20V under all ac supply conditions.

At lower output voltages the power is restricted by the 50 amps current maximum.

OUTPUT PROTECTION

Output Protection:	Output will withstand forward voltages of up to 70V a. Reverse protection by diode clamp.
Fault Condition Trip:	The output will be shut down if any of the four trip conditions listed below occur
Over Voltage (OVP):	Settable 2V to 65V in 0.1V steps
Over Current (OCP):	Settable 2A to 55A in 0.1A steps
Over Temperature:	Monitors internal temperature rise to protect against excess ambient temperature or blocked ventilation slots.
Sense Error:	Monitors the voltage between the remote sense terminals and output terminals to protect against mis-wiring.

METERING

Display Type:	Large dot-matrix black-on-white backlit LCD.
Meter Function:	5 digit voltage meter and 4 digit current meter. Display of limits values, memory contents etc. Wide range of alpha-numeric messages.
Limits Display:	Limits settings can be displayed simultaneously with measurements.
Meter Resolution:	Voltage: 1mV. Current: 10mA
Meter Accuracy:	Voltage: 0.1% of reading ± 2 digits Current: 0.3% of reading ± 2 digits

BUS INTERFACES

Quasi-Analog:	Voltage or current, 0 - 5V or 0 - 10V. (Digitised)
USB:	Standard USB harware connection.
RS-232:	Variable baud rate 19,200 max.
LAN:	Conforming to Ethernet standard and LXI. (Option TBA)

N.B. All bus interfaces incorporate full control, readback and status reporting.

Bus Type Selection:	From front panel (RS232/USB/LAN).
Address Selection:	From front panel (1 to 31).
Baud Selection:	RS-232 only. From front panel (600 to 19200 baud).
Setting Resolution:	Voltage - 1mV, Current 1mA.
Readback Resolution:	Voltage - 10mV, Current 10mA.
Accuracy:	See specifications under Outputs and Metering.

GENERAL

AC Input:	110V to 240V AC ±10%, 50/60Hz. Installation Category II.
Power Consumption:	1600VA max.
Operating Range:	+5°C to +40°C, 20% to 80% RH.
Storage Range:	-40°C to + 70°C.
Environmental:	Indoor use at altitudes to 2000m, Pollution Degree 2.
Safety:	Complies with EN61010-1.
EMC:	Complies with EN61326.
Size:	350 x 130 x 413mm (WxHxD) (3U height) .
Weight:	9.2kg (20lb).
Benchtop Operation:	Folding legs are incorporated that can be used to angle the front panel upwards when required.
Rack Mount Option:	19 inch 3U rack mount.

Thurlby Thandar Instruments Ltd. operates a policy of continuous development and reserves the right to alter specifications without prior notice.

82100-1320

Fig. 10.8: Electrical characteristics of QPX 1200L power supply [58]

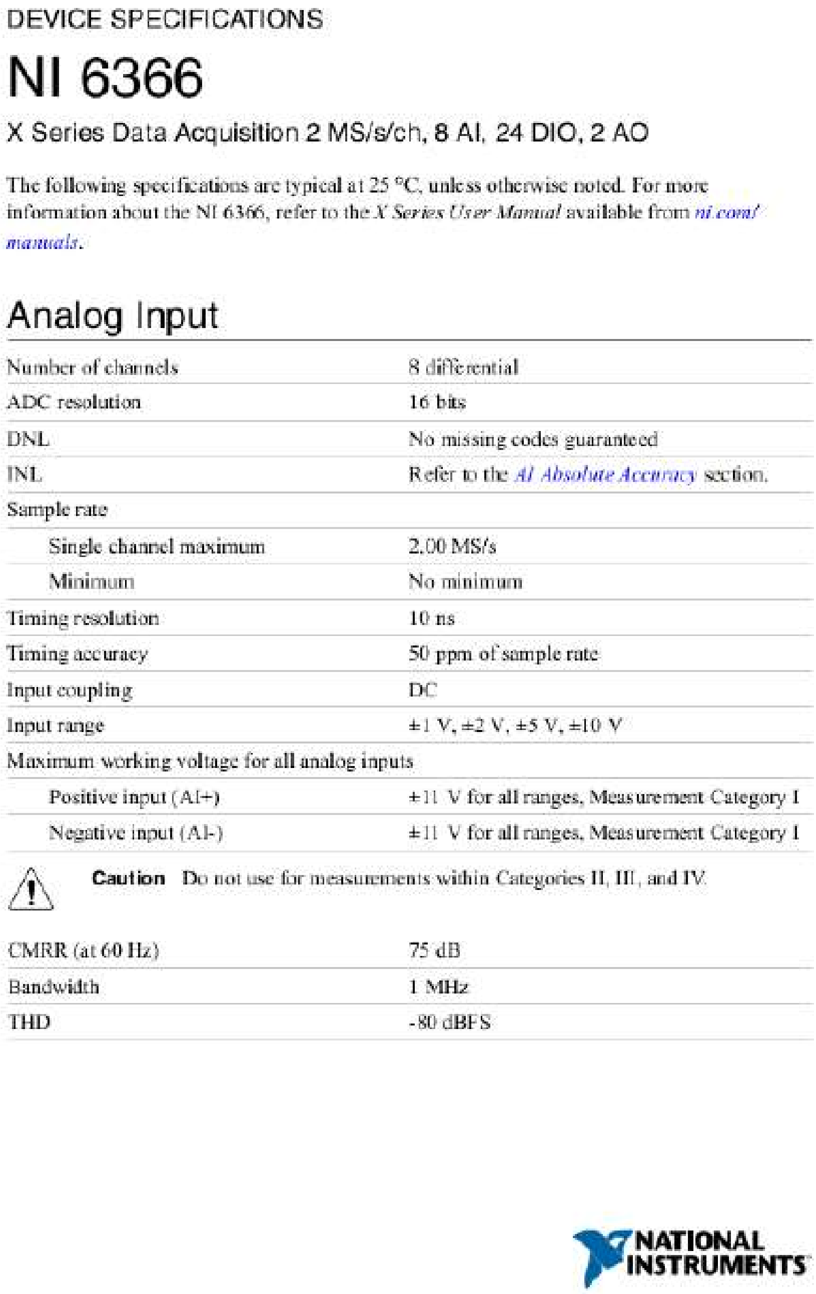
DEVICE SPECIFICATIONS

NI 6366

X Series Data Acquisition 2 MS/s/ch, 8 AI, 24 DIO, 2 AO

The following specifications are typical at 25 °C, unless otherwise noted. For more information about the NI 6366, refer to the *X Series User Manual* available from *ni.com/manuals*.

Analog Input

Number of channels	8 differential
ADC resolution	16 bits
DNL	No missing codes guaranteed
INL	Refer to the *AI Absolute Accuracy* section.
Sample rate	
Single channel maximum	2.00 MS/s
Minimum	No minimum
Timing resolution	10 ns
Timing accuracy	50 ppm of sample rate
Input coupling	DC
Input range	±1 V, ±2 V, ±5 V, ±10 V
Maximum working voltage for all analog inputs	
Positive input (AI+)	±11 V for all ranges, Measurement Category I
Negative input (AI-)	±11 V for all ranges, Measurement Category I

Caution Do not use for measurements within Categories II, III, and IV.

CMRR (at 60 Hz)	75 dB
Bandwidth	1 MHz
THD	-80 dBFS

Fig. 10.9: NI USB 6366 device specifications [63]

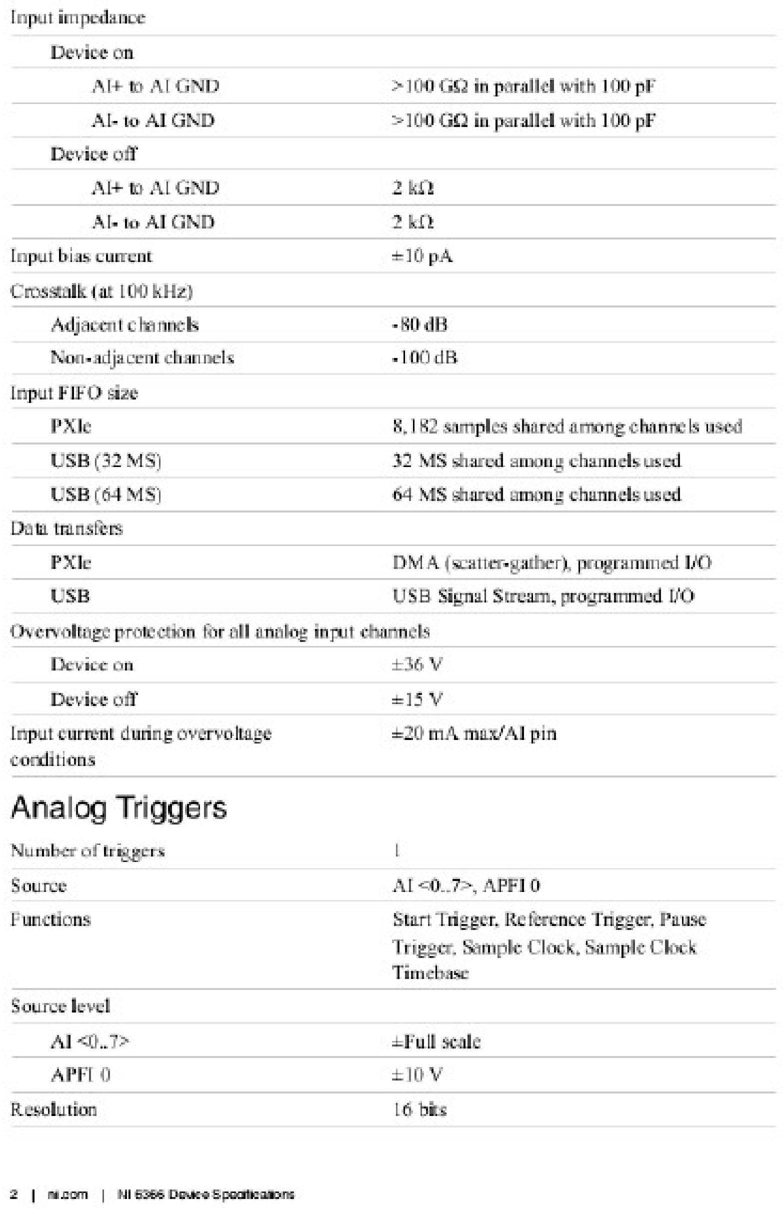

Input impedance	
Device on	
AI+ to AI GND	>100 GΩ in parallel with 100 pF
AI- to AI GND	>100 GΩ in parallel with 100 pF
Device off	
AI+ to AI GND	2 kΩ
AI- to AI GND	2 kΩ
Input bias current	±10 pA
Crosstalk (at 100 kHz)	
Adjacent channels	-80 dB
Non-adjacent channels	-100 dB
Input FIFO size	
PXIe	8,182 samples shared among channels used
USB (32 MS)	32 MS shared among channels used
USB (64 MS)	64 MS shared among channels used
Data transfers	
PXIe	DMA (scatter-gather), programmed I/O
USB	USB Signal Stream, programmed I/O
Overvoltage protection for all analog input channels	
Device on	±36 V
Device off	±15 V
Input current during overvoltage conditions	±20 mA max/AI pin

Analog Triggers

Number of triggers	1
Source	AI <0..7>, APFI 0
Functions	Start Trigger, Reference Trigger, Pause Trigger, Sample Clock, Sample Clock Timebase
Source level	
AI <0..7>	±Full scale
APFI 0	±10 V
Resolution	16 bits

2 | ni.com | NI 6366 Device Specifications

Fig. 10.10: Analog input specifications for NI USB 6366 [63]

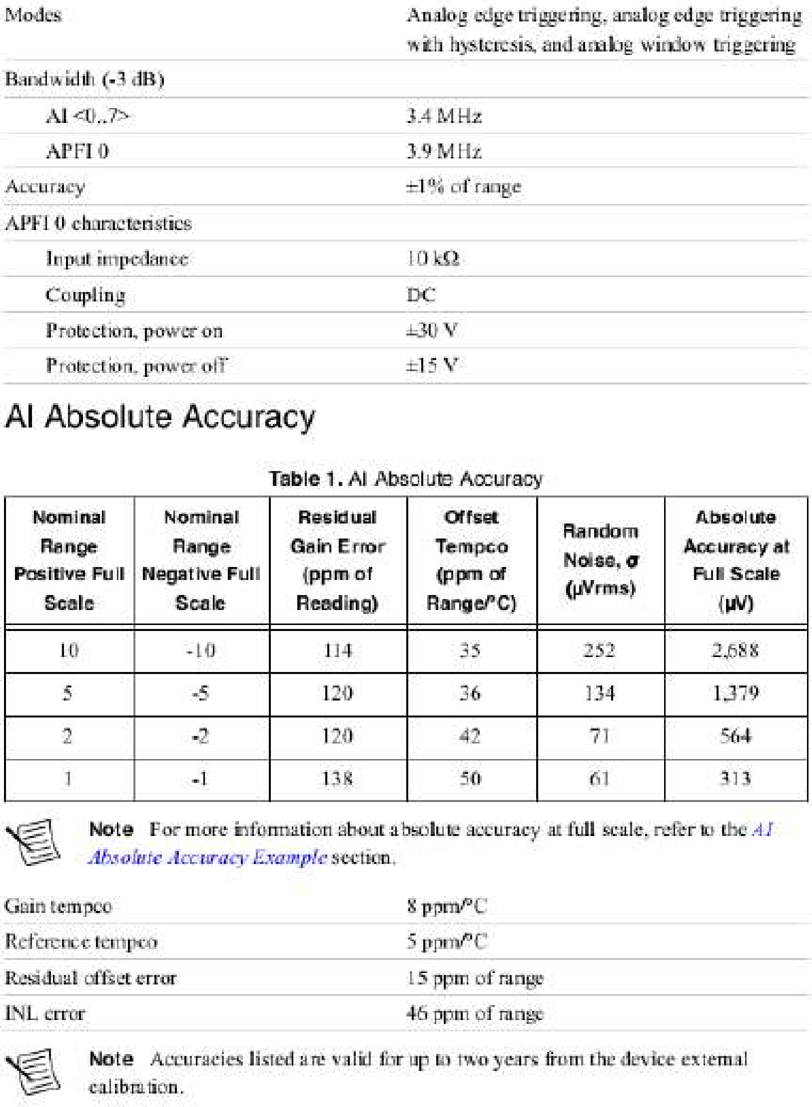

Modes	Analog edge triggering, analog edge triggering with hysteresis, and analog window triggering
Bandwidth (-3 dB)	
AI <0..7>	3.4 MHz
APFI 0	3.9 MHz
Accuracy	±1% of range
APFI 0 characteristics	
Input impedance	10 kΩ
Coupling	DC
Protection, power on	±30 V
Protection, power off	±15 V

AI Absolute Accuracy

Table 1. AI Absolute Accuracy

Nominal Range Positive Full Scale	Nominal Range Negative Full Scale	Residual Gain Error (ppm of Reading)	Offset Tempco (ppm of Range/°C)	Random Noise, σ (μVrms)	Absolute Accuracy at Full Scale (μV)
10	-10	114	35	252	2,688
5	-5	120	36	134	1,379
2	-2	120	42	71	564
1	-1	138	50	61	313

Note For more information about absolute accuracy at full scale, refer to the *AI Absolute Accuracy Example* section.

Gain tempco	8 ppm/°C
Reference tempco	5 ppm/°C
Residual offset error	15 ppm of range
INL error	46 ppm of range

Note Accuracies listed are valid for up to two years from the device external calibration.

Fig. 10.11:Absolute Analog accuracy for NI USB 6366 [63]

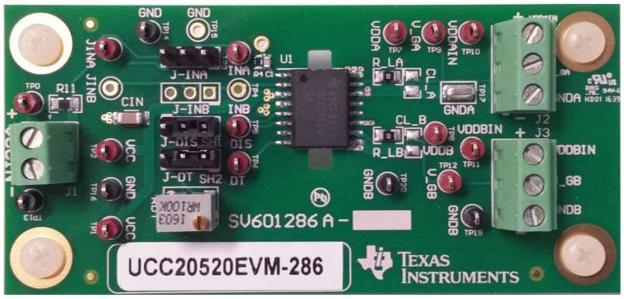

Fig. 10.12:MOSFERT driver UCC20520EVM-286

Appendix D MATLAB code

B.3 *Impedance estimation for single sinusoid*

```
%%%This determine the impedance of a single sinusoid sigal,it uses the
%%%Measured singal,with the known period, frequency and smapling frequency
%%%Update Fs,N_priod and freq
%%%This is code modified but originally used by akIN Aroge and share online on
https://github.com/akin-aroge/thesis-code/tree/master/matlab_code
Fs=200000; %%%Sampling frequency
freq=1;%%Fruquecny of sampled signal
t_period = 1/freq; % signal period
n_samp_period = t_period*Fs; % sample period of signal (samples in one period
n_period=3; %%number of periods
N =int16(n_samp_period*n_period);
%%%Update Fs,N_priod and freq
Ts=1/Fs;
start_eis=0.2/Ts;
n_period=3;
%%Slicing the signal,to remove the transient state
volt= voltage(start_eis+1:end) - mean(voltage(start_eis+1:end));
curr = current(start_eis+1:end) - mean(current(start_eis+1:end));
%  volt=filter(lpFilt,volt);
%  curr=filter(lpFilt,curr);

%%Perform the Fast Fourier Transform
v_fft = fft(volt);
i_fft = fft(curr);

%%Index my fast fourier arrays, to obtain the EIS impedance
imp_cmplx = v_fft(n_period+1)/(i_fft(n_period+1));
z_re = real(imp_cmplx); % the impedance gotten is negative (already)
z_im = -imag(imp_cmplx);
```

Appendix E Simulink diagrams

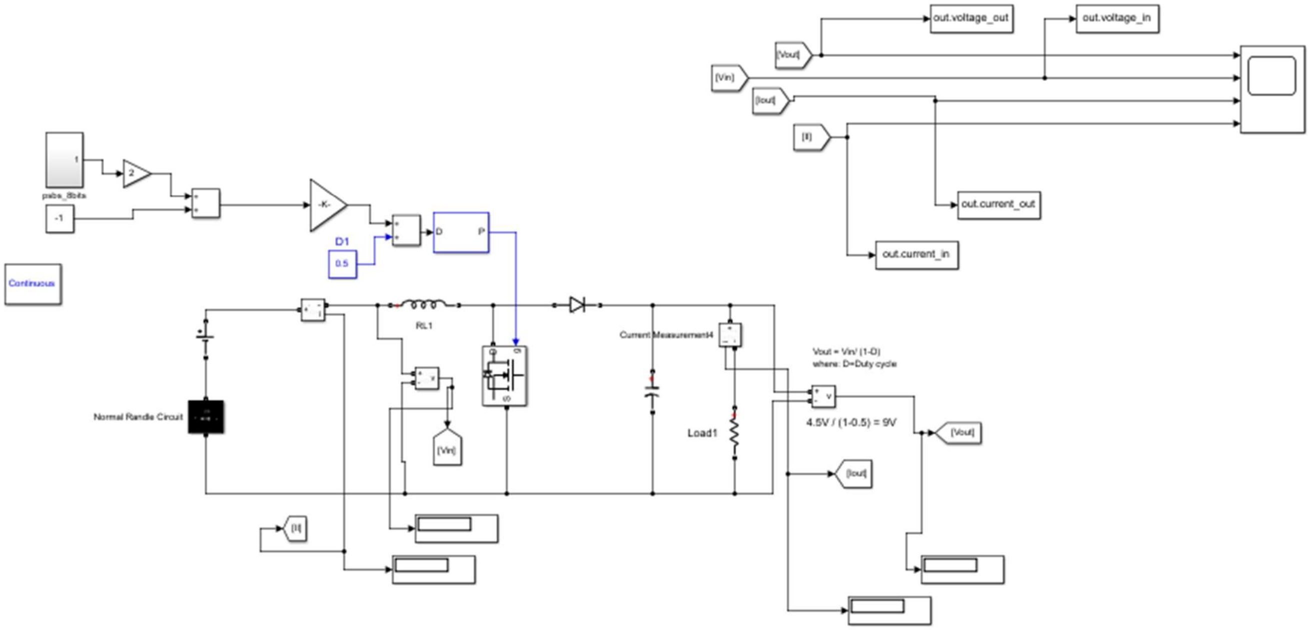

Fig. 10.13: Boost converter open-loop configuration

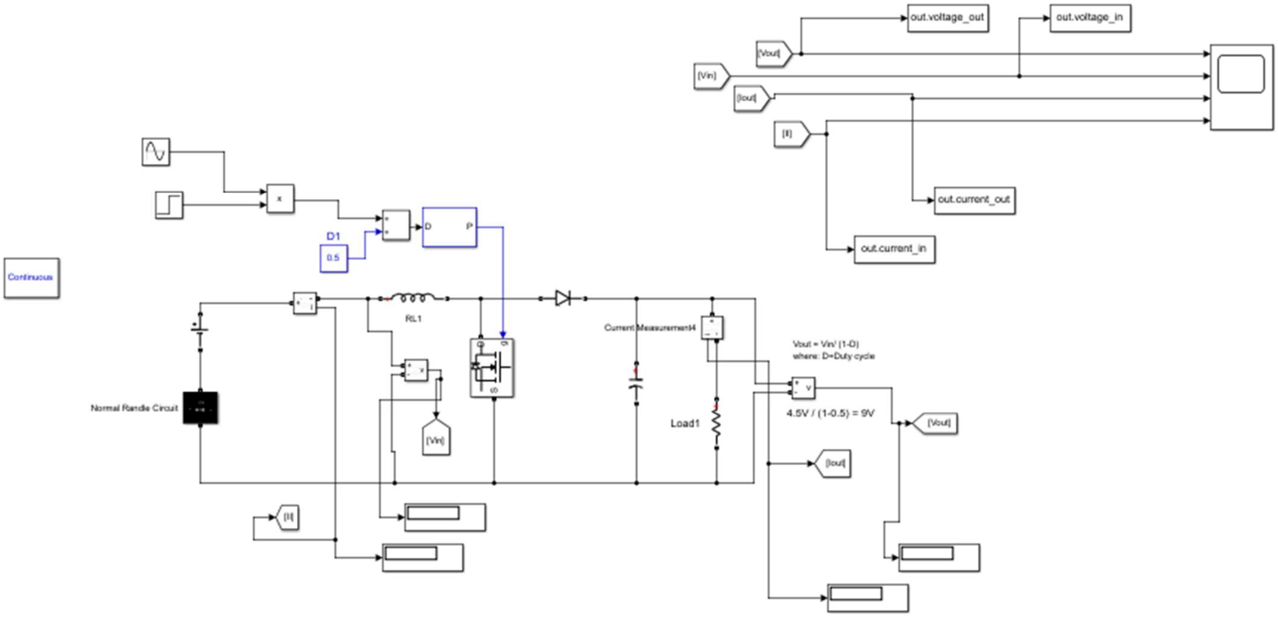

Fig. 10.14: Boost converter open-loop configuration

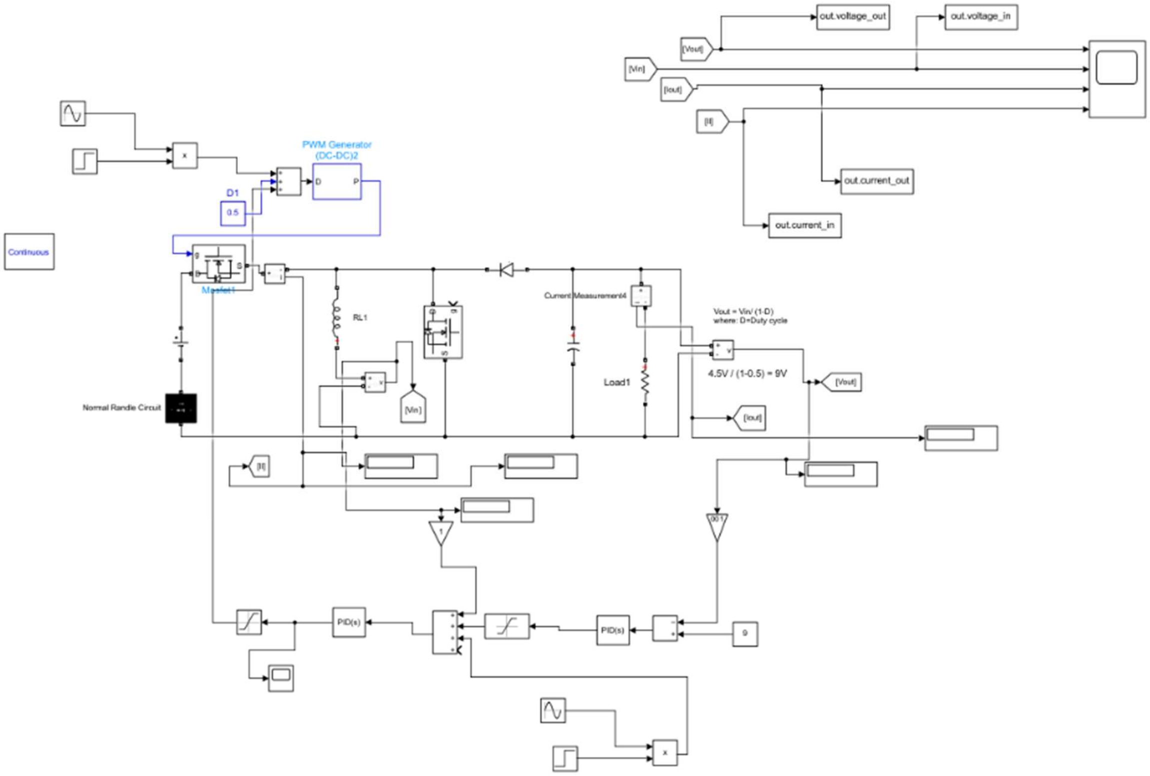

Fig. 10.15: Buck-boost converter closed-loop configuration

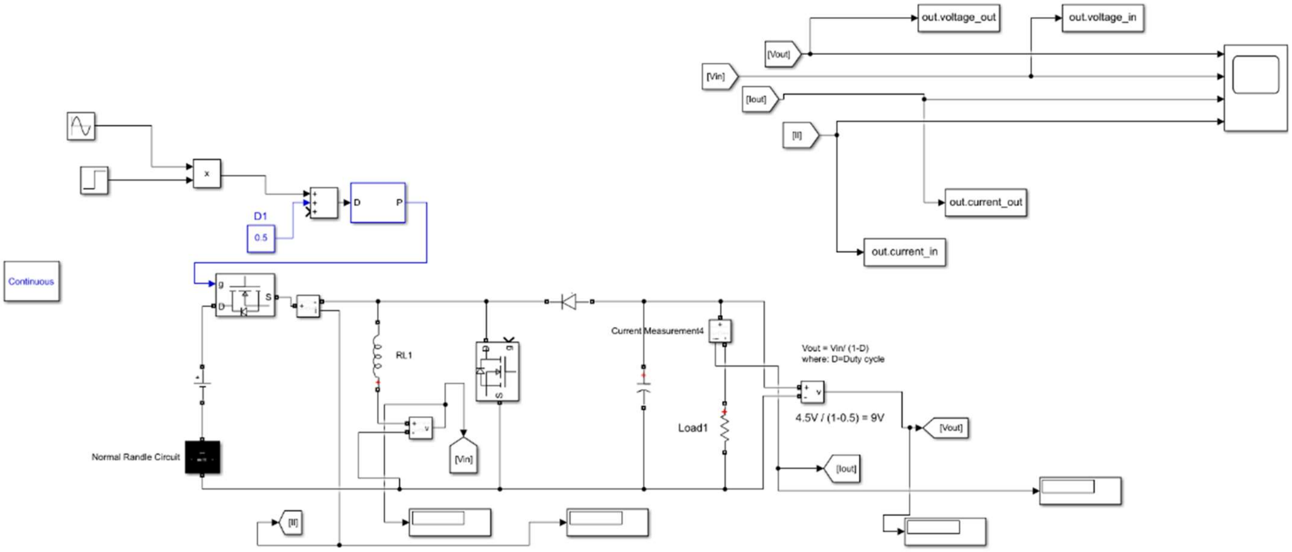

Fig. 10.16: Buck-boost converter open-loop configuration

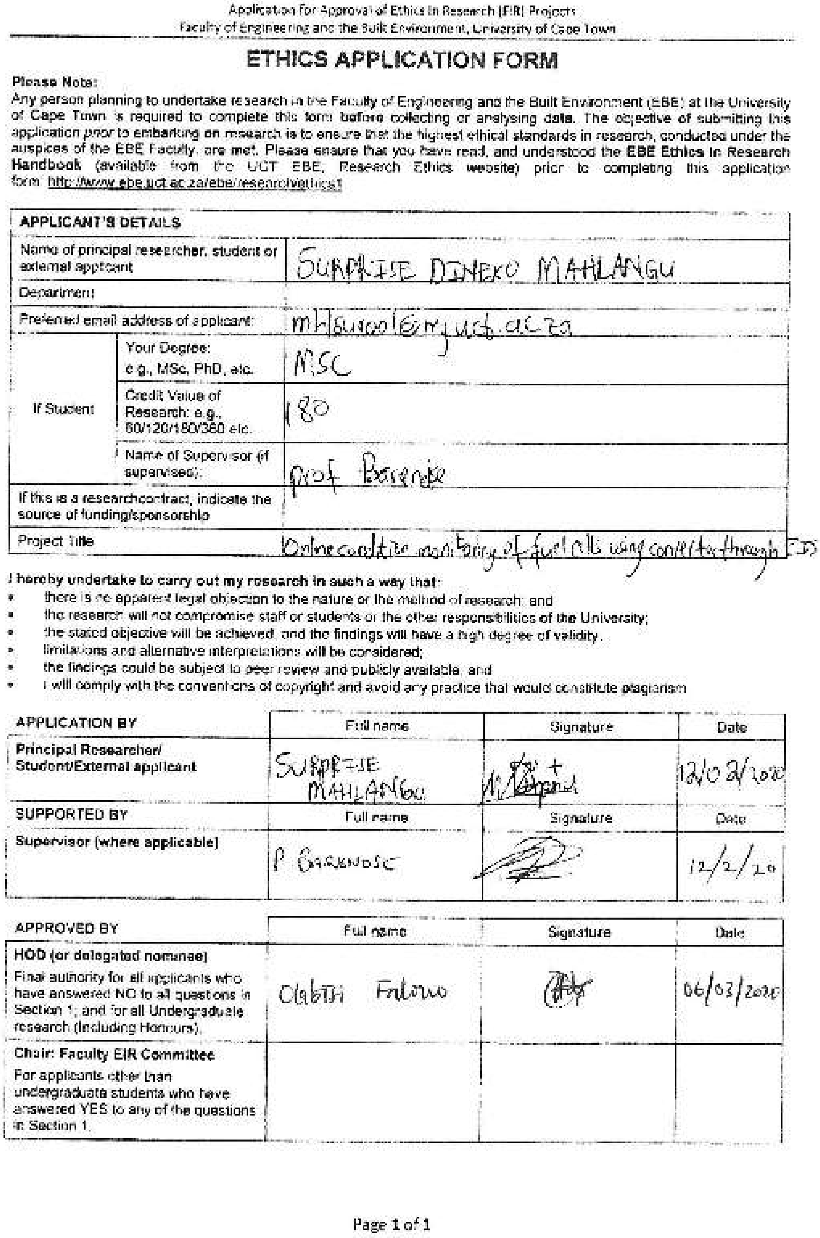

Application for Approval of Ethics in Research (EiR) Projects
Faculty of Engineering and the Built Environment, University of Cape Town

ETHICS APPLICATION FORM

Please Note:
Any person planning to undertake research in the Faculty of Engineering and the Built Environment (EBE) at the University of Cape Town is required to complete this form **before** collecting or analysing data. The objective of submitting this application *prior* to embarking on research is to ensure that the highest ethical standards in research, conducted under the auspices of the EBE Faculty, are met. Please ensure that you have read, and understood the **EBE Ethics in Research Handbook** (available from the UCT EBE, Research Ethics website) prior to completing this application form: http://www.ebe.uct.ac.za/ebe/research/ethics1

APPLICANT'S DETAILS		
Name of principal researcher, student or external applicant		SURPRISE DINEKO MAHLANGU
Department		
Preferred email address of applicant:		mhlsur001@myuct.ac.za
If Student	Your Degree: e.g., MSc, PhD, etc.	MSC
	Credit Value of Research: e.g., 60/120/180/360 etc.	180
	Name of Supervisor (if supervised):	prof Barendse
If this is a researchcontract, indicate the source of funding/sponsorship		
Project Title		Online condition monitoring of fuel cells using converter through EIS

I hereby undertake to carry out my research in such a way that:

- there is no apparent legal objection to the nature or the method of research; and
- the research will not compromise staff or students or the other responsibilities of the University;
- the stated objective will be achieved, and the findings will have a high degree of validity.
- limitations and alternative interpretations will be considered;
- the findings could be subject to peer review and publicly available, and
- I will comply with the conventions of copyright and avoid any practice that would constitute plagiarism

APPLICATION BY	Full name	Signature	Date
Principal Researcher/ Student/External applicant	SURPRISE MAHLANGU		12/02/2020
SUPPORTED BY	Full name	Signature	Date
Supervisor (where applicable)	P BARENDSE		12/2/20

APPROVED BY	Full name	Signature	Date
HOD (or delegated nominee) Final authority for all applicants who have answered NO to all questions in Section 1; and for all Undergraduate research (Including Honours).	Olabiyi Falowo		06/03/2020
Chair: Faculty EIR Committee For applicants other than undergraduate students who have answered YES to any of the questions in Section 1.			

Page 1 of 1